THE CDF CENTRAL ELECTROMAGNETIC CALORIMETER FOR PROTON-ANTIPROTON COLLISION EXPERIMENT AT TEVATRON

TERUKI KAMON

THE CDF CENTRAL ELECTROMAGNETIC CALORIMETER FOR PROTON-ANTIPROTON COLLISION EXPERIMENT AT TEVATRON

June 1986

TERUKI KAMON

Submitted in partial fulfillment of the requirements
for the degree of Doctor of Science
in Doctoral Program in
University of Tsukuba

ABSTRACT

The CDF central electromagnetic (EM) calorimter modules were calibrated with test beam and cosmic ray muons. It is found that (a) the modules are identical to each other by 1 % on the response map and (b) the uncertaity on the measurement of the energy of showering particle is better than 1.1 % in the 85 % of whole area. This suggests that the masses of W and Z can be determined with 0.7 %. The values of $\sin(\theta_w)$ and ρ can be determined within 1.4 % and 0.5 %. The values are improved as compared with the corresponding values for UA1 and UA2 experiments.

Part of CDF and data acquisition system were tested at the first operation of Tevatron in October 1985. All the system containing the central EM calorimeters properly worked in the test run. The proton-antiproton collision events at a center-of-mass energy of 1.6 TeV were taken. The data were analyzed on the energy flow and charged multiplicity per unit of pseudorapidity. The result was all the events are consistent with the non-single diffractive events characterized by a naive extraporation from ISR and SPS energy. The signature of calorimeter for Centauro is also studied. The expected signature was not found to about 6 mbarn at 1.6 CM energy.

In the future operation, a high luminosity make a detailed study of physics processes in the framework of the standard model and outside of the model possible. One of them is to search for a hypothesis heavy lepton at the high luminosity. Here the heavy

lepton is assumed to come from the W decay. The technique to serach for the lepton is presented.

ACKNOWLEDGEMENT

I would like to expressed my gratitude to Professor K.Kondo for his guidance and encouragement throughout my graduate career.

Professors K.Takikawa, S.Miyashita, S.Mori, S.Mikamo, M.Mishina, Drs. S.Kim, Y.Fukui and F.Abe are appreciated for their continuous encouragement and criticism.

This experiment would have been impossible without the very successful operation of the Tevatron Collider by staffs and coordinators. I gratefully acknowledge for their collective effort. A great number of people, each giving his or her unique contribution to the construction of CDF are also appreciated for their effort.

The experiment described in this thesis is the product of many collaboratiors:

The construction of wedge calorimeter was greatly assisted by the continued efforts of the Fermilab crews conducted by R.Krull and R.Peto of Argonne National Laboratory in Industrial Building IV at Fermilab. Dr. H.Jensen is appreciated for his effort of managing the calorimeter construction.

I thank Messers H.Chugun, R.Nakano, T.Shimizu, N.Takegoshi of Kyowa Gas Chemical Ind. Co. for cooperation in the routine work of quality control of the scintillator and WLS during the mass production. Miss. Y.Kikuchi, Messers F.Ukegawa and A.Yamashita are appriciated for the cooperation of data taking and analysis on quality control data. Drs. D.Underwood and

K.Yasuoka and Mr. Yamashita are appreciated for their effort on the quality control of wavelength shifters. Drs. L.Nodulman and P.Schossow are also appreciated for the the EM calorimeter construction at ANL.

I am grateful to Dr. R.G.Wagner for his cooperation and effort in the course of the cosmic ray test. Professors S.Mikamo, S.Kobayashi and A.Murakami, Drs. A.D.Virgilio, J.Elias and K.Yasuoka are appreciated for their collaboration in the cosmic ray test. The maintenance of muon chembers was assisted by the continued efforts of Dr. S.Cihangir, Messers D.Smith and T.Westhuging. Thanks are due to Dr. R.Dieblod for his helpful suggestion in data analysis, Dr. E.Focardi for his help in development of data analysis program, Drs. S.Beltolocci, M.Curatolo and A.Sansoni for their help in the cosmic ray test. Also many thanks are due to Dr. G.Drake and other people of P.I.G. group to understand the CDF front end electronics system. Special thanks are again due to Drs. R.G.Wagner and S.Mikamo for their advices and encouragements throughout the course of this work.

I wish to thank Drs. J.W.Cooper, S.Hahn, D.Hahn, J.Proudfoot, and K.Yasuoka, Messers D.Conor and M.Miller and other wedge test collaborators for their cooperation and continuous efforts in the wedge beam test. I also thank Dr. A.B.Wicklund for understanding the central strip chamber in the analysis of the test beam data.

Professor T.Devlin and Dr. U.Joshi are appreciated for their effort on phototube test for cosmic ray test and beam test.

Drs. Y.Takaiwa and J.Yoh are greatly helpful for understanding and improvement of event generation package. I wish to thank Drs. Y.Hayashide and J.E.Freeman for the development of offline package on the detector simulation with me. Dr. G.P.Yeh is appreciated for his effort on the software development of the track simulation and display on VTPC.

Many thanks are due to Dr. D.Quarrie, C.van Ingen, T.Carroll and other people of online group for the development of the software on the online data taking system. Especially the conversation with Dr. D.Quarrie is helpful for writing the consumer process for the trigger status check. in 1985 run.

I wish to thank Professor H.J.Frisch and Dr. T.M.Liss for the development of BBC system and their helpful suggestions in the data analysis.

Dr. T.Yamanouchi is also appreciated for his helpful discussion on the data analysis on BBC trigger and his encouragement.

I wish to thank Mr. M.Sekiguchi for understanding the VTPC system in the first collision data analysis.

Messers L.Demortier, D.Brown, R.St.Dennis, R.Harris, M.Shibata, Y.Morita, T.Ozaki, T.Mimashi, and S.Kanda are appreciated for their encouragement.

I am also grateful to other CDF collaborators for their effort throughout this detector construction.

The present work was carried out as a program of the Collider Detector at Fermilab (CDF) under the accord of US-Japan collaboration in high energy physics. I gratefully acknowledge the support of the U.S.DOE and the Japanese Ministry of Education, Science and Culture. I wish to express my special thanks to Dr. A.Tollestrup (CDF co-leader), Professor R.Schwitters (CDF co-leader), Drs. K.Stanfield (Head of Research Division) and L.Lederman (Director) of Fermilab.

CONTENTS

ABSTRACT

ACKNOWLEDGEMENT

CHAPTER 1 INTRODUCTION

1.1 PHYSICS MOTIVATION 1

1.2 GENERAL DESIGN CONSIDERATION OF THE CDF 10

1.2.1 Detector Design 10

1.2.2 Detector Calibration 15

1.3 OUTLINE OF THE ARTICLE 16

CHAPTER 2 THE CENTRAL EM CALORIMETER

2.1 GENERAL DESCRIPTION OF THE STRUCTURE 17

2.2 SCINTILLATOR: SCSN38 19

2.3 WAVELENGTH SHIFTER: Y7 19

2.4 PHOTOTUBE: HAMAMATSU MODEL R580B 20

2.5 STRIP CHAMBER 21

CHAPTER 3 QUALITY CONTROL IN PRODUCTION OF SCINTILLATOR FOR EM CALORIMETER

3.1 INTRODUCTION 23

3.2 MASS PRODUCTION 25
3.3 MEASUREMENT FOR LIGHT YIELD 26
3.3.1 Test Samples 26
3.3.2 Measurement 27
3.4 MEASUREMENT FOR THICKNESS 28
3.4.1 Test Samples 28
3.4.2 Measurement 28
3.5 MEASUREMENT FOR ATTENUATION LENGTH 30
3.5.1 Test Samples 30
3.5.2 Measurement 30
3.6 RESULTS 31
3.6.1 Non-uniformity On Light Yield 31
3.6.2 Non-uniformity On Thickness 33
3.6.3 Non-uniformity On Attenuation Length 34
3.7 EFFECTS ON CALORIMETER RESPONSE 35

CHAPTER 4 THE CALIBRATION MONITORING SYSTEM

4.1 SOURCE CALIBRATION SYSTEM 38
4.2 LED AND XENON FLASHER SYSTEM 39

CHAPTER 5 ELECTRONICS

5.1 THE RABBIT SYSTEM 41
5.2 HIGH VOLTAGE SYSTEM 44

CHAPTER 6 DETECTOR CALIBRATION: BEAM AND COSMIC RAY TESTS

6.1 CALIBRATION PROCEDURE 46
6.2 TEST BEAM SET UP 47
6.2.1 NW Beam Line 48
6.2.2 Trigger And Data Acquisition System 49
6.3 COSMIC RAY TEST STAND 50
6.3.1 Trigger Counters And Rates 50
6.3.2 Muon Tracking 52
6.3.3 Trigger And Data Acquisition Electronics 53
6.3.4 On-line Computer And Data Recording 56
6.4 FRONT END ELECTRONICS CALIBRATION 57
6.5 DATA ANALYSIS 58
6.5.1 Test Beam Data 58
6.5.2 Cosmic Ray Data 60
6.5.3 Source Calibration Data 64

CHAPTER 7 DETECTOR PERFORMANCE: RESULTS OF TESTS

7.1 CALIBRATION CONSTANT 66
7.2 LINEARITY/RESOLUTION 67
7.3 MUON PULSE HEIGHT DISTRIBUTION 68
7.4 RESPONSE MAP 71
7.4.1 Similarity Of Response Maps 71
7.4.2 Parameters W And L 73
7.4.3 Comparison With Beam Test Results 76
7.4.4 Parametrization Of Response Map 77
7.5 LONG-TERM STABILITY 79

7.6 STRIP CHAMBER 80

CHAPTER 8 THE FIRST COLLISION

8.1 1985 CDF RUN HISTORY 83
8.2 EXPERIMENTAL APPARATUS 84
8.2.1 Calorimetry 84
8.2.2 VTPC 84
8.2.3 Beam-Beam Counter System 85
8.3 TRIGGER SYSTEM 86
8.3.1 Beam-Beam Counter Trigger 86
8.3.2 Calorimeter Level 1 Trigger 87
8.4 DATA ACQUISITION SYSTEM 88
8.4.1 Master Clock System 88
8.4.2 Electronics 88
8.4.3 Data Acquisition Hardware And Computing 89
8.5 EVENT SELECTION 90
8.5.1 Scan Of VTPC Data 90
8.5.2 Scan Of BBC Data 92
8.6 LEVEL 1 TRIGGER THRESHOLD AND EFFICIENCY FOR UNBIASED EVENTS 93
8.7 MONTE CARLO DATA SAMPLE TO BE COMPARED WITH REAL DATA 94
8.7.1 Event Generation Model 94
8.7.2 Detector Simulation 97
8.8 RESULTS: BEAM-BEAM EVENTS 98
8.8.1 Charged Multiplicity Of Observed Events Compared

With MC Results. 98
8.8.2 Energy Flow Of Observed Events Compared With MC Events 101
8.9 BACKGROUND FOR BBC TRIGGER 102
8.9.1 Rate Of Beam-Beam Events 103
8.9.2 Rate Of Beam-Gas Events 103
8.9.3 Backward Scattering In BG Event 104
8.9.4 Coincidence Of BG(proton) And BG(antiproton) . . 106
8.9.5 Coincidence Of BG And BB 106
8.9.6 L1 Trigger Efficiency 107
8.9.7 Consideration And Summary 108

CHAPTER 9 MONTE CARLO STUDY ON DETECTION OF HEAVY LEPTON

9.1 INTRODUCTION 110
9.2 EVENT GENERATION/SIMULATION 110
9.3 EVENT ANALYSIS 111
9.4 RESULTS 113

CHAPTER 10 SUMMARY AND CONCLUSIONS

APPENDIX A CDF COLLABORATION

APPENDIX B FERMILAB PROTON-ANTIPROTON COLLIDER

APPENDIX C

C.1 CORRECTION FOR SYSTEMATIC ERRORS 126

C.2 CORRECTIONS FOR SAMPLE THICKNESS 127

REFFERENCES

FIGURE CAPTIONS

TABLES

FIGURES

CHAPTER 1

INTRODUCTION

1.1 PHYSICS MOTIVATION

The first operation of the Fermilab proton-antiproton collider (Tevatron) was successfully made in October 1985. Collisions in Tevatron at a center of mass energy of 1.6 TeV were observed with the Collider Detector at Fermilab (CDF) [1.1] (*). The collider energy will be raised up to 2 TeV in the future.

Future experiments with CDF in this new energy frontier will provide many exciting results for particle physics. Here the author would like to pick up typical examples of physics subjects to be persued with CDF, assuming the cases of Tevatron operation with (1) high and (2) low luminosity. Those interesting events to be discussed below are (1) events related to the electroweak interaction, namely W and Z and (2) non-diffractive events (minimum bias events).

(*) The members and their institutions of CDF collaboration are listed in Appendix A. A brief description of Tevatron is provided in Appendix B.

Physics at high luminosity

The Glashow-Salam-Weinberg Model (SU(2) x U(1) Standard Model) [1.2] of the electroweak interaction is now a part of the furniture of high energy physics. The $W\pm$ [1.3] and Z0 [1.4] bosons which mediate electroweak interactions of leptons and quarks [1.5] were observed through their leptonic decay modes in CERN proton-antiproton Collider (SPS) experiments. However, Higgs particle or the neutral spin zero particle, which is required in the standard model, is not observed yet. The mass is essentially a free parameter.

A measurement of the mass ratio of W and Z is of paticular interest for checking the standard model. The masses of W and Z0 determine the Weinberg angle (θw) and rho parameter for the standard model:

$$\sin^2(\theta w) = A / Mw^2 \quad ; A = (38.65\ GeV/c^2)^2 \qquad (1.1)$$

$$\rho = Mw^2 / Mz^2 \cos^2(\theta w) \ . \qquad (1.2)$$

Since ρ is 1 in the minimal model with only one Higgs doublet, ρ is a good probe to check the minimal standard model. The results on the measurement of masses of W and Z0 in UA1 and UA2 experiments at CERN are presented in Table 1.1 [1.3, 1.4, 1.6]. Combining the results, one obtains

$$\sin^2(\theta w) = 0.223 \pm 0.008,$$

$$\rho = 1.007 \pm 0.033.$$

They are in agreement with the prediction of the minimal model.

In the standard model, the family patterns are implied by the weak isospin doublets such as

$$\begin{pmatrix} u \\ d \end{pmatrix} \quad \begin{pmatrix} c \\ s \end{pmatrix} \quad \begin{pmatrix} t \\ b \end{pmatrix} \cdots$$

$$\begin{pmatrix} \nu \\ e \end{pmatrix} \quad \begin{pmatrix} \nu \\ \mu \end{pmatrix} \quad \begin{pmatrix} \nu \\ \tau \end{pmatrix} \cdots$$

The number of quarks and leptons in Nature is presently unknown and outside of the standard model's predictive capabilities. However, a constraint arises from the Adler's anomalies [1.7],

$$\sum_{\text{fermions}} Q = 0 , \qquad (1.3)$$

which is individually satisfied by each generation (counting quarks three times for colour). The values of the masses of quarks and leptons also are not explained within the standard model. This raises a question about how many generations exist in Nature. Forty or fifty years ago, only a few "elementary" particles - the proton and neutron, the electron and neutrino, together with photon were known. However, attempts to understand the details of the nuclear force between protons and neutrons led to the observation of many hundreds of hadron states. The regularities and patterns among the hadron states are interpreted by the qurak model. Just as such attempt, the search of the fourth generation particles (heavy object) will lead to a new step of constitution for quarks and leptons.

A direct measurement of the total width of the Z0 yield information about the number (N_ν) of light neutrinos [1.8]. The

UA1 and UA2 experimental bounds [1.6] of the width are less than 8.3 GeV and 4.6 GeV, respectively, at 90 % confidence level. One obtains a limit on N_ν as 33 from UA1 and 13 from UA2 results. Here it is assumed that the QCD-corrected theoretical width for three families in the standard model is 2.83 GeV and the partial width for $Z \rightarrow \nu \bar{\nu}$ is 0.182 GeV [1.9].

Another method [1.10] to evaluate the decay width is to measure the ratio of production rates of $W \rightarrow e \nu$ and $Z \rightarrow e e$ events. In terms of production cross sections, $\sigma(W^{\pm})$ and $\sigma(Z0)$, and branching ratios, $B(W \rightarrow e \nu)$ and $B(Z \rightarrow e e)$, of the two processes, the ratio is given by

$$R = \frac{\sigma(W^{\pm})\ B(W \rightarrow e \nu)}{\sigma(Z0)\ B(Z \rightarrow e e)} \ . \qquad (1.4)$$

This ratio can be expressed in terms of theoretically calculable quantities as

$$R = \frac{\Gamma(W \rightarrow e \nu)}{\Gamma(Z \rightarrow e e)} \ \frac{\Gamma z}{\Gamma w} \ \frac{\sigma(W^{\pm})}{\sigma(Z0)} \ , \qquad (1.5)$$

where Γ is the width for the decay channel. The first and the third ratios can be calculated. The Γw in the second ratio is also calculable quantity if the masses of the forth or higher generation charged leptons are larger than the mass of W. Only Γz depends on the accessible decay channels. In the standard model with three generations, the second ratio is about 1. With more generations, Γz increases because of additional $Z \rightarrow \nu \bar{\nu}$ decays while Γw is unaffected because of lack of phase-space for

new decay. The upper limit of R provides the upper limit of the decay width. This method gives a limit on N_ν as 10 and 5 for UA1 and UA2, respectively [1.6].

The future operation at 2 TeV will provide an opportunity for further study of W's and Z's. At an integrated luminosity of 10^{37} cm^{-2}, which is a realistic goal of the Tevatron collider, about 49,000 Z's and 110,000 W's of each sign will be produced at 2 TeV [1.11]. Such huge number of W's and Z's will make detailed studies of various decay modes possible.

The branching ratios for $Z \rightarrow e\ e$ and $W \rightarrow e\ \nu$ are about 3 % and 8 %, respectively. A total of 1500 $Z \rightarrow e\ e$ and 17600 $W \rightarrow e\ \nu$ will be produced by Tevatron. The mass and transverse mass of Z and W are obtained as

$$Mz^2 = Ee^+\ Ee^-\ (1 - \cos\theta), \qquad (1.6)$$

$$Mw_T^2 = Ee_T\ E_T\ (1 - \cos\varphi), \qquad (1.7)$$

where θ is the opening angle between e+ and e- and φ is the opening angle between e and ν in the plane perpendicular to the beams. The expected measurement error in the mass of Z, for example, is

$$\frac{dMz}{Mz} = \frac{1}{2}\sqrt{\left(\frac{dEe^+}{Ee^+}\right)^2 + \left(\frac{dEe^-}{Ee^-}\right)^2}\ , \qquad (1.8)$$

where θ is assumed to be precisely mesured. The experimentral uncertainty of masses is estimated to be the sum in quadrature of (1) the inherent resolution of the calorimeter due to sampling

fluctuations and photonstatistics and (2) uncertainties in the calibration procedure. The transverse energy of the electrons from W and Z0 decay is about 40 GeV. Provided the energy resolution from the inherent resolution of calorimeter is of the order of 2 % for electrons from Z and W decay, the statistical error of mass determination would be less than 0.1 % in the CDF experiment. The uncertainties in the calibration procedure dominates the resolution for electrons from Z and W decay. Both UA1 and UA2 determined the masses of Z and W with statistical error of 1.4 %. However, the systematic errors for UA1 and UA2 are 3 % and 1.6 %, respectively. Therefore, the calibration of the CDF electromagnetic calorimeter should be done at a level of 1 % with respect to the systematics. The error of mass of Z for $Z \rightarrow e\ e$, for instance, will be 0.7 % if the uncertainty is 1 %. The errors of $\sin(\theta w)$ and rho will be 1.4 % and 0.5 %.

With high luminosity operation of Tevatron study of other decay modes of W and Z will be possible. For instance, one can search for heavy particles such as top quark of the third generaton and the heavy lepton (L) of the fourth generation.

The UA1 collaboration has reported a signal for associated production of an isolated large-transverse-momentum lepton and two jets at the CERN SPS [1.12]. The events were topologically in agreement with the process $W \rightarrow t\ b$ followed by $t \rightarrow b\ e\ \nu$. However, Grosso and Odorico suggested that selection cut induces a topological event structure on the surviving background ($c\ \bar{c}$ + X and $b\ \bar{b}$ + X) [1.13]. Recently, a preliminary study on the detection of the top quark in the same mode at 2 TeV was made by

CDF members including the author [1.14]. In the final state, an electron plus 2 jets plus missing neutrino were expected. The QCD background ($b \bar{b} + X$) suggested by Grosso and Odorico was compared to the signal. Even with an isolation cut for electron, the signal to background ratio was 1/3 to 1/2. Furthermore, the QCD recoil jets were frequently misidentified as b-quark jets. The misidentification is more frequent at Tevatron than SPS energy. It seems difficult topologically to separate the signal from background. Further study is needed.

Next, we will discuss briefly on serch for the fourth generation of the sequential leptons through the decay of W, $W \rightarrow L \nu$. As was pointed out by Barger et al. [1.15], the subsequent semi-leptonic decay mode $L \rightarrow u d \nu$ (or $c s \nu$) yield a signature less polluted by various backgrounds compared with pure leptonic decay mode e.g. $L \rightarrow e$ (or μ) $\nu \nu$.

Here the mass of heavy lepton neutrino is assumed to be light. If the fourth generation lepton exists, the branching ratio decaying into the channel $W \rightarrow L \nu$ as Fig. 1.1 depends on the mass of the lepton (see Fig. 1.2) [1.16].

In the leptonic decay chain $W \rightarrow L \nu$ followed by $L \rightarrow e \nu \nu$, the transverse momentum distribution and angular distribution of positron are shown in Fig. 1.3 [1.15].

The distribution from $W \rightarrow \tau \nu$ channel is also shown in the figure.

On the basis of naive mass scaling [1.17], the heavy lepton mass is estimated by S.Pakvasa et al. to be 30 GeV. If renormalization group equations describing the evolution of couplings possess stable infrared fixed points [1.18], then the heavy lepton mass is expected by C.Hill and E.Pashos to be 55 GeV [1.19, 1.20].

Physic at low luminosity

The UA1 and UA5 have shown, as in Fig.1.4(a), that the average multiplicity per unit of pseudorapidity rises with increasing energy in the non-diffractive events [1.21, 1.22]. The width of the central pseudorapidity distribution had grown less than would have been expected from ISR data. This was suggested to be explained by rising average transverse momentum (see Fig. 1.4(b)) [1.22]. Later UA1 result showed that average momentum for the charged particles is about 0.43 GeV/c which increaces by about 20 % from ISR data as in Fig. 1.4(c) [1.23]. Thus, the rise of the central pseudorapidity density [1.22] violates Feynman scaling [1.24]. Also an apparent violation of KNO scaling [1.25] is observed as seen in Fig. 1.5 [1.26]. Thus, the central pseudorapidity density and the average transverse momentum of charged particles at Tevatron energy is expected to increase. The expected values of the two quatities extraporated from ISR and SPS energy will be about 4 and 0.56 GeV/c, respectively [1.27].

The CDF can also check the existence of a new type of interaction observed in a cosmic ray experiment. The event in the interaction is called "Centauro" [1.28]. About one hundred hadrons were produced without any significant emission of neutral mesons in the Centauro event with the extremely high energy. Assuming that they are from a nuclear interaction in the atmosphere with emission and decay of a paticular type of fire-ball, the rest energy of the fire-ball and the decay temprature are estimated to be 100 - 300 GeV and 1 - 2 GeV, respectively. Nucleons and antinucleons are the most plausible candidates for the decay products as conjectured from the decay tempreture. The average transverse momentum is measured to be 1.7 GeV. The characteristics observed in cosmic ray experiments are summarized in Table 1.2.

There is a persistence of pion multiple production at least up to 1000 TeV of the laboratory system energy. In the energy range above 1000 TeV, the Centauro interaction occurs in the ratio of 2 events/13 events (= 0.15) [1.29]. Such extremely high energy can be achieved in the collider machine. The CERN SPS with a center of mass energy of 900 GeV corresponds to 432 TeV, while the Fermilab Tevatron with a center of mass energy of 1600 GeV corresponds to 1362 TeV. In the search for the Centauro events at SPS energy, no events were found [1.30]. This is still consistent with expectation from cosmic ray data from which the Centauro threshold was estimated to be higher than 1000 TeV at the laboratory system. The search for Centauro events at the Tevatron energy may give a conclusion for the new interaction.

1.2 GENERAL DESIGN CONSIDERATION OF THE CDF

1.2.1 Detector Design

The CDF [1.31] is a general purpose detector assembled at the B0 straight section of Fermilab Tevatron. A perspective view of the detector is shown in Fig. 1.6. It consists of a central detector and forward-backward detectors. Each angular range of the CDF consists of components with different functions, namely, tracking detectors, calorimeters and muon detectors. The calorimeters are constructed in tower geometry with towers aiming at the interaction point. The total weight is approximately 4500 tons, half of which is in the central detector. The approximate size of the central detector is that of a box 9.4 m high, 7.6 m wide and 7.3 m long. A cut through one half of the detector is shown in Fig. 1.7. The interaction region is in the center of the detector. The description for each part is given below [1.1, 1.31].

Magnets

The Central Detector contains a 1.5 Tesla superconducting solenoid, 3 m in diameter and 5 m long. The coil thikness, expressed in radiation length (X0) is 0.85 X0. The flux return is through the steel plates of the Endplug and Endwall hadron calorimeters. Separate steel return legs outside the central calorimeters carry the flux from end to end, as can be seen in Fig. 1.5. Only a minor part of the flux passes through the central calorimeter steel plates. The Forward-Backward detectors

each contain two large magnetized steel toroids, 7.6 m in diameter and 1 m thick. Four coils per toroid generate a 1.8 Tesla field in the steel.

Charged Particle Tracking

The tracking systems are designed to measure charged particle tracks over the full solid angle. In the central region of the solenoid field, momenta are also measured. The components are:

(1) A set of Vertex Time Projection Chambers (Vetex TPC's) to measure charged particle multiplicities over a large solid angle, and to determine accurately the Z-position of the interaction vertex. If overlapping events with different vertex positions are recorded, these TPC's will be able to identify such events. They are operated at atmospheric pressure, and have been sized such that the maximum drift time is less than 3.5 us. This is the time between bunch crossings in the Tevatron when there are six proton and six antiproton bunches in the machine.

(2) The Central Tracking Chamber (CTC), a large cylindrical drift chamber to measure accurately the trajectories and momenta of charged particles in the magnetic field volume. The momentum resolution at a polar angle θ = 90 degrees to the proton beam is expected to be dPt/Pt = 0.002 Pt (in GeV/c). The chamber is operated at atmospheric pressure.

(3) Drift tubes on the outside shell of the drift chamber to measure the Z-coordinate of tracks with good precision using charge division.

(4) Forward Tracking Chambers for measuring the trajectories of those charged particles which leave the Central Detector through the 10 degrees hole in the Endplug. These chambers have radial sense wires, which is a natural way continue the geometry of the axial sense wires in the cylindrical drift chamber

(5) Forward Silicon Detectors inside the Tevatron beam pipe to measure small angle scattering. A Silicon Vertex Detector to measure the decay length of long-lived particles will be installed around the beam pipe inside the Vertex TPC's at a later date.

Trigger Counters

(1) Beam-beam counters are installed around the beam pipe in front of the Forward EM calorimeters and used to provide a relatively unbiased trigger. These counters have good time resolution and determine the event time. They are also used together with the Forward Silicon Detectors as luminosity monitors.

(2) Scintillator counters in the Forward Muon System are used for the muon trigger.

Calorimetry

Both electromagnetic (EM) and hadron calorimeters are outside of the tracking detectors. All the calorimeters are of the sampling type. The EM calorimeter contain lead plates as the absorber, whereas the hadron calorimeters have steel plates. The active medium is scintillator in the angle region of $30 < \theta < 150$ degrees and proportional tubes at small angles of $2 < \theta < 30$ degrees.

The calorimeters are all subdivided into many cells. Each cell is solid angle element of EM and hadron calorimeters. The angular coverage of the calorimeters is 2 pi in the azimuth and from -4 to 4 in pseudorapidity. The tower size is approximately 0.1 in pseudorapidity by 0.26 in azimuth for the scintillator calorimeters, while 0.1 by 0.09 for the proportional tube calorimeters. It is fine compared with 0.17 by 0.26 in UA2 [1.32]. The high angular segmentation is necessary to ensure an optimum separation of the particles, or jet of particles of interest from the many other secondaries produced in the events. The fine segmentation makes it possible;

(1) to resolve localized clusters of energy deposition,

(2) to minimize the overlap probability of a hard neutral pion with a soft charged pion which could be misinterpreted as an electron.

The summary of the CDF calorimetry is presented in Table 1.3 and the brief description for each calorimeter is given below.

(1) The Central Calorimetetrs, consisting of calorimeter "wedge" which are built into "arches". A wedge modules containes both EM calorimeter (CEM) and hadron calorimeter (CHAD). One arch is composed of 12 wedges. A total of 4 arches compose the central calorimeter. The EM calorimeters contain lead plates as the absorber, whereas the hadron calorimeters have steel plates. The sampling medium is scintillator. The total thickness of CEM and CHAD are 18 radiation lengths and $4.7/\sin(\theta)$ absorption lengths.

(2) The Endwall Hadron Calorimeters (WHAD), which also use scintillator. They are mounted on the steel Endwalls of the magnet yoke, and are part of the flux return path. The total thickness of WHAD is $4.5/\cos(\theta)$ absorption lengths.

(3) The Endplug Calorimeters, both EM and hadron calorimeters, which use proportional tubes with cathode pad readout for the energy measurement. The EM calorimeter and the first few steel plates of the hadron calorimeter are located inside the solenoid field, as can be seen in Fig. 1.5. The longitudinal depth is 18 radiation lengths for EM calorimeter, 6.0 absorption length for hadron calorimeter.

(4) The Forward (-Backward) EM and hadron calorimeters, which are located between 6 m and 10 m from the interaction region on both sides of the Central Detector, also use proportional tubes with cathode pad readout. The longitudinal depth of the calorimeters is 26 radiation lengths for EM, 8.5 absorption lengths for hadron.

Muon Detection

Outside the calorimeters are muon detectors. They are:

(1) The Central Muon Detector. These drift chambers are located between the last two steel plates of the central wedge calorimeters. Charge division is used for the determination of the Z-coordinates. They are operated at high gain (limited streamer mode) to give good charge division resolution.

(2) The Forward (-Backward) Muon Detectors. Each detector consists of two magnetized steel toroids and three sets of drift chambers. These drift chambers are so-called electrodeless drift chambers in which the uniform drift field is shaped by an equilibrium distribution of charges on the inside surfaces of the insulating chamber walls rather than by metallic electrodes. The expected momentum resolution is dP/P = 20 %.

1.2.2 Detector Calibration

For calorimeters, an absolute calibration is needed to convert a measured pulse height (expressed in ADC channels) to an energy deposition in the calorimeter. All calorimeter types have had their response in test beams of known energy measured as a function of incident energy, position and angle for electrons, pions or muons. In some cases, all modules of a given type have been individually calibrated. The gains at the time of calibration have been monitored by measuring the response to radioactive sources. These are, in most cases, built into the

calorimeters. The absolute calibration at a later date can then be established simply by measuring again the response to these sources. The accuracy of this calibration method has been shown to be better than 1 % in some cases.

The CTC is, in a certain sense, selfcalibrating. This means that the drift constants in the chamber can be determined from track data. The constants are determined by demanding continuity across the boundaries. A similar method can be used in the Vertex TPC's.

1.3 OUTLINE OF THE ARTICLE

The present article is organized as follows: (1) The design, construction and performance of the CDF central EM calorimeter, on which the author has been working, are described on the former part of the article (Chapters 2 - 7). (2) How the CDF worked and what we observed with the CDF in the first collision are discussed in Chapter 8. A discussion is also made on search for the Centauro events. (3) A Monte Carlo study on the event topology and detection of the heavy lepton at the future CDF experiment is given in Chapter 9. (4) The conclusion is finally provided in Chapter 10.

CHAPTER 2

THE CENTRAL EM CALORIMETER

The CDF central electromagnetic (EM) calorimeters [1.31, 2.1] are composed of 48 modules, each consisting of a lead/scintillator stack of 31 layers with a strip chamber embedded near the shower maximum. In addition to the 48 modules surrounding the proton-antiproton interaction points, 2 modules are to be used for monitoring at test beam line. In total, about 9 metric tons of scintillator were needed to complete the entire modules. The total number of towers is 480. Each tower size is typically 0.1 in pseudorapidity by 15 degrees in azimuth.

In this Chapter, the calorimeter structure and the characteristics of scintillator, wavelength shifter, phototube and strip chamber are described.

2.1 GENERAL DESCRIPTION OF THE STRUCTURE

The calorimeter module begins with the inner aluminum base plate at a perpendicular radius of 68" (Fig. 2.1). Its nominal 1" thickness is reduced to 3/8" at each tower center.

The calorimeter consists of 31 scintillator plates of the type SCSN-38 [2.2], each 5.0 mm thick, and alternately stacked with 30 lead plates, each 1/8" thick. Each scintillator plate is polished on internal edges and wrapped in two layers of 0.0015" vellum drawing paper to form ten towers. The lead plates are clad on both sides with 0.015" aluminum.

Light from the scintillator in each tower is collected on either side of the stack by 3 mm thick UVA acrylic wavelength shifter doped with 30 ppm Y7 [2.3], which is inserted in the gap between the surface of the stack and the 3/16" steel cover plate (see Fig. 2.2). The light is transmited to two phototubes through UVA acrylic rods and transition pieces. The transition piece is doped with 30 ppm Y7. The phototube is 1.5" bialkali, 10 stage HAMAMATSU R580.

A proportional strip chamber is inserted between the eighth lead layer and ninth scintillator layer of the stack. In order to obtain a constant depth in radiation length to the chamber with polar angle, a few acrylic plates are substituted for lead in some layers for some towers as shown in Fig. 2.3. The sides of scintillator behind the acrylic are painted black.

Also is made the substitution to fix the total thickness of the stack, held under 20 psi, is kept to 12.6" $\pm$ 0.1" by selective insertion of layers on 0.01" mylar.

The summary of central EM calorimeter is tabulated in Table 2.1.

2.2 SCINTILLATOR: SCSN38

The polystyrene base of scintillator SCSN-38 [2.4] is doped with two kinds of fluors, i.e. b-PBD and BDB. The wavelength of light emitted from b-PBD and BDB is about 360 nm and 430 nm respectively at the emission peak as in Fig. 2.4, which correspond to a shorter ($\sim$ 10 cm) and longer ($\sim$ 100 cm) attenuation length. This configuration gives rise to an increase of light output for an impact near the edge of scintillator on the phototube side, causing the necessity of a uniformity study.

As is described in Chapter 3, the scintillator plates were shuffled so that the total thickness of 31 layers of the scintillator plates used in each module was fixed within a variation of 1 %.

2.3 WAVELENGTH SHIFTER: Y7

The Y7 wavelength shifter [2.4] converts (WLS) the scitillator light into light of wavelength 490 nm (see Fig. 2.4). The wavelength shifter response was made uniform to 3 % rms in construction of a module by a backing [2.5] that selectively suppressed the response of the nonuniform regions. Figure 2.5 shows typical examples on WLS responses without the backing and with the backing. There is a 3 mm (air) gap between waveshifter plates servicing adjacent towers.

The displacement and shrinkage of WLS is effective to change the response map. A simulation study had beed made on how

sensitive the response map of the scintillator is to the displacement and the shrinkage [2.6]. The result show that the conditions to keep the difference within 1 % over 95 % of the area of the scintillator are: (a) assuming no displacement, the shrinkage should be less than 2.0 mm in full width, and (b) assuming no shrinkage, the displacement should be less than 0.8 mm.

The goal of positioning the WLS to the central EM calorimeter is to set the WLS in a position as symmtric as possible with respect to the corresponding boundaries of the tower scintillator stack. This positioning will necessarily involve compromises in fitting both WLS position and angle while fitting the rod in the module. The procedure shall be to center the WLS on the scintillator just above the strip chamber as accurately as possible. The positions of WLS should be measured to check the assembly procedure. From the simulation study, we set the allowarance in the size and displacemant of WLS, and the production and attachment to EM calorimeter was performed within 1.3 mm.

2.4 PHOTOTUBE: HAMAMATSU MODEL R580B

The specifications for the phototubes of the central EM calorimeters are tabulated in Table 2.2. The drawing of phototube is shown in Fig. 2.6.

Approximately 1050 phototubes with bases were "burned in" and tested to ensure that each of them met specifications and to

detect failures before installation into the calorimeters [2.7].

For each tube, the manufacturer was required to provide measurements of the high voltage, pulse height resolution and dark current at a current gain of 4×10^5 and the quantum efficiency [2.7].

After this test, phototubes were installed into calorimeters at Industrial Building IV at Fermilab. After installaton and light tighting, the high voltage for each tube was set by using radioactive sources (Cs-137) as described in Chapter 4. The typical value of high voltage was 1000 volts. The dark current of each phototube was required to be less than 0.5 nA at 1000 volts of high voltage, because a nominal current from Cs-137 source is of the order of 50 nA as descrived in Chapter 4. The typical values of the gain and quantum efficiency were 10^5 and 14.4% respectively at the high voltage [2.7].

2.5 STRIP CHAMBER

The strip chamber is a wire proportional chamber as shown in Fig. 2.7, located at a depth near shower maximum in the EM calorimeter [2.1]. The position is presented in Table 2.3. The chamber covers all ten towers in a single wedge, 15 degrees in azimuth by wires and 40 to 90 degrees in polar angle by strips.

Strip chambers are similar to the prototype [1.31, 2.8]. Dimensional details are different. Strips are copper backed 1/16 in. PC board with plated through holes for ease of connection.

A three piece aluminum extrusion is used as well as injection molded delrin wire locators. Details of the chambers are listed in Table 2.4. There is a placement error in locating the chamber in the stack of $\pm$ 1 mm. Distortion of the chamber due to unevenness of the stack gives smooth strip gain variations of up to 40%. Corrections for this may limit strip/wire pulse height correlation to $\pm$ 10%.

The 62 anode wires are separated by aluminum extrusion and ganged together in pairs except for two edge wires. The logical channel width is 14.53 mm. The wires are divided at tower 4 - 5 boundary giving a total of 64 channels. The wire numbering starts at 0 for the side of the strip chamber closest to 90 degree side and increases as X decrease, to a maximum 31. Wire number starts again on the second part of the chamber, starting at 32 for the largest X and increasing to 63 for the last wire.

The 128 cathode strips are oriented perpendicular to the wires and form the cover for the open channel extrusions containing the wires. The logical width is 16.67 mm for towers 0 to 4 (channels 0 to 68) and 20.07 mm for towers 5 to 9 (channels 69 to 127).

The high voltage was fed to each logical wire channel from 4 external distribution boxes connected to a common voltages supply set at 1.42 kV. The gas is a mixture of Ar/CO2 (95/5).

CHAPTER 3

QUALITY CONTROL IN PRODUCTION OF SCINTILLATOR FOR EM CALORIMETER

3.1 INTRODUCTION

Calibration of the CDF electromagnetic (EM) calorimeters was done at Fermilab as discribed in Chapter 6. The calibration was made with injection of 50 GeV electron beams at a standard point of each tower, namely, at the tower center. Then there remains a question: What can we say about the calibration at other points of the calorimeter ? The present Chapter is intended to provide same information which is useful in answering this question.

A requirement to our EM calorimeter system is that the modules are as identical as possible to each other. Quality fluctuation of the scintillator plates and light collection system (wavelength shifter plus light guide) will lead to variations in performance of the assembled modules. Therefore the quality control was carefully done during mass production.

Fluctuation among scintillator plates was actually examined for the following quantities :

(a) light yield (fluor uniformity),

(b) thickness,

(c) attenuation length.

Variations in the concentration of the fluor components, for example, give rise to variations in the light yield. Table 3.1 shows the fluor concentration dependence of light yields of the SCSN series of scintillator [2.4]. Thus the light yield uniformity corresponds to uniformity in fluor concentration.

Variation in the thickness of plates will cause non-uniformity of response as follows. Secondaries in the electromagnetic shower may have energy greater than a critical energy in the lead sheet. It is 7.2 MeV in the lead [3.1]. The average energy loss rate of the secondary in scintillator plate is about 2 MeV/cm [3.2]. Shower calorimeter measures the total energy deposited by the secondaries. It is proportional to sum of track length of all the secondaries in the scintillator plates. Hence the light output will depend on the total thickness of 31 layers of the scintillator plates even if the fluor concentration is uniform.

The attenuation length directly effects the response, so that the variation from plate to plate has to be carefully controlled in the production.

The mass production of scintillator plates is described in section 3.2. The measurements for quantities (a) - (c) mentioned above and the results are given in section 3.3, 3.4, and 3.5. In

section 3.7, effects on the response are discussed.

3.2 MASS PRODUCTION

Scintillator plates were produced by a casting method [3.3]: The scintillator solution was made by mixing fluors into the polystyrene base in a mixing tank. The solution was poured into a mold and it was solidified under temperature control in a furnace. The mold consisted of two parallel plates of hard glass with a gap of 5 mm between them. Each mold produced one mother-board of scintillator with a size of 2700 mm x 1900 mm x 5 mm. The mother-board was cut into three or four plates with a typical size of 2400 mm x 480 mm x 5 mm, corresponding to one layer of scintillator from tower 0 to 9 in a module. The width of the scintillator plate varies with the layer number from 440 mm to 524 mm as shown in Fig. 2.2.

According to production process, there are three stages of unit to define quantities :

(1) batch = unit of scintillator solution,
(2) lot = unit of furnace,
(3) cell = unit of casting (mold).

The relations between them and a mother-board are given by

1 batch = 4 lots,
1 lot = 20 cells,
1 cell = 1 mother-board.

From 1 mother-board we cut 3 or 4 plates of the final sizes defined by tower geometry. Each plate corresponds to 1 layer for all 10 towers. The two faces of each plate are covered with protective papers to prevent them from any damage. The total number of plates to be used for central EM calorimeters is

31 plates/module x 50 modules = 1550 plates.

All the scintillator plates were made in two separate periods. The first production worth of 16 modules was done in Feb. 1982, and the second production for the remaining 34 modules in Oct. 1982.

3.3 MEASUREMENT FOR LIGHT YIELD

3.3.1 Test Samples

Considering the production scheme, we examined the light yield uniformity (A) between cells and (B) within a cell. Two types of test samples were taken as (A) 1 sample per cell, and (B) 14 samples from a typical cell per every batch. The size of samples were 60 mm x 60 mm for both types.

The type A samples were cut at random positions of the mother-board after the 3 (or 4) plates were taken. The type B samples were taken from sampling positions defined in Fig. 3.1(a).

For each sample we measured both light output and thickness.

The thickness measurement was made by using a micrometer at 4 points as shown in Fig. 3.1(b) and the average value of the four was used in our analysis. Differences in thickness at the four points were less than 0.05 mm peak-to-peak. A total of 7 monitor samples were also taken each from different mother-board of a Lot number for checking the systematic fluctuation of the experimental setup.

3.3.2 Measurement

In the measurement of light output, the number of photoelectrons (Npe) was calculated by the inefficiency method with a beta-ray source Ru-106 [2.4]. The experimental setup is shown in Fig. 3.2. The light outputs of the test and the monitor samples were alternately measured to remove systematic errors (e.g. due to gain drifts of phototubes). The Npe was adjusted by combination of neutral density (N.D.) filters with various transmittances.

The relations between the number of photoelectrons and the transmittance were measured at various tube voltage, and were fit to the form $Npe = a\ t + b$, where t is the transmittance of the N.D. filters. The tube voltage was optimized, so that the parameters a and b were in the plateau region for the change of high voltage. Furthermore the parameter b was set to a value close to zero. Figure 3.3 shows the linearly at the optimized voltage. The linearity between Npe and t seems to be valid in the Npe range of 0.4 to 1.0. The transmittance was set to 0.01 for this light yield measurement.

As mentioned above, the light outputs of test samples and a monitor sample were alternately measured to remove systematic errors. The correction for the systematic errors was made as described in Appendix C. The calculation of non-uniformity is also presented in Appendix C.

3.4 MEASUREMENT FOR THICKNESS

3.4.1 Test Samples

The measurement for the thickness was made for all the scintillator plates used in the EM calorimeters. As described in section 3.2, the typical size was 2400 mm x 480 mm x 5 mm. The tolerance in the thickness was set to $\pm$ 0.3 mm for a nominal value of 5.0 mm.

3.4.2 Measurement

As mentioned in section 3.4.1, the tolerance is set to a range from 4.7 mm to 5.3 mm. To reject a plate with the thickness out of the tolerance in the production line, the thickness of all plates were measured and the data were recorded into a chart by a pen recorder at the factory [3.4]. The schematic view of the setup of thickness measurement is shown in Fig. 3.4. The plate moved on rotating rollers at a speed of 5.4 m/min. Two probes traced on the surface of the plates. Each probe was positioned at 10 cm from the center line of the plate (Fig. 3.4). The vertical position of each probe was converted into a voltage by a thickness-meter. The accuracy of mesurement

for the thickness is 20 μm. A typical output from the thickness-meter is shown in Fig. 3.5. The probes and the rollers never damaged the plate due to the protective paper mentioned before. The thickness of the papers, each being nominally 95 ± 5 μm is subtracted in this recording.

An analog data recorder (TEAC Model XR-50) was connected in parallel to the thickness-meter with the pen recorder for offline analysis (Fig. 3.4). The data recorder can record the analog signal from DC to a few kHz by frequency modulation into VHS type video cassette. The 50 mV output from the thickness-meter corresponds to the thickness deviation of 1 mm. To adjust the full scale of the data-recorder (± 1 V), an amplifier with a gain of 20 was put before input. Calibration signals (0 V and -50 mV) were recorded at the head of each cassette. A total of 8 cassettes were used for recording the data on the thickness of all the plates.

Analog-to-Digital conversion for the data were made at the university. Figure 3.6 shows the schematic view of the setup. A LeCroy model 2259A, voltage sensitive type ADC, was used for the conversion. Since the range of ADC input was from 0 to -2 V, an amplifier with a gain of 1 was put to give a bias of -1 V to the analog data, so that the data matched the range of ADC input.

For scintillators produced at the first production, 65 points per line were digitized. A typical result is shown in Fig. 3.7, that is the same data as Fig. 3.5. As shown in Fig. 3.7, 65 points per line seems to be excessive because of slow

change. Hence the number of points was reduced to 27 points per line in the second production.

Calibration signal were recorded at the beginning of the each measurement. Digitization was made relative to that signal. Data were stored on floppy disk by MIK-11 microcomputer contained in a CAMAC crate. Data on disk were read and analyzed with a VAX-11/780 computer.

3.5 MEASUREMENT FOR ATTENUATION LENGTH

3.5.1 Test Samples

During the production, 2 test samples were taken from a typical cell per every lot to examine the uniformity of attenuation lengths between lots. The samples had a size of 1000 mm x 50 mm x 5 mm and the four edges were polished. The sampling position was at random. A total of 84 samples were obtained from the 1st and the 2nd production.

3.5.2 Measurement

Figure 3.8 shows the experimental setup of the measurement for the attenuation length. The UV light was used as the light source. The position of the light was controlled by the shutter. The light spot moves from right edge to left edge. We measure the light outputs from the both ends and calculate the attenuation length (L) as

$$P1 / P2 = C \exp(-2 X / L),$$

where P1 and P2 are the phototube outputs from the left and right ends, respectively, X is the position of the light spot from the left end, C is a constant. The phototubes were very stable during the measurement for one sample. The advantage of this measurement is that it is independent of the intensity of the light source. The accuracy for the measurement was of the order of 5 % for a nominal attenuation length of 90 cm.

3.6 RESULTS

3.6.1 Non-uniformity On Light Yield

On the basis of the measurements and analysis described in the preceding section, the non-uniformity of the scintillator in the light yield (fluor concentration) is estimated as follows,

(A) The non-uniformities in the 1st and the 2nd productions were 0.94 % and 1.08 % (see Table 3.2). The weighted average is 1.04 %.

(B) The non-uniformity in one mother-board was less than 0.5 % (see Table 3.3).

Now we consider module-to-module non-uniformity in the light output for high energy particles. It can be caused by fluctuations of (a) fluor concentration, (b) thickness, and (c) attenuation length. Among these, non-uniformity caused by the fluor concentration variations is estimated as follows.

The CDF central EM calorimeter consists of 31 layers of

scintillator/lead plates. The total light output is a sum of outputs from these plates. Here we assume the variation is at random and neglect plate-to-plate variations in thickness and attenuation length. For a punch-through particle which deposits on average equal amount of energy to each plate, the module-to-module variation of the response is reduced to 0.19 %. The electron or the gamma ray gives energy deposit to plate according to the shower curve. The longitudinal shower profile can be parametrized [3.1] as

$$S(t) = A\, t^{a} \exp(-\, b\, t),$$

where t is depth in radiation length, A, a and b are parameters. The profile for 50 GeV electron is taken from Ref. 3.5. The module-to-module variation is estimated by applying weight according to the shower profile. It is obtained to be 0.22 % from a Monte Carlo simulation. The module-to-module variation described above is eliminated by the module calibration with 50 GeV electrons.

What remains even after the modules are calibrated at the center of tower by 50 GeV electrons are module-to-module variations in the response: It is not natural that the variations at other points in a tower are zero. These variations are estimated on the basis of local non-uniformity, namely the non-uniformity of the light yield in one mother-board. The variation for punch-through particles is estimated to be less than 0.09 %. For 50 GeV electrons, it is found to be less than 0.10 % in the same manner mentioned above. Here again we assumed

random non-uniformity and neglected the plate-to-plate variations in thickness and attenuation length.

3.6.2 Non-uniformity On Thickness

Histograms of deviation in thickness measured for the first and second productions are shown in Figs. 3.9(a) and 3.9(b), respectively. The mean and rms values of the distributions are presented in Table 3.4. There were a little difference between two productions.

We decided the combination of the plates used for the stack to minimize the deviation of the thickness in a calorimeter

By electromagnetic shower development, the thickness of the scintillator at different positions will cause different effects on the total response. If the scintillator at shower maximum has a large deviation in thickness, the effect on response should be greater than that at the beginning and end of shower development. Hence the deviation in thickness were estimated with weight by a shower curve for 50 GeV electrons. The parametrization of the shower curve in section 6.1 was used for the above estimation.

Figures 3.10(a) and 3.10(b) show a typical thickness of each stack in the first and second production. Figures 3.11(a) and 3.11(b) show the distributions of deviation from total thickness of 31 layers of scintillator plates, which is nominally 155 mm. Those are weighted by the 50 GeV shower curve for electrons. These histograms show the deviation of calorimeter response expected from deviation in thickness. The distributions for

non-weighted thickness, that is physical thickness of the stacked scintillators, are also shown in Figs. 3.12(a) and 3.12(b). In Tables 3.5 and 3.6, the mean and standard deviation of each measurement are presented.

As is discussed in section 3.6.1, however, the local variation remains even after the calibration with 50 GeV electrons. We must consider the deviation in thickness in a tower. Figure 3.13 shows distributions of difference in peak to peak in a tower. For about 96 % of 480 towers, the peak-to-peak deviation is less than 1.5 mm, coresponding to 0.97 % for the total thickness of the stack. The mean of the distribution was found to be 0.81 mm, corresponding to 0.5 % for total thickness of the stack.

3.6.3 Non-uniformity On Attenuation Length

The results for measurement for the attenuation length are 94.7 $\pm$ 10.1 cm for the 1st production, 90.6 $\pm$ 13.7 cm for the 2nd production, and 92.0 $\pm$ 12.8 cm for both productions. The distribution of the attenuation length measured are shown in Figs. 3.14(a), 3.14(b) and 3.14(c). The attenuation length measured in this experiment will be different from that in the actual calorimeter. However, the variation will be useful for the estimate of the non-uniformity in the calorimeter.

The plate-to-plate variation in the attenuation length was estimated to be 14 % . In a Monte Carlo simulation, however, the module-to-module deviation of the attenuation length averaged for

31 layers of the scintillator sheets will be reduced to 2.4 % for punch-through particles and 2.9 % for 50 GeV electrons.

If the attenuation curve R is parametrize as exp(- X / L), then the variation of the respose viewed at one of the ends is

$$dR/R = (X / L) (dL / L).$$

The value of dR/R will be 0.63 % for X = 20 cm, L = 92 cm, and dL/L = 2.9 %, where the response is normalized by that at tower center. If the values of L and dL/L change to 50 cm and 5 % due to the deterioration of the scintillator, then the variation will be 2.0 %. The variation of the attenuation length is not small for the module-to-module variations of the response.

3.7 EFFECTS ON CALORIMETER RESPONSE

Once the modules are calibrated at a standard beam injection point for each tower, there remains only the effect of local non-uniformity of light yield and thickness as module-to-module variation in the response. The variation on attenuation lengths from stack to stack also gives variation of the response.

In the production process of scintillator plates for the CDF central EM calorimeters, light yield of fluor components and the attenuation length were measured on samples cut from mother-boards of scintillator. Measurement for the thickness of all the plates used for the EM calorimeters was made and the combination of the plates for stack was selected to minimize the

deviation of the total thickness of the stack.

From these measurements, the local non-uniformities on the light yield and thickness for 50 GeV electron are estimated to be less than 0.1 % and 0.5 %, respectively. For attenuation length in stack, the deviation at X = 20 cm will be 2.9 %.

Such variations on light yield, attenuation length and thickness of the stack will reflect the dissimilarity of the response by 0.1 %, 0.63 %, and 0.5 %, respectively, after each calorimeter is calibrated at the tower center. If these variations are independent each other, the total effect will be 0.81 %. If an accurate module dependent attenuation length correction is made, this would reduce to 0.51 %.

CHAPTER 4

THE CALIBRATION MONITORING SYSTEM

As is discussed in Chapter 6, the initial calibration was made with the test beam. The calorimeter gain could vary due to the deterioration of the scintillator and/or the gain drift of the phototube. To monitor the gains and to set the tube voltage correctly, source calibration system [4.1, 4.2] was developed for monitoring the calorimeter gain. LED [4.3] and Xenon flasher [4.4] systems were also developed for interpolation between source calibrations.

The first source calibration system used a single Co-60 source [4.5]. The gain of the phototubes of 13 of 50 modules was set using Co-60 source. This system was later replaced with Cs-137 source systems [4.6] because of the advantages [4.1] of

(1) having a source on each module and being able to do calibrations on many modules simultaneously as opposed to the Co-60 system that had to be moved from module to module,

(2) being able to do calibrations with the arch in place in the collision hole,

(3) the longer half-life of Cs-137 (30.17 years) compared to Co-60 (5.27 years),

(4) having the same source system service both the e-m and hadron calorimeters.

The main disadvantage of the Cs-137 source system are the lack of position information and the lower energy of the gamma rays. The latter results in the source sampling fewer layers of the calorimeter than the Co-60 system.

In the present chapter, general descriptions of Cs-137 source, LED and Xenon flasher systems are given.

4.1 SOURCE CALIBRATION SYSTEM

A schematic drawing of the 45 degree end of a central calorimeter module and its Cs-137 source system is shown in Fig. 4.1 [4.1]. A cylindrical stainless steel tubes were inserted into the square brass tube to prevent the guide wire from sagging. The Cs-137 source (3 mCi) is contained in a brass cylinder 0.062" in diameter and 0.4" long. It is attached to 0.020" diameter teflon-coated stainless steel wire that forms a continuous loop through the EM and hadron source tube. Figure 4.1 also shows the pulleys used to guide the source movement into the calorimeter and the low voltage DC motor and flexible chain drive used to drive the source. Because the source is unable to

to travel around the pulleys inside the calorimeter at the 90 degree end, it is necessary to have a means of sensing when the source is at its extreme mechanical limit inside either caorimeter. To know when the source is in the lead "garage", EM limit, and hadron limit, the teflon coating is stripped from a small portion of the wire when the source is put into each of the three positions. When the bare wire moves through the limit contacts shown in Fig. 4.1, the appropriate limit circuit is closed. The control circuitry for the system is located on a RABBIT card described in Chapter 5. The speed of the motor is also controlable via a multi-turn potentiometer located on the control card.

4.2 LED AND XENON FLASHER SYSTEM

Figure 4.2 shows a schematic picture of a wavelength shifter and a light quide attaching LED and Xenon flasher system.

The LED flasher system injects light near the top of the light guide and the Xenon flasher system injects light into the bottom of the wavelength shifter.

The flasher systems are sampled by very stable PIN diode results [4.7]: (1) Two quartz fibers glued into the transitions are terminated with optical connectors which can connect to a LED flasher. One of each pair is a apare or overlap. The LED flasher containes 3 LEDs each driving 8 fiber channels for the twenty tubes plus two overlaps plus two PIN diode monitors per wedge. (2) Quartz fibers glued to the prisms at installation are

directoly bundled to a wedge based Xenon flasher system which also has two PIN diode channels.

This systems are used to interpolate between source calibrations. We can maintain the short-term calibrations to 0.5 % [4.7].

CHAPTER 5

ELECTRONICS

A new crate-based front end system [5.1], called RABBIT system, has been built, which is suitable for readout of a large number of channels via parallel multiprocessor data acuisition. A driver for the voltage supplied to phototubes is also developed for CDF. As is described in Chapter 6, for the strip chamber and phototube signals, prototype version of the system is used both to faciliate comparisons with test beam data and cosmic ray data and to avoid electronics cross normalizationn problems between calibration data and collider operation.

In this Chapter, we describe the general outline of the RABBIT system and the power supply system to phototubes.

5.1 THE RABBIT SYSTEM

The Redundant Analog Bussed Based Information Transfer (RABBIT) system performs the front end readout of signals from the detector [5.1, 5.2]. All detector inputs to RABBIT are charge pulses. The basic function of the RABBIT system for

charge input signals is to integrate the input pulse, provide an analog amplifier output voltage proportional to the integrated charge, and digitize this voltage. The output of a charge integrating amplifier is sampled just prior to arrival of the detector signal (BEFORE sample) and after the integrated output has reached its "flattop" value (AFTER sample). Subtracting the BEFORE sample from the AFTER sample gives a net integrated signal which is stable against pedestal drifts in the amplifier. The ADC performs the digitization of this difference. The digitized signal includes a pedestal resulting from a fixed offset in the ADC and from the slight difference in the BEFORE and AFTER sample and hold circuits. This pedestal is periodically measured during data collection and subtracted to give the final net signal from the detector channel. The RABBIT system contained the following components: the RABBIT hutch, EWE, BAT, phototube amplifier cards, and strip chamber wire and strip amplifier cards. One ADC is contained in the EWE that digitizes analog voltage signals for all the detector channels serviced by the RABBIT hutch. The function of each of these devices is described below.

The RABBIT hutch is a 25 slot crate plus a printed circuit backplane. The backplane has four sets of staked pin connectors per slot. The outer two sets accept input cables from the detector and the inner two sets connect to the TOP and BOTTOM redundant busses.

The EWE functions as the RABBIT hutch control device in the colliding beam experiment. The EWE handles addressing of the

cards and subaddresses within a card. It also contains the 16 bit ADC that performs signal digitization.

The BAT card handles the timing of the BEFORE and AFTER gating. Gating signals are output to the backplane from which they are available to all cards in the hutch.

The phototube amplifier cards, PM AVC cards [5.2], service both the electromagnetic and hadronic calorimeter phototubes. The design of phototube card is given in Figs. 5.1 and 5.2. Three amplifier functions are associated with each phototube. A charge integrating amplifier handles pulse input from phototubes responding to energy deposition in the calorimeter or from light flashers. The gain of the circuit gives approximately 11.4 fC/ADC count. Because this gain is not sufficient to give adequate resolution for minimum ionizing particles, a second circuit is provided that gives a 16-fold amplification of the charge integrator. The ADC system measure the charge to an accuracy better than 0.1 % over nearly the full scale (300 MeV to 375 GeV). The pedestal variations over time are better than 0.015 % of full scale. Finally, a current amplifier is provided for each phototube. This circuit measures the voltage across the feedback resistor of the charge integrating amplifier. This voltage is directly proportional to the current from the phototube and is used to measure detector responses to radioactive sources.

The strip chamber amplifier cards are charge integrating amplifiers for readout of wires (negative polarity signals) and

strips (positive polarity signals) from the electromagnetic calorimeter strip chamber.

Both phototube and strip cards contain additional circuitry for handling BEFORE-AFTER gating on the card, for decoding addresses, and for switching the selected subaddress analog signal onto the backplane.

5.2 HIGH VOLTAGE SYSTEM

The voltage supplied to the phototubes was controlled by a driver [5.3]. A microprocessor in the divider allows voltages to be set or readout via CAMAC interface module. The precision to which a tube can be set is limited by the least count of the voltage devider wich is 0.5 V [5.4]. For EM phototubes, a voltage change of 0.5 V produces about a 0.35 % gain change. In practice, it was found that a tolerance of 0.55 % was needed to prevent a setting program from oscillating about the final set voltage by 1-2 least counts.

CHAPTER 6

DETECTOR CALIBRATION: BEAM AND COSMIC RAY TESTS

The energy calibration for 50 modules of the central calorimeter was made with the test beam at NW (neutrino west) beam line at Fermilab [6.1]. The correlation between the responses of the calorimeter against the beam and the radioactive source was studied to establish monitoring of the absolute calibration constant. Before the calibration, each module was set on the cosmic ray test stand in Industrial building IV at Fermilab, and the high voltage on the phototubes was set based on the measurement of the signal against the radioactive source.

The cosmic ray test [6.2] was one of a series of quality control and calibration test performed on each of the 50 modules. The principal objective of the cosmic ray testing is to obtain the response maps over the face of each tower in all 48 modules (plus 2 spares) in order to study the similarity of the response maps from module to modules. In addition, this testing provides an important quality control function for production line and a necessary equipment checkout function before the modules are installed in the calibration test beam.

Figure 6.1 shows a simplified diagram of data acquisition system. For the strip chamber and phototube signals, prototype version of the CDF front end electronics (RABBIT) were used both to faciliate comparisons with test beam data and cosmic ray data and to avoid electronics cross normalization problems between calibration data and collider operation. The prototype version of the RABBIT system is essentially same as a version of RABBIT system used in collider operation.

We here provide the description of the calibration procedure, the dedicated test beam line and cosmic ray test stand, and the data analysis.

6.1 CALIBRATION PROCEDURE

The criterion for the gain of the central EM calorimeter phototube is that the anode output from each tube is 2 pC per GeV of energy deposited in the calorimeter for showering particles incident on tower centers of the calorimeter.

The obvious way of setting the phototube voltage to give this gain is to use a known energy electron beam and adjust the voltage to give the correct output. The test beam was unsuitable for phototube voltage setting, however, because of the time required to set each module's tubes (many hours per module) and because of the desire to take the cosmic ray data with the correct volatges in the cosmic ray test stand where modules were tested before going to the test beam line. A method using Cs-137 source to set the phototubes to this gain is developed [4.1,

4.2]. The method provided the voltage setting that was both quick and sufficiently accurate.

The procedure was as follows:

(1) Several final preparation tasks were performed on a module before installing it in the Cosmic Ray Test Stand; checking for light tightness, rough setting of the tube voltages and gas purging of the strip and muon chambers.

(2) Final setting of tube voltage and verification of the integrity of the data acquisition electronics were made on the Cosmic Ray Test Stand.

(3) Cosmic ray data taking was made and generally continued uninterrupted for four days during which 320,000 cosmic ray events were recorded. During early running of the cosmic ray test in 1984 the test beam was running simultanously and total event samples had to be limited to much less than 320,000 in order to keep the test beam continuously supplied with modules for test beam.

(4) The module moved to the beam line and the calibration was performed with 50 GeV test beam incident at each tower center. Also taken are Cs-137 source data successively after the beam calibration. For several modules, both energy and position scanning were made

6.2 TEST BEAM SET UP

Figure 6.2 shows a schematic view of NW (neutrino west) beam

line at Fermilab. The beam line provides the electrons and pions from 10 GeV/c to 150 GeV/c. The calorimeter module to be calibrated is placed on NWA (neutrino west area) with the data acquisition system.

6.2.1 NW Beam Line

The particles (mostly pions), which are created by the interaction of primary protons with an aluminum target, go to a sweep magnet (NW4S). If the NW4S is on and a lead sheet, called "electron creator" (NW4PB), is inserted, the charged particles in the beams are swept out and only neutral particles pass through the magnet. The neutral particles (mostly photons) hit the NW4PB and create the electrons. On the other hand, if the NW4S is off and the NW4PB is removed, then all the beams go through. To remove the neutral particles in the beams, a bending magnet NW4 is placed after NW4S. Only charged particles (pions and electrons) are bent to a 1/4" thick lead sheet.

The lead sheet, named NW6PB, is inserted or removed after the bend to supress the electron in the beams. The supression power of NW6PB for electrons is of order 10^{-2} .

At this stage, the beams are mostly composed of charged pions or electrons. The beams are bent again by magnet NW9E and reach at the calorimeter module on a turn table. The deflection angle is fixed to 28.58 mrad [6.3] for a nominal beam momentum, so that the correct momentum can be obtained from measurement of the deflection angle. The deflection angle is obtained from two

tracks before and after bending. Each track is reconstructed from two multi wire proportional chambers placed either before and after NW9E (NW8, NW9-U/S, NW9-D/S, NWA) as is shown in Fig. 6.2.

The tagging system for the beams is composed of three scintillation counters (S0 - S2) and a veto counter (V). The tagging for electrons and pions are as follows (Fig. 6.2).

e- = S0*S1*S2*V*(NW4S= On)*(NW4PB= In)*(NW6PB=Out),

pi- = S0*S1*S2*V*(NW4S=Off)*(NW4PB=Out)*(NW6PB= In).

6.2.2 Trigger And Data Acquisition System

Figures 6.3 and 6.4 show the trigger logic and the RABBIT timing logic. Data readout and on-line analysis is performed using a VAX 11/730 minicomputer. Events are logged onto magnetic tape with a Storage Tek (Model 1935) 6250 bpi drive. All data readout is based in CAMAC using a Jorway model 411 serial branch driver. For the CDF prototype front end electronics, a special CAMAC based interface module was constructed to drive the remote scanning ADC to digitize the sample and hold values. In addition to the event data modules, the CAMAC system contained a variety of control and status modules to provide a complete monitoring of the test stand enviroment and control over the operating parameters.

The on-line main program, RUNCONTROL [6.4] allow the user to link the event stream to analysis routines, display and

histogramming services (YHIST), and data management routines (YBOS). The device drivers which service interrupts from CAMAC readout the event data, and execute CAMAC programmed I/O commands. As a debugging aid and a tool for quick test runs or studies, a limited interactive capability was available to define, clear, and display HBOOK/HPLOT results without recompiling. This feature made remote access to the histogram data on the run in progress a convenient and much used capability.

6.3 COSMIC RAY TEST STAND

In order to minimize systematic variations from module to module and allow data taking to proceed unattended for long periods of time, a dedicated cosmic ray test stand facility was constructed [6.2]. Functions provided by this test stand included triggering on isolated penetrating cosmic ray muons, fine grained tracking of the muon trajectories, computer based data acquisition and online monitoring, and gain calibrations for both the readout electronics and the calorimeter towers. The various components of the test stand are described in this section.

6.3.1 Trigger Counters And Rates

Figure 6.5 shows two views of the cosmic ray test stand apparatus with a calorimeter module in place. Three planes of trigger scintillators called Upper, Lower, and Side are used to define the ten trigger roads which correspond to the ten

projective towers within the EM section of the calorimeter module. The scintillator pieces were cut to match the projected size of each tower individually - virtually eliminating any trigger from muons which cross tower boundaries. Two fold coincidences of either Ui*Li or Si*Li determine the ten trigger roads where i refers to the tower number.

The spectrum of cosmic ray muons has a steep energy dependence and varies with zenith angle. The thickness of the calorimeter module is sufficient to absorb the copious soft component in cosmic rays, except for the towers near the 45 degree side. To ensure that the energy of muons satisfying the trigger requirement is in the region of minimum ionization and reduce the effects of multiple scattering and straggling, an additional 8" thick iron absorber was placed under the Lower trigger counters. Another scintillator counter plane, called Hardner, was insalled below this absorber and included in the trigger requirement. Since the projective tower trigger roads are already established by the U, S, and L counters, the Hardner is implemented as two large counters for convenience.

The U, S, and L counters were cut from 7 mm thick polystyrene based scintillator and viewed by Hamamatsu type R329 phototubes. For the Hardner counters, 0.25" thick polystyrene scintillator was used along with RCA type 4522 phototubes. After plateauing the trigger counters, it was observed that a 50 Volt decrease in the high voltage produced no discernable effect on the trigger rates.

The total trigger rate over all the ten towers is 1.8 Hz with hardner. Figure 6.6 shows the relative trigger rate for each tower obtained with the calorimeter module and the hardner in the configuration of Fig. 6.4. A Monte Carlo simulation result is presented with the histogram, which involves the effects of (1) the muon energy spectrum obtained by Green et al [6.5] and (2) the minimum ionization loss of muon energy in the calorimeter materials. With the extra hardner absorber in place, the minimum muon energy for triggering varies from 1.5 to 1.7 GeV across towers 0 through 5 and from 1.2 to 0.5 GeV for towers 6 to 9. From the simulation, we estimate the average energy of trigger muons to be 3.4 GeV.

6.3.2 Muon Tracking

Since the trigger roads correspond to the full size of each tower, a set of drift chamber are used to measure the trajectories of trigger muons within the more coarse roads. The upper drift chamber is actually the central muon chamber which is an integral part of the CDF calorimeter module design [6.6]. The side and lower drift chambers were designed and constructed specifically for the test stand. An additional constraint on the trajectory of a muon was provided by the strip chamber embedded in the EM calorimeter module at the shower maximum depth. Thus, cosmic ray testing also helped to commission both the central muon chambers and the strip chamber. The fine grained spatial information provided by the chambers was useful to the data analysis in rejecting triggers caused by multiple particles.

The drift chamber consist of four layer packages containing rectangular cells with dimensions of 2.5" by 1". There are 48 cells in a package with an external cross section that is 32" wide by 4" thick. Sence wires in alternate layers are offset by 2 mm to resolve the left-right ambiguity. Operating of the chambers in limited streamer mode with a 50/50 mixture of argon and ethane (containing 1 % ehyl alcohol) provided the longitudinal coordinate using charge division on the resistive sense wires. The voltage on the cell walls was -2.5 kVolts, and that on the sense wire was +3.1 kVolts. Transverse resolutions of 250 microns on the 3.1 cm drift space and longitudinal resolutions of 47 mm on the 230 cm long sense wires were achieved in this test [6.6]. However the longitudinal resolution is expected to be improved to better than 5 mm with a Fe-55 source calibration.

6.3.3 Trigger And Data Acquisition Electronics

A block diagram of the cosmic ray trigger electronics is shown in Fig. 6.7. The ten two fold coincidences of the pairs of trigger counters Ui*Li and Si*Li are done with a resolving time of 10 nsec and then summed by an OR circuit to form the basic cosmic ray signal CR. A parallel set of circuits is used to determine whether either the U plus S plane or the L plane contained multiple hits (DBLE) within 50 nsec. The single cosmic ray signal SNGL was then formed by combining CR with the Hardner counter signal (HARD) and the multiple hit veto.

To insure that cosmic ray triggers determined by the SNGL logic are not contaminated by other cosmic ray particle occurrences during the data acquisition gate live time, the presence of any late particle hits (LP) is monitored by a coincidence between SNGL and a late hit in either the U plus S or L planes. This LP monitor is formed with a resolving time equal to the gate width and recorded. The final event rate was reduced from 1.8 Hz to 1.6 Hz by rejecting LP events in the offline analysis.

For each cosmic ray trigger, the data acquisition system recorded the charge from the calorimeter phototubes, the trajectory information from the muon and strip chambers, and the trigger counter hit patterns. Standard commercial CAMAC TDC, ADC, and latch modules were used to digitize the muon chamber drift time and charge division signals and to record the trigger counter pattern. For the strip chamber and phototube signals, prototype versions of the CDF front end electronics were used both to facilitate comparisons with test beam data and to avoid electronics cross normalization problems between calibration data and collider operation. In the CDF front end electronics system [5.1, 5.2], high gain-bandwidth charge integrators are followed by synchronous sample and hold buffers which are then multiplexed to a local scanning ADC in the same crate for digitization and readout for data recording Correlated double sampling is used to remove any base line from prior signals and reduce noise. The CDF electronics is attached to the back of each calorimeter module providing a minimum noise short interconnect enviroment

and eliminating the need for preamplifiers and driver/receivers to remote digitizers. A 16-bit dynamic range is provided with 11 to 30 femtoCoulombs (fC) rms noise.

When used in the collider, the basic data acquisition cycle of reset, measure, and hold for the CDF front end electronics is synchronized to the beam crossings. However, cosmic ray triggers are random occurences which need a special synchronization in the data acquisition control logic as shown in Fig. 6.8. Gating cycles (reset, measure, and hold) for both the CAMAC and CDF electronics are generated by a fixed frequency oscillator and appropriate delays. A dead time flip flop allows the cycles to continue until a cosmic ray trigger occurs within the legitimate live time window of the cycle. This coincidence then sets the dead time flip flop to inhibit further cycles and freeze the event for digitization and computer readout. On completion of readout, the dead time flip flop is reset permitting gate cycles to resume until the next cosmic ray trigger. With the oscillator period set to 20 microsec, a live time window of 18 microsec was achieved corresponding to trigger efficiency of 90 %. It was essential to select CAMAC modules which provided a fast clear function to be compatible with this mode of free running gate cycles.

The data acquisition control logic also accomodated a variety of ancillary triggers by means of a CAMAC output register used as a trigger mask for selecting options. In addition to the cosmic ray trigger, the system allowed operation with LED, Xenon

flash lamp, pedestal, charge injection calibration, or test triggers. Electronics checkout and system gain monitoring were automated using these options.

6.3.4 On-line Computer And Data Recording

Data readout and on-line analysis is performed using a VAX 11/730 minicomputer. Events are logged onto magnetic tape with a standard DEC model TS-11 1600 bpi drive. All data readout is based in CAMAC using a Jorway model 411 serial branch driver. For the CDF prototype front end electronics, a special CAMAC based interface module was constructed to drive the remote scanning ADC to digitize the sample and hold values. A typical cosmic ray trigger produced approximately one hundred 16-bit words of data, so that there were about 40,000 events on a tape. In addition to the event data modules, the CAMAC system contained a variety of control and status modules to provide a complete monitoring of the test stand enviroment and control over the operating parameters.

The on-line main program, MIDAS [6.7], provides sharable images that allow the user to link the event stream to analysis routines, display and histogramming services (HBOOK/HPLOT), and data management routines (YBOS). the device drivers which service interrupts from CAMAC, readout the event data, and execute CAMAC programmed I/O commands are included in MIDAS. As a debugging aid and a tool for quick test runs or studies, a limited interactive capability was available to define, clear, and display HBOOK/HPLOT results without recompiling. This

feature made remote access to the histogram data on the run in progress a convenient and much used capability.

6.4 FRONT END ELECTRONICS CALIBRATION

All front end electronics servicing the phototube, strip chamber, and muon drift chamber systems proved to be quite stable over periods of many months. Since the phototube pulse heights were the critical measurements made at the test stand, the gains of the charge integrators and the current readout channels were routinely recalibrated and updated in the offline analysis approximately every two weeks. Calibration was performed in a separate front end crate with the ADC scanner interfaced to an IBM personal computer. Known charges were injected to the amplifier by charging a 472 pF capacitor with pulses from a programmable BNC 9010 pulse generator. The observed pulse heights from the charge integrator were fit to a straight line to obtain the amplifier gain. The current channel was calibrated by injecting current from a Keithley 261 Picoampere Source. Figures 6.9(a) and 6.9(b) show, respectively, representative plots of channel gains as a function of time for the charge and current channels. The current channel gains shown are from two prototype amplifier boards. The final version of the electronics has a nominal current channel gain of 11 pA/ADC count and boards of this type were used during the last three months of operation of the test stand. The data of Fig. 6.9(b) are shown since these cards were in service for a longer period and have more calibration data available. The stability of the newer

electronics was found to be equal to that of the prototypes. The obvious feature of the plots is the similarity in the gain fluctuations from channel to channel. This indicates that the calibration system itself is less stable than the front end electronics. The absolute gain of the charge channels is, thus, uncertain to a level of as much as 2 % while the more accurate current source allows the absolute gain of the current channels to be known to approximately 0.5 % which is the accuracy of the current source calibration by Keithley. Considering only the relative stability, the figures indicate that the charge amplifiers' gains are constant to a level of 0.76 % while the current gains are stable to 0.10 %.

The electronics servicing the muon and strip chambers did not need periodic calibration since the gains were stable enough for the accuracy required for tracking. The muon TDC and ADC system was only calibrated when CAMAC modules were replaced. The gains of the strip and wire amplifiers for the strip chamber came hand set to within a few percent to 0.25 fC/ADC count and 1.0 fC/ADC count, respectively, and no calibration was required when replacing the electronics boards.

6.5 DATA ANALYSIS

6.5.1 Test Beam Data

The energy calibration at each tower center was made with 50 GeV electrin beams for 50 modules. Also were taken the mapping data for 5 modules to make the response maps to be used in a

database. The total number of modules is due to the limited relating to the schedule of beam testing.

Reference Points

The position for the normalization of the response is defined at each tower center (see Fig. 6.10). The position is tabulated in Table 6.1 [6.8]. For Tower 9, the position is not the physical tower center because of the structure. The position is defined to give a minimum leakage for the longitudinal shower.

Calibration Constant at Tower Center

As described before, the data for electron beam were taken towice for each module. To compare the data each other, the calibration constant at each tower center was obtained in the online data analysis at NW beam line. The difference is required to be less than 1 %. If there is any channel with the difference more than 1 %, the module was calibrated again. The average of the differences is 0.3 %.

Response Map

The mesh elements on the plane of the strip chamber are defined by dividing into 250 in Z and 50 in X [6.8] The size is 1 cm by 1 cm. The average and rms values of the response for 50 GeV electrons are calculated for each mesh element.

Parametrization of Response Map

The response map is normalized by that at tower center and parametrized [6.8] as

$$S(X,Z) = F1(Z)\ F2(Z)\ \cosh(\ X/w(Z)\ )\ F3(X,Z)\ , \qquad (6.1)$$

where

$$F1(Z) = P1\ \left[1 + P2\ \exp(P3\cdot Z)\ \right]^{-1}, \qquad (6.2)$$

$$F2(Z) = 1 + P4\ Z + P5\ Z^{2}, \qquad (6.3)$$

$$w(Z) = P6\ P7\ (1 + P8\ Z + P9\ Z^{2}\ )\ , \qquad (6.4)$$

$$F3(X,Z) = \left[1 + P10\ \exp(P11\ |X| + P12\ |X\cdot Z|)\ \right]^{-1}. \qquad (6.5)$$

The functions F1 and F2 are provided to fit data at theta boundary between towers and at central area of the tower. The function w(Z) is used for the Z dependence of phi response which is parametrized by cosine hypobablic. The function F3(X,Z) is fit to data at phi boundaries.

6.5.2 Cosmic Ray Data

A total of 50 modules were tested at the cosmic ray test stand. Typically about 200,000 events were used for making response map for each module as listed in Table 6.2. There are several modules with less statistics, which is merely due to the limited time relating to the schedule of beam testing.

For muon tracking, two different procedures were applied. One is track selection in which the muon tracks were reconstructed by using muon chamber data selecting for only those pointing to the interaction region in the configuration of proton-antiproton collisions. The other is no track selection in which all the triggered muons were accepted within an angular

acceptance of about 40 mrad for each tower and the positions were determined from the strip chamber. Since the former reduced the statistics to 10 % or less of the total events, we applied the latter in most of the cases. It has been demonstrated that for mapping at the 1 - 2 % level, the no track selection method can be applied. For either case, the effect of multiple scatterings is estimated to be small [6.6].

With a total of 200,000 events and a required statistical precision of 1 - 2 %, it was possible to subdivide the ten towers into a 650 element grid. The mesh size was typically 4.4 cm by 3.3 cm for towers 0 - 4 and 4.4 cm by 4.0 cm for towers 5 - 9 on the plane at the strip chamber depth.

The response was obtained from the sum of 2 tube outputs for each mesh element. The measurement of response of minimum ionizing particles is sensitive to the pedestal variation for a long run time such as was typical during normal data acquisition. Correction for the time variation of pedestals was made in the offline analysis.

Response Map

The definition of local coordinates in a tower is shown in Fig. 6.11. where Z (θ) is the coordinate along the beam direction and X (φ) is the one around the beam axis in the configuration of proton-antiproton collisions. The boundaries of X and Z in a tower are $-12\ \text{cm} < Z < 12\ \text{cm}$ and $-23\ \text{cm} < X < 23\ \text{cm}$, respectively. The mesh elements on the plane of the strip

chamber are defined by dividing the strips into 65 groups in Z and wires into 10 groups in X. The definition of the strip and wire groups is tabulated in Tables 6.3(a) and 6.3(b).

As stated previously, 200,000 cosmic ray events per module gives a statistical precision of 1 - 2 % for each mesh element. The response data is normalized to the response in the central area of a tower, $|X| < 8$ cm and $|Z| < 5$ cm in this case.

Although the pulse height distribution of muons is expressed by a convolution of 31 Landau distributions, a fit to a Gaussian function was adequate to estimate the peak value. For incident particles crossing the tower boundaries, which are mostly rejected in triggering, the response is obtained by summing the pulse heights in two adjacent towers.

Parametrization

The calorimeter response along X was expected to be symmetric from the structure of EM calorimeter. It is observed that the light attenuation curve viewed by a single phototube is not a simple exponential function. The main reason for this is due to the reflection of the light on the edge and the wave length dependence of the attenuation. As for the edge, the light collection is different from that in the central region due to the presence of a gap between neighboring waveshifters as mentioned in section 3.1.

In fitting the response in X to a function, the following parametrization is chosen:

$$P0 + P1 = A \cosh(X / w) , \qquad (6.6)$$

where P0, P1 are the phototube pulse heights, and A and w are parameters which are functions of Z. The following parametrization is also made:

$$P0 / P1 = B \exp(- 2 X / L) , \qquad (6.7)$$

where B and L are parameters which are functions of Z, and L corresponds to the conventional attenuation length.

Time Variation of Pedestals

Data taking runs continued for about 4 days in order to accumulate 200,000 events per module. A significant time variation of pedestals against the muon pulse height was observed during the run. Figure 6.12 shows the time variation of pedestals in a worst case where the variation amounts to 7 - 8 % of the muon peak value. The correction was made in the offline analysis by using the fact that all tubes were read out for each cosmic ray event, not just those in the trigger road. This allowed an event-by-event pedestal to be accumulated using all towers not associated with the trigger. In this procedure, the average pedestal value for each tube was calculated every 250 triggers which correspond to a running time of 2 - 3 minutes.

6.5.3 Source Calibration Data

Since the Cs-137 calibration system lacks any position information on the source, the current from each tube is read as the source moves through the calorimeter and a fit is made to the resulting map of source current vs. read number. The number serves as a convenient indicator of the relative position. Therefore the reproducibility of thecalibrations depends crucially on the fit.

Typical plots of the pulse height in ADC counts from current channel of RABBIT card vs. read number are shown in Figs. 6.13(a) and 6.13(b). A response map of a tower 0 is shown to illustrate the fact that the mechanical limit of the source travel prevents a complete peak from being mapped out.

A calibration current is determined as follows [4.2]: The dark current pulse height is determined first. Next, the current peak value is estimated by fitting the pulse height to a 6th order polynomial for all towers except for tower 0. For tower 0 the value of the fit at the read number of maximum pulse height is calculated. All points with a net (dark current subtracted) pulse height greater than 80 % of the maximum reading are used in the fit of the pulse height vs. rean number. Typically about 50 points are used in the fit for towers 1-9 and about 30 for tower 0. Figures 6.14(a) and 6.14(b) shows expanded plots of the peak regionns from Figs. 6.13(a) and 6.13(b) along with the fitting curves. As can be seen in the figure, the data are well-represented by the fit.

CHAPTER 7

DETECTOR PERFORMANCE: RESULTS OF TESTS

All 50 modules were calibrated at each tower center with 50 GeV electrons. The calibration cnstant, typically 2 pC/GeV/tube, at each tower center was obtained with 0.1 % of statistical error and 0.3 % of systematic error. For 5 modules of them, the mapping data were taken. The cosmic ray data were taken for 41 modules.

The goal of the energy calibration is to obtain the response map which make a correction for the non-uniformity of the response and is used for the measurement of the energy of the electromagnetic particle with a minimum systematic error.

We present here the result on the response map and the correction of the non-uniformity with other performance of the central electromagnetic (EM) calorimeter (calibration constant, voltage, linerity, energy resolution, pulse height for the punch-through particle, and stability) and the performance of the strip chamber.

7.1 CALIBRATION CONSTANT

Using radioactive sources, the volatge of the central EM calorimeter phototubes are set so as to give 2 pC/GeV for electrons showering in the calorimeter [4.1]. The gain of phototubes of 13 modules set using Co-60 was found from test beam mesurements to have a mean corresponding to 2.05 pC/GeV with a standard deviation of 2.47 % as shown in Fig. 7.1(a). The results from 20 modules using Cs-137 indicate a mean of 2.04 pC/GeV with a standard deviation of 2.91 % as shown in Fig. 7.1(b). Table 7.1 presents contributions to standard deviation of individual phototube average pulse heights [4.1]. After subtraction of known contributions (electronic calibration etc.) a module-to-module deviation of about 2.35 % remains.

As described in Section 6.1, final setting of high volatge was made to get target currents. A set of target currents for 20 phototubes was obtained from the result of the high voltage setting for a standard module (No. 26). However, the actual value of current for the individual tube in other modules should change when the attenuation length for the module changes. From the cosmic ray test, the average and rms values of attenuation length are 99.3 and 9.0 % as mentioned in Section 7.4.2. If the attenuation of the light is expressed as a single expornent function, exp(-X/L), the current for the individual tube will varies with a standard deviation of 2.1 % from module to module. The value is consistent with the above deviation of 2.35 %. This deviation can be cancelled by making a correction of energy scale with the calibration constant for the individual tower.

7.2 LINEARITY/RESOLUTION

Figure 7.2 shows data on the linearity which are expressed as E/P normalized by E/P at 50 GeV vs beam energy, where E and P are calorimeter response in GeV and beam momentum. As seen in Fig. 7.2, a non-linearity is observed at the range less than 30 GeV by a few percents and it depends on towers. A Monte Carlo simulation on the linearity is carried out with the simulation package GEANT3. The package contains EGS for electromagnetic shower simulation and GEISHA for hadron shower simulation. The result on tower 3 is also shown in Fig. 7.2. The simulation shows non-linearity but it is smaller than data. We don't have enough data on linearity to study the module-to-module deviation of the non-linearity at energy less than 30 GeV. The author hope detailed study of the linearity at energy less than 30 GeV will be made in the future.

Figure 7.3(a) shows the energy resolution vs beam energy without any correction on the londituginal shower leakage. Figure 7.3(b) shows polar angle dependence of energy resolution for 50 GeV electrons. The data of typical 4 modules are plotted for each tower. These results show 14 % / $\sqrt{\text{E (GeV)}}$.

The energy resolution for scintillator sampling calorimeter can be parametrized [7.1] as

$$dE/E = R \sqrt{t / E}, \qquad (7.1)$$

where R is 14.8 % and t is a unit absorber thickness in radiation length. In our calorimeter, t is 0.57. Hence the energy

resolution for sampling is given by

$$(dE/E)samp = 11.2\ \% / \sqrt{E}. \qquad (7.2)$$

The statistical fluctuation of the number of photoelectrons contributes to the energy resolution, and it is written as

$$(dE/E)pe = 1 / \sqrt{Npe\ E}. \qquad (7.3)$$

where Npe is number of photoelectrons per GeV. The value of Npe for the sum of two phototube pulse heights was obtained from LED measurements as Npe = 230 photoelectrons/GeV (see Fig. 7.4). Hence the fluctuation is 6.6 %/ $\sqrt{E}$. The overall resolution resulting from these contribution is given as

$$dE/E = 13.0\ \% / \sqrt{E}. \qquad (7.4)$$

Our result is in agreement with the above estimate.

In our calorimeter, the thickness of one layer (t) varies as $1 / \sin(\theta)$, where θ is polar angle. From Eq. 7.1, the energy resolution depends on $\sqrt{t}$. Therfore the anglar dependence of the energy resolution is expected as $1 / \sqrt{\sin(\theta)}$. The dashed line in Fig. 7.3(b) is expected $1 / \sqrt{\sin(\theta)}$ dependence of the resolution.

7.3 MUON PULSE HEIGHT DISTRIBUTION

A typical pulse height distribution for cosmic ray muons viewed by a single phototube is shown in Figs. 7.5(a) and 7.5(b). Figure 7.5(c) is the distribution viewed by two phototubes, i.e. (P0+P1)/2. As seen in these figures, the

distributions for single phototube and two phototubes have an rms width of 20 - 21 % and 16 - 17 %, respectively.

The main contributions to the width of the peak are:

(a) statistical fluctuation in sampling photoelectrons,

(b) Landau fluctuation in energy deposited in each scintillator,

(c) variation in path length due to different incident angles of the cosmic ray muons,

(d) position dependence of the light attenuation.

The average number of photoelectrons per GeV is estimated to be 115 from LED measurements for several modules (see Fig. 7.4). This was confirmed by the electron beam test. Thus the fluctuation in photoelectron statistics $1 / \sqrt{Npe}$ is 17.0 % for an EM shower energy of 0.3 GeV, corresponding to the calorimeter response for the muon. The Landau fluctuation in multi-layer traversal was calculated by a Monte Carlo simulation. The value ranges from 4.5 % to 9.7 % depending on the tower number. These values include the effect of item (c), which varies from 1 to 6 % with increasing tower number. The value 4.5 % in tower 0 is consistent with the value calculated from a simplified formula given, for example, by Amaldi [7.2]. The variation in the response due to position dependence is also estimated by a Monte Carlo simulation to be 11.5 % for a single tube, 2 % for (P0+P1)/2.

Thus the total contribution is expected to be about 21 - 23 % for the case of single tube and 13 - 16 % for the case of the two tubes. These estimates are consistent with the observation.

The average muon peak value for all towers in the EM calorimeter was 623 fC $\pm$ 37 fC as shown in Fig. 7.6(a). Since the calorimeter gain was set to be 2 pC/GeV/phototube, the calorimeter response for a minimum ionizing particle was estimated to be 0.31 GeV. The average and rms values of the peak pulse height for each tower over 44 modules are tabulated in Table 7.2.

We notice here that the peak value of cosmic ray muons is different from that of punch-through particles (mainly non-interacting pions) of 50 GeV in the beam test as shown in Fig. 7.7. The data for all the towers 0 - 8 of 6 modules are plotted in the figure. No significant tower dependence is found. The average value of the ratios of the peak pulse height for punch-throuh particles to that for cosmic ray muons are presented in Table 7.3 for several modules. It is seen that the test beam data are higher than the cosmic ray data by as much as 10 %. This seems to be due to the fact that when the energy loss of muons and punch-through particles increases by other processes than ionization, such as bremsstrahlung, pair production, take place more frequently in the calorimeter and give a higher most probable peak value.

7.4 RESPONSE MAP

Only 5 of 50 modules have the individual response mapping data with 50 GeV electrons. There remains a question: How can the response maps for other modules be provided ? The present section is intended to answer the question.

7.4.1 Similarity Of Response Maps

As mentioned in Chapter 3, the calorimeter modules are constructed to be as identical as possible to each other. The conclution derived in the Chapter is that the calorimeter response should be identical to 0.8 %. Here the value is again examined with cosmic ray test and beam test data.

Study of the similarity of the response maps tower-to-tower and module-to-module over all modules is essential for the cosmic ray test. A total of 41 modules with the data having more than 150,000 events were used for the study.

The module-to-module similarity is defined in terms of the deviation from the average response value at each mesh point over all the modules tested. The average response is shown in Fig. 7.8. The overall rms deviation obtained this way is 1.5 %, where the data of tower 9 are excluded. The value still involves a statistical uncertainty of measurement. In order to extract the intrinsic similarity the following treatment is applied.

The normalized response in mesh element (i,j) of module m is expressed as follows:

$$Rmij = Rij + dR(sys)mij + dR(stat)mij \ , \qquad (7.5)$$

where Rij is the average response for all 41 modules in mesh element (i,j), dR(sys)mij is the systematic component of the deviation of response in module m, and dR(stat)mij is the uncertainty due to statistical fluctuaton of the measurement. Assuming that dR(sys)mij is independent of dR(stat)mij, the following expression can be written:

$$\sum_{m=1}^{41} (Rmij - Rij)^2 = \sum_{m=1}^{41} dR(sys)mij^2 + \sum_{m=1}^{41} dR(stat)mij^2 \ , \qquad (7.6)$$

The module-to-module deviation from average, hereafter called dissimilarity, is defined as follows:

$$Dij^2 = \frac{1}{41} \sum_{m=1}^{41} dR(sys)mij^2$$

$$= \frac{1}{41} \left(\sum_{m=1}^{41} (Rmij - Rij)^2 - \sum_{m=1}^{41} dR(stat)mij^2 \right). \qquad (7.7)$$

The resulting mean value of D and its rms deviation over the whole area are 0.95 % and 0.47 %, respectively (see Table 7.4(a)). The value of dissimilarity is almost independent of towers. However there exists a dependence of D on the regions in a tower. Figures 7.9(a) - (d) show the distributions of D's in towers 0 - 8 for four different regions, i.e. the entire region, the central region ($|X| < 17$ cm, $|Z| < 10$ cm), the θ -edge region ($|X| < 17$ cm, $|Z| > 10$ cm) and the φ -edge region ($|X| > 17$ cm, $|Z| < 12$ cm), respectively. As is seen in Fig. 7.9(b) the dissimilarity obtained in the central region is 0.76 %. The average and rms values of dissimilarity for each tower were

calculated using all of the 41 modules and are listed in Table 7.4(a) dividing into several regions. As for tower 9, the distributions are shown in Figs. 7.10(a) - (d).

Next, the X dependence of D is examined. The average dissimilarity along a fixed X is presented in Table 7.4(b). The distribution for each X is given in Fig. 7.11. The average value increases as X increases. The value in the region of $|X| >$ 17 cm exceeds 1 % for towers 0 - 8.

7.4.2 Parameters W And L

The parameters w and L were obtained for 65 points in Z defined by strip groups The definition of strip groups is given in Table 6.3(a). A typical response map in x at the Z center in a tower is shown in Fig. 7.12(a), where the solid curve is fit to an expression cosh(X/w) for the region $|X| <$ 17 cm. The distribution of the ratios of two tube outputs in X at the Z center is shown in Fig. 7.12(b), where the solid curve is fit to exp(-2 X/L) again for the same region $|X| <$ 17 cm. The errors in w and L in the above fitting are 1 % and 5 %, respectively.

Figures 7.13(a) and (b) show the distribution of w's and L's at the Z center of each tower over 46 modules. The correlation plot between w and L in the cosmic ray test is shown in Fig. 7.14. The average values of w and L are 55.0 cm and 99.3 cm, respectively. Here we examine the tower-to-tower and module-to-module deviations in w's and L's obtained at the tower centers. The result is listed in Table 7.5, and indicates that

the deviations from tower to tower within a module for both quantities are significantly smaller than those for module-to-module. This may be a consequence of the quality control in construction of the calorimeter modules: The edges of calorimeter module facing to the wavelength shifters were poloshed with diamond cutters. The polished surface is not optical plane. The reflection coefficient for the light possibly changes from module to module, but it will be small for tower-to-tower.

This suggests the necessity of a set of uniformity corrections for each module depending on the required precision of correction.

The Z dependences of w's and L's for 46 modules are shown in Figs. 7.15(a) and (b) respectively, in which the data points are normalized by their average values at tower centers. As is seen in the figures, the mean value of L increases as the hit position becomes closer to the tower boundary, while that of w does not show clearly such a trend within the spread of about 9 % of the rms deviations. One of the reasons for the difference is considered to be due to the fact that the cosmic ray data involves incident particles with different impact angles, which causes a change in track lengths within a certain angular acceptance. The effect seems to be more sensitive to w than L because in the derivation of L, the ratio of two phototube outputs is involved, which tends to cancel the above effect.

In order to test this point, we applied the track selection

procedure mentioned previously to a particlar module with high statistics. In this procedure, the muon track was required to pass through the same subdivision, divided into 12 per tower, in the upper and lower muon chambers. The result indicates that the value of w is reduced by 12.3 % while that of L is reduced by only 3.5 %. In this sense, the cosmic ray test with the present analysis procedure is capable of providing a reliable value of L. The increase of L in approaching to the tower boundary is obviously an effect of the presence of a gap in the light collection at the tower boundary.

The dependence of L on Z for each tower can be expressed by using a polynomial:

$$L = L0\ (1 + C1\ Z + C2\ Z^{2}) , \qquad (7.8)$$

where L0 is the value of L at each tower center of each module. The resultant fits are shown in Fig. 7.16 as the solid curves. The average and deviation in these values for each tower using 46 modules are presented in Table 7.6.

Finally we mention the magnitude of deviation of the response reflected from the deviation of w. The average value of w is 55.0 cm and the module-to-module deviation is 9.2 %. The deviation of the response R is expressed in terms of that of w as

$$dR/R = (dw/w)\ (X/w)\ \tanh(\ X/w) , \qquad (7.9)$$

where $R = A \cosh(\ X/w\ )$. At X = 15 cm and 20 cm, for example, the values dR/R are 0.7 % and 1.2 %, respectively. The estimate is consistent with the results shown in Table 7.4(b).

7.4.3 Comparison With Beam Test Results

For the mapping purpose in the beam test, 5 modules were scanned precisely with 50 GeV electrons. The response at each point was measured with a statistical error of less than 0.5 %. The mesh size was chosen to be 1 cm by 1cm, while the impact point separation and beam size were 4 cm and 2.5 cm in diameter, respectively [6.8].

The similarity for each mesh was examined in the same manner as that for the cosmic ray data. The overall rms deviation in dissimilarity is found to be 0.8 %. The deviation in the central area ($|X| < 20$ cm and $|Z| < 10$ cm) is 0.6 %. The results from both beam and cosmic ray tests are consistent with the estimate in Chapter 3.

Typical response maps as a function of Z are shown in Fig. 7.17. Since the tower structure differs in its geometical characteristics among tower 0, towers 1-8 and tower 9, the Z response map is shown separately in Figs. 7.17(a), 7.17(b) and 7.17(c), respectively. The response maps from the cosmic ray muons for this particular module are also shown in the figure. Shown in Figs. 7.18(a), 7.18(b) and 7.18(c) are the response maps in X at the tower center in the same module and same towers above mentioned. The corresponding cosmic ray muon data are also shown in the figures.

The above figures indicate that mapping with cosmic ray muons does not provide accurate and useful maps of response for

theta-boundaries and phi-edges. This mapping should be made by scanning with the electron beam.

The parametrization of X-dependence of the response map by w and L is made for the electron data. The parametrization is to be compared with those from cosmic ray data. The distributions of w's and L's are shown in Figs. 7.19(a) and 7.19(b). The mean values of w's and L's obtained from electron data are 44.2 cm and 89.2 cm, respectively. The values are those obtained from the data in the range $|X| < 19$ cm. The values are smaller than those from cosmic ray data by 18.0 % and 9.5 %, respectively. The fact is already mentioned and explained in Section 6.3. The rms deviations of w and L obtained from 5 modules are 10.3 % and 3.8 %, respectively. The correlation between w and L is also examined and is found to be slightly stronger than that in cosmic ray data as shown in Fig. 7.20. A larger dispersion for module-to-module than for tower-to-tower is observed as in the cosmic ray data.

7.4.4 Parametrization Of Response Map

The shape of the response map in a tower is a saddle shape. Figure 7.21 shows the typical response of the towers 0 and 1 obtained from electron data. As seen in the figure, the data is not completely filled in the mesh elements which are defined to make a map. However, the response at the mesh element missing data can be obtained by parametrizing the response map. The response can be parametrized [6.8] as

$$S(X,Z) = F1(Z)\ F2(Z)\ \cosh(\ X/w(Z)\ )\ F3(X,Z)\ , \qquad (6.1)$$

where

$$F1(Z) = P1 \left[1 + P2 \exp(P3\ Z)\right]^{-1}, \qquad (6.2)$$

$$F2(Z) = 1 + P4\ Z + P5\ Z^2, \qquad (6.3)$$

$$w(Z) = P6\ P7\ (1 + P8\ Z + P9\ Z^2), \qquad (6.4)$$

$$F3(X,Z) = \left[1 + P10 \exp(P11\ |X| + P12\ |X \cdot Z|)\right]^{-1}. \qquad (6.5)$$

The functions F1 and F2 are provided to fit data at theta boundary between towers and at central area of the tower. The function w(Z) is used for the Z dependence of phi response which is parametrized by cosine hypobablic. The function F3(X,Z) is fit to data at φ boundaries.

Figure 7.22 shows typical response of a tower obtained from the parameters, which is normalized at tower center. Table 7.7 presents the value for each parameter from average map of 5 modules. The values for parameters for each module are given in Ref. 6.8.

Using these parameters raises the question on accuracy of the energy determination. Using 5 module data, the study on the accuracy of energy determination was carried out. A deviation of response from the average map is defined as reproducibility of the map for each module.

Figure 7.23(a) shows the non-uniformity of the response, which is subtracted by 1.00. There seem to be a higher tail by +13 %. The main peak in the distribution of non-uniformity is from central region and bump from the region around |X| = 20 cm. A lower tail is due to the response at tower boundaries on

φ -cracks. The rms deviation of the distribution is 3.9 %. The value at φ -cracks is 7 %.

Figure 7.23(b) shows the non-uniformity of the response after correction with the parametrization for a averaged map over 5 modules. A dot-dashed line in Fig. 7.23(b) shows a reproducibility for towers 0 - 9 of 5 modules. It is from similarity (solid line) and fitting error (dashed line).

Figure 7.24 shows a dependence of reproducibility, similarity and fitting error on the distance (r) from phi-edge at the depth of the strip chamber over all towers of 5 modules. Figures 7.25(a) - 7.25(j) shows the same dependence but for for each tower. As seen in Fig. 7.24, the uncetainty is 1.1 % at r = 3 cm. The energy can be determined by this parametrized map better than 1.1 % in the region of $|X| < 20$ cm if the absolute energy scale for each tower is exactly obtained at the reference point.

7.5 LONG-TERM STABILITY

We have studied the long-term stability of the central EM calorimeter by comparing the cosmic ray test data for a particular module (No.17) taken at an interval of 7.5 months [7.3].

The following possibilities would cause the deterioration of the calorimeter response: (a) damage to fluors in the scintillator, (b) decrease in the transparency of the

scintillator base, (c) deterioration of the light collection system which consists of the wavelength shifter and light guide, (d) change of the pototube gain.

The pulse height was measured to estimate effects (a) to (d). The measurement of the attenuation length (L) was useful for estimating (b).

Details can be found in Ref. 7.3. The following conclusions are drawn:

(1) The deterioration in muon pulse height is estimated to be 2.0 $\pm$ 0.6 % per year.

(2) The deterioration in the attenuation length (L) is 2.7 $\pm$ 2.9 cm per year.

when the calorimeter is left alone.

7.6 STRIP CHAMBER

The pulse height response and shower position determination in the strip chamber have been investigated with test beam [7.4].

The pulse height response is consistent with expected electron shower profiles. The angular dependence of the pulse height response is consistent with $1/\sin(\theta)$ expected from the geometry.

The shower profile seems to be consistent with a universal shape which is independent of energy and angle, viewed in the

plane perpendicular to the electron direction. The position resolution achieved behaved as $1 / \sqrt{\text{pulse height}}$, and is around 1.1 mm at 100 GeV in the wire view, the resolution on the strips being slightly worse. Even in the worst case, when therw is a dead channel, a position resolution of 2.7 mm was achieved at 50 GeV.

CHAPTER 8

THE FIRST COLLISION

In October 1985, the first operation of the Fermilab proton-antiproton collider (Tevatron) [Appendix B] provided beam-beam collisions at a center of mass energy of 1.6 TeV. The Collider Detector at Fermilab (CDF) detected 23 beam-beam events. The brief description of this run is given in Ref. 8.1. Figure 8.1 shows an event display of the VTPC wire data for the beam-beam interaction. Note that the aspect ratio is distorted. Figure 8.2 shows central calorimetry lego plot for the event in Fig. 8.1.

The Tevatron was operated with 1 bunch of protons and 1 bunch of antiprotons. The proton bunch was composed of 1 main bucket and 2 small satellites, the antiproton bunch of about 10 buckets. The estimated number of particles in the main bucket is approximately $1.5 - 1.8 \times 10^{10}$ for protons and $1.4 - 3.8 \times 10^{5}$ for antiprotons [8.2]. The luminosity is given by

$$L = f\ n\ Np\ N\bar{p} / A, \quad (cm^{-2}\ s^{-1}) \qquad (8.1)$$

where

f = revolution frequency = 1 / 21 μ sec,

n = number of bunches = 1,

Np = number of p's / bucket = 1.5×10^{10},

$N\bar{p}$ = number of $\bar{p}$'s / bucket = 2×10^{5},

A = cross sectional area of beams = $(0.02\ cm)^2$ for low beta.

A luminosity of $3.6 \times 10^{23}\ cm^{-2}\ s^{-1}$ is obtained from the above parameters. The trigger rate was about 0.06 Hz on the average. Most of triggers were due to beam-gas events.

In this chapter, a detailed study of the data is presented as compared with a Monte Carlo simulation. Also is discussed the background for the trigger in this chapter.

8.1 1985 CDF RUN HISTORY

The 1985 CDF run collected proton-antiproton collision events in 3 runs on the night October 12-13, 1985. A total of 887 triggers were recorded in the 3 runs. Blow-by-blow account of the 3 runs is presented in Table 8.1 with time and event number.

From the information, one sees that proton-antiproton collisions should take place only during Events 404-542 (Run 489), Events 1-16 (Run 493), and Events 204-333 (Run 494). As described in section 8.5, all 23 beam-beam events are in these interval (although Event 203 of Run 494 presumably comes just before the beam was fully squeezed).

8.2 EXPERIMENTAL APPARATUS

Parts of the CDF with associated electronics and readout systems were installed in the B0 collision hall in September 1985, which were composed of the central calorimeter, Vertex TPC (VTPC), and the beam-beam counter (BBC). We give in this section a description of CDF, trigger system and data acquisition system in the 1985 run.

8.2.1 Calorimetry

The calorimetry consists of the central EM (CEM), central hadron (CHAD), and endwall hadron (WHAD) calorimeters, each being of the sampling type (see Fig. 8.3). The EM calorimeters contain lead plates as the absorber, whereas the hadron calorimeters have steel plates. The active medium is scintillator. The angular coverage of the central calorimetry is 2 pi in the azimuthal angle (φ) and from -1 to 1 in pseudorapidity (η). The tower size is approximately given by $d\eta \times d\varphi = 0.1 \times 0.26$, The total thickness of CEM and CHAD are 19 radiation lengths and 4 absorption lengths. The WHAD calorimeters are mounted on the steel (magnet yoke). The total thickness of WHAD is 5 absorption lengths.

The central strip chambers for 2 modules were available for the data taking because of the lack of the strip chamber cards.

8.2.2 VTPC

A set of vertex time projection chambers (VTPC) is one of

the major components of the CDF tracking system to measure charged particle multiplicities and to determine accurately the Z-position of interaction vertex [8.3]. It consists of 8 double time projection chambers surrounding the beampipe in the central region of the CDF detector (see Fig. 8.4). They are operated at atmospheric pressure, and have been sized such that the maximum drift time is less than 3.5 micro seconds. This is the time between bunch crossings in the Tevatron when there are six proton and six antiproton bunches in the machine. In 1985 run, only wire channels (TDC's) were read.

8.2.3 Beam-Beam Counter System

The BBC system [8.4] was set up to provide a relatively unbiased trigger as one of the trigger systems for CDF. The system consists of 2 BBC modules, i.e. West and East modulues, FASTBUS/CAMAC system hardwares, and gating logic [8.5].

The West and East modules had 15 and 14 scintillation counters, respectively, during the 1985 run [8.5]. A complete system should have 16 counters for each module, where the angular segmentation is 4 in azimuth by 4 in pseudorapidity. The counters take approximately equal bites in units of pseudorapidity. The modules were placed at the forward (east) and backward (west) position of 581.6 cm from the origin of CDF coordinate system. Each module ranges 5.7 mRads (0.33 degrees) to 80.6 mRads (4.62 degrees).

8.3 TRIGGER SYSTEM

The expected interaction rate is of the order of 0.07 Hz at a luminosity of 10^{24} cm^{-2} s^{-1} . The rate was less than that of background events i.e. beam-gas event, cosmic ray event etc. Trigger system was used to identify the beam-beam events, and to cause the data for these to be written to magnetic tape at a rate of a few Hz. The trigger system is based on FASTBUS system.

The trigger condition for beam-beam events in this run was

$$\text{BBC} * \text{L1}, \tag{8.2}$$

where BBC is a beam-beam counter trigger without halo veto (*) and L1 is a level 1 calorimeter (Et) trigger. Both BBC and L1 are described below.

8.3.1 Beam-Beam Counter Trigger

The BBC trigger was used to provide a relatively unbiased trigger: The mean time signal of signals from phototubes of each counter was sent to Latch module and the counter was latched when the timing coincide with beam-beam gate and/or halo gate, each being 30 nsec wide gate. The latch information was received by a Fast Logic Board which makes W * E and (W + E), where W and E are OR'ed logic for the counters latched in beam-beam gate in West and East modules, respectively, and (W + E) is OR'ed logic for the counters latched in beam-gas gate. Finally, the logic used

(*) "Halo" event here stands for the event in which any particle hits the beam-beam counters within 30 nsec wide halo gate.

in this experiment was

$$BBC = W * E. \tag{8.3}$$

8.3.2 Calorimeter Level 1 Trigger

The calorimeter level 1 trigger (L1) was provided on total transverse energy over all towers above a programable threshold. We here describe the level 1 trigger provided in this run below [8.6].

The trigger signals from the calorimeters comes from dedicated outputs on the front-end boards, and come to the trigger electronics on dedicated cables. The signals are DC level (typically 0 - 100 GeV is 0 - 1 volts) from the before-and-after sampling of the crossing.

All the phototube signals are brought up individually and summed upstairs, four tubes per channel into the trigger tower with size of 15 degrees in azimuth by approximate 0.2 units of pseudorapidity.

The output from each of the trigger towers in both the EM and hadron calorimeters goes to a receive and weight (RAW) card, which function to subtract a pedestal and to weight by $\sin(\theta)$ or any other normalization required. Towers above thresholds are latched and the total energy of these towers is summed by the cluster sum card.

The Level 1 trigger will be generated by comparison with the following preset values:

$$L1 = \begin{cases} \text{Single Tower} & 1.4\ \text{GeV} \\ \text{Total Et (EM)} & 1.5\ \text{GeV} \\ \text{Total Et (Had)} & 1.5\ \text{GeV} \\ \text{Total Et (EM+Had)} & 3.1\ \text{GeV} \end{cases} \qquad (8.4)$$

These parameters were determined to reject the background events, mainly come from the beam-gas interaction in the beampipe and cosmic ray.

8.4 DATA ACQUISITION SYSTEM

A simplified diagram of data acquisition system is shown in Fig. 8.5. The data acquisition system consists of a clock system, the RABBIT system hardware, 3 SSP and 7 MX scanners, FASTBUS hardware, a VAX cluster. Brief descriptions for these components are given below.

8.4.1 Master Clock System

The Master Clock system serves to deriver the timing signal, synchronized to the beam crossing. A brief description of the gating is given in Ref. 8.7.

8.4.2 Electronics

The RABBIT system performs the front end readout of signals

from the detector. The detailed description is provided in Chapter 5.

For electronics for VTPC, preamplifiers on the chambers send the signals via 10 m long cables to Amplifier-Shaper-Discriminator (ASD) crates located outside the field volume. From there, 60 m long cables carry the signals to LecRoy 1879 FASTBUS TDC crates in the counting rooms. A SLAC Scanner Processor (SSP) is scanner for this system.

8.4.3 Data Acquisition Hardware And Computing

All data readout is based on FASTBUS. The FASTBUS crate segment includes a UPI interface to the VAX, Multiple Event Port (MEP) interface to the MX and RABBIT crates, SSP and ASD to SI, and Trigger Supervisor (TS) and SI to remote crate.

Data acquisition and online analysis is performed with a VAX 11/785 computer that communicates with FASTBUS via a UPI. The online data acquisition program is called RUNCONTROL. It provides access to shareable images that allows the user to analyze the data by user's analysis routines and histogramming routines (YHIST) through data management routines (YBOS).

The FASTBUS protocal for one trigger is as follows:

(1) Level 1 sets accept line to TS.

(2) TS broadcasts start scan message to the MEP.

(3) MEP receives broardcast, clear DONE and starts MX.

(4) MX reads RABBIT crate and load buffer with data in YBOS format. SSP functions the same as MX.

(5) MEP and SI asserts DONE.

(6) TS receives DONE, enables Level 1 for next trigger and send "Event Ready" message to the VAX software Buffer Manager (BM).

(7) BM sends "New Event" message to VAX software Event Builder (EVB), instructing EVB to read next event from specified buffer.

(8) EVB reads data from MEP-MX and SI-SSP, and send "Read OK" message to BM.

(9) BM informs TS that specified event buffer is now free.

8.5 EVENT SELECTION

Beam-beam interactions were selected by cuts on the reconstructed vertex and timing cuts on the beam-beam counters (see Fig. 8.6). All the 23 good events were found by scans of both VTPC and BBC data.

8.5.1 Scan Of VTPC Data

The scanning of VTPC data was done by eyes and with a computer independently. The selection crireria for the computer

scan was [8.8] as follows:

(1) Choose good tracks.

(2) Calculate vetrex from any two tracks and get the total number of the vertices (N). If N is less than 3, the event is rejected.

(3) Find vertex-clusters with the bin size of 6 cm. Then the average of the Z-components of vertex (Zi), the rms value (dZi) and number of vertices (Ni), i = 1,2,.. N, in each cluster are calculated.

(4) Check if each Zi is inside VTPC region (-140 cm $<$ Z $<$ 140 cm). If all the vertices are outside VTPC region, then the event is rejected. Among the remaining vertices, the vertex with a maximum number of Ni is assumed to be the beam-beam event: Z0 = Zi, dZ0 = dZi, and N0 = Ni.

(5) If N0 is less than 6, the event is rejected.

(6) If dZ0 is greater than 4 mm, the event is rejecetd. This insure that the position resolution is less than 2 mm.

(7) If the asymmetric parameter of the multiplicity (A) is greater than 0.6, the event is rejected. The parameter A is defined as

$$A = \frac{| Nf - Nb |}{| Nf + Nb |} , \qquad (8.5)$$

where Nf (Nb) is the number of tracks in the forward (backward) region.

(8) If the event remained, the event is a candidate for the beam-beam event.

From the scanning by eyes, all 23 good events plus 3 additional candidates were found. From the computer scan, only the 23 good events were found.

8.5.2 Scan Of BBC Data

The computer scan of BBC data was made [8.5] as follows:

(1) Select events with good TDC and ADC data in BBC, called BBC events.

(2) Select BBC events without halo.

(3) Check the number of counters latched within beam-beam gate (Fig. 8.7):

$$Nwest \geq 5 \text{ for West module,}$$
$$Neast \geq 5 \text{ for East module.}$$

(4) Check the diffrence of Zint between BBC and VTPC with 4- σ cut, assuming the position resolution of Zint(BBC) is 10 cm (Figs. 8.8(a) and 8.8(b)).

The result of the scan is presented in Table 8.2. From the scan, 21 good events plus 2 candidates which are same events obtained from the scan of VTPC data. The 2 events plus 1 candidates were

removed due to the reconstruction efficiency of BBC [8.5]. The characteristics of 23 good events plus the 3 candidates are listed in Table 8.3.

8.6 LEVEL 1 TRIGGER THRESHOLD AND EFFICIENCY FOR UNBIASED EVENTS

During the 1985 beam-beam collision period, colliding beam data was collected only with one trigger condition, namely, beam-beam counter E*W in coincidence with a low level 1 single tower trigger. The nominal threshold for a single trigger tower was 1.4 GeV (actually closer to 2.2 GeV). The threshold was determined by using data taken with the level 1 trigger in the cosmic ray runs just prior to the colliding beam runs [8.9]. The threshold rates and efficiencies are shown in Fig. 8.9; the upper figure plots the pulse height summed over the four tubes in the CEM or CHAD trigger tower. Here the trigger tower is defined as a tower which has the largest pulse height sum in the event (and thus presumably caused the trigger). The lower plot shows the efficiency obtained from the observed yield divided by the uncut rate; for run with nominal threshold values of 1.6 GeV and 3.0 GeV, the uncut rate was defined by the lower threshold run with a nominal threshold of 1.4 GeV. For the latter run, we estimated the uncut rate so that the threshold efficiency curve has the same shape as that for the 1.6 GeV threshold run. There are probably a 5 % uncertainty in the energy scale of the threshold turn-on.

Level 1 trigger cut as determined above have been

parameterized and implemented into a program which can make the cut. The nominal energy scale of 1 GeV equals 350 counts in the sum of the 2 tubes in each tower. The parameterization gives the probability of a CEM or CHAD tower passing the level 1 trigger as follows:

(1) 0% if less than 1.3 GeV,

(2) $EXP(-(3.43-E)^4$ /2.68 between 1.3 and 2.2 GeV,

(3) $EXP(-(3.72-E)^4$ /6.23) between 2.2 and 3.7,

(4) 100% if more than 3.7 GeV.

8.7 MONTE CARLO DATA SAMPLE TO BE COMPARED WITH REAL DATA

In order to understand whether the events observed in the 1985 run is as expected, we will compare the properties of these events with events from Monte Carlo simulation (with the detector simulation and a level 1 cut being made).

8.7.1 Event Generation Model

There is no obvious and well-defined way to generate a sample of unbiased events. No Monte Carlo program (such as ISAJET, LUND, etc) claims to understand how to generate such a sample of events.

A event generation program was adjusted to give a correct average behavior of event (transverse momentum and multiplicity

as extrapolated from ISR and SPS collider data), and a correct cross section for jets at large Pt.

Generation for Unbiased Events

UA1 and UA5 studied the "minimum bias" event, which refer to non single diffractive events [1.21, 1.22]. The data on charged particle multiplicities have been obtained as a function of pseudo-rapidity. The average inclusive charged particle multiplicity increases as a quadratic function of ln(s). The central rapidity plateau height observed in UA1 and UA5 is about 3 as shown in Fig. 1.4(a). It also increases as ln(s). A cylindrical phase spase distribution with $\langle Pt \rangle$ = 0.5 GeV describes the UA5 data. However, the UA1 experiments give $\langle Pt \rangle$ = 0.42 GeV/c. On the other hand, the ISR data is described with $\langle Pt \rangle$ = 0.35 GeV/c (Figs. 1.4(b) and 1.4(c)).

For the minimum bias event at 1.6 TeV, a naive parametrization and extraporation [1.27] from SPS energy were performed, by using ISR and SPS data, in central rapidity plateau height and transverse momentum distribution. This parametrization gives at 1.6 TeV CM energy the central rapidity plateau hight of about 4 and the average transverse momentum $\langle Pt \rangle$ of 0.56 GeV/c.

The event generation program written by Odorico [8.10] are available in CDF/OFFLINE Package. Hereafter they are refered to as ODORICO. The ODORICO has an unbiased event option which gives

events without any significance in their event topologies (generated by cylinderical phase space model) and hard collision events at a resonable ratio of two kinds of events. Therefore ODORICO's program is used for event generation with $\langle Pt \rangle$ = 0.56 GeV/c.

Generation for Centauro Events

The Centauro is a paticular type of nuclear interaction, where a multiple production of baryons takes place without any significant emission of neutral pions. The characteristics of the Centauro events are tabulated in Table 1.2 for two typical events, i.e. Centauro-I and IV [1.28, 1.29].

For the sake of comparison with our collider data, we assume that all the Centauro events were produced by the decay of a new massive object (fire-ball) with unusual properties:

(1) The total number of baryons emitted in the Centauro event is about one hundred,

(2) The angular distribution decay seems to be isotropic in the CMS,

(3) The transverse momentum distribution follow the exponential low, and the average transverse momentum is 1.7 $\pm$ 0.7 GeV/c,

although other possible interactions have been suggested [8.11].

The decay products are assumed to be baryons which belong to

the octet and decuplet of baryons with spin-parity 1/2+ and 3/2+. Both octet and decuplet are characterized by symmetry of the three-quark wavefunction in both flavor and spin, where the flavor are u, d and s. We have three hypotheses for the decay products:

C1 - Nucleons,

C2 - Octet baryons J(P) = 1/2(+), and

C3 - Octet and Decuplet baryons J(P) = 1/2(+) and 3/2(+).

According to the above models, we generate the events to give average transverse momentum <Pt> of 1.7 GeV/c and average multiplicity of baryons Nb of 100.

The lorentz boost along beam axis results in angular distribution which are consistent with being isotropic and hence 77 % of the hadrons would be directed toward our central calorimeter which covers the angular rage $40 < \theta < 140$ degrees. It is also assumed that the Centauro is produced with only a low Lorentz factor (less than 0.5) in our experiment.

8.7.2 Detector Simulation

The detector simulation program CDFSIM [8.12] is available in CDF/OFFLINE package, which was developed by CDF/OFFLINE group with contributions from CDF collaborators from several detector groups.

To make a data set of biased events, detector simulation is

made with the offline package (CDFSIM), which also simulates the Level 1 trigger used in 1985 run.

8.8 RESULTS: BEAM-BEAM EVENTS

A total of 2000 unbiased events were generated. After successive detector simulation (*) for the events, only 182 events of them remained with Level 1 filter used in 1985 run. Hence the trigger efficiency for the unbiased events is estimated to be 9.1 $\pm$ 0.6 %. The error comes from only statistics in the simulation.

The total cross section of proton-anriproton collision will be about 90 mbarn at a center-of-mass of energy of 1.6 TeV (see Fig. 8.10). An inelastic cross section of proton-antiproton collision can be taken to be 70 mbarn by assuming that ratio of elastic cross section to total cross section is about 0.2. This trigger was expected to see 6.4 mbarn. shows the cross section is 6.4 mbarn. The efficiency for each model was presented in Table 8.4. We expect if the Centauro existed, the events would not have been filtered. In this study, we evaluated the total number of events to be 17 for unbiased trigger, assuming an inelestic cross-section to be 70 mbarn [8.13]. This number is consistent with observed number of events, 23.

8.8.1 Charged Multiplicity Of Observed Events Compared With MG Results.

(*) Elapsed CPU time was 17 - 18 hours per 1000 events with VAX 8600 computer.

Track multiplicity from interaction vertex is compared with Detailed analysis of track multiplicity is presented here.

We have based our preliminary analysis on hand scan rather than computer VTPC track reconstruction. This is due to several reasons --(1) While the computer reconstruction can find clean tracks within a particular half-module of VTPC, it is not currently capable of joining these track segments from different half-modules. This is because the correct alignment of VTPC's has not been studied yet. (2) The data contains many tracks (especially those at steep angles) with multiple hits per wire. The reconstruction of these tracks are difficult. So, rather than basing our results on computer reconstruction of unkonwn veracity, we tried to obtain some indications using scanning by eyes. Double scans of several events leads to an estimate of systematic error of about 15% in number of tracks.

Several issues must be discussed before we describe the results:

(1) Z-VERTEX - Our results are based only on the 13 beam-beam events that have Z vertex between -60 cm and +60 cm. Many of the remaining events have Z vertex near the edge of the VTPC so that multiplicity on one side can not be determined easily.

(2) VTPC OVERFLOW - Of the 15 events passing Z vertex cut, 6 had data overflow on the VTPC buffer of about 4100 words and thus have some octants not being read out. A total

of 13 octants out of 120 octants were data missing. We scale the results of the particular events up by a factor 8/n where n stands for number of octants with data. This should lead to a small 5-10% systematic error in number of tracks.

Figure 8.11 shows the average charged particle multiplicity per unit pseudo rapidity vs. rapidity for the 13 events. Also shown is the Monte Carlo results.

Figure 8.12 shows the average charge particle multiplicity per unit pseudorapidity vs. rapidity obtained from simulation for the following three cases:

(1) Biased sample with Level 1 triggrer containing two effects with beam pipe: photon conversion and hadronic interaction.

(2) Biased sample by Level 1 trigger without photon-conversion and hadronic interaction.

(3) Unbiased sample without photon-conversion and hadronic interaction.

Figure 8.13 shows comparision between UA1/UA5 data and our simulation at 540 GeV center-of-mass energy. The simulation can clearly reproduce those data.

Our data at 1.6 TeV is in good agreement with the simulation. Therefore one can conclude the the central platau

density is 4 in the unbiased trigger samples.

8.8.2 Energy Flow Of Observed Events Compared With MC Events

We present here some results on the energy flow of the BB events and compare the results with that obtained from MC/L1 events.

Figures 8.14(a) and 8.14(b) show the tower energy distribution for the central EM and hadron calorimeters, respectively, compared with ODORICO events. Figure 8.14(c) and 8.14(d) show the same distributions, but compared with Centauro events.

As seen in Figs. 8.14(a) and 8.14(b), the data shows the many soft particles (hadrons and gammas) exist, which are probably created in a material (beam pipe and solenid coil).

However when hadron calorimter tower has a energy deposit, EM calorimter tower shows a minimum ionization peak as shown in Fig. 8.15(a). Monte Carlo simulation result is also shown in Fig. 8.15(b).

If the energy of hadron is less than 200 MeV, the priticle will stop in the central EM calorimeter.

The fluctuation of phototube dark current is a few ADC counts for EM tubes and 20 - 30 ADC counts for Hadron tubes. This corresponds to the energy of 6 - 9 MeV/tube for EM tubes and 60 - 90 MeV/tube for hadron tubes. For hadron calorimeter, the

fluctuation is consistent with the range in which there is different between data and simulation in Fig. 8.14(b). For EM calorimeter, the difference in Fig. 8.14(a) will be possible if hadron and gammas of 120 - 180 MeV comes into the EM calorimeter.

Figures 8.16(a) - (c) show total Et information. Figures 8.17(a) - (c) show number of towers. Figures 8.18(a) - (c) show φ -dependence of Et. Figures 8.19(a) - (c) show Et(max) distribution.

All data are consistent with the Monte Carlo results of ODORICO events; Centauro is not found to the cross section of 6 mbarn at 1.6 TeV.

8.9 BACKGROUND FOR BBC TRIGGER

We had a background against BBC trigger [8.14]. The background events gave high multiplicity in the BBC-East module and low multiplicity in the BBC-West module (see Fig. 8.20). The distribution of the interaction positions reconstructed by the BBC is shown in Fig. 8.21. The average and rms spread values of the interaction positions are estimated to be - 1 m and 1 m, respectively. The question here is what types of events gave triggers in the run. As mentioned in Ref. 8.14, the source of background is beam-gas events with backward scattered particles. The schematic view of such events is shown in Fig. 8.22. The purpose of the present note is to understand quantitatively the background source.

8.9.1 Rate Of Beam-Beam Events

Hence many bucket crossings took place during each bunch crossing. However, because of the timing logic of the BBC system, the BBC would trigger the beam-beam event from only one of the bucket crossings. Therefore the beam-beam (BB) event rate is given as

$$R(BB) = \sigma(BB)\ n\ Np\ N\bar{p}\ /\ A \quad \text{(int./rev.)}, \tag{8.6}$$

where

$\sigma(BB)$ = inelastic cross section for p $\bar{p}$ collision.

The other parameters are given in Eq. 8.1. The luminosity was $3.6 \times 10^{23}\ cm^{-2}\ s^{-1}$. Assuming a $(\log s)^2$ dependence of total cross section [8.13], one can take the inelastic cross section at 1.6 TeV to be of the order of 70 mbarn. Using

$\sigma(BB) = 70$ mbarn,

$$R(BB) = 5.3 \times 10^{-7} \quad \text{(int./rev.)}. \tag{8.7}$$

8.9.2 Rate Of Beam-Gas Events

The beam-gas (BG) event rate is given as

$$R[BG(p)] = \sigma[BG(p)]\ n\ Np\ Ng \quad \text{(int./rev.)}, \tag{8.8a}$$

$$R[BG(\bar{P})] = \sigma[BG(\bar{p})]\ n\ N\bar{p}\ Ng \quad \text{(int./rev.)}. \tag{8.8b}$$

where

Ng = number of atoms in gas between W and E modules per unit area,

$\sigma[BG(p)]$ = inelastic cross section for p-gas collision,

$\sigma[BG(\bar{p})]$ = inelastic cross section for $\bar{p}$-gas collision.

The p-p and p-$\bar{p}$ inelastic cross section are about 33 mbarn at $\sqrt{s}$ = 40 GeV. Assumption that the gas is 85 % hydrogen and 15 % heavy species (CO, N2) [8.15] gives an effective cross section of 64 mbarn per atom for inelastic interactions.

The density of gas molecules in the beampipe, ρ , is estimated as

$$\rho = 3.5 \times 10^{8} \quad \text{molecules/cm}^{3} \tag{8.9}$$

at a pressure of 10^{-8} torr [8.16]. If we take 11.6 meters of pipe at a pressure of 5×10^{-8} torr [8.16], then the total number of atoms is

$$Ng = 2 \times 5 \times 3.5 \times 10^{8} \times 1160 = 4.1 \times 10^{12} \quad \text{atoms/cm}^{2}. \tag{8.10}$$

Therefore the beam-gas event rates for proton and antiproton are obtained as follows.

$$R[BG(p)] = 3.9 \times 10^{-3} \quad \text{(int./rev.)}, \tag{8.11a}$$

$$R[BG(\bar{p})] = 5.2 \times 10^{-8} \quad \text{(int./rev.)}. \tag{8.11b}$$

8.9.3 Backward Scattering In BG Event

In the previous sections, the rate of the proton-gas interactions is found to be much higher than that of beam-beam interactions. It is necessary to consider the rate of beam(proton)-gas events where the particles scatter not only to the East-BBC (forward) but also to the West-BBC (backward).

The trigger for an event which takes place at Z greater than 0 will be suppressed, because the backward scattered particle will be too slow to arrive at the West-BBC within the beam-beam (BB) gate (see Fig. 8.22). On the other hand, the particle will also miss the BB gate as the position of the event is closer to the West-BBC. Therefore the interaction position triggered by the BBC will be limited to a range. From Fig. 8.21, we estimate that this range will be from Z = - 2 m to Z = 0 m. So, the effective length of beampipe for the events is 2 m. Then the backward coverage of the BBC is from - 3.0 to - 5.7 in units of pseudorapidity.

We here assume that an interaction with a nucleon in gas will take place in beam-gas event. With a Lorentz factor γ = 20, the coverage in the CM frame is from - 6.7 to - 9.3. Figure 8.23 shows the charged multiplicity distribution at ISR energy [1.22].

The pseudorapidity distribution can be parametrized [8.17] as

$$\frac{1}{\sigma}\frac{d\sigma}{d\eta} = a\left[1 + \exp\left[\frac{\eta - \eta_0}{D}\right]\right]^{-1} \qquad (8.12)$$

where a = 1.8, η_0 = 3.13, D = 0.59. According to the above parametrization, the average charged particle multiplicity in the range from 6.7 to 9.3 is 2.5×10^{-3}. Hence the probability that any charged particle hits the BBC will be calculated to be 2.5×10^{-3} with a Poisson distribution. Therefore the unbiased

yield for the events is obtained as follows:

$$Y1 = R[BG(p)] \times 200/1160 \times 2.5 \times 10^{-3}$$
$$= 1.7 \times 10^{-6} \quad \text{(int./rev.)}. \qquad (8.13)$$

Also obtained is the yield for antiproton-gas event as

$$Y2 = R[BG(\bar{p})] \times 200/1160 \times 2.5 \times 10^{-3}$$
$$= 2.2 \times 10^{-11} \quad \text{(int./rev.)}. \qquad (8.14)$$

Actually it will be needed to check the A-dependence of the charged multiplicity distribution in beam-gas collision. However it will not be discussed in this Chapter.

8.9.4 Coincidence Of BG(proton) And BG(antiproton)

If proton and antiproton BG events take place simultaneously between West and East modules, then the forward scattered particles in the beam-gas collisions will arrive at the BBC modules at the same time as the particles in a beam-beam event. It will be a background for trigger of unbiased events. Such events can not be rejected even by using a narrow gate. The yield of such events is estimated to be

$$Y3 = R[BG(p)]\ R[BG(\bar{p})] = 2.0 \times 10^{-10} \quad \text{(int./rev.)}. \qquad (8.15)$$

8.9.5 Coincidence Of BG And BB

Also calculated are the yields of the cases when a BB event coincides with a BG events due to proton or antiproton:

$$Y4 = R[BG(p)]\ R[BB] = 2.1 \times 10^{-9} \quad \text{(int./rev.)}, \qquad (8.16)$$

$$Y5 = R[BG(\bar{p})]\ R[BB] = 2.7 \times 10^{-14}\ \text{(int./rev.)}. \qquad (8.17)$$

8.9.6 L1 Trigger Efficiency

Since L1 calorimeter trigger (Et) was required in 1985 run, the triggers for the above mentioned events might be biased. The threshold for Et was of the order of 2 GeV. We here estimate the trigger efficiency of L1. The average transverse momentum of the event increases with $\sqrt{s}$. We roughly parametrize the distribution of the transverse momentum as follows:

$$\frac{d\sigma}{dPt} = C\ \frac{Pt}{(Pt + Pt0)^{n}}\ , \qquad (8.19)$$

where n and C are constant and Pt0 = 1.30 GeV/c. The trigger efficiency above Pt,th is given by

$$\varepsilon trig = \frac{1}{\sigma} \int_{Pt,th}^{\infty} \frac{d\sigma}{dPt}\ dPt\ . \qquad (8.20)$$

The data of n from estimated from ISR and SPS data [1.27, 8.18, 8.19] are fitted a function of $\ln(\sqrt{s})$ [1.27] as follows:

$$n = 4.0 + \frac{35.85}{\ln(\sqrt{s}\ /\ 0.3)}\ . \qquad (8.21)$$

The value of n is taken to be 11 for $\sqrt{s}$ = 40 GeV and 8 for 1.6 TeV. The ratio, $r = \varepsilon trig(\sqrt{s} = 40\ \text{GeV})\ /\ \varepsilon trig(\sqrt{s} = 1.6\ \text{TeV})$ is calculated to be 8.6×10^{-2} for Pt,th = 2 GeV/c. The r depends on the Pt,th. The values of the r, for example, for Pt,th = 1 GeV/c and Pt,th = 1.5 GeV/c are 2.5×10^{-1} and 1.4 x

10^{-1} , respectively. The value for Pt,th = 2 GeV/c is used for an estimate made in next section.

Note that L1 calculates Et based on the collision point Z = 0 for sin(θ). Figure 8.21 shows a 1 m of average offset toward the West-BBC. In this case, L1 actually overestimates a given Et(BG). Therefore the value of r calculated above is given as a lower limit.

8.9.7 Consideration And Summary

The trigger yields biased by L1 are summarized in Table 8.5. As mentioned in Section 8.9.1, a total of 81 background events without halo were reconstructed by the BBC. However, 69 events (only 33 events of them were reconstructed by BBC) occurred while the low-beta was squeezed. The event trigger rate is 9.5 x 10^{-3} Hz from the 94 kHz scaler. On the other hand, the rate for 23 beam-beam events is 3.2 x 10^{-3} Hz. In the previous section, it was pointed out that L1(bias) would be underestimated. These values are of the same magnitude as the above estimate. Therefore the 81 background events is from the beam-gas events with the backward scattered particles.

Thus it is found that the most serious background for a relatively unbiased trigger by the BBC came from the beam-gas events with backward scattering. These events give high multiplicity in one module and low multiplicity in the other module. Trigger for such events can be prevented by requiring high multiplicity in both modules. It is also effictive to use a

narrow beam-beam gate and/or to reduce the total number of atoms in the beampipe.

So far, only events without halo have been considered: Any interaction took place between BBC modules as shown in Figs. 8.24(a), 8.24(b), and 8.24(c). There could be a trigger for a BG event which took place outside the BBC as seen in Figs. 8.24(d) and 8.24(e). Such events, however, will be recorded as a halo event. Most triggers with halo seem to come from such events.

CHAPTER 9

MONTE CARLO STUDY ON DETECTION OF HEAVY LEPTON

9.1 INTRODUCTION

As described in Chapter 1, one expects 220,000 W's for both sign at an integrated luminosity of 10^{37} cm^{-2} . This makes the study of a heavy lepton at CDF experiment possible. As was pointed out by Barger et al. [1.15], the semi-leptonic decay mode L $\rightarrow$ q1 $\bar{q}$2 ν yield a signature less polluted by various backgrounds. The mass of the heavy lepton is estimated to be 30 GeV [1.17] and 55 GeV [1.19, 1.20] as in Chapter 1.

Therefore, a Monte Carlo study on the detection of the heavy lepton is carried out. In this study, the heavy lepton mass is taken to be 30 GeV and 60 GeV.

9.2 EVENT GENERATION/SIMULATION

The signal with respect to the decay chain

$$W \rightarrow L\ \nu \rightarrow u\ d\ \nu\ (\text{or } c\ s\ \nu)\ \nu \qquad (9.1)$$

is large missing transverse momentum which is balanced by two quark jets. Hence the following events have to be studied as background:

$$
\begin{aligned}
&W \rightarrow \tau\ \nu \\
&W \rightarrow t\ b \\
&Z \rightarrow \nu\bar{\nu} \qquad\qquad (9.2) \\
&t\ \bar{t}\ \text{jets} \quad (15 < Pt < 200\ \text{GeV/c}) \\
&b\ \bar{b}\ \text{jets} \quad (20 < Pt < 200\ \text{GeV/c})
\end{aligned}
$$

These events can have large missing Et in the final state.

These background events were generated with ISAJET. The heavy lepton events were also generated with ISAJET which was modified by Takaiwa for this study.

The simple detector simulation were performed with the same eta-phi segmentation as CDF, but the energy resolutions of electromagnetic and hadron calorimeters were assumed as 15 % / $\sqrt{E}$ and 80 % / $\sqrt{E}$, respectively. The identification for electron (positron) and muon is also assumed to be perfect.

9.3 EVENT ANALYSIS

Figure 9.1 shows event view of L $\rightarrow$ 2 jets + missing: A neutrino of W decay give a large missing Et and heavy lepton decay gives 2 jets plus probably small missing Et. The 2 jets and missing Et should be balanced. Hence the following cuts are applied:

(1) lepton veto,

(2) missing Et cut (=10,15,20,25 GeV),

(3) total scalar Et 120 GeV,

(4) $\cos(\theta 12) = \vec{P1}\cdot\vec{P2} \;/\; P1\ P2 > 0.5$

(5) $\cos(\varphi 01) = \vec{P0}_T\,\vec{P1}_T \;/\; P0_T\,P1_T < -0.8$,

where $\vec{P1}$, $\vec{P2}$ and $\vec{P0}$ are momentum vectors of jet-1, jet-2, and missing Et. Those cuts are chosen to optimize the signal against the background. A cluster algorism, called CLUST2 [9.1], is used for the jet reconstruction.

We also check the transverse mass distribution from a jet plus missing Et. Figure 9.2 shows the mass distribution $Mj\nu$ for $W \to \tau\ \nu$. If one jet from tau is correctly picked up, then $Mj\nu$ should be transverse mass of W. To reject such event, we apply the $Mj\nu$ cut:

(6) $Mj\nu 1 < 60$ GeV, $\quad Mj\nu 2 < 50$ GeV.

To reject event with tau jet, the following cuts on number of charged tracks with Pt $>$ 1 GeV/c and number of towers in cluster were applied

(7) $Nch1 \leq 3$, $\quad Nch2 \leq 3$.

(8) $Ntow1 \leq 3$, $\quad Ntow2 \leq 3$.

These cuts, (7) and (8), the events redudec to 1/3. The same

cuts are applied to other background events. Figure 9.3 shows the analysis diagram used in this study.

9.4 RESULTS

The numbers of events detected at an integrated luminosity of 10^{37} cm^{-2} are estimated as in Table 9.1. Missing Et cut is a tool of reduction of the background events; The values for L-mass = 30 and 60 GeV seem to be 20 GeV or more. Since W has one recoil jet or more (see Fig. 1.1), the identification of jet-1 and jet-2 from the heavy lepton is not always unique. Figures 9.4(a) show the angular distributions of 2 quarks from semi-leptonic decay for the heavy lepton mass of 60 GeV. Figures 9.4(c) show the angular distribution for reconstructed 2 jets in the case of correct selection. In the case of misidentification, the distributions are shown in Fig. 9.4(d). Misidentified events shown in Table 9.1 are those which are confused with the recoil jet.

Figure 9.5 shows the reconstructed transverse momentum of W in $W \rightarrow L \nu$ events (solid line). True distribution is also shown with dashed line in the figure.

Figure 9.6 shows the reconstructed masses for L(30) and W. The masses of L and W are determined by looking at the mass distribution of 2 jets and 2 jets + missing Pt, respectively. The same type of distribution for L(60) are shown in Fig. 9.7. The ends of mass distributions obviously show the masses of the objects. As seen in these figures, the reconstrution of jet

works well.

The number of background events after cuts is comparable with signal events in Table 9.1. The mass distributions Mjj and Mjjν, pollutes the distribution for single events (see Fig.9)

The signal is comparable to the backgrounds events. It seems to be hard to deterime the heavy lepton mass from Mjj distribution.

However the remaining number of events after cuts can tell the evidence of the such signature. Figure 9.9 shows the number of events detected vs missing Et (GeV) at integrated luminosity of 10^{37} cm^{-2} . Here the following values are defined:

$$d = Ns / \sqrt{Ns + Nb}, \qquad (9.3)$$

where Ns and Nb are number of events detected after cuts for the signal and backgrounds, respectively. This shows the confidence level that Ns + Nb is significantly high compared with Nb. The values are also presented in Fig. 9.9. If such heavy lepton, one can see an evidence of L(30 GeV) with 12 standard deviations, while 3.0 standard deviation for L(60 GeV).

CHAPTER 10

SUMMARY AND CONCLUSIONS

A.Calorimeter Performance

The performance of the CDF central EM calorimeter studied by the beam test and cosmic ray test is summarized as follows:

(1) Energy resolution is typically 14 % / $\sqrt{E\ (GeV)}$ and the tower dependence is given by $1/\sqrt{\sin(\theta)}$ as expected.

(2) The linearity of calorimeter response is better than 1 % in the range of 30 GeV to 75 GeV. There is non linearity in the energy smaller than 30 GeV. The non-linearity depends on tower, and in the worst case of tower 8 it is 5 - 6 % at 10 GeV. A Monte Carlo simulation for the development of shower in the calorimeter was carried out. The simulation could reproduce nonlinearity qualitatively but a quantitative agreement with data was not achieved.

(3) On cosmic ray data, similarity between equivalent towers in different modules was studied. The dissimilarity of the response maps was less than 1 % in the region of -17 cm to +17 cm in X after the determination of the absolute response at tower center.

(4) In the electron beam test, the position dependence of the sensitivity within a tower was studied for all towers in 5 modules. The response map was parametrized by a function with 12 parameters. The reproducibility is better than 1.1 % for the region $|X| < 20$ cm, where X is the local coordinate on the tower in phi direction. Such region covers 85 % of whole area.

(5) The avearge peak pulse height for muons was 623 fC ($\pm$ 37 fC), which corresponds to 0.31 GeV of EM shower energy.

(6) The deterioration of the pulse height at the center of each tower is estimated to be 2.0 $\pm$ 0.6 % per year when the calorimeter is left alone.

The conclusion on the mass determination of W and Z is as follows: The CDF central electromagnetic calorimeter with its systematic uncertainty of 1.1 % can determine the masses of W and Z with 0.7 %, if the non-linearity is corrected. At an integrated luminosity of 10^{37} cm^{-2}, the statistical error will be 0.1 % or less. The values of $\sin^2(\theta w)$ and ρ can be determined within 1.4 % and 0.5 %. The values are improved compared with the corrsponding values for UA1 and UA2.

B. The First Collision

The first collision data was analized. The results are summarized as follows:

(1) Trigger efficiency is about 9 %, correspoding to about 6 mbarn of cross section if an inelastic cross section is 70 mbarn at a center of mass energy of 1.6 TeV.

(2) The data on pseudorapidity distribution of charged tracks was studied by visual scanning. The result agrees well with simulation. The simulation also agrees reasonably well with UA1/UA5 results. The central density is estimated to be about 7.5 with following assumptions; (a) The central density for the unbiased samples is about 4, which is expected by an extraporation from ISR and SPS data. (b) There are effects on photon-convertion and hadron interaction with the beam pipe. (c) The events were triggered with threshold energy of 1.4 GeV at Level 1 trigger.

(3) The data on the energy flow information is consistent with the simulation for unbiased event plus L1 trigger. However, there is an excess of hits of energy less than 200 MeV for the EM and hadron calorimeters. This suggests an existence of very soft hadrons and gammas.

(4) If the Centauro event exists, the trigger efficiency in the 1985 run should have been 100 %. The expected signature for calorimeter was not found to about 6 mbarn

at 1.6 TeV.

At a center-of-mass energy of 1.6 TeV, CDF data of the first collisions show that all the events are consistent with the non-single diffractive events charecterized by a naive extraporation from ISR and SPS energy.

C. Monte Carlo Study on the Detection of Heavy Lepton

The study on the detection of the fourth generation heavy lepton was made with a Monte Carlo simulation. The results are summarized as follows:

(1) Missing Et is a useful tool to reduce the background. It was pointed out that a cut greater than 20 GeV for missing Et suppress the background.

(2) The backgrond from electroweek interaction and QCD jets is comparable to the signature on the mass distribution. However, the total number of events after cuts is useful information for indicating an existence of heavy lepton. At an integrated luminosity of 10^{37} cm^{-2}, the total number of events of signal events is found to be greater than 12 and 3 standard deviations of the total number of events (signal + background) at 30 GeV and 60 GeV, respectively, if such lepton exists.

Although the backgrond from electroweek interaction and QCD jets is comparable to the signature, CDF can search for the hypothesical heavy lepton by the mass of 60 GeV.

APPENDIX A

CDF COLLABORATION

Argonne National Laboratoty

R.Diebold, W.Li, L.Nodulman, J.Proudfoot, P.Schoessow, D.Underwood, R.Wagner, A.Wicklund.

Brandeis University

J.Bensinger, C.Blocker, M.Conteras, L.DeMortier, P.Kesten, L.Kirsch, H.Piekarz, L.Spencer, S.Tarem.

University of Chicago

D.Amidei, M.Campbell, H.Frisch, C.Grosso-Pilcher, J.Hauser, T.Liss, G.Redlinger, H.Sanders, M.Shochet, R.Snider, J.Ting, Y.Tsay.

Fermi National Accelerator Laboratory

M.Atac, E.Barsotti, P.Berge, M.Binkley, J.Bofill, A.Brenner, J.T.Carroll, T.Collins, J.Cooper, C.Day, F.Dittus, T.Droege, J.Elias, G.W.Foster, J.Freeman, I.Gaines, J.Grimson, D.Hanssen, J.Huth, H.Jensen, R.Kadel, H.Kautzky, R.Kephart, C.Nelson, C.Newman-Holmes, J,O'Meara, T.Ohska(1), M.Ono(1), S.Palanque, A.Para, J.Patrick, R.Perchonok, D.Quarrie, S.Segler, D.Theriot, A.Tollestrup, K.Turner, C.van Ingen, R.Vidal, R.Wagner, V.White, R.Yamada, T.Yamanouchi, G.P.Yeh, J.Yoh.

---

(1) Now at KEK, Japan.

INFN -- Frascati, Italy

S.Bertolucci, M.Cordelli, M.Curatolo, B.Esposito, P.Giromini, S.Miozzi, S.Miscetti, A.Sansoni.

Harvard University

G.Brandenburg, D.Brown, R.Carey, M.Eaton, A.Feldman, E.Kearns, R.Schwitters, M.Shapiro, R.St.Denis.

University of Illinois

G.Ascoli, S.Bhadra, R.Downing, S.Errede, L.Holloway, I.Karlinger, H.Keutelian, U.Kruse, R.Sard, V.Simaitis, D.Smith, T.Westhusing.

KEK, Japan

Y.Fukui, S.Mikamo, M.Mishina, K.Ogawa.

Lawrence Berkeley Laboratory

W.Carithers, W.Chinowsky, R.Ely, M.Franklin, C.Haber, R.Harris, B.Hubbard, J.Siegrist.

University of Pennsylvania

D.Connor, L.Gladney, S.Hahn, N.Lockyer, M.Miller, T.Rohlay, R.VanBerg, J.Walsh, H.Williams.

INFN -- University of Pisa, Italy

G.Apollinari, F.Bedeschi, G.Bellettini, N.Bonavita, L.Bosisio, F.Cervelli, R.Del Fabbro, M.Dell'Orso, E.Focardi, P.Giannetti, M.Giorgi, A.Menzione, R.Paoletti, G.Punzi, L.Ristori, A.Scribano, P.Sestini, A.Stefanini, G.Tonelli, F.Zetti.

Purdue University

V.Barnes, A.Byon, K.Chadwick, A.Di Virgilio(2), A.Garfinkel, S.Kuhlmann, A.Laasanen, M.Schub, J.Simmons.

---

(2) Now at INFN Pisa, Italy.

Rockefeller University

S.Belforte, T.Chapin, G.Chiarelli, N.Giokaris, K.Goulianos, R.Plunkett, S.White.

Rutgers University

A.Beretvas, T.Devlin, U.Joshi, K.Kazlauskis, N.Pearson, T.Watts.

University of Tsukuba, Japan

F.Abe, Y.Hayashide, M.Ito(3), T.Kamon, S.Kanda, Y.Kikuchi(4), S.Kim, K.Kondo, M.Kurisu(5), M.Masuzawa(4), T.Mimashi, S.Miyashita, H.Miyata(6), S.Mori, Y.Morita, T.Ozaki, M.Sekiguchi, M.Shibata, Y.Takaiwa, K.Takikawa, F.Ukegawa, A.Yamashita, K.Yasuoka.

University of Wisconsin

J.Bellinger, D.Carlsmith, D.Cline, R.Handler, J.Jaske, G.Ott, L.Pondrom, J.Rhoades, M.Sheaff, J.Skarha, T.Winch.

Visitors

M.Sivertz - Harverford College, Harverford, PA.
S.Kobayashi, A.Murakami - Saga University, Japan.
Y.Muraki - ICRR, Tokyo University, Japan.

---

(3) Now at Hitachi Co, Japan.
(4) Now at Toshiba Co, Japan.
(5) Now at NEC Co, Japan.
(6) Now at Virginia Institute of Technology, USA.

APPENDIX B

FERMILAB PROTON-ANTIPROTON COLLIDER

The Fermlab proton-antiproton collider (Tevatron) is designed to provide an intense source of antiprotons and to arrange head-on collisions of protons and antiprotons at 2 TeV center of mass energy at a luminosity greater than 10^{30} cm^{-2} sec^{-1} .

Fermilab's accelerator consists of a series of accelerators:

(1) Cockroft-Walton electrostatic accelerator which raises the energy from zero to 750 KeV.

(2) A linear Accelerator (750 KeV to 200 MeV) and the Booster Ring (200 MeV to 8 GeV) which follow Cockroft-Walton accelarator to increase the energy to 8 GeV.

(3) Main Ring which brings particles (protons or antiprotons) to 150 GeV for injection into the Tevatron.

(4) Tevatron which provides the final push to 800 GeV (soon to be raised to nearly 1000 GeV).

The antiprotons are produced as follows [B.1]: In the Collider mode, protons are accelerated in the Main Ring to 120 GeV, and by strategic manipilation of radio frequency fields, the protons are grouped to be optimally organized for producting antiprotons. The protons are extracted at location F17 and are incident upon a specially constructed target where collisions generated a large flux of nuclear particles including antiprotons (one per 30,000 incident protons). A fraction of the antiprotons, those near 8 GeV, are focussed by a "lens" made of a cylinder of lithium through which flows a pulse of 600,000 amperes. The large current creates a magnetic field which concentrates the valuable antiprotons. Their forward momentum carries them in a highly evacuated pipe to the Debuncher.

The Debuncher is a 1700-foot circumference ring of 345 magnets where a combination of magnetic fields and radio-frequency impulses cools and compresses the antiprotons into a smaller sausage-shaped volume. The technique, invented by Simon Van der Meer of CERN, is called Stochastic cooling [B.2]. These circulate around th ring at an energy of 8 GeV. When the sausage is properly prepared, it is passed on to the Accumulator ring.

The Accumulator ring of 176 magnets is inside the Debuncher and has the task of further compressing the antiproton sausage and gradually accumulation these in a core stack. An accumultion time of several hours yields enough antiprotons to preceed to the next step.

About half the antiproton core is extracted into a beamline toward the Main Ring, circulating in the opposite direction to the protons and accelerated to 150 GeV. After acceleration to 150 GeV, the antiprotons are transferred to the Tevatron ring, where waiting protons are already stored in circulating bunches. Both groups of particles are accelerated to the maximum energy, passing each other in bunches that are still not dense enough for significant numbers of collisions to take place.

At full energy, they are stored for many hours and powerful focussing quadrupole magnets ("low beta quads") squeeze the beams at two places around the Tevatron ring. At location B-zero and D-zero, the two sharply focussed beams cross each other about 50,000 times per second. At the design specification, about 50,000 collisions will take palce at each location per second.

APPENDIX C

C.1 CORRECTION FOR SYSTEMATIC ERRORS

As mentioned in section 3.3.2, the light outputs of test samples and a monitor sample were alternately measured to remove systematic errors. The light output S(i) of the i-th test sample was normalized to the light outputs of the monitor sample to yield the relative light output Y(i) :

$$(C.1)\quad Y(i) = \frac{2\,S(i)}{R(i) + R(i+1)}\,,\quad (i = 1, 2, 3, \ldots, N),$$

where R(i) and R(i+1) are the light outputs of the monitor sample measured before and after the measurement of S(i), and N is the total number of test samples.

We assume that the sample-to-sample fluctuations of S(i) are caused by statistical uncertainties, systematic errors, fluor concentrations and thickness variations, and that the sample-to-sample change of R(i) are caused only by statistical and systemtic fluctuations. We therefore write S(i) and R(i) as follows.

$$(C.2)\quad S(i) = S0 + \Delta Sst(i) + \Delta Ssys(i) + \Delta Sf(i) + \Delta St(i),$$

$$(C.3)\quad R(i) = R0 + \Delta Rst(i) + \Delta Rsys(i),$$

where the mean light outputs S0 and R0 are given by

$$S0 = \frac{1}{N}\sum_{i=1}^{N} S(i) \quad , \qquad R0 = \frac{1}{N}\sum_{j=1}^{N} R(j) \quad .$$

Eq.(C.1) can be rewritten with Eqs.(C.2) and (C.3) as

$$(C.4)\quad Y(i) = \frac{S0}{R0}\left(1 + \frac{\Delta Sf(i)}{S0} + \frac{\Delta St(i)}{S0} + \frac{\Delta Sst(i)}{S0} - \frac{\Delta Rst(i)}{2\ R0} - \frac{\Delta Rst(i+1)}{2\ R0} \right),$$

if we assume that

$$\frac{\Delta Ssys(i)}{S0} = \frac{\Delta Rsys(i) + \Delta Rsys(i+1)}{2\ R0} \quad .$$

The relation is considered to be a plausible assumption since the measurements S(i), R(i), and R(i+1) are made in a short interval. Notice that systematic errors are removed in Eq.(C.4).

C.2 CORRECTIONS FOR SAMPLE THICKNESS

Figure C.1 shows the correlation plots between the sample thickness and the light output. We assume for simplicity that the light output (Y) is a linear function of the sample thickness (X):

$$(C.5)\quad Y = c\ X + d.$$

The light yield Yc corrected for the fluctuation $\Delta St(i)$ in the

sample thickness is then given by

$$(C.6)\quad Yc(i) = Y(i) - \left(c\,X(i) + d\right) + Y0$$
$$= Y0 + Y0 \left(\frac{\Delta Sf(i)}{S0} + \frac{\Delta Sst(i)}{S0} - \frac{\Delta Rst(i)}{2\,R0} - \frac{\Delta Rst(i+1)}{2\,R0} \right),$$

where $Y0 = S0/R0$. The standard deviation of $Yc(i)/Y0$ is calculated by

$$(C.7)\quad \sigma_{Yc}^{2} = \left[\frac{1}{Y0}\right]^{2} \frac{1}{N} \sum_{i=1}^{N} \left\{ Yc(i) - Y0 \right\}^{2}.$$

From Eqs.(C.6) and (C.7), we have

$$(C.8)\quad \sigma_{Yc}^{2} = \sigma_{s,f}^{2} + \sigma_{s,st}^{2} + 0.5\,\sigma_{R,st}^{2},$$
$$= \sigma_{s,f}^{2} + 1.5\,\sigma_{s,st}^{2},$$

where we have put

$$\sigma_{s,st}^{2} = \sigma_{R,st}^{2}.$$

The non-uniformity of the light yield is estimated by $\sigma_{s,f}$ in Eq.(C.8).

REFERENCES

Chapter 1

1. H.B.Jensen (CDF Collaboration), "The Collider Detector at Fermilab", Invited talk presented at the IEEE Nuclear Science Symposium, San Francisco, October, 1985; to be published in IEEE NS-33 (1986); Fermilab-Pub/85-150/Conf (1985); CDF Internal Report 356 (1985).

2. S.L.Glashow, Nucl. Phys. 22 (1961) 579.
   A.Salam, Proc. 8th Nobel Symposium, Aspenasgarden 1968 (Almquist and Wiskell, Stockholm, 1968), P.367.
   S.Weingerg, Phys. Rev. Lett. 19 (1967) 1264; Phys. Rev. D5 (1972) 1412.

3. G.Arnison et al. (UA1), Phys. Lett. 122B (1983) 103.
   G.Arnison et al. (UA1), Phys. Lett. 129B (1983) 273.
   G.Arnison et al. (UA1), Phys. Lett. 134B (1984) 469.
   G.Arnison et al. (UA1), Phys. Lett. 135B (1984) 250.
   M.Banner et al. (UA2), Phys. Lett. 122B (1983) 476.
   P.Bagnaia et al. (UA2), Z.Phys. C24 (1984) 1.

4. G.Arnison et al. (UA1), Phys. Lett. 126B (1983) 398.
   G.Arnison et al. (UA1), Phys. Lett. 147B (1984) 241.
   P.Bagnaia et al. (UA2), Phys. Lett. 129B (1983) 130.

5. M.Gell-Mann, Phys. Lett. 8 (1964) 214.
   G.Zweig, CERN Report 8182/TH.401 (1964); CERN Report 8419/TH.412 (1964).

6. G.Arnison et al. (UA1), Europhys. Lett. 1 (1986) 327.
J.A.Appel et al, (UA2), Z. Phys. C30 (1986) 1.
H.D.Wahl, CERN-EP/84-127 (1984), Invited talk at the 15th International Symposium on Multiparticle Dynamics, Lund, Sweden, 1984.

7. S.Adler, Phys. Rev. 177 (1969) 2426.
D.J.Gross and R.Jackiw, Phys. Rev. D6 (1972) 477.
C.Bouchiat, I.Iliopoulos and P.Meyer, Phys. Lett. 38B (1972) 519.

8. M.J.Marciano, Electroweak interaction parameters, Invited talk at the 4th Topical Workshop on proton-antiproton Collider Physics, Bern, 1984, BNL 34728.
K.Hikasa, Univ. of Wisconsin, Madison, MAD/PH/144 (1983).

9. N.G.Deshpande et al., Phys. Rev. Lett. 54 (1985) 1757.

10. F.Halzen and K.Mursula, Phys. Rev. Lett. 51 (1983) 857.
K.Hikasa, Phys. Rev. D29 (1984) 1939.

11. E.Eichten, Fermilab-Pub/85-178/Conf (1985); The production cross section of W of each sign and Z at 2 TeV are estimated to be 11.2 nanobarn and 4.9 nanobarn.

12. G.Arnison at al. (UA1), Phys. Lett. 147B (1984) 493; CERN-EP/84-134 (1984).

13. A.Grosso and R.Odorico, IFUB 84/18 (preprint).

14. T.Kamon, S.Kim, A.Yamashita, G.P.Yeh, and J.K.Yoh, "A Monte Carlo study on the detection of top quark from W → t b followed by t → b e ν at the CDF experiment" (1986), unpublished.

15. V.Barger, UW-Madison report MAD/PH/165 (1984); Invited talk at Physics of 21st Century Conference, Tucson, Arizinna, December 1983.

16. V.Barger et al., Phys. Lett. 133B (1983) 449 and MAD/PH/135 (1983).

17. S.Pakvasa, H.Sugawara and S.F.Tuan, Z. Phys. C4 (1980) 53;
S.Pakvasa and K.Tennakone, Phys. Rev. Lett. 13 (1981) 757.

18. B.Pendleton and G.G.Ross, Phys. Lett. 98B (1981) 291.

19. C.Hill, Phys. Rev. D24 (1981) 691.

20. E.Paschos, UW-Madison report MAD/PH/162 (1984).

21. G.Arnison et al. (UA1), Phys. Lett. 107B (1981) 320.
G.Arnison et al. (UA1), Phys. Lett. 123B (1983) 108.

22. K.Alpgard et al., (UA5), Phys. Lett. 107B (1981) 310.
K.Alpgard et al., (UA5), Phys. Lett. 107B (1981) 315.

23. G.Arnison et al., (UA1), Phys. Lett. 118B (1982) 167.

24. R.P.Feynman, Phys. Rev. Lett. 23 (1969) 1415.

25. Z.Koba, H.B.Nielsen and P.Oleson, Nucl. Phys. B40 (1972) 317.

26. G.J.Alner et al. (UA5), Phys. Lett. 138B (1984) 304.

27. Y.Takaiwa, CDF Event Generation Program - MB1.

28. C.M.G.Lattes, Y.Fujimoto, and S.Hasegawa, Phys. Rep. 65 (1985) 151.

29. M.Tamada, Nuovo Cimento, 41B (1977) 245.

30. C.Rubbia, Proceedings of the 1985 Internal Symposium on Lepton and Photon Interactions at High Energies, P242, August Kyoto, Japan.
G.Arnison et al. (UA1), Phys. Lett. 122B (1983) 189.
K.Alpgard et al. (UA5), Phys. Lett. 115B (1982) 71.

31. D.Ayres et al., CDF Design Report, CDF Internal Report 111 (1981), (unpublished, updated).

32. A.Beer et al., Nucl. Instr. Meth. 224 (1984) 360.

Chapter 2

1. L.J.Nodulman et al., Nucl. Instr. Meth. 204 (1983) 351.

2. Scintillator, SCSN38, was made by Kyowa Gas Chemical Ind. Co., Japan.

3. Wavelength shifter, Y7, was made by Kyowa Gas Chemical Ind. Co., Japan.

4. T.Kamon et al., Nucl. Instr. Meth. 213 (1983) 261.

5. Design of the backing was made by D.Underwood of ANL. The data on the wavelength shfter respnses were taken by members of ANL and University of Tsukuba at ANL.

6. T.Kamon et al., CDF Internal Report 172 (1983).

7. T.Devlin and U.Joshi, Private cominucations; Approximately 1050 phototubes for the central EM calorimeters were tested at Rutgers University.

8. L.Nodulman, Nucl. Instr. Meth. 176 (1980) 345.

Chapter 3

1. S.Iwata, DPNU-13-80 (1980).

2. R.M.Sternheimer, Phys. Rev. 103 (1956) 511.

3. H.Chugun and T.Shimizu (Kyowa Gas Chemical Ind. Co.), private communications.

4. Nakajyo Factory, Kyowa Gas Chemical Ind. Co., Nakajyo, Niigata, Japan.

5. Y.Hayashide, T.Kamon, and J.Freeman, CDF Internal Report 287 (1985), [50 GeV electron shower curve by experiment].

Chapter 4

1. R.G.Wagner et al., CDF Internal Report 374 (1986).

2. T.Selberg and R.G.Wagner, CDF Internal Report 367 (1985).

3. LED system was developed by D.Underwood of ANL.

4. Xenon flasher system was developed by University of Pennsylvania.

5. Co-60 source system was developed by R.G.Wagner of ANL.

6. Cs-137 surce system was developed by University of Pennsylvania.

7. S.Hahn et al., Proceedings of the Annual DPF Meeting, Sante Fe, NM (1984); CDF Internal Report 281 (1985); ANL-HEP-CP-85-10.
D.Underwood, private communcation.

Chapter 5

1. G.Drake et al., CDF Internal Report 358 (1985), to be published to IEEE Trans. Nucl. Sci.

2. G.Drake et al., CDF Internal Report 357 (1985), to be published to IEEE Trans. Nucl. Sci.

3. The control driver was developed at INFN-Pisa, Italy for CDF.

4. INFN-Pisa group, private communication.

Chapter 6

1. J.W.Cooper et al. (Wedge Test Collaboration); The central electromagnetic and hadron calorimeters were calibrated with 50 GeV electrons and pions, respectively. The gain of the calorimeter was set nominally to 2 pC/GeV.

2. R.G.Wagner et al., CDF Internal Report 396 (1986), to be published in Nucl. Instr. Meth.

3. K.Yasuoka and J.Elias, CDF Internal Report 398 (1986).

4. D.Quarrie, CDF Internal Report 208 (1985). - Runcontrol
D.Quarrie, CDF Internal Report 209 (1985). - Histogram Display
D.Quarrie, CDF Internal Report 166 (1985). - Consumer Process/DAQ

5. P.J.Green et al., Phys. Rev. D20 (1979) 1598.

6. T.Kamon et al., CDF Internal Report 279 (1985).

7. J.L.Schlereth and E.N.May, MIDAS User's Guide, DAN-4 (1983).

8. K.Yasuoka et al., CDF Internal Report 399 (1986).

Chapter 7

1. S.L.Stone et al., Nucl. Instr. Meth. 151 (1978) 387.

2. U.Amaldi, Physica Scripta, 23 (1981) 409.

3. T.Kamon et al., CDF Internal Report 299 (1985).

4. N.Solomey and A.B.Wicklund, CDF Internal Report 247 (1984).

Chapter 8

1. M.Binkley (CDF Collaboration), "First Events and Prospects at the Fermilab Collider", Aspen Winter Conference Proceedings (1986).

2. J.W.Cooper et al., CDF Internal Report 402 (1986).

3. M.Binkley et al., CDF Internal Report 350 (1985).

4. H.Frisch et al., CDF Internal Report 250 (1984).

5. H.J.Frisch, T.Kamon, T.M.Liss, CDF Internal Report 416 (1986).

6. M.Campbell et al., CDF Internal Report 157 (1984).

7. C.Rotolo, "Synchronizing the clock to the beam for the september run", (1985) (unpublished).

8. G.P.Yeh, private communication.

9. J.K.Yoh, private communication.

10. Y.Takaiwa, CDF/ODORICO User's Guide (1986).

11. J.D.Bjorken and L.D.Mclerran, Phys. Rev. D20 (1979) 2353.

12. J.Freeman, "Guide to the CDF Detector Simulation".

13. G.Arnison et al. (UA1), Phys. Lett. 128B (1983) 336
R.Battiston et al. (UA4), Phys. Lett. 117B (1982) 126.

14. T.Kamon, CDF Internal Report 407 (1986).

15. J.E.Elias, Private communication.

16. J.E.Elias, CDF Internal Report 344 (1985).

17. W.Thome et al. (ISR), Nucl. Phys. B129 (1977) 365.

18. B.Alper et al., Nucl. Phys. B100 (1975) 237.

19. G.Arnison et al., Phys. Lett. 118B (1982) 167.

Chapter 9

1. CLUST2 is one of standard clustring algorisms used in CDF.

Appendix

B1 J.Peoples, IEEE Trans. Nucl. Sci. NS-30 (1983) 1970.

B2 D.Mohl, G.Petrucci, L.Thorndahl and S.van der Meer, Phys. Rep. 58 (1980) 73.

Figure Captions

Chapter 1

1. Production mechanism of a heavy lepton.
   (a) Drell-Yan process.
   (b) Annihilation with a hard gluon recoiling from W.
   (c) Compton scattering with a hard quark recoiling from W.

2. W and Z branching fraction and total widths versus the charged heavy lepton mass (Ref. 1.16).

3. Positron angular distributions from $W \rightarrow e \nu$, $W \rightarrow \tau \nu$ and $W \rightarrow L \nu$ decays for various transverse momentum intervals of positron (Ref. 1.15).

4. (a) The central pseudorapidity density as a function of center of mass energy; Fig. 3 in Phys. Lett. 123B (1983) 108.
   (b) Pseudorapidity distribution at $\sqrt{s}$ = 540 GeV compared with data obtained at ISR at $\sqrt{s}$ = 53 GeV (open points). The dashed and dot-dashed curves are predicted from Pt limited phase-space for $\langle Pt \rangle$ = 350 MeV. The solid curve for $\sqrt{s}$ = 540 GeV is from the same model but for $\langle Pt \rangle$ = 500 MeV; Fig. 1(b) in Phys. Lett. 107B (1981) 310.
   (c) The mean transverse momentum of charged hadrons ($\sqrt{s}$ = 540 GeV) as a function of charged track multiplicity in the rapidity range from -2.5 to +2.5. Points without

error bars give the global average of Pt as a function of the mean number of charged particles per unit of rapidity at FNAL, ISR and SPS; Fig. 4 in Phys. Lett. 118B (1982) 167.

5. (a) Distributions in charged multiplicity for non single-diffractive events; Fig. 1(a) in Phys. Lett. 138B (1984) 304.
   (b) Charged multiplicity distribution plotted as a function of z compared with the distributions from the ISR and from Serpukhov and FNAL; Fig. 1(b) in Phys. Lett. 138B (1984) 304.

6. Perspective view of the CDF.

7. A cut through the forward half of CDF.

Chapter 2

1. (a) Elevation view of the central detector.
   (b) Layouts of the CDF central electromagnetic calorimeters of one of 48 modules. A hypothetical design of rod lightguides is shown.

2. Cross section of central EM calorimeter.

3. Schematic drawing of the central EM calorimeter module on both substitution of acrylic plates for lead plates and inactive scintillator plates. This substitution was

made to fix the longitudinal depth of the calorimeter and to keep the position of the strip chamber near shower maximum.

4. Absorption and re-emission spectra of fluors, b-PBD, BDB, and Y-7. The wavelengths for maximum emission are 366, 430 and 490 nm, while those for maximum absorption are 305, 430 and 460 (and 437) nm, for b-PBD, BDB and Y-7, respectively.

5. Typical response maps of wavelength shifter (a) without backing and (b) with bacing.

6. Drawing of phototube and u-metal. The tube is Hamamatsu Model R580 (1.5" bialkali, 10 stages).

7. (a) Cross section of strip chamber.
   (b) End geometry of the channel of strip chamber.

Chapter 3

1. (a) Sampling positions for testing the light yield uniformity in one mother-board. The circles indicate places where samples were cut.
   (b) Four points for thickness measurements. The average value was used in our analysis.

2. Setup for the measurement of light outputs. S1*2 and S2 mean the scaler counts. The number of photoelectrons (Npe) is estimated from them by the following equation [2.4] : Npe = - ln (1-S1*2/S2).

3. Number of photoelectrons (Npe) vs transmittance (t) of N.D. filters at the optimized high voltage (2.15 kV). The solid line is given by fitting the data to a function Npe = a t + b, where a = 63.2, b = -0.0317, and t = transmittance. The dotted line given by Npe = 60.0 t is also shown for coparison.

4. Setup for measurement of the thickness of the scintillator plate whose size is typically 2500 mm x 500 mm x 5 mm.

5. Typical output from the pen recorder.

6. Diagram on the digitization of analog data and offline analysis.

7. Example of digitized data in the first production. The data is same as Fig. 3.5.

8. Setup for measurement of the attenuation length of the scintillator test sample, whose size is 1000 mm x 50 mm x 5 mm. The position of the light spot from U.V. lamp is determined by controlling 11 electromagnetic shutters. In this measurement, only the first stage in each phototube is used.

9. Distribution of the thickness of the scintillator plate for the digitized data on (a) the first production and (b) the second production. The nominal thickness is 5 mm. The rms values for the first and the second productions are 88.9 um and 110.0 um, respectively.

10. Position dependence of the thickness for a stack of 31 layers of the scintillator plates on (a) the first production and (b) the second production.

11. Distribution of the thickness of the stack of 31 layers of the scintillator plates: (a) the first production, (b) the second production. They are weighted by a 50 GeV electron shower. The mean and rms are presented in Table 3.5.

12. Distribution of the thickness of the stack of 31 layers of the scintillator plates: (a) the first production, (b) the second production. They are non-weighted. The mean and rms are presented in Table 3.6.

13. Distribution of peak-to-peak diffrence obtained in each tower over all 480 towers. The mean is 0.81 mm.

14. Distribution of the attenuation length measured for the test samples: (a) the first production, (b) the second production, and (c) both productions.

1. Schematic drawing of Cs-137 source system.

2. Schematic picture of a wavelength shifter and light guide attaching LED and Xenon flasher system.

Chapter 5

1. RABBIT PM ADC.

2. PM ADC amplifier shematic.

Chapter 6

1. A simplified diagram of data acquisition system.

2. Schematic view of NW beam line at Fermilab.

3. Trigger logic used in the beam test.

4. RABBIT timing logic used in the beam test.

5. Schematics of the setup of the cosmic ray test stand.

6. Observed relative trigger rate for each tower. The total trigger rate is 1.8 Hz. The histogram shows the result of a Monte Carlo simulation.

7. Block diagram of the trigger electronics.

8. Diagram of data aquisition control logic. The solid and dashed lines are related to the CAMAC and RABBIT systems.

9. (a) Calibrated charge integrator gains as a function of date of calibration for three channels on three different boards. The data between June 1984 and December 1984 have been rescaled by a factor of 0.979 to correct for a charge in the voltage calibration of the BNC 9010 pulse generator. The boards were prototype versions of the final front end electronics. The nominal gain of the charge channels was unchanged between the prototype and final versions.
(b) Calibrated current amplifier gains as a function of date of calibration for two channels on two different prototype front end electronics boards. The final electronics design used a nominal gain of 11 pA/ADC count and had a stability similar to that implied by the data in this figure.

10. Reference points used for normalization of response map.

11. (a) Global coordinates in X and Z in cosmic ray stand.
(b) Local coordinates in X and Z in a tower. The typical sizes of a scintillator plate on the strip chamber are also shown in the figure.

12. Worst case of time variation of phototube pedestals.

13. Typical plots of the pulse height in ADC counts vs. read number.

14. Expanded plots of the peak regions from Fig. 13.

Chapter 7

1. (a) Average pulse height distribution for tubes in towers 0 - 8 on 13 modules with phototube voltages set using a Co-60 source.
   (b) Average pulse height distribution for tubes in towers 0 - 9 on 20 modules with phototube voltages set using Cs-137 sources.

2. Calorimeter response vs beam energy. The calorimeter response is expressed as E/P normalized by E/P for 50 GeV electrons, where E and P are the calorimeter response in GeV and the beam momentum in GeV/c. The non-linearity is found at the energy smaller than 30 GeV. The non-linearity depends on towers. A Monte Carlo simulation was carried out. It reproduce the non-linearity qualitatively, but the effect was smaller than data.

3. (a) Energy resolution vs $1/\sqrt{E\ (GeV)}$. This data are obtained with no cut on the shower leakage to the hadron calorimeter. This shows a typical energy resolution is $14\ \% / \sqrt{E}$.

   (b) Energy resolution vs tower number for 50 GeV electrons. This data are obtained with no cut on the shower leakage to the hadron calorimeter. The typical energy resolution is $14\ \% / \sqrt{E}$ and a dependence on $1/\sqrt{\sin(\theta)}$ can be seen in this figure.

4. Number of photoelectrons per GeV for each phototube in a module from LED measurements.

5. (a) Typical pulse height distribution of cosmic ray muons viewed by a left tube.

   (b) Typical pulse height distribution of cosmic ray muons viewed by a right tube.

   (c) Typical pulse height distribution of cosmic ray muons viewed by two tubes.

6. Distributions of muon peak pulse heights at tower centers for various towers over all the modules tested.

7. Scatter plot of pulse heights of cosmic ray muons and 50 GeV punch-through particles.

8. Average response along Z for each fixed X over 41 modules with more than 150,000 cosmic ray events. (a) X = 15.3 cm and (b) X = 2.2 cm.

9. Dissimilarity distribution for towers 0-8.

10. Dissimilarity distribution for tower 9.

11. Dissimilarity distributions for various X's (phi's); (a) X = 0 cm, (b) |X| = 6.5 cm, (c) |X| = 10.9 cm, (d) |X| = 15.3 cm, (e) |X| = 19.6 cm for towers 0 - 8; (f) X = 0 cm, (g) |X| = 6.5 cm, (h) |X| = 10.9 cm, (i) |X| = 15.3 cm, (j) |X| = 19.6 cm for tower 9.

12. (a) Typical response map in X at the Z center in a tower and fit to to cosh(X/w).
(b) The distribution of the ratios of two tube outputs in X at the Z center in a tower and fit to exp(-2 X/L).

13. Distributions of w's and L's measured at tower centers.

14. Correlation plot between L and w using the values at tower centers of towers 0 - 8 over 46 modules.

15. Dependences of w and L on Z, where the values w and L are normalized by the average value over tower centers for each module.

16. Polynomial fit of Z dependence of L for each tower using 46 modules. The data are averaged L/L(mean) over 46 modules.

17. Typical Z-response maps with electron beam and cosmic ray muons.

18. Typical phi-response maps with electron beam and cosmic ray muons.

19. Distributions of w's and L's measured at tower centers in the electron data.

20. Correlation plot between L and w obtained from the electron data at tower centers of towers 0 - 9 over 5 modules.

21. Typical response map from electron data for towers 0 - 1.

22. Example of response map reproduced by using a function with 12 parameters. The function is described in the test in detail.

23. (a) Non uniformity of the CDF central EM calorimeter before correction by the parametrization on response map.
(b) Non uniformity of the CDF central EM calorimeter after correction by the parametrization on response map.

24. Uncertainty of energy determination for all towers as a function of the distance (r) from the phi-edge of the calorimeter.

25. Uncertainty of energy determination for each tower as a function of the distance (r) from the phi-edge of the calorimeter.

Chapter 8

1. Event display of the VTPC wire data for the beam-beam interaction in 1985 run.

2. Central calorimetry lego plot for the event in Fig. 8.1.

3. Central calorimeres (Central EM, Central hadron, Wall hadron calorimeters).

4. An isometric view of two VTPC modules. They are rotated in azimuth by 11.3 degrees with respect to each other.

5. A simplified diagram of data acquisition.

6. Scatter plot of TDC values in nsec for West and East beam-beam counters.

   (a) 224 BBC events without halo. The 104 of 224 BBC events are included in the region of $30 < T(Wets) < 65$ nsec and $45 < T(East) < 60$ nsec.

   (b) 23 beam-beam events.

7. Number of counters latched in beam-beam gate (30 nsec wide).

   (a) 224 BBC events without halo.

   (b) 23 beam-beam events.

8. (a) Correlation plot between Zint(VTPC) and Z(BBC) in 23 beam-beam events.

   (b) Distribution of Zint(BBC) - Zint(VTPC) in 23 beam-beam events. The mean and rms values are -1.5 cm

and 5.6 cm.

9. Trigger frequency and Efficiency curves.

10. Total cross section of proton-antiproton collision at 540 GeV CM energy.

11. Average charged track multiplicities per unit of pseudorapidity for data and simulation. The simulation include the effects of L1 bias, photon conversion and hadron interaction in beampipe.

12. Average charged track multiplicities per unit of pseudorapidity for simulation samples: (a) L1 bias plus photon conversion and hdron interaction in beampipe, (b) L1 bias and no other effect in beam pipe, (c) unbiased samples

13. Average charged track multiplicities per unit of pseudorapidity for simulation samples at 540 GeV CM energy. The simulation is in good agreement with UA1 and UA5 data.

14. (a) Energy distribution of EM towers. The solid line and dotted lines are for the data and ODORICO.
(b) Energy distribution of hadron towers. The solid line and dotted lines are for the data and ODORICO.
(c) Energy distribution of EM towers. The solid line and dotted lines are for the data and Centauro (Model 2).
(d) Energy distribution of hadron towers. The solid

line and dotted lines are for the data and Centauro (Model 2).

15. Minimum ionizing peak in EM. (a) Data, (b) simulation.

16. Distribution of total scalar sum of Et.

    (a) Data.

    (b) ODORICO.

    (c) Centauro (Model 2)

17. Distribution of number of towers over threshold of 0.2 GeV.

    (a) Data.

    (b) ODORICO.

    (c) Centauro (Model 2)

18. Eta-dependence of transverse energy flow. The energy threshold for tower is set to 0.2 GeV.

    (a) Data.

    (b) ODORICO.

    (c) Centauro (Model 2)

19. Distribution of maximum energy in towers. Each bin corresponds to the eta-segmentation of the calorimeter i.e. 0.1 units of pseudorapidity. The energy threshold for tower is set to 0.2 GeV.

    (a) Data.

    (b) ODORICO.

    (c) Centauro (Model 2)

20. Multiplicity of BBC between West to East. The multiplicity is obtained from ADC data in BBC system.

21. Distribution of the interaction position for 81 background events with 23 beam-beam events.

22. Schematic view of beam-beam and beam-gas events in the Z-T plane.

23. Multiplicity distribution at ISR and SPS energies [Phys. Lett. 107B (1981) 310]. The dashed and dot-dashed curves are predicted from Pt limited phase-space for $\langle Pt \rangle$ = 350 MeV/c. The solid curve for $\sqrt{s}$ = 540 GeV/c is from the same model but for $\langle Pt \rangle$ = 500 MeV/c. The dotted curve shows the parametrization by Eq. 8.12.

24. Possible patterns of triggerd events in beam-beam and beam-gas collisions.

Chapter 9

1. Experimental signature for heavy lepton production via W decays in p $\bar{p}$ reaction: 2 hadronic jets in events with a large missing energy.

2. Transverse mass (Mjν) distribution of 1 jet plus missing energy system.

   (a) Heavy lepton events.

   (b) $W \rightarrow \tau \nu$.

Distribution of the mass Mjv for the leading energy cluster (CL-1) in W $\rightarrow$ $\tau\,\nu$ events has three peaks. Higher peak is due to the τ jet and missing energy via W decay.

3. Analysis diagram.

4. Angular distribution between the leading energy cluster and the second energy cluster in W$\rightarrow$ L(60) ν events.

   (a) for q q

   (b) for all the reconstructed 2 jets

   (c) for correct combination that reconstructed 2 jets are from two quarks via L decay.

   (d) for wrong combination that reconstructed jet is from recoiling QCD jet.

5. Transverse momentum distribution of the W. Solid line means reconstruction from 2 jets and missing energy. The true distribution is shown with dashed line.

6. Invariant mass spectrum of jet-jet system and transverse mass spectrum of the jet-jet plus missing energy system in the W $\rightarrow$ L(30) ν events. The former corresponds to the heavy lepton mass, the latter is for the transverse mass of W.

7. Invariant mass spectrum of jet-jet system and transverse mass spectrum of the jet-jet plus missing energy system in the W $\rightarrow$ L(60) ν events. The former corresponds to the heavy lepton mass, the latter is for the transverse

mass of W.

8. Invariant mass spectra of jet-jet system in several backgrounds.

9. Number of events detected vs missing Et at luminosity of 10^{37} cm^{-2}.

Table 1.1 Results from the UA1 and UA2 experiments

UA1	1982-1983 run	1984 run
Mw	$80.9 \pm 1.5 \pm 2.4$	$83.5 \pm {}^{1.1}_{1.0} \pm 2.7$
Mz	$95.6 \pm 1.5 \pm 2.9$	$93.0 \pm 1.4 \pm 3.0$
$\sin^2(\theta w)$	$0.228 \pm 0.008 \pm 0.14$	$0.214 \pm 0.006 \pm 0.15$
ρ	$0.928 \pm 0.038 \pm 0.016$	$1.026 \pm 0.037 \pm 0.019$
R	$9.6 \, {}^{+3.0}_{-2.1}$	
	($\leq$ 13.5 at 90 % C.L.)	

UA2	1982-1983 run	1984 run
Mw	$83.1 \pm 1.9 \pm 1.3$	$81.2 \pm 1.1 \pm 1.3$
Mz	$92.7 \pm 1.7 \pm 1.4$	$92.5 \pm 1.3 \pm 1.5$
$\sin^2(\theta w)$	$0.216 \pm 0.010 \pm 0.007$	$0.226 \pm 0.005 \pm 0.008$
ρ	$1.006 \pm 0.043 \pm 0.01$	$0.996 \pm 0.033 \pm 0.009$
R	$7.4 \, {}^{+2.4}_{-1.7}$	
	($\leq$ 10.6 at 90 % C.L.)	

Table 1.2 Characteristics of Centauro Events

	Centauro Event No. I	IV
Estimated number of nuclear active particles in the Centauro interaction	74	90
Estimated number of gamma-rays in the Centauro interaction	0	4
Estimated E-M energy sum in TeV	330	338
k : Gamma-ray inelasticity	0.2	0.2
Total energy of the Centauro event in TeV	1650	1690
Total number of nuclear active particles emitted from the Centauro fireball after extrapolation to zero energy	94	120
Pt : Average transverse momentum in GeV	1.7	1.7
En : Average energy in GeV 1)	2.3	2.3
Estimated rest energy of the Centauro fireball in GeV 2)	216	276
Lorentz factor	7640	6120

1) Assuming that the decay products are nucleons, the average energy of nucleons in the fire-ball frame is obtained from the average Pt.

2) The rest energy of Centauro is estimated by multiplying the average multiplicity by the average energy.

Table 1.3 Summary of CDF Calorimetry

EM Calorimetry Summary

	Forward	End Plug	Central
Ang. Range	2° *to* 10°	10° *to* 37°	37° *to* 90°
Towers in η	18	16	10
Tower Size	$\Delta\eta \sim 0.1$ $\Delta\phi = 5^\circ$	$.05 < \Delta\eta < 0.1$ $\Delta\phi = 5^\circ$	$.087 < \Delta\eta < .13$ $\Delta\phi = 15^\circ$
Construction	Pb-gas tubes	Pb-gas tubes	Pb-scintillator
R.L. per Layer	$.9X_o$	$.53X_o$	$.6X_o$
Layers	15 15	5 24 5	31
R.L. per Sect.	$13X_o$ $13X_o$	$2.7X_o$ $13X_o$ $2.7X_o$	$19X_o$
$\Delta E/E$	$\sim 27\%/\sqrt{E}$	$\sim 24\%/\sqrt{E}$	$\sim 14\%/\sqrt{E}$
Position Resol.	2-4 mm	1-2 mm	1.5-3 mm

Hadron Calorimetry Summary

	Forward	End Plug	End Wall	Central
Ang. Range	2° *to* 10°	10° *to* 30°	30° *to* 45°	45° *to* 90°
Tower Size	$\Delta\eta = 0.1$ $\Delta\phi = 5^\circ$	$\Delta\eta = .09$ $\Delta\phi = 5^\circ$	$.08 < \Delta\eta < .12$ $\Delta\phi = 15^\circ$	$.1 < \Delta\eta < .15$ $\Delta\phi = 15^\circ$
Construction	2 in. Fe + gas tubes	2 in. Fe + gas tubes	2 in. Fe + scintillator	1 in. Fe + scintillator
Layers	28	20	15	32
$\Delta E/E$	$\sim 125\%/\sqrt{E}$	$\sim 14\%$ at 50 Gev	$\sim 14\%$ at 50 Gev	$\sim 70\%/\sqrt{E}$

Table 2.1 Summary of Central EM Calorimeter

Modules		
	12/arch + 2 spare	50
	Length	98 in.
	Width	15 degrees @68+ in. (18.2+")
	Depth (including base plate)	13.6 in.
	Weight	2 metric tons
Towers		
	10/module	478
	Length	DY 0.11 (1/2 of width)
	Thickness (see table M)	18 x0, 1 Labs (+coil etc.)
	Layers	20-30 lead 21-31 scintillator 1 strip chamber
	Lead	1/8 in. aluminum clad
	Scintillator	5 mm SCSN-38 polystyrene
	Wavelength shifter	3 mm Y7 UVA acrylic
	Photomultiplier tubes (956 channels)	Hamamatsu R580 (1 1/2 in.)
Chambers (see table M+1)		
	Depth	5.9 X0 (including coil)
	Wire channels 64/module	3072
	Strip channels 128/module	6130
Angular coverage		
	Theta	about 39-141 degrees
	Phi	complete
	Eta	about $\pm$ 1.1
Performance (high = 30+ GeV)		
	pe/GeV	100+/tube
	Energy resolution sigma/E (GeV)	$14\%/\sqrt{E}$
	Position resolution (high)	$\pm$ 2 mm
	Strip/wire PH correlation	8-10%
	Wire PH resolution (high)	$\pm$ 25%
	Hadron rejection (high)	10^{-3}

Table 2.2 Photomultiplier Specifications

1 High voltage for current gain of 4.0×10^5 less than 1700 V. Total range of required high voltage within 300 V.

2 Bialkali or Multialkali; quantum efficiency for Y7 spectrum greater than 8% (all tubes).

3 No tube dark current above 5 nA for gain of 4×10^5 .

4 Linearity within 1% up to output pulses of 1200 pC.

5 Gain stability after burnin within 1% for 100 hours for anode currents up to 2 microA, within 2% for 1000 hours at 50 nA.

6 Gain change between 50 nA and 2 microA within 5%, between 5 nA and 500 nA within 1.5%.

7 Recovery to within 2% of nominal gain within 1 msec after a full scale pulse (1200 pC).

8 Gain dependence on temperature within 0.5% per degree C.

9 Expected useful lifetime within specifications greater than 50000 hours.

Table 2.3 Stack Thickness of Strip Chamber

TOWER	ANGLE	TO CHAMBER		TOTAL STACK		COIL	
	XO	LABS	XO	LABS	XO	LABS	
0	86.3	4.9	0.26	17.9	0.89	0.86	0.20
1	79.15	5.0	0.27	18.2	0.91	0.88	0.20
2	72.2	5.1	0.28	18.2	0.91	0.90	0.20
3	65.65	4.8	0.28	17.8	0.93	0.95	0.21
4	59.75	5.0	0.29	18.0	0.97	1.00	0.23
5	54.5	4.6	0.29	17.7	1.00	1.06	0.24
6	49.85	4.9	0.31	18.1	1.05	1.13	0.26
7	45.9	4.5	0.32	17.7	1.09	1.20	0.27
8	42.2	4.8	0.34	18.0	1.13	1.28	0.29
9	39.9	5.0	0.36	10.	1.	1.34	0.30

Note) Stack Thickness. Does not include the coil or tracking material. Outer tracking material is approximatly 0.11 XO and 0.026 LABS devided by sin(θ).

Table 2.4 Chamber Specifications

Perpendicular distance to beamline 185 cm
Wire channels (64)
There are 62 cells in the extrusion. They are ganged in pairs except at edges:

```
                                333
0112233    . . .                001  (add 32 other side)
```

The wires are split at the tower 4-5 boundary which is also the strip width change
The logical wire boundary separation is 1.453 cm
The total width is 45 cm (15 degrees implies 48.7 cm)
The wire 15-16 (47-48) boundary is centered in Phi
Readout is through 200 pF
Strip channels (128)
Corresponding to wires 0-31 towers 0-4
69 strips of width 1.667 cm (0-68)
Begins 6.16 cm, ends 121.16 cm
(from 90 degree ouside steel face)
Corresponding to wires 32-63 towers 5-9
59 strips of width 2.007 cm (69-127)
Begins 121.16 cm, ends 239.56 cm
Overall placement error +/- 1 mm both dimensions
Physical characteristics
Cell 0.250 in. deep by 0.239 in. wide
Walls 0.047 in. thick (16.4%)
Wire 0.002 in. gold coated tungsten
Total thickness 0.75 in.
0.069 radiation lengths
0.022 absorbtion lengths
High voltage
Separate feedin for each logical wire channel from 4 external boxes (at each corner)
One box has an input filter and test point for putting pulses on the wires
1 Mohm feedin on chamber and 100k ohm in box for debug
Gas
Parralel flow internally manifolded
Two input and two output 1/4 in. black polyflow (no preferred end)

Table 3.1 Light Yields of Scintillator SCSN Series

Scintillator	Concentration of Fluors		Light Yield 1) (% NE110)
	b-PBD (%)	BDB (%)	
SCSN 11	1.0	0.01	100
25	2.0	0.02	112
38	1.0	0.02	112
39	1.0	0.03	104
43	0.5	0.02	100

(1) The light yields relative to NE110 are given in %. These values are taken from Ref. 2.4.

Table 3.2 Plate-to-plate Nonuniformity in Light Yields

		1st production	2nd production
No. of modules		16	34
No. of samples 1)		176 (175)	400 (399)
Sample number out of tolerance 2)		93-17 (5.33 mm)	729-10 (5.32 mm)
Thickness (mm)	Mean	5.03	5.07
	S.D.	0.12	0.10
Npe 3)	Mean	0.723	0.647
	S.D.	0.009	0.010
σ_{Yc} (%) 4)	Eq.C.7	1.017	1.155
$\sigma_{s,st}$ (%)	Eq.C.8	0.318	0.330
Fluor nonuniformity $\sigma_{s,f}$ (%)	Eq.C.8	0.94	1.08
	Average	1.04	

(1) The numbers in parentheses are the number of samples of which the thickness are within the limit 5.0 $\pm$ 0.3 mm. In the analysis, the data for the samples within the limit in the thickness are used.

(2) The sample number is expressed by two numbers. The first and the second numbers mean the lot and cell number, respectively.

(3) The difference in the number of photoelectrons between the 1st and the 2nd production is due to the fact that different filters were used, although they were commercially the same type.

(4) The deviation of Y in Eq. C.1 is 1.1 % and 1.3 % for the 1st and the 2nd productions.

Table 3.3 Light Yield Nonuniformity in One Mother-board

Prod. No.	Lot No. - Cell No.			1) σ_{Yc} (%)	2) $\sigma_{s,f}$ (%)
1	95	-	06	0.50	-
	99	-	04	0.39	-
	102	-	01	0.64	-
			Average	0.51	0.33
2	730	-	14	0.56	-
	733	-	17	0.90	-
	734	-	20	0.59	-
	739	-	15	0.54	-
	740	-	03	0.63	-
	743	-	07	0.46	-
	745	-	16	0.74	-
			Average	0.63	0.48

(1) See Eq. C.7.
(2) See Eq. C.8. The result estimated by Eq. C.8 is statistically limited by the number of samples : A total of 14 samples was taken from one mother-board as shown in Fig. 3.1. Therefore, only the average value is estimated for each production.

Table 3.4 Thickness of One Plate

	Mean (mm)	RMS (μm)
1 st prod.	4.950	88.9
2 nd prod.	4.964	110.0

Table 3.5 Total Thickness of Stack of 31 Layers of Plates
(weighted by 50 GeV shower for electron)

	Mean (mm)	RMS (μm)
1 st prod.	153.60	546.7
2 nd prod.	153.93	879.0

Table 3.6 Total Thickness of Stack of 31 Layers of Plates
(non-weighted)

	Mean (mm)	RMS (μm)
1 st prod.	153.48	548.7
2 nd prod.	153.91	814.3

Table 6.1 Reference Points and Boundaries

Tower	Angle (deg.)	Z (cm)
	88.687 (1)	4.22
0	85.594 (2)	14.19
-------	82.526	24.16
1	78.867	36.24
-------	75.297	48.32
2	71.841	60.40
-------	68.516	72.48
3	65.336	84.56
-------	62.130	96.64
4	59.443	108.72
-------	56.735	120.80
5	54.187	132.88
-------	51.790	144.97
6	49.542	157.05
-------	47.436	169.12
7	45.463	181.20
-------	43.614	193.28
8	41.884	205.36
-------	40.261	217.45
	39.676 (3)	222.00
9	38.476	231.71
	36.822	245.96

(1) Edge of scintillator at 90 degree end.

(2) Center of scintillator at position of strip chamber.

(3) Best point for the normalization with the minimum effects on both longitudunal and lateral shower leakage.

Table 6.2 Statistic of Cosmic Ray Data

Number of events analyzed (1)	Number of modules	Statistical Error (2)
200 K events	29	1.2 %
150 K - 200 K	12	1.3 - 1.2 %
100 K - 150 K	1	1.6 - 1.3 %
50 K - 100 K	2	2.3 - 1.6 %
50 K	2	2.3 %
0 K	4	-
	50	

(1) The number includes the strip chamber efficiency.

(2) The calculation is performed by assuming energy resolution = 20 % and uniform distribution of cosmic ray for 650 meshes.

Table 6.3(a) Definition of Meshes on Strip Channels

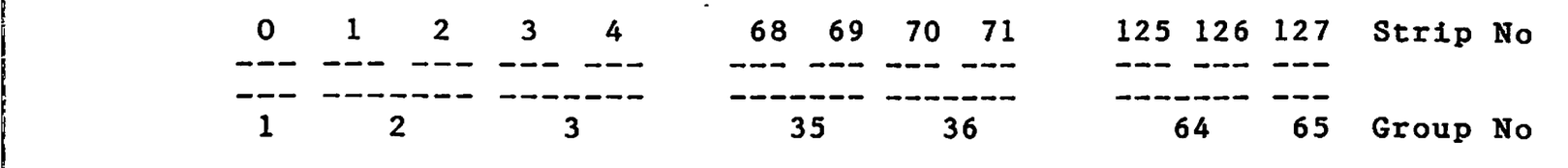

Tower	Strip No. 1)	Group No. 2)	Angle (degree) max	Angle (degree) center	Zcenter (cm) 3)
0	0 - 10	1 - 6	88.687	85.594	14.19
1	11 - 24	7 - 13	82.526	78.867	36.24
2	25 - 39	14 - 21	75.297	71.841	60.40
3	40 - 54	21 - 28	68.516	65.336	84.56
4	55 - 68	29 - 35	62.130	59.443	108.72
5	69 - 80	36 - 41	56.735	54.187	132.88
6	81 - 92	42 - 47	51.790	49.542	157.05
7	93 - 104	48 - 53	47.436	45.463	181.20
8	105 - 116	54 - 59	43.614	41.884	205.36
9	117 - 127	60 - 65	40.261	38.476	231.71

(1) Each tower boundary is defined with an accuracy of 3 mm except for the boundary between tower 0 and 1 (-0.64 cm) using the strips.

(2) Strip groups 1 and 65 includes 1 strip.

(3) Zcenter is Rs tan(θc), where Rs is 184.153 cm and θc is polar angle for the tower center.

Table 6.3(b) Definition of Meshes on Wire Channels

1) Group	Wire	X (cm)	2) Phi	Group	Wire	X (cm)	Phi
	0	-22.158			31	22.158	
	1	-21.069			30	21.069	
10	2	-19.616	-6.306	1	29	19.616	6.306
	3	-18.163			28	18.163	
	4	-16.710			27	16.710	
9	5	-15.257	-4.736	2	26	15.257	4.736
	6	-13.804			25	13.804	
	7	-12.351			24	12.351	
8	8	-10.898	-3.387	3	23	10.898	3.387
	9	- 9.445			22	9.445	
	10	- 7.992			21	7.992	
7	11	- 6.539	-2.034	4	20	6.539	2.034
	12	- 5.086			19	5.086	
	13	- 3.633			18	3.633	
6	14	- 2.180	-0.6782	5	17	2.180	0.6782
	15	- 0.7265			16	0.7265	

(1) The width of one group is 4.359 cm except for the groups 1 and 10 for which the widths are 7.359 cm.

(2) Phi is the azimuthal angle (degrees) in X.

Table 7.1 Contribution to Standard Deviation of Individual Phototube Average Pulse Heights and Calculation of Source-Electron Non-Tracking.

	Contribution to Standard Deviation as % of Mean	
	Cs-137	Co-60
Tolerance for Declaring Phototube High Voltage Set (Tolerance = 0.55 % for Co-60, 0.8 % for Cs-137)	0.46	0.32
Source Run Resproducibility	0.30	0.25
RABBIT Card Current Channel Calibration	0.1	0.1
Test Beam Electron Calibration Accuracy	0.18	0.18
RABBIT Card Charge Channel Calibration	0.05	0.05
Relative Source Avtivity Determination	1.7	----
Average of RMS/Mean for Individual Tubes	2.91	2.47
Contribution from Non-tracking of Source and Electron Response	2.29	2.43

Table 7.2 Average Peak Value for Cosmic Ray Muons

Tower	:	0	1	2	3	4	5
Average	:	595.31	599.20	616.02	603.71	602.81	609.99
Deviation	:	26.15	24.29	25.56	28.64	31.97	27.78

Tower	:	6	7	8	9
Average	:	655.29	651.02	657.21	624.79
Deviation	:	28.89	26.79	27.33	28.65

1. A total of 44 modules are used for the calculation:
   Missig - 18,23,29,40
   Spare - 21,30
2. Peak value is defined by average value of two tubes.
3. Unit : fC

Table 7.3 Ratio of Pulse Heights between Punch-through Particles and Cosmic Ray Muons

Wedge No.	x 1	x16
21	1.10 +/- 0.014	1.11 +/- 0.018
22	1.11 +/- 0.011	1.08 +/- 0.010
24	1.25 +/- 0.050	1.14 +/- 0.051
25	1.09 +/- 0.011	1.10 +/- 0.010
26	1.21 +/- 0.028	1.11 +/- 0.015
27	1.09 +/- 0.021	1.06 +/- 0.020

Table 7.4(a) Dissimilarity

Tower	All Area	Central Area	Edge Area		(*)
			Theta-edge	Phi-edge	
0	0.84 ± 0.39	0.71 ± 0.18	0.60 ± 0.31	1.46 ± 0.20	1.01
1	0.98 ± 0.40	0.80 ± 0.25	0.98 ± 0.30	1.46 ± 0.42	0.89
2	0.79 ± 0.37	0.64 ± 0.24	0.71 ± 0.33	1.30 ± 0.25	0.85
3	0.86 ± 0.36	0.68 ± 0.26	1.04 ± 0.30	1.20 ± 0.31	0.74
4	1.13 ± 0.42	0.96 ± 0.26	1.15 ± 0.48	1.54 ± 0.38	0.86
5	1.13 ± 0.35	1.00 ± 0.24	1.02 ± 0.32	1.55 ± 0.27	0.94
6	1.00 ± 0.68	0.62 ± 0.27	0.99 ± 0.41	1.78 ± 0.83	0.85
7	0.91 ± 0.48	0.71 ± 0.22	0.73 ± 0.36	1.54 ± 0.51	0.84
8	0.94 ± 0.61	0.71 ± 0.28	0.76 ± 0.36	1.76 ± 0.77	1.05
9	2.14 ± 0.77	1.20 ± 0.42	2.13 ± 0.69	2.76 ± 0.62	1.51
0 - 8	0.95 ± 0.47	0.76 ± 0.28	0.87 ± 0.46 1.20 ± 0.55	1.48 ± 0.44	

(*) Dissimilarity from electron data in whole area.

Table 7.4(b) Dissimilarity along X

Median X (cm)	Wire Group Number	Dissimilarity (%) Cosmic Ray Data		Test Beam
		Towers 0-8	Tower 9	Towers 0-9
0.0	5, 6	0.39 +/- 0.60	1.86 +/- 0.52	0.56 %
6.5	4, 7	0.66 +/- 0.32	1.79 +/- 0.75	
10.9	3, 8	0.77 +/- 0.32	2.16 +/- 0.90	
15.3	2, 9	0.93 +/- 0.27	2.18 +/- 0.55	
19.6	1,10	1.48 +/- 0.44	2.76 +/- 0.62	1.79 %

Table 7.5 Deviations of w and L

	Average (cm)	Tower-to-tower deviation (%)	Module-to-module deviation (%)
w	55.0	5.6	9.2
L	99.3	3.3	9.0

(1) The errors for w and L are typically 6 % and 2 %.

Table 7.6 Parameterization of Z dependence of L

Tower	L0 (cm)	C1 (x 10**-3)	C2 (x 10**-3)	Zoff (cm)
0	100.9 +/- 8.1	7.18 +/- 5.76	1.44 +/- 0.71	-2.49
1	101.2 +/- 8.7	0.19 +/- 4.84	1.19 +/- 0.37	-0.08
2	97.9 +/- 8.5	0.42 +/- 3.86	0.94 +/- 0.38	-0.22
3	98.0 +/- 9.3	3.74 +/- 3.52	1.25 +/- 0.43	-1.50
4	98.2 +/- 8.9	1.79 +/- 3.39	1.15 +/- 0.48	-0.78
5	96.7 +/- 8.9	4.17 +/- 6.23	1.32 +/- 0.53	-1.58
6	96.7 +/- 8.7	1.58 +/- 4.25	1.11 +/- 0.68	-0.71
7	98.2 +/- 8.8	-0.03 +/- 4.12	1.20 +/- 0.53	0.01
8	99.9 +/- 7.9	0.90 +/- 3.81	1.26 +/- 0.63	-0.36
9	85.9 +/- 6.3	-3.24 +/- 4.09	2.17 +/- 0.79	0.75

(1) The Z dependence of L is parametrized by a polynomial:

$$L = L0\ (1 + C1\ Z + C2\ Z^2)\ ,$$

where L0 is the attenuation length at tower centers of each module and Z the local corrdinate in a tower as defined in the text. The fitting for each tower is shown in Fig. 7.16.

(2) The dependence is symmetric for Z = Zoff. The position Zoff is nearly close to the physical tower center.

Table 7.7(a) Fitting Parameters (Towers 0 - 5)

TOWER 0

1	0.100E+01	+-	0.885E-03
2	0.171E-04	+-	0.771E-05
3	-0.790E+00	+-	0.201E-01
4	0.183E-02	+-	0.117E-02
5	-0.552E-03	+-	0.422E-05
6	0.447E+02	+-	0.386E+00
7	0.100E+01	+-	0.000E+00
8	0.117E-01	+-	0.757E-03
9	0.721E-08	+-	0.573E-04
10	0.445E-06	+-	0.357E-06
11	0.552E+00	+-	0.364E-01
12	-0.168E-02	+-	0.211E-03

TOWER 1

1	0.100E+01	+-	0.734E-03
2	0.343E-04	+-	0.340E-04
3	0.587E+00	+-	0.870E-01
4	-0.832E-03	+-	0.870E-04
5	0.000E+00	+-	0.000E+00
6	0.485E+02	+-	0.537E+00
7	0.100E+01	+-	0.000E+00
8	0.146E-02	+-	0.592E-03
9	0.349E-03	+-	0.663E-04
10	0.268E-06	+-	0.294E-06
11	0.563E+00	+-	0.473E-01
12	-0.164E-03	+-	0.929E-04

TOWER 2

1	0.998E+00	+-	0.679E-03
2	0.106E-05	+-	0.124E-05
3	0.923E+00	+-	0.100E+00
4	-0.941E-03	+-	0.985E-04
5	0.000E+00	+-	0.000E+00
6	0.477E+02	+-	0.457E+00
7	0.100E+01	+-	0.000E+00
8	0.196E-02	+-	0.618E-03
9	0.965E-04	+-	0.667E-04
10	0.444E-08	+-	0.908E-10
11	0.762E+00	+-	0.429E-04
12	-0.128E-02	+-	0.131E-03

TOWER 3

1	0.100E+01	+-	0.906E-03
2	0.936E-04	+-	0.750E-04
3	0.496E+00	+-	0.682E-01
4	-0.357E-03	+-	0.902E-04
5	0.000E+00	+-	0.000E+00
6	0.457E+02	+-	0.381E+00
7	0.100E+01	+-	0.000E+00
8	0.586E-02	+-	0.535E-03
9	0.722E-03	+-	0.615E-04
10	0.198E-08	+-	0.153E-09
11	0.798E+00	+-	0.262E-04
12	0.876E-03	+-	0.665E-04

TOWER 4

1	0.999E+00	+-	0.126E-02
2	0.146E-03	+-	0.215E-03
3	0.425E+00	+-	0.128E+00
4	-0.529E-03	+-	0.107E-03
5	0.000E+00	+-	0.000E+00
6	0.416E+02	+-	0.335E+00
7	0.100E+01	+-	0.000E+00
8	0.114E-01	+-	0.636E-03
9	0.169E-02	+-	0.735E-04
10	0.170E-07	+-	0.698E-09
11	0.724E+00	+-	0.219E-03
12	-0.374E-03	+-	0.122E-03

TOWER 5

1	0.998E+00	+-	0.793E-03
2	0.315E-04	+-	0.582E-05
3	0.539E+00	+-	0.807E-02
4	-0.369E-03	+-	0.123E-03
5	0.000E+00	+-	0.000E+00
6	0.430E+02	+-	0.347E+00
7	0.100E+01	+-	0.000E+00
8	0.113E-01	+-	0.597E-03
9	0.117E-02	+-	0.727E-04
10	0.293E-07	+-	0.289E-07
11	0.696E+00	+-	0.455E-01
12	-0.145E-03	+-	0.124E-03

Table 7.7(b) Fitting Parameters (Towers 6 - 9)

TOWER 6

1	0.999E+00	+-	0.124E-02
2	0.339E-03	+-	0.275E-03
3	0.406E+00	+-	0.719E-01
4	-0.117E-02	+-	0.128E-03
5	0.000E+00	+-	0.000E+00
6	0.482E+02	+-	0.534E+00
7	0.100E+01	+-	0.000E+00
8	0.645E-02	+-	0.714E-03
9	0.125E-03	+-	0.804E-04
10	0.995E-08	+-	0.762E-09
11	0.743E+00	+-	0.283E-03
12	0.396E-03	+-	0.149E-03

TOWER 7

1	0.100E+01	+-	0.211E-02
2	0.114E-02	+-	0.117E-02
3	0.287E+00	+-	0.943E-01
4	-0.116E-02	+-	0.157E-03
5	0.000E+00	+-	0.000E+00
6	0.460E+02	+-	0.474E+00
7	0.100E+01	+-	0.000E+00
8	-0.431E-02	+-	0.689E-03
9	0.169E-09	+-	0.475E-04
10	0.106E-07	+-	0.775E-09
11	0.754E+00	+-	0.258E-03
12	-0.123E-03	+-	0.121E-03

TOWER 8

1	0.100E+01	+-	0.138E-02
2	0.458E-03	+-	0.401E-03
3	0.364E+00	+-	0.773E-01
4	-0.555E-03	+-	0.115E-03
5	0.000E+00	+-	0.000E+00
6	0.499E+02	+-	0.477E+00
7	0.100E+01	+-	0.000E+00
8	0.956E-02	+-	0.820E-03
9	0.543E-04	+-	0.912E-04
10	0.158E-07	+-	0.859E-09
11	0.738E+00	+-	0.262E-03
12	-0.502E-03	+-	0.168E-03

TOWER 9

1	0.100E+01	+-	0.113E-02
2	0.589E-02	+-	0.780E-04
3	0.350E+00	+-	0.281E-03
4	-0.466E-02	+-	0.257E-03
5	-0.301E-06	+-	0.233E-06
6	0.509E+02	+-	0.948E+00
7	0.100E+01	+-	0.000E+00
8	-0.106E+00	+-	0.598E-02
9	0.125E-01	+-	0.101E-02
10	0.158E-07	+-	0.117E-08
11	0.736E+00	+-	0.360E-03
12	0.646E-02	+-	0.275E-03

Table 8.1 1985 CDF Run History

RUN	EVENT	TIME	COMMENT
		(October 12, 1985 --Saturday)	
(489)	0	18:10	Run started (E.W.Lllow)
	61	18:47	Unstacking Pbars, cogging, lost most of pbar's
	85	19:00	
	110	19:43	Unstacking Pbars; only Pbar in main ring; dumped
	137	20:07	Unstacking Pbars
		20:11	Accelerating Pbars; reached 800 GeV
	147	20:12	Ready to cog
	* 233	20:47	Pbars are cogged; lost Pbars ?
	353	22:20	Unstacking Pbars (shot 18)
	358	22:27	Commence cogging
	385	22:35	Pbars are cogged
	* 404	22:42	Squeezed
	421	22:44	Halo veto put into trigger
	451	23:04	Flying wire scan starts
	459		Flying wire scan finished
	506	23:47	
	542		Tape logger bombed; no EOF on tape; do not try
			to read tape after event 542.
(492)			Lost (overwritten by run 493)
		(October 13, 1985 -- Sunday)	
(493)		02:30	Started run
	11	02:32	Event 11 observed to be a BB collision
	16	02:35	Tape logger bombed.
(494)			(Run 494 only on disk)
		03:15	Shot 20 unstacked
		03:20	Lost in cogging
	113	03:52	Shot 21 unstacked (9th of the stack)
	119	03:55	Pbars accelerated
	139	04:00	Cogging in progress
	191	04:05	Pbars cogged
	* 204	04:10	Squeezed
	218	04:20	Clock resynched
	220	04:25	Raise F.S. wire voltage to 1.65 KV
		04:40	.06 Hz trigger rate
	301	05:12	
	333	05:50	End run

Table 8.2 Event Selection

Condition	Events selected	Comments
No cut	887 (23/26)	All events in Runs 489,493,494
1	387 (21/23)	BBC events (w/ halo, w/o halo)
2	224 (21/23)	BBC events w/o halo
3	36 (21/23)	Latch information used
4	23 (21/23)	VTPC added

) Number in each parenthesis is number of beam-beam events in the format (BB/BB+BB), where BB* means probable beam-beam event.

Each condition number means:

(1) Select events with good TDC and ADC data in BBC, called BBC events in the obove comments.

(2) Select BBC events without halo.

(3) Check the number of counters latched within beam-beam gate:

$$N_{west} \geq 5 \text{ for West module,}$$
$$N_{east} \geq 5 \text{ for East module.}$$

(4) Check the diffrence of Zint between BBC and VTPC with $4-\sigma$ cut, assuming the position resolution of Zint(BBC) is 10 cm.

Table 8.3 Scan List of Beam-Beam Events from BBC/VTPC

Zint - Interaction position in cm
Tint - Interaction time in nsec
Tdev - Cluster size in nsec
M.I.P. - Number of minimum ionizating particles
RUN TIME - 94 kHz scaler counts in min

///// RUN 489 /////

	BBC										VTPC
	Number of Counters IN TIME		GOOD					M.I.P.		RUN	VTPC
EVENT	WEST	EAST	WEST	EAST	Zint	Tint	Tdev	WEST	EAST	TIME	Zint
424	15	14	1	2	-108.0	29.8	0.1	139	67	233.1	-110.5
430	13	14	2	2	-108.7	27.8	0.1	90	68	237.0	-110.2
434	15	13	3	1	-91.4	30.1	0.3	106	71	239.9	-89.4
#439	15	14	3	0	*****	****	****	121	81	243.7	145.0
446	15	14	3	4	2.0	32.7	0.4	109	70	248.2	5.8
479	15	13	3	5	-108.9	30.0	0.5	100	16	272.4	-104.6
485	6	13	2	3	-115.4	30.3	0.4	7	25	278.3	-105.0
487	15	14	2	2	-65.2	30.7	0.1	113	57	279.6	-59.1
491	13	14	2	3	-48.2	32.5	0.1	72	57	282.5	-52.3
#497	15	11	3	3	123.0	39.1	0.2	109	8	284.9	131.0
498	15	14	2	2	-112.2	30.7	0.2	49	71	285.3	-108.2
503	15	14	3	2	-73.0	29.7	0.1	135	85	293.2	-73.0
509	12	14	3	2	124.1	36.3	0.2	41	94	298.2	123.2
538	14	14	2	1	5.5	35.5	0.2	56	74	313.5	5.4
					///// RUN 493 /////						
11	10	14	1	6	128.4	35.5	0.6	23	14	11.3	125.9
15	10	10	2	2	-20.2	32.0	0.3	10	15	12.2	-19.9
					///// RUN 494 /////						
203	13	13	1	1	-15.0	31.9	0.0	53	55	76.9	-17.7
223	14	14	1	2	54.0	34.1	0.2	123	80	89.8	42.0
226	13	14	0	1	*****	****	****	50	82	91.5	73.4
227	15	14	0	1	*****	****	****	151	93	92.2	-44.5
244	11	14	2	2	-34.4	32.9	0.2	11	20	99.4	-22.1
246	15	14	2	2	-16.0	34.3	0.1	56	82	101.1	-15.3
247	15	14	2	3	27.9	32.8	0.3	83	53	101.2	23.0
257	14	14	1	2	-30.3	33.6	0.2	58	55	105.2	-30.2
271	15	14	3	2	2.2	35.0	0.3	124	89	113.4	2.1
#276	15	13	2	4	33.0	34.5	0.3	112	19	116.1	45.5

*) A mark # indicates a probable beam-beam event in the VTPC information.
*) Antiprotons was cogged by 1.5 m toward East before Run489 Event 509.

Table 8.4 Parameters for Simulation Models

Model	Ecm (GeV)	Multiplicity All	Multiplicity PiO	Multiplicity Baryons	Transverse Momentum All	Transverse Momentum PiO	Transverse Momentum Baryons	L1-pass (%)
MB		76	18	9	0.55	0.51	0.63	9
C1	210.	91	0	91	1.7	-	1.7	100
C2	240.	95	0	95	1.7	-	1.7	100
C3	270.	153	21	93	1.2	0.4	1.7	100

(1) Model names MB, C1, C2, and C3 mean Minimum Bias (ODORICO), Centauro hypothesis 1, 2, and 3, respectively.

(2) The different CMS energies among Centauro models come from average mass of the baryons generated.

(3) The average multiplicity and transverse momentum (GeV) are presented for each models.

(4) L1 means the level 1 calorimeter trigger used in 1985 run.

Table 8.5 Beam-Beam and Beam-Gas Events

Event Type	Y(int/rev)	L1 bias [1]	Ybias	Nevents [2]	Rate(Hz) [2]
BB	5.3×10^{-7}	1	1.0	17	2.3×10^{-3}
BG(p)	1.7×10^{-6}	0.086	0.28	5	6.4×10^{-4}
BG(p)	2.2×10^{-11}	0.086	3.6×10^{-6}	-	-
BG(p)*BG(p)	2.0×10^{-10}	0.165	6.2×10^{-5}	-	-
BB*BG(p)	2.1×10^{-9}	1	4.0×10^{-3}	-	-
BB*BG(p)	2.7×10^{-14}	1	5.1×10^{-8}	-	-
Total				22	2.9×10^{-3}

(1) L1bias is normalized by that of BB events.

(2) Nevents and Rate are calculated by using the relative Ybias, and by assuming σ(BB) = 70 mbarn, L = 3.6×10^{23} cm^{-2} s^{-1}, and εtrig(BB) = 9.1 %. The trigger efficiency is obtained from the calorimeter simulation for the event generated by ODORICO. The period for squeezing low-beta is estimated to be 7230 sec from 94 kHz scaler.

Table 9.1 Number of Events Detected at $L\,dt = 10^{37}\ cm^{-2}$

	σ (nb)	B (%)	Missing E_T (GeV) Cut 10	15	20	25
$W \to L(30)\,\nu$	1.50	6.4	304 (86)	292 (81)	253 (65)	183 (40)
$W \to L(60)\,\nu$	0.58	2.4	83 (28)	72 (25)	55 (19)	32 (11)
$W \to \tau\ \nu$	1.94	8.6	44	40	31	22
$W \to t\ b$	3.81	19.0	110	74	45	24
$Z \to \nu\,\nu$	0.97	18.0	50	45	33	20
$t\,\bar{t}$	104.7	--	22	20	15	9
$b\,\bar{b}$	103.7	--	2166	366	50	7

(*) The number in each parenthesis is the number of misidentified events.

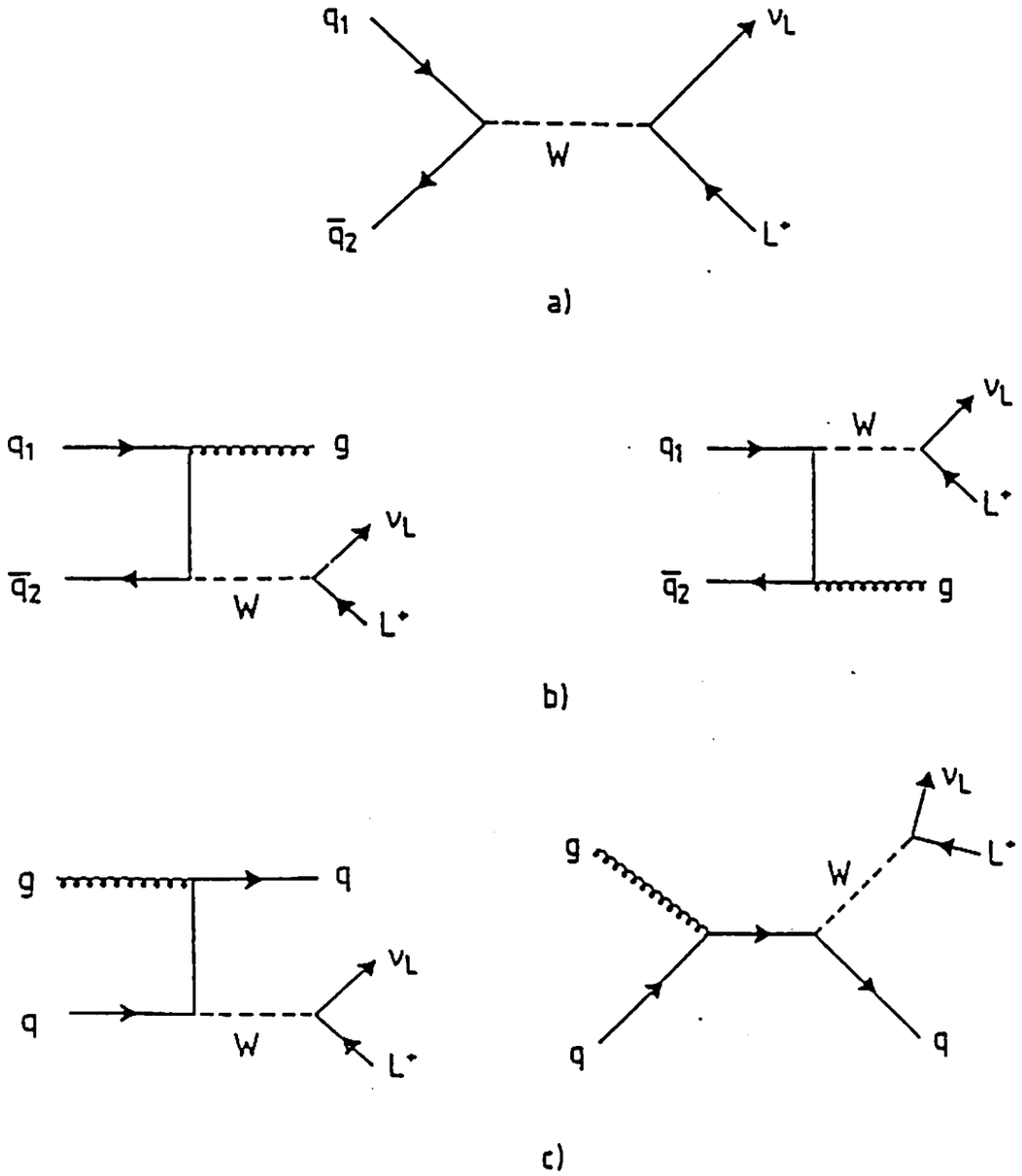

Fig. 1.1

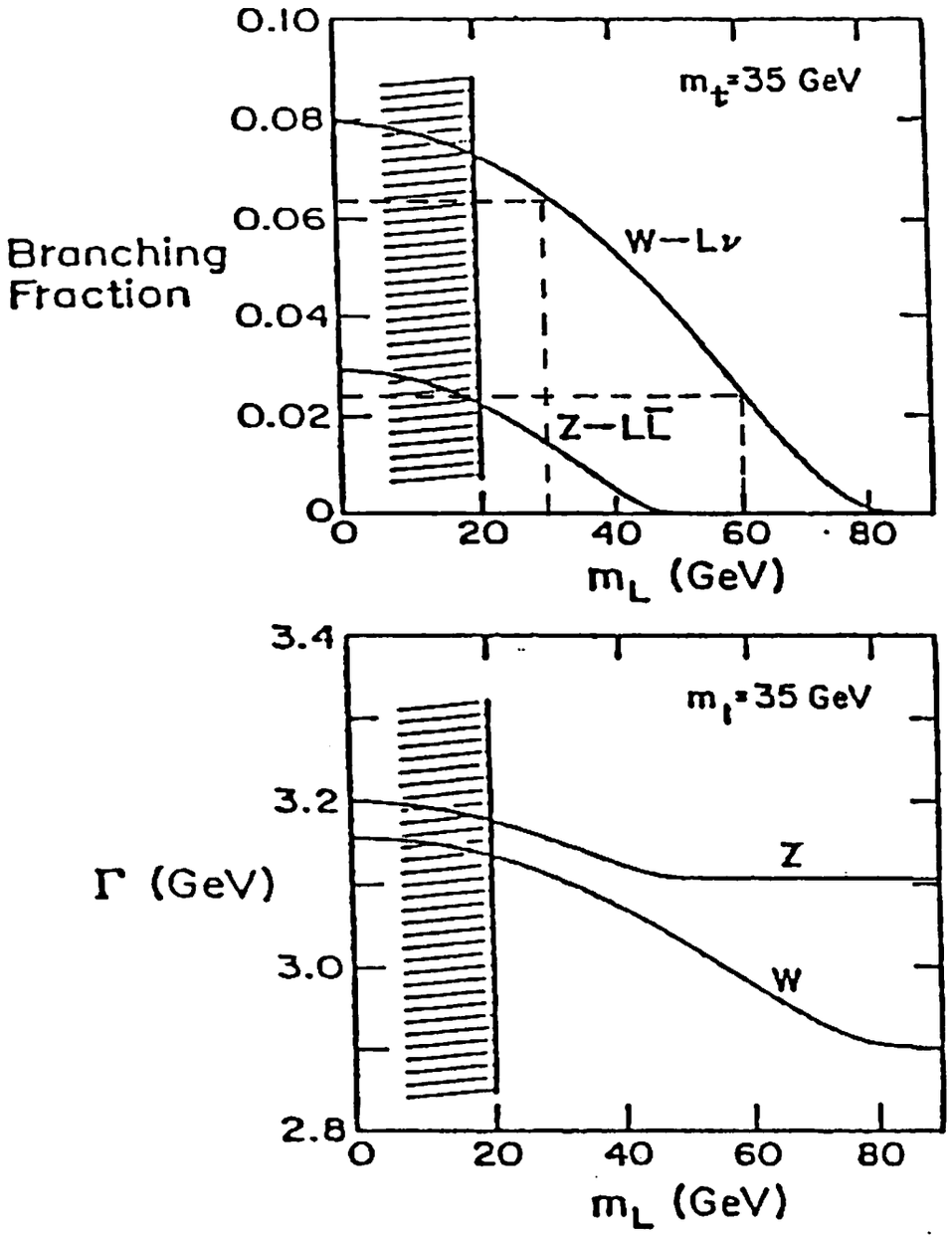
0.10
0.08
0.06
0.04
0.02
0
Branching Fraction
m_t=35 GeV
W—Lν
Z—LL̄
0
20
40
60
80
m_L (GeV)
3.4
3.2
3.0
2.8
Γ (GeV)
m_t=35 GeV
Z
W
0
20
40
60
80
m_L (GeV)

Fig. 1.2

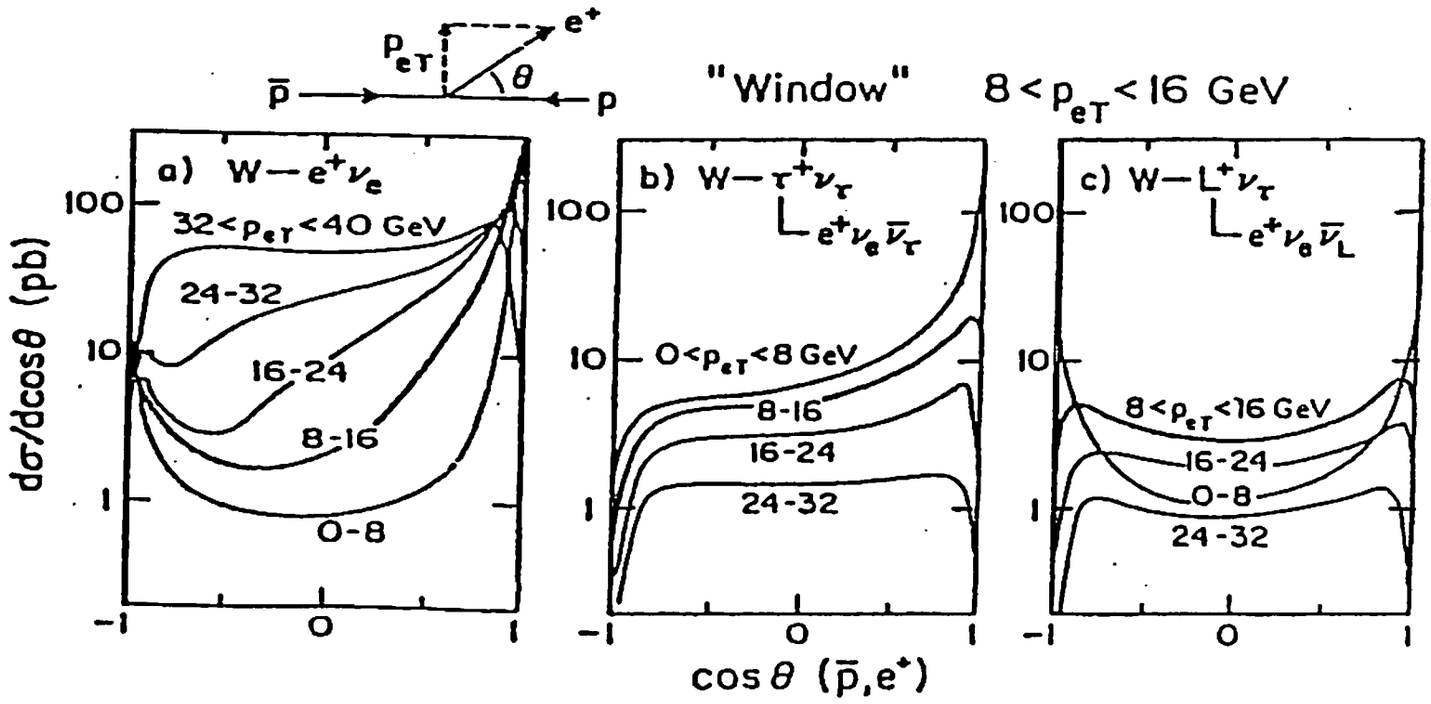
p_{eT}
e^+
θ
$\bar{p}$
p
"Window" $8 < p_{eT} < 16$ GeV
a) $W \to e^+\nu_e$
$32 < p_{eT} < 40$ GeV
24-32
16-24
8-16
0-8
b) $W \to \tau^+\nu_\tau$
$\hookrightarrow e^+\nu_e\bar{\nu}_\tau$
$0 < p_{eT} < 8$ GeV
8-16
16-24
24-32
c) $W \to L^+\nu_\tau$
$\hookrightarrow e^+\nu_e\bar{\nu}_L$
$8 < p_{eT} < 16$ GeV
16-24
0-8
24-32
$d\sigma/d\cos\theta$ (pb)
100
10
1
-1
0
1
$\cos\theta\ (\bar{p}, e^+)$

Fig. 1.3

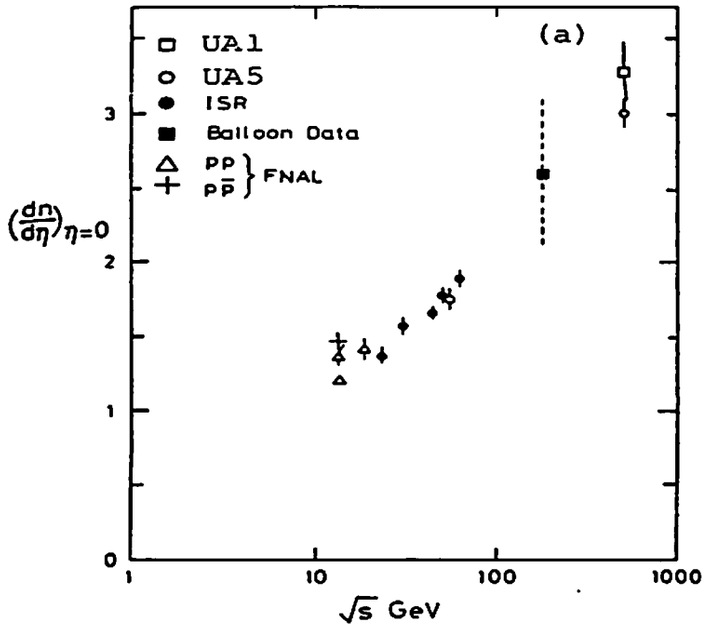
(a)
UA1
UA5
ISR
Balloon Data
pp
pp̄
FNAL
$(\frac{dn}{d\eta})_{\eta=0}$
$\sqrt{s}$ GeV

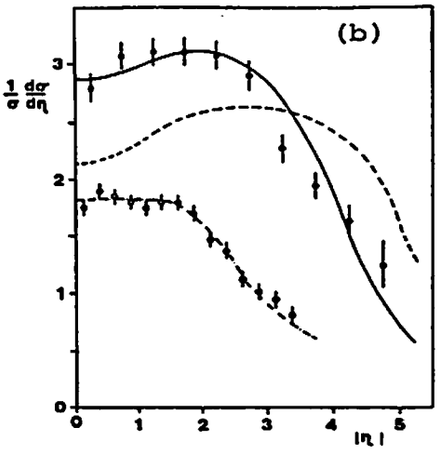
(b)
$\frac{1}{\sigma}\frac{d\sigma}{d\eta}$
|η|

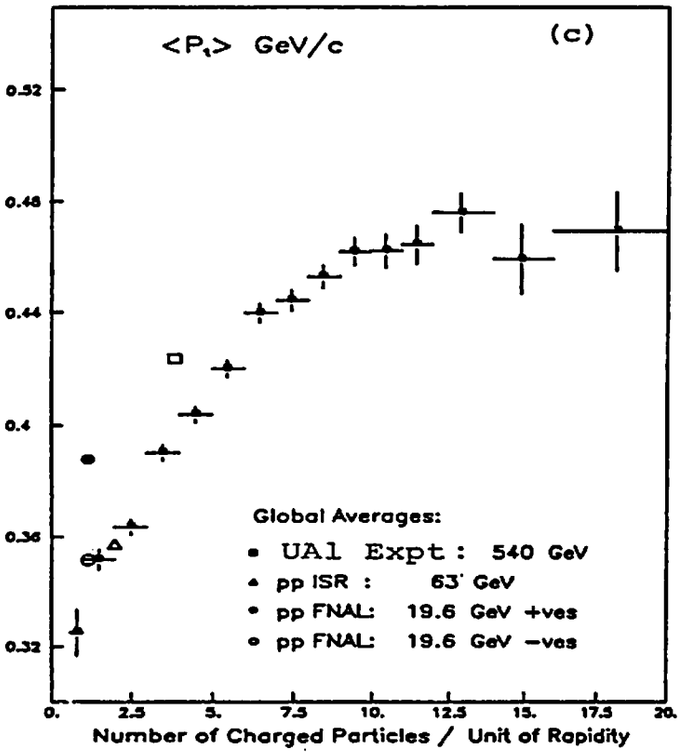
$\langle P_t \rangle$ GeV/c
(c)
Global Averages:
UA1 Expt : 540 GeV
pp ISR : 63 GeV
pp FNAL: 19.6 GeV +ves
pp FNAL: 19.6 GeV −ves
Number of Charged Particles / Unit of Rapidity

Fig. 1.4

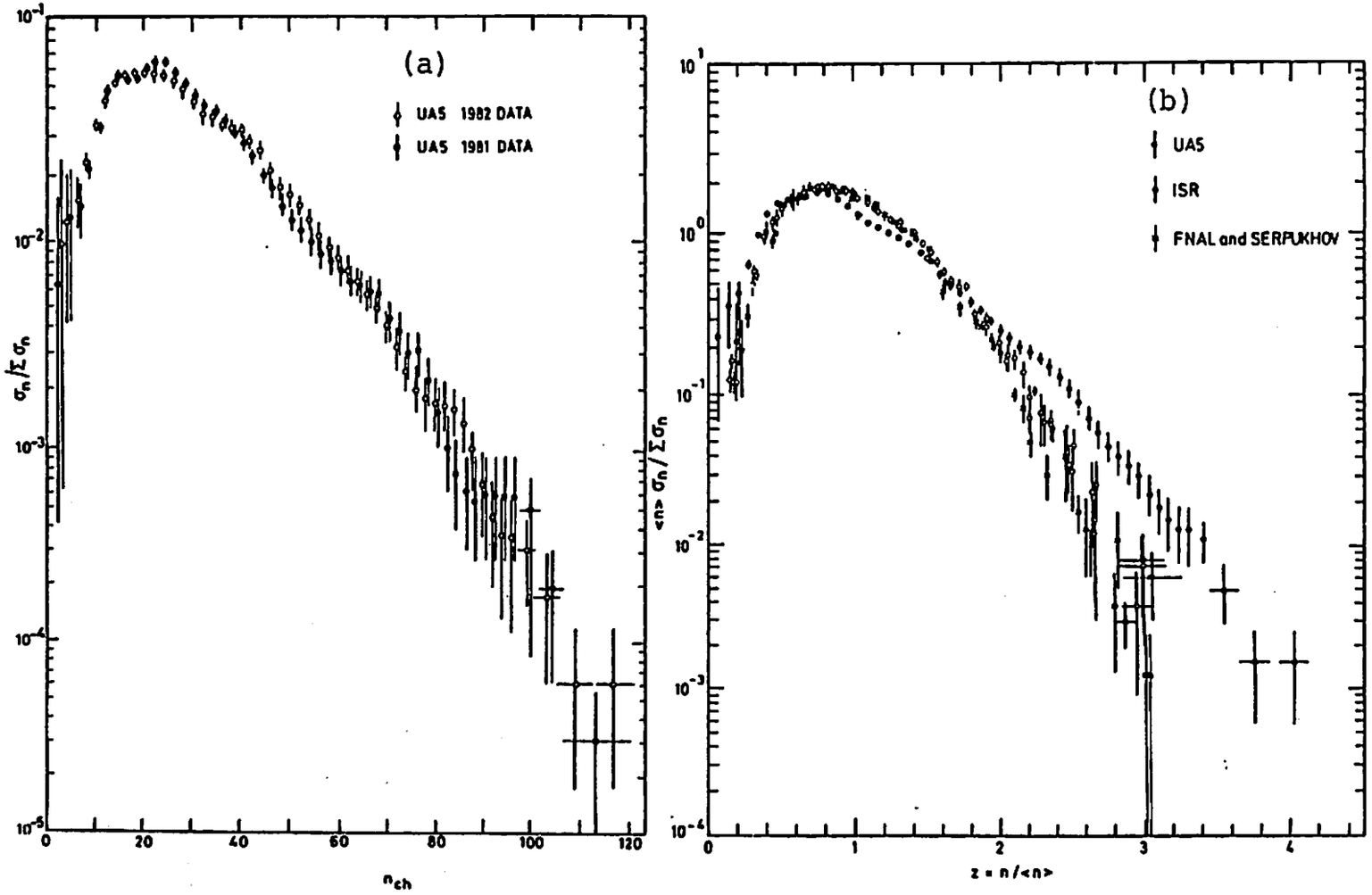
(a)
UA5 1982 DATA
UA5 1981 DATA
$\sigma_n/\Sigma\sigma_n$
n_{ch}
(b)
UA5
ISR
FNAL and SERPUKHOV
$\langle n\rangle\sigma_n/\Sigma\sigma_n$
$z = n/\langle n\rangle$

Fig. 1.5

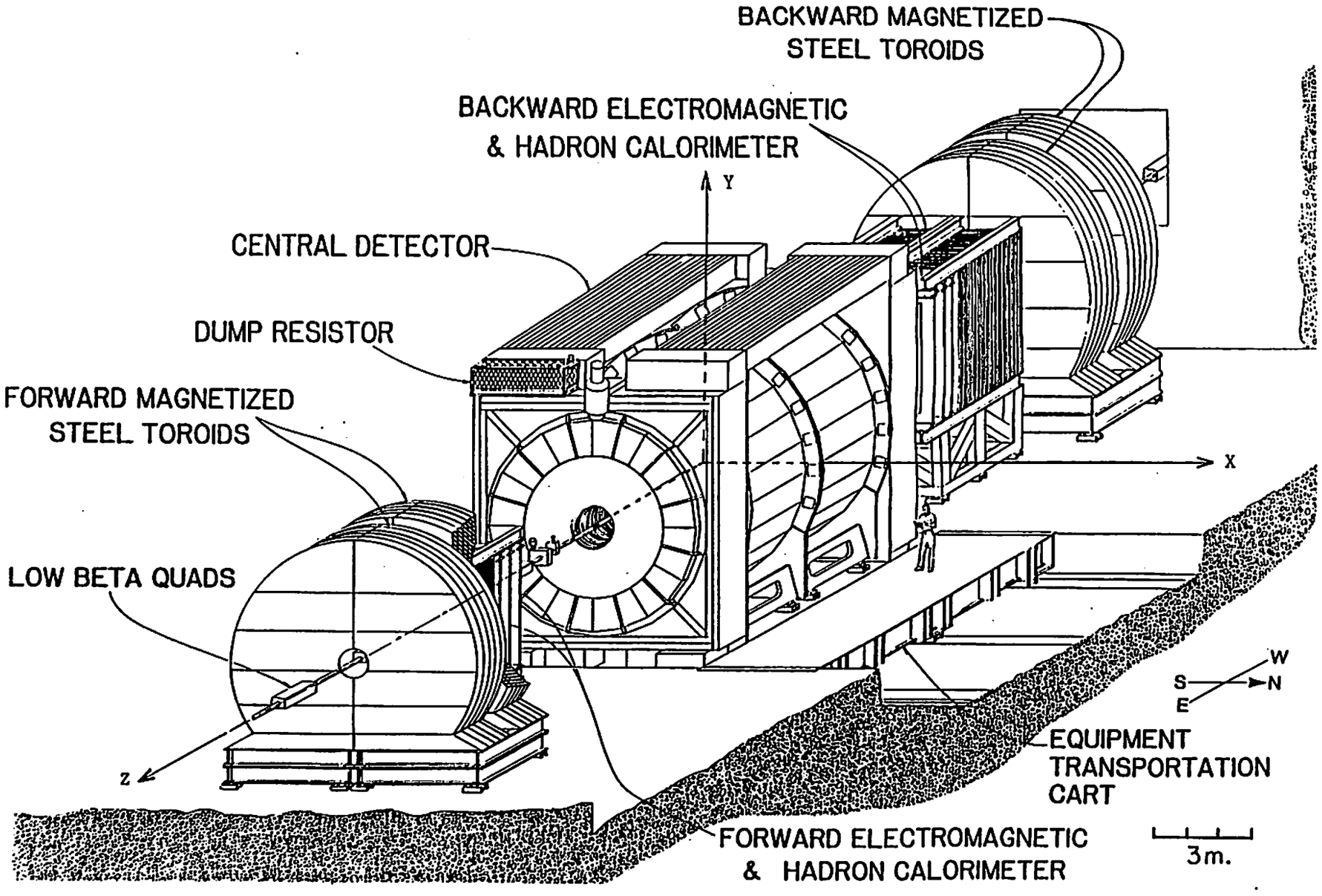
BACKWARD MAGNETIZED
STEEL TOROIDS
BACKWARD ELECTROMAGNETIC
& HADRON CALORIMETER
Y
CENTRAL DETECTOR
DUMP RESISTOR
FORWARD MAGNETIZED
STEEL TOROIDS
X
LOW BETA QUADS
Z
W
S
N
E
EQUIPMENT
TRANSPORTATION
CART
FORWARD ELECTROMAGNETIC
& HADRON CALORIMETER
3m.

Fig. 1.6

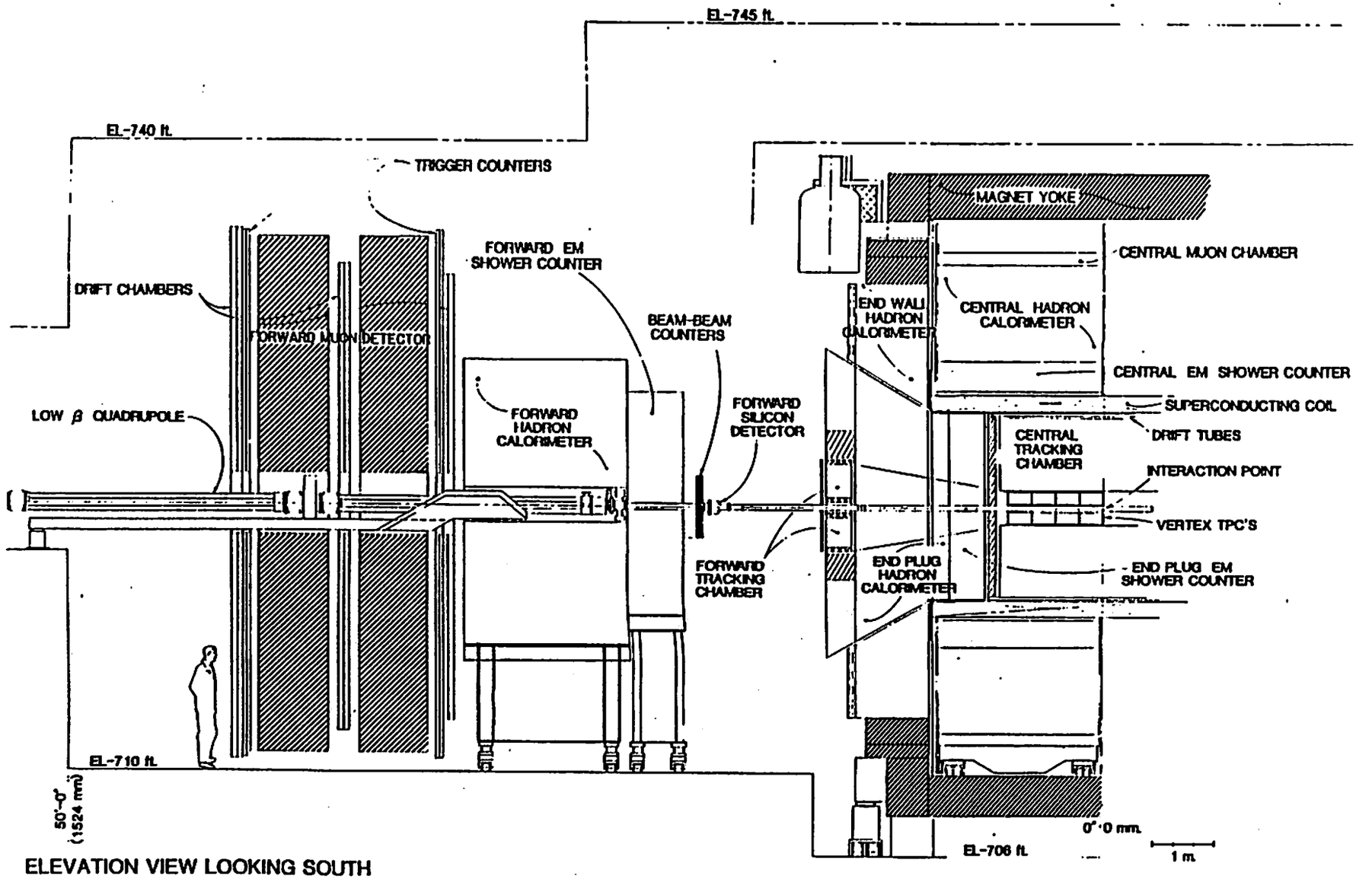

ELEVATION VIEW LOOKING SOUTH

Fig. 1.7

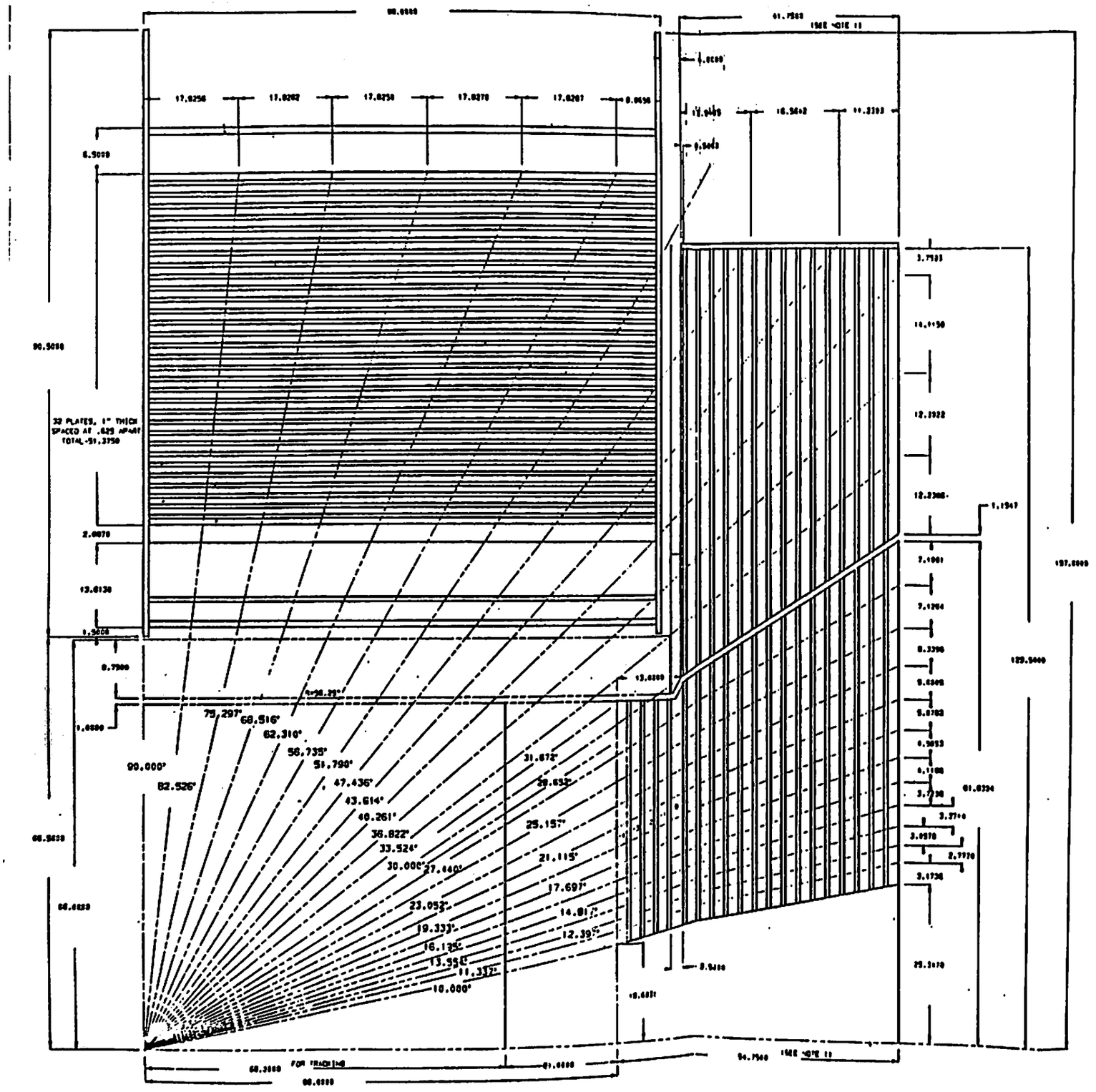
32 PLATES, 1" THICK
SPACED AT .625 APART
TOTAL=51.3750
99.000°
82.526°
75.297°
68.516°
62.310°
56.735°
51.790°
47.436°
43.614°
40.261°
36.822°
33.524°
30.000°
27.660°
23.052°
19.333°
16.135°
13.55°
11.317°
10.000°
31.672°
29.652°
25.157°
21.115°
17.697°
14.81°
12.39°
FOR TRACING

Fig. 2.I (a)

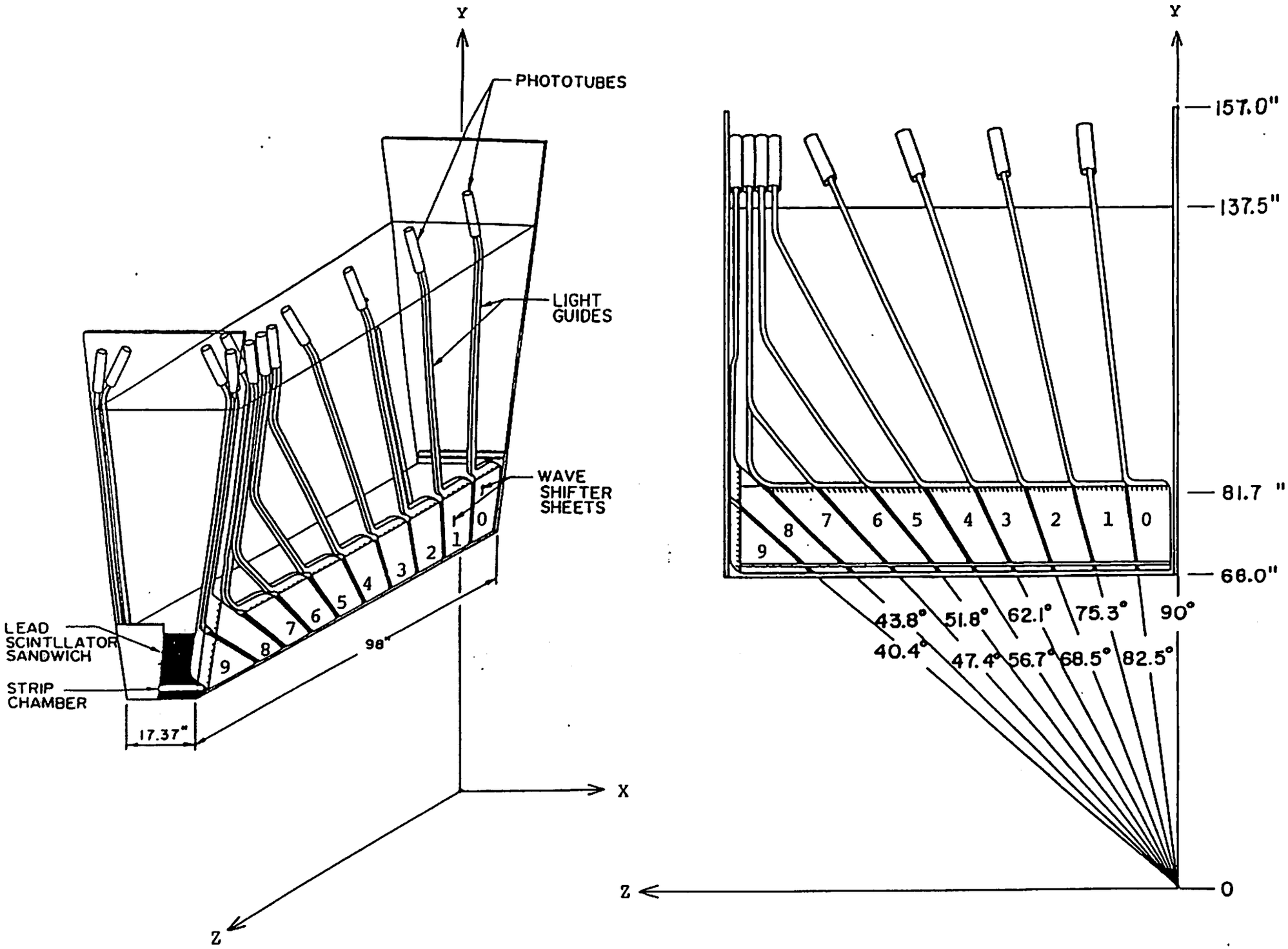
Y
PHOTOTUBES
LIGHT GUIDES
WAVE SHIFTER SHEETS
LEAD SCINTLLATOR SANDWICH
STRIP CHAMBER
17.37"
98"
0
1
2
3
4
5
6
7
8
9
X
Z
Y
157.0"
137.5"
81.7 "
66.0"
43.8°
51.8°
62.1°
75.3°
90°
40.4°
47.4°
56.7°
68.5°
82.5°
Z
0

Fig. 2.1 (b)

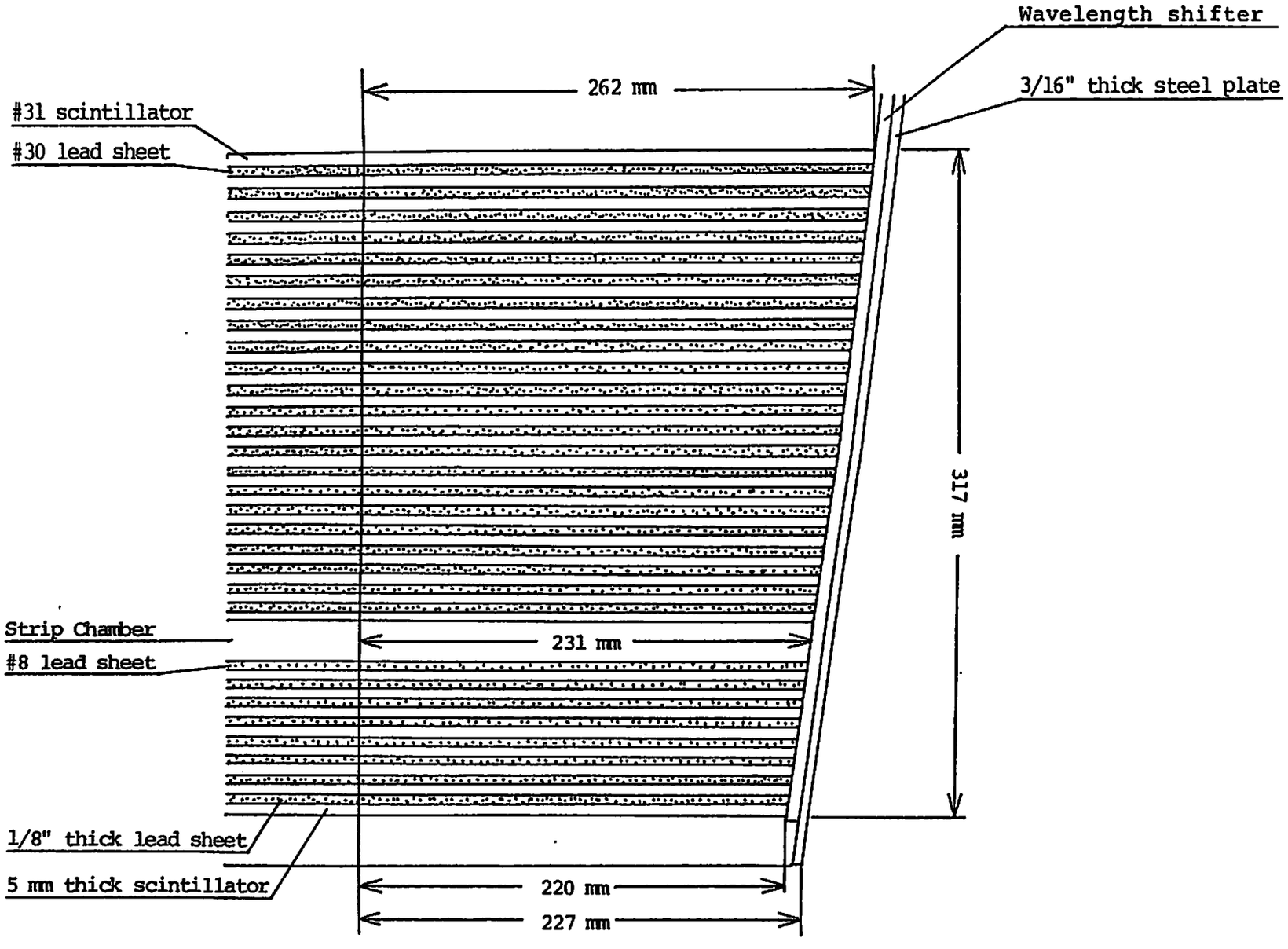
Wavelength shifter
3/16" thick steel plate
262 mm
#31 scintillator
#30 lead sheet
317 mm
Strip Chamber
231 mm
#8 lead sheet
1/8" thick lead sheet
5 mm thick scintillator
220 mm
227 mm

Fig. 2.2

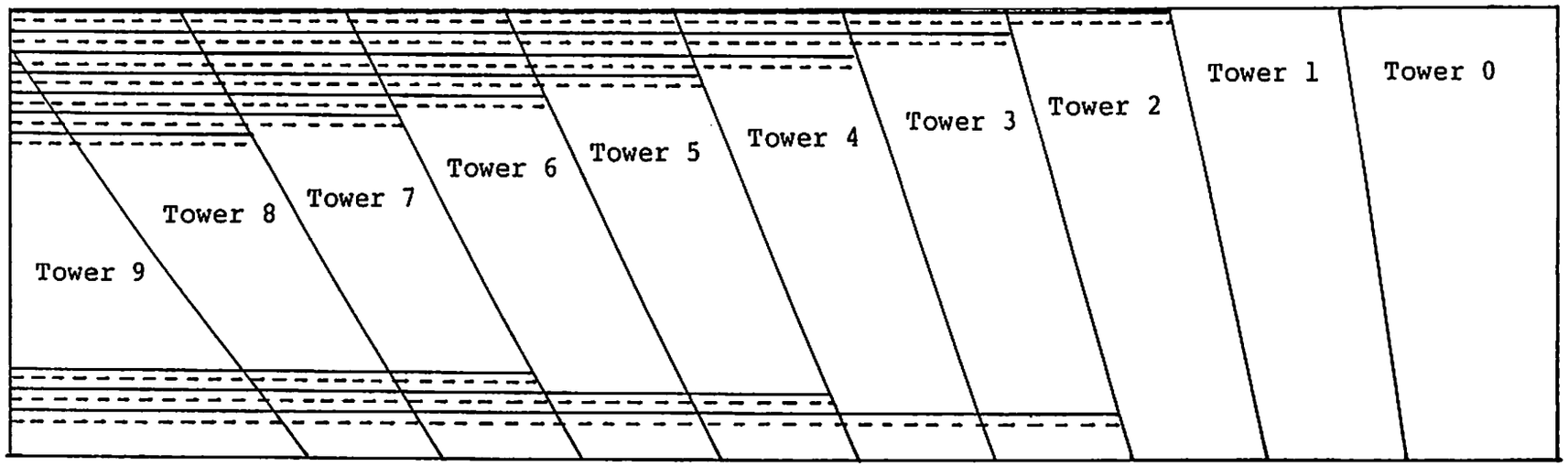

---------- Substitutive Plastic Plate for Lead Plate

———————— Inactive Scintillator Plate

Fig. 2.3

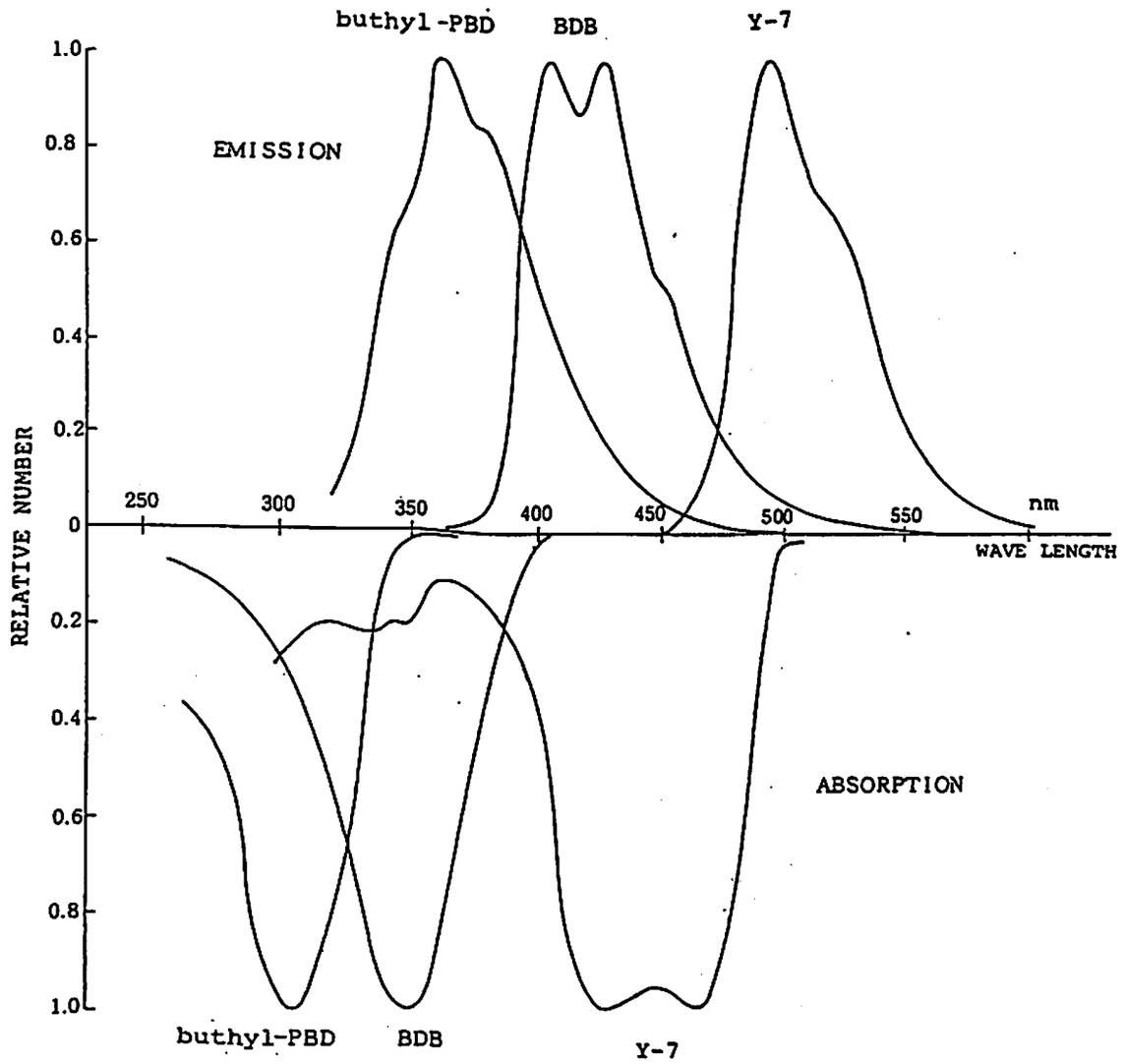
buthyl-PBD
BDB
Y-7
EMISSION
1.0
0.8
0.6
0.4
0.2
0
250
300
350
400
450
500
550
nm
WAVE LENGTH
RELATIVE NUMBER
0.2
0.4
0.6
0.8
1.0
ABSORPTION
buthyl-PBD
BDB
Y-7

Fig. 2.4

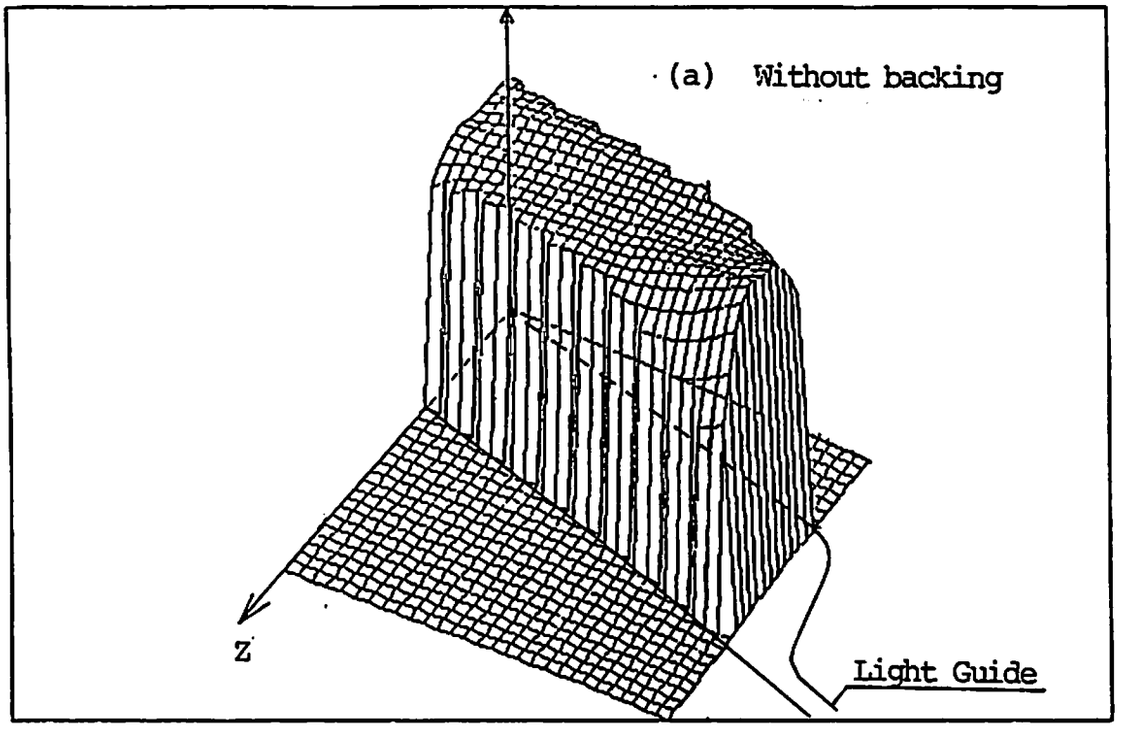

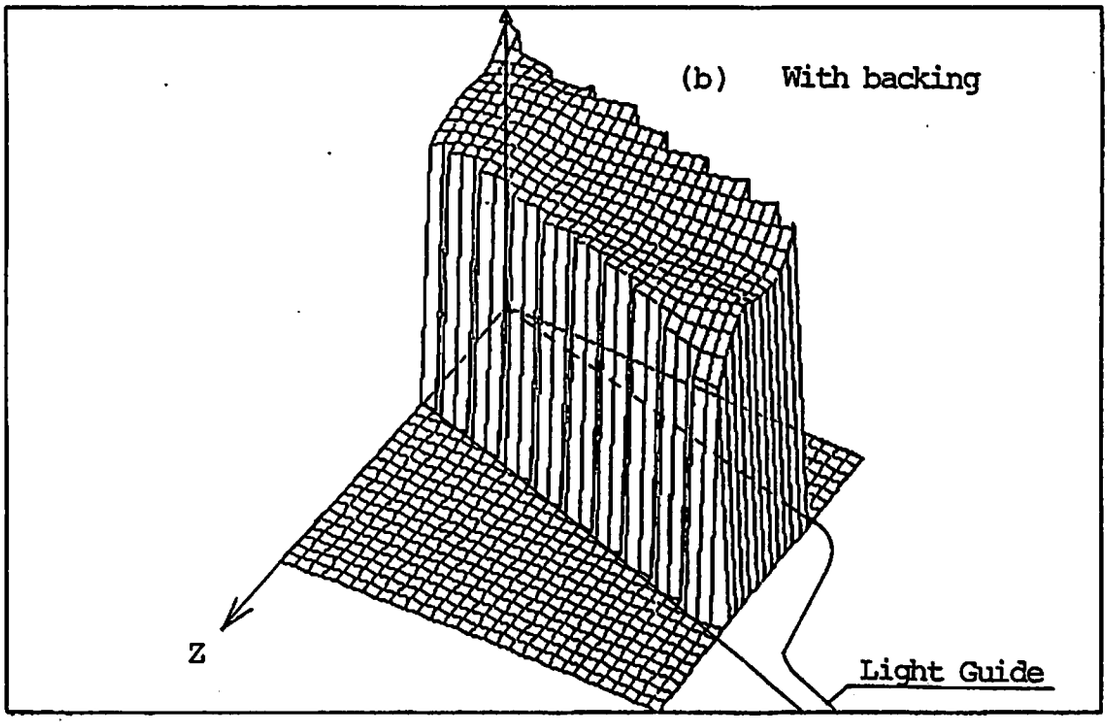

Fig. 2.5

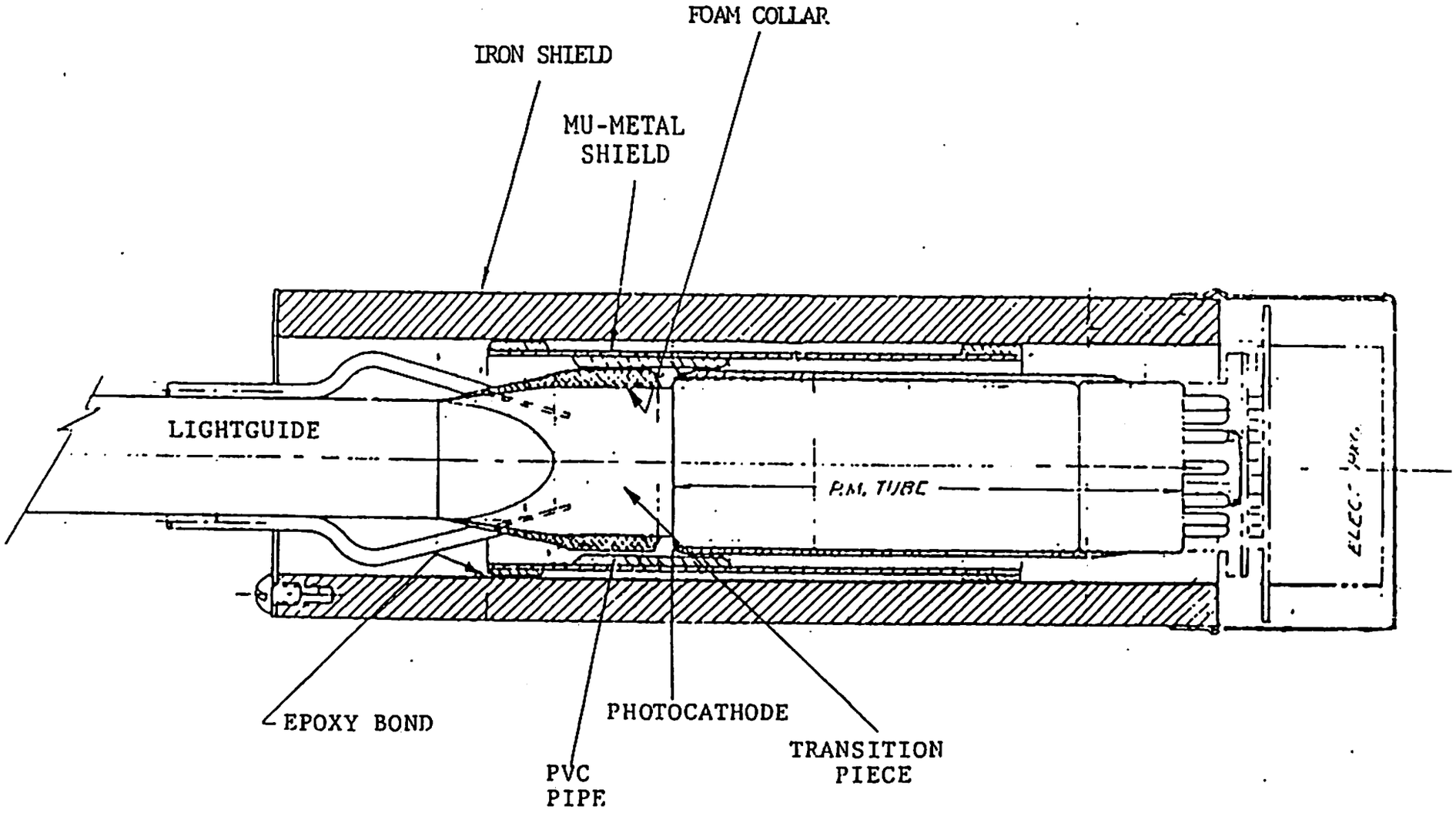
FOAM COLLAR
IRON SHIELD
MU-METAL
SHIELD
LIGHTGUIDE
P.M. TUBE
EPOXY BOND
PHOTOCATHODE
TRANSITION
PIECE
PVC
PIPE

Fig. 2.6

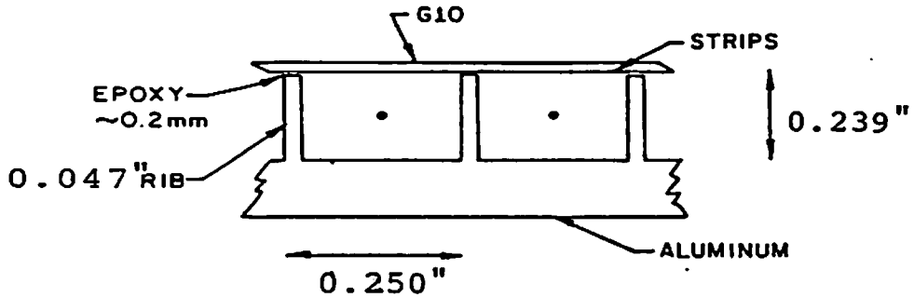
G10
STRIPS
EPOXY
~0.2mm
0.047" RIB
0.239"
ALUMINUM
0.250"

(a)

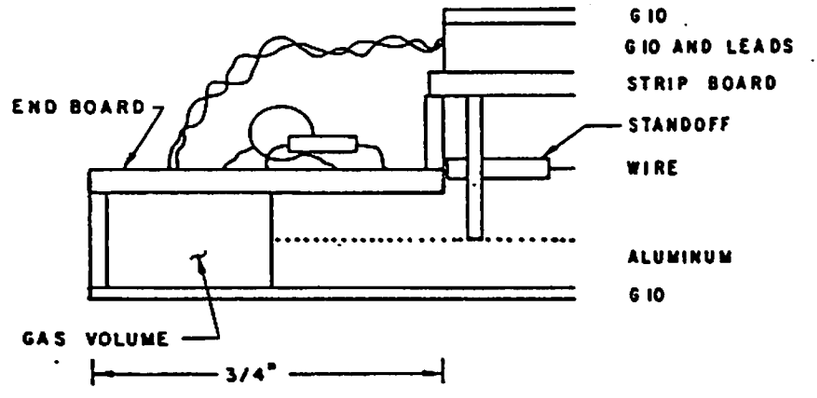
G10
G10 AND LEADS
STRIP BOARD
STANDOFF
WIRE
ALUMINUM
G10
END BOARD
GAS VOLUME
3/4"

(b)

Fig. 2.7

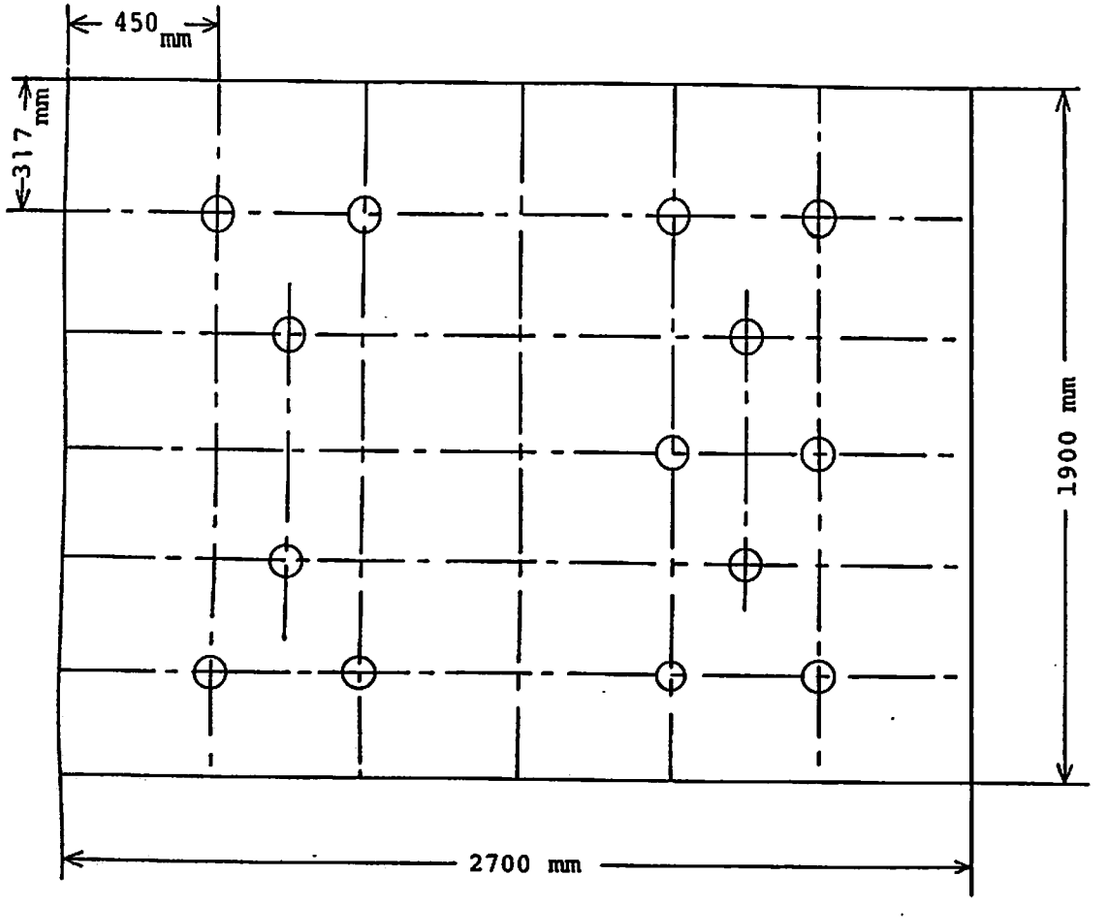

(a)

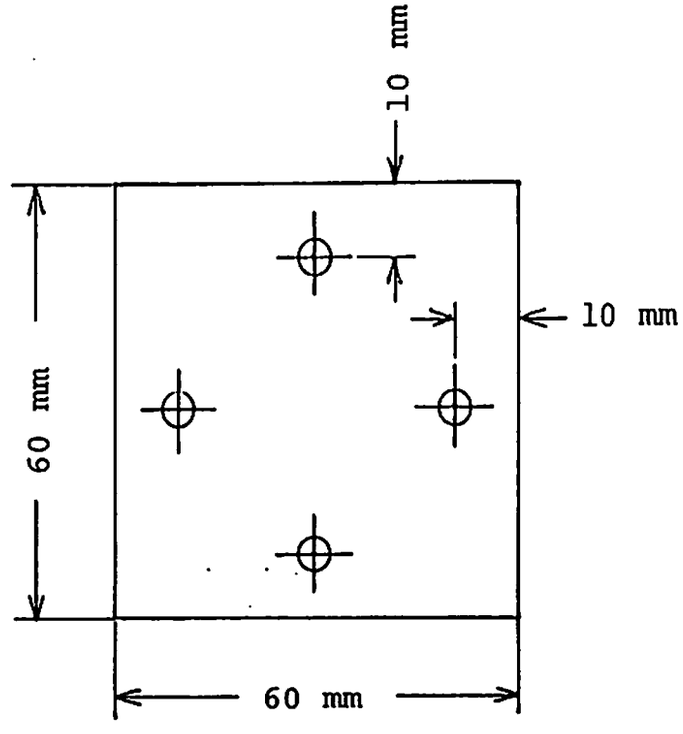

(b)

Fig. 3.1

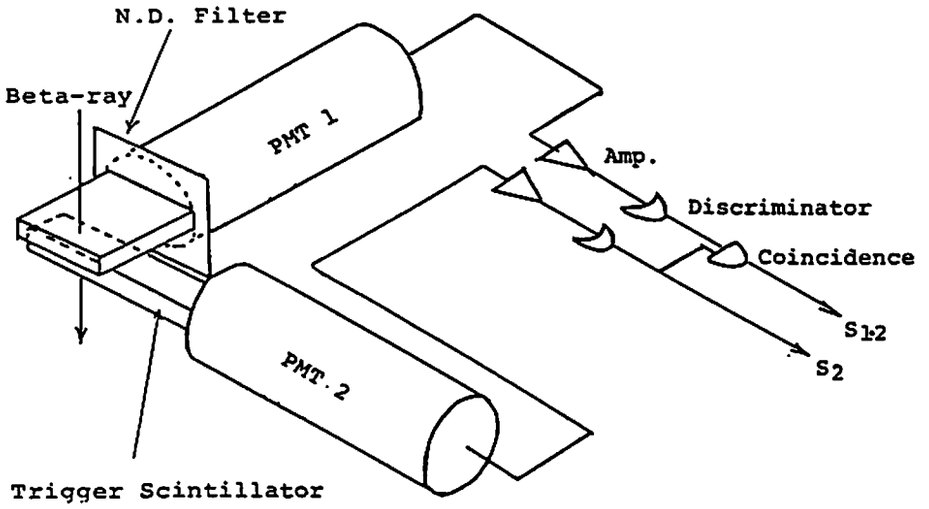
N.D. Filter
Beta-ray
PMT 1
PMT 2
Amp.
Discriminator
Coincidence
S1·2
S2
Trigger Scintillator

Fig. 3.2

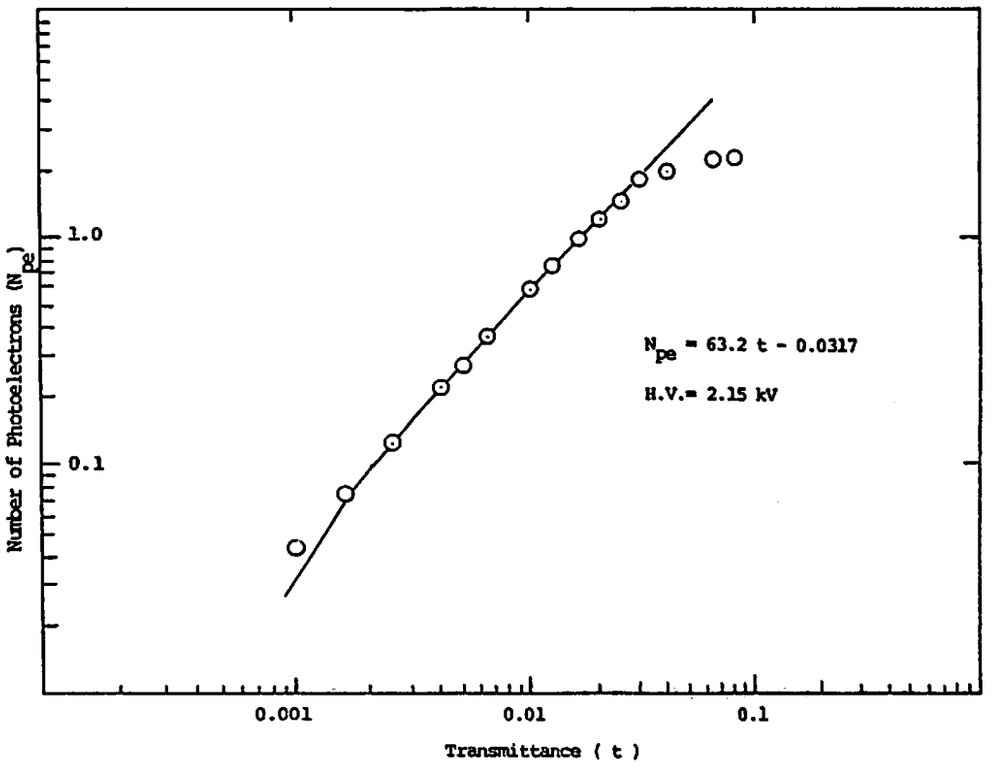
Number of Photoelectrons (N_{pe})
1.0
0.1
0.001
0.01
0.1
Transmittance (t)
N_{pe} = 63.2 t - 0.0317
H.V.= 2.15 kV

Fig. 3.3

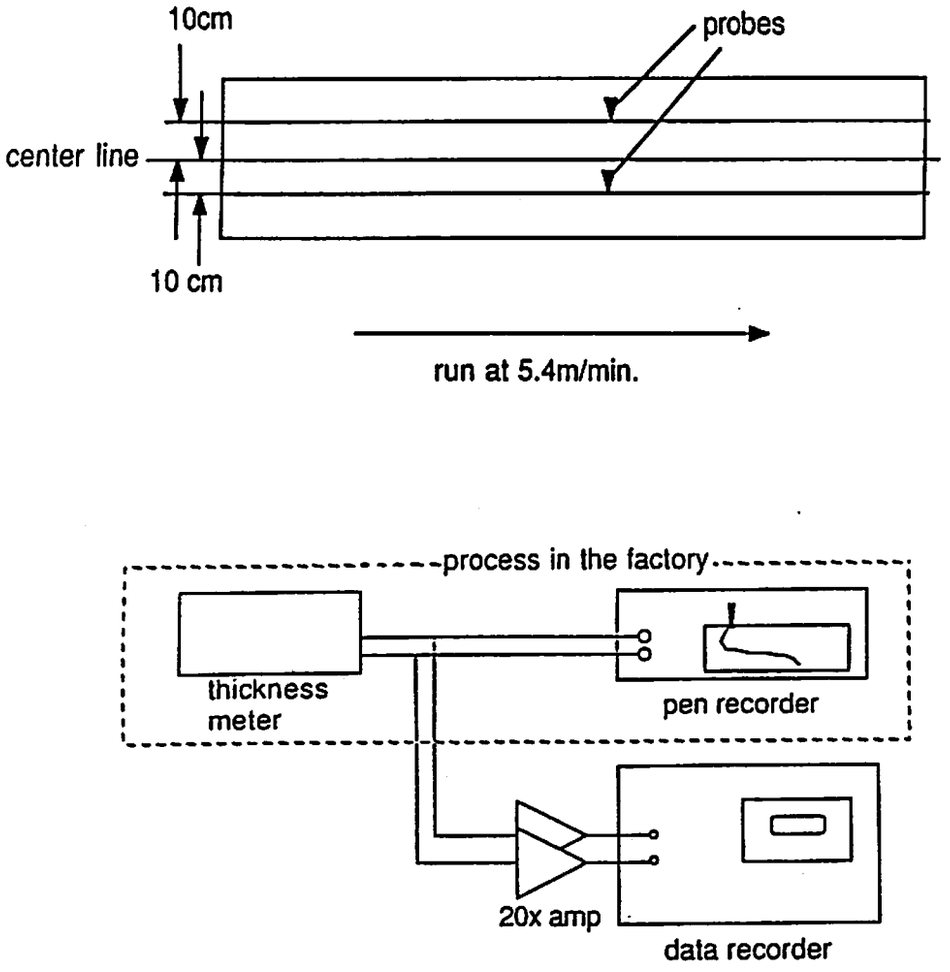
10cm
probes
center line
10 cm
run at 5.4m/min.
process in the factory
thickness
meter
pen recorder
20x amp
data recorder

Fig. 3.4

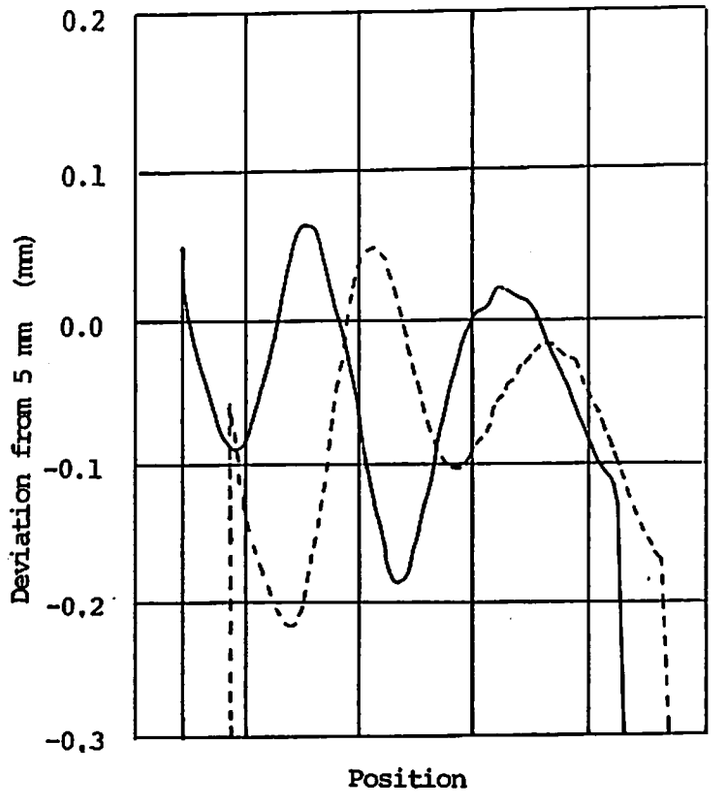
0.2
0.1
0.0
-0.1
-0.2
-0.3
Deviation from 5 mm (mm)
Position

Fig. 3.5

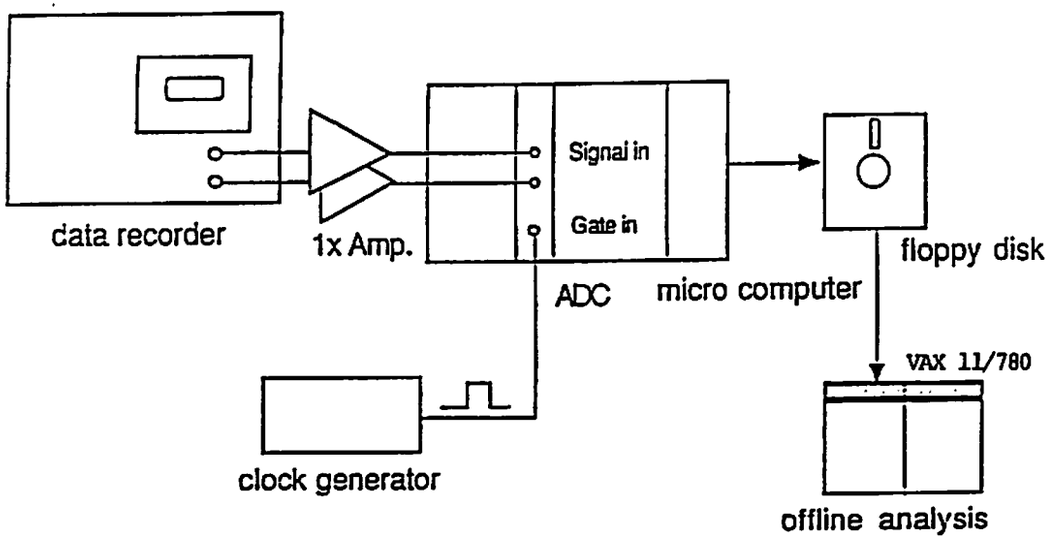
data recorder
1x Amp.
Signal in
Gate in
ADC
micro computer
floppy disk
VAX 11/780
clock generator
offline analysis

Fig. 3.6

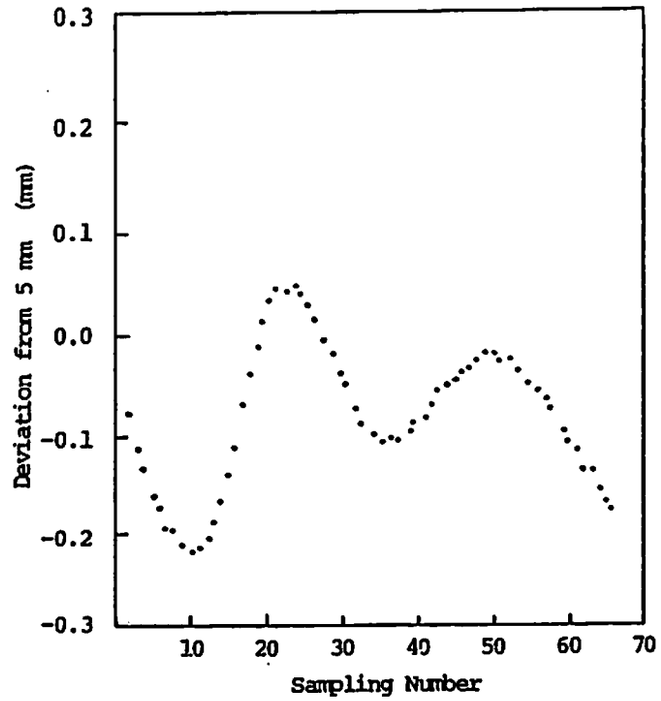
0.3
0.2
0.1
0.0
-0.1
-0.2
-0.3
Deviation from 5 mm (mm)
10
20
30
40
50
60
70
Sampling Number

Fig. 3.7

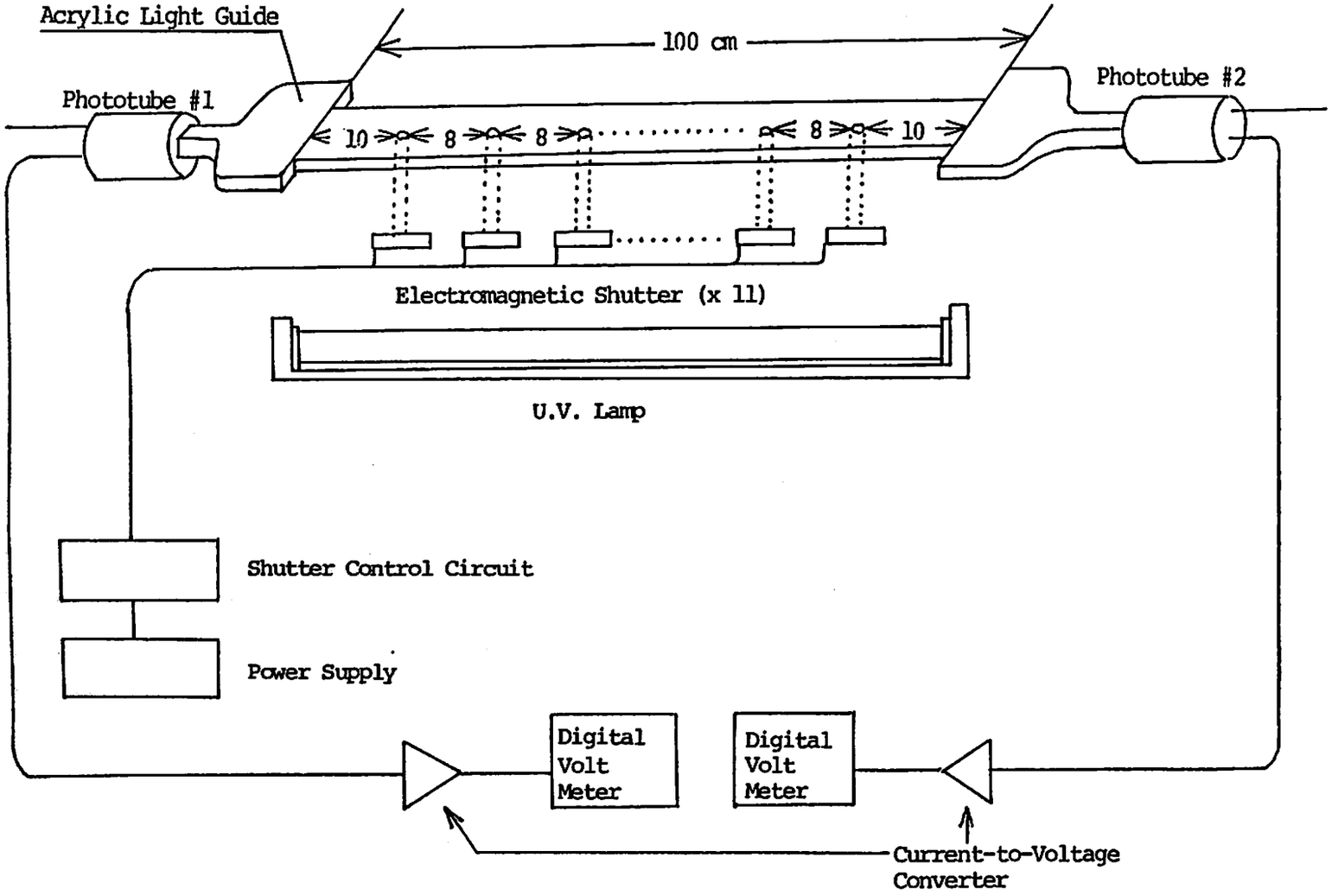
Acrylic Light Guide
100 cm
Phototube #1
Phototube #2
10
8
8
8
10
Electromagnetic Shutter (x 11)
U.V. Lamp
Shutter Control Circuit
Power Supply
Digital Volt Meter
Digital Volt Meter
Current-to-Voltage Converter

Fig. 3.8

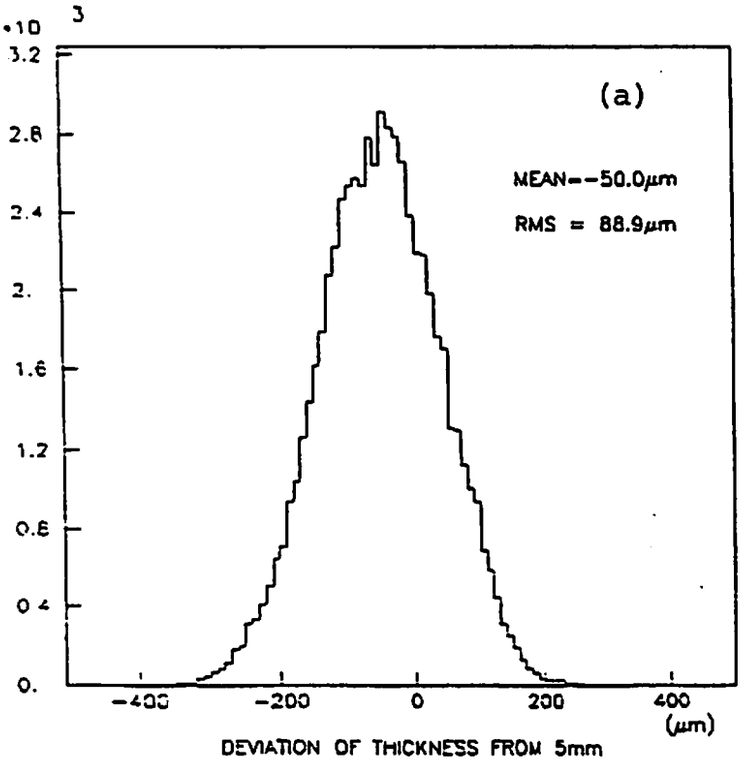
•10 3
3.2
2.8
2.4
2.
1.6
1.2
0.8
0.4
0.
(a)
MEAN=-50.0μm
RMS = 88.9μm
-400
-200
0
200
400
(μm)
DEVIATION OF THICKNESS FROM 5mm

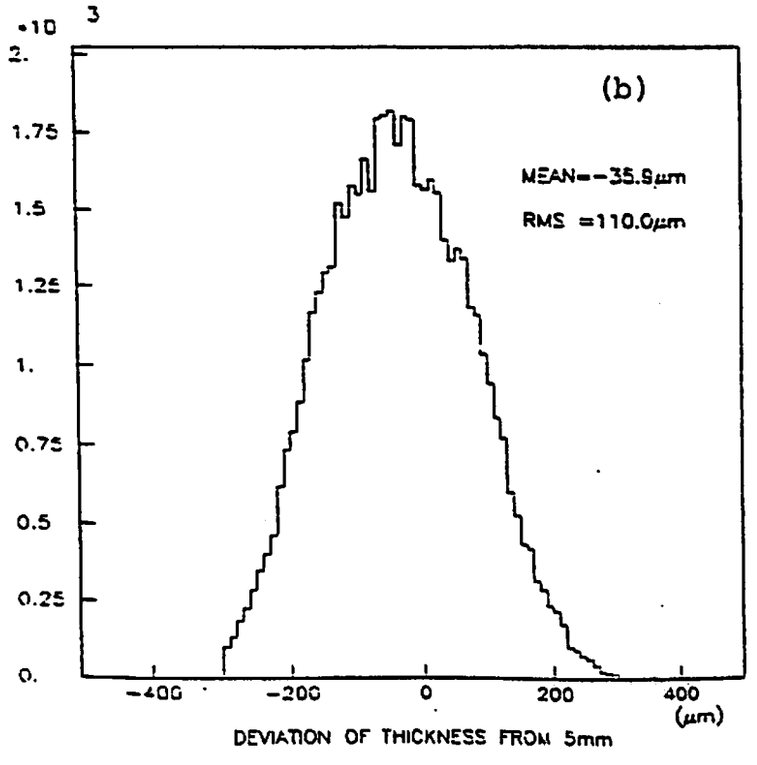
•10 3
2.
1.75
1.5
1.25
1.
0.75
0.5
0.25
0.
(b)
MEAN=-35.9μm
RMS =110.0μm
-400
-200
0
200
400
(μm)
DEVIATION OF THICKNESS FROM 5mm

Fig. 3.9

(a) 1 st Production

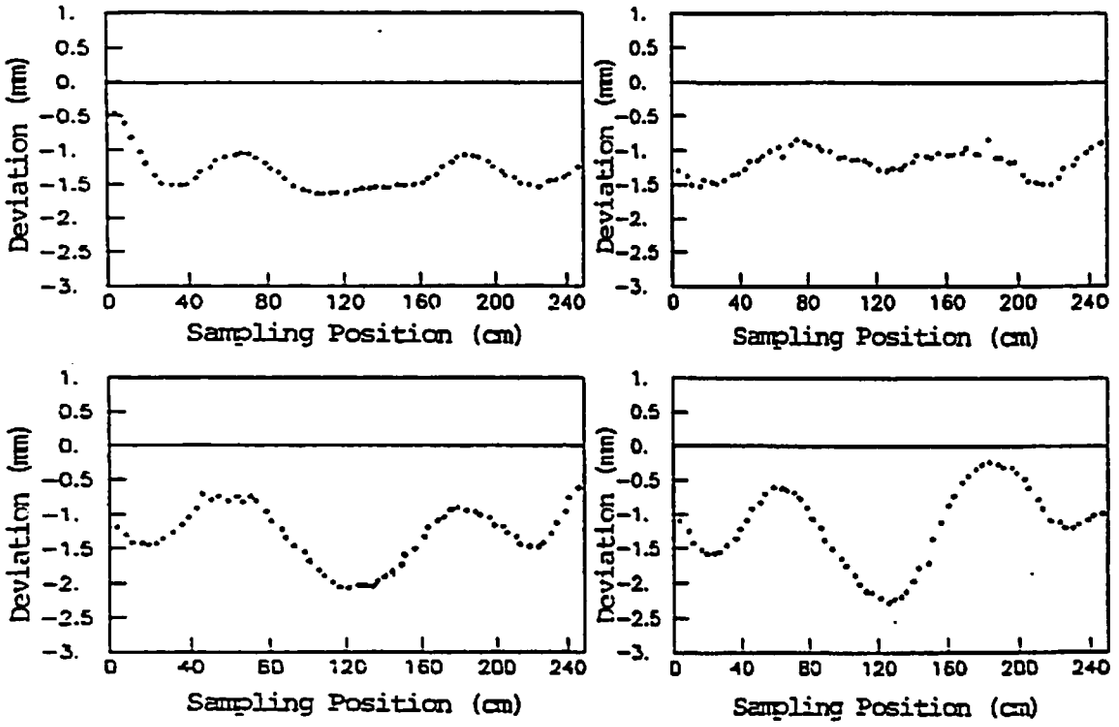

(b) 2 nd Production

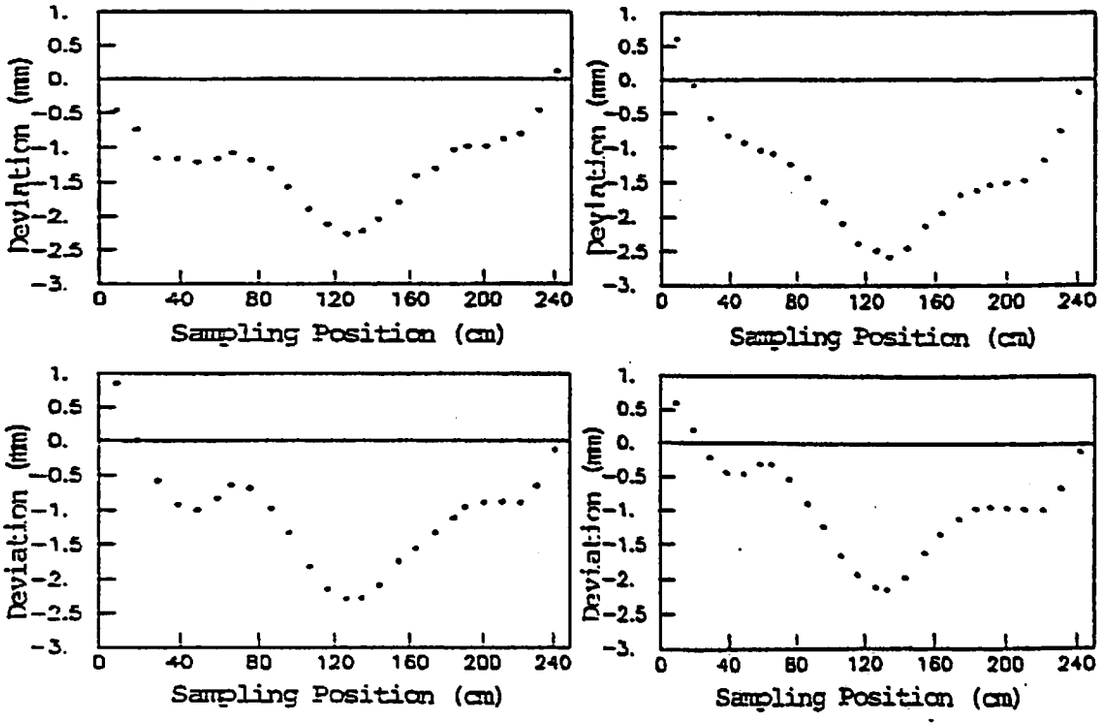

Fig. 3.10

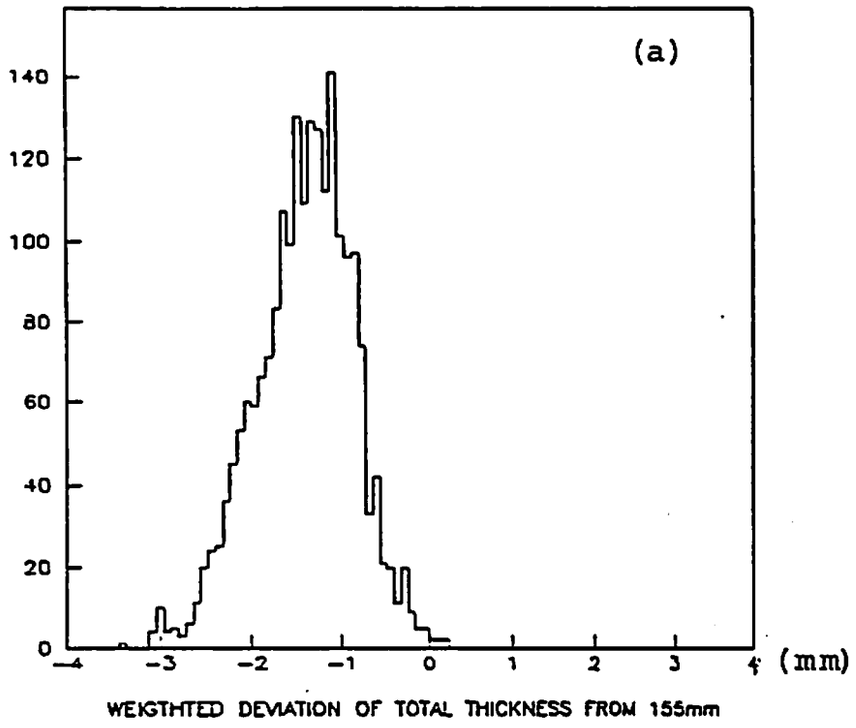
(a)
140
120
100
80
60
40
20
0
−4
−3
−2
−1
0
1
2
3
4
(mm)
WEIGTHTED DEVIATION OF TOTAL THICKNESS FROM 155mm

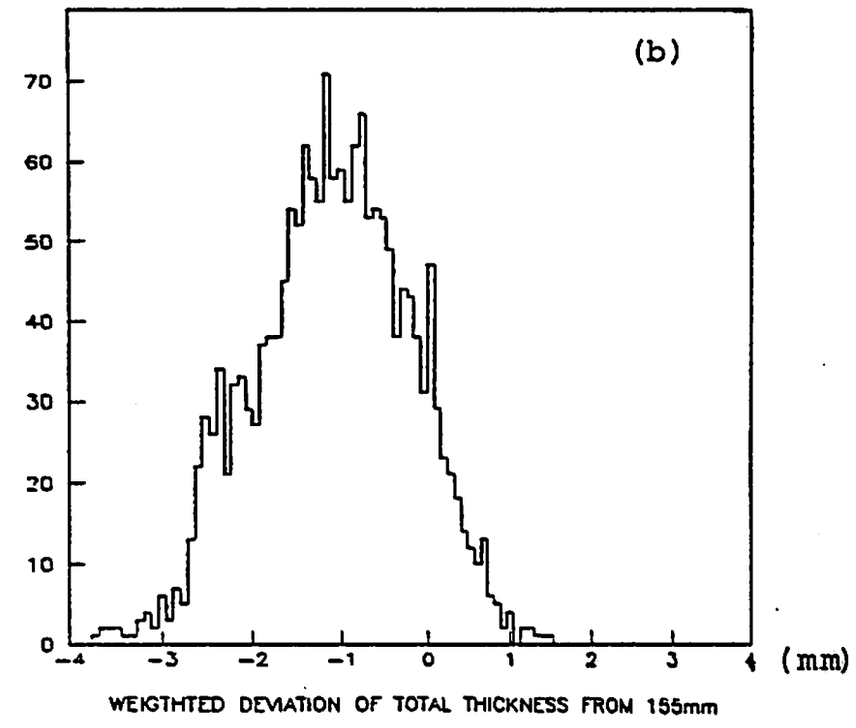
(b)
70
60
50
40
30
20
10
0
−4
−3
−2
−1
0
1
2
3
4
(mm)
WEIGTHTED DEVIATION OF TOTAL THICKNESS FROM 155mm

Fig. 3.11

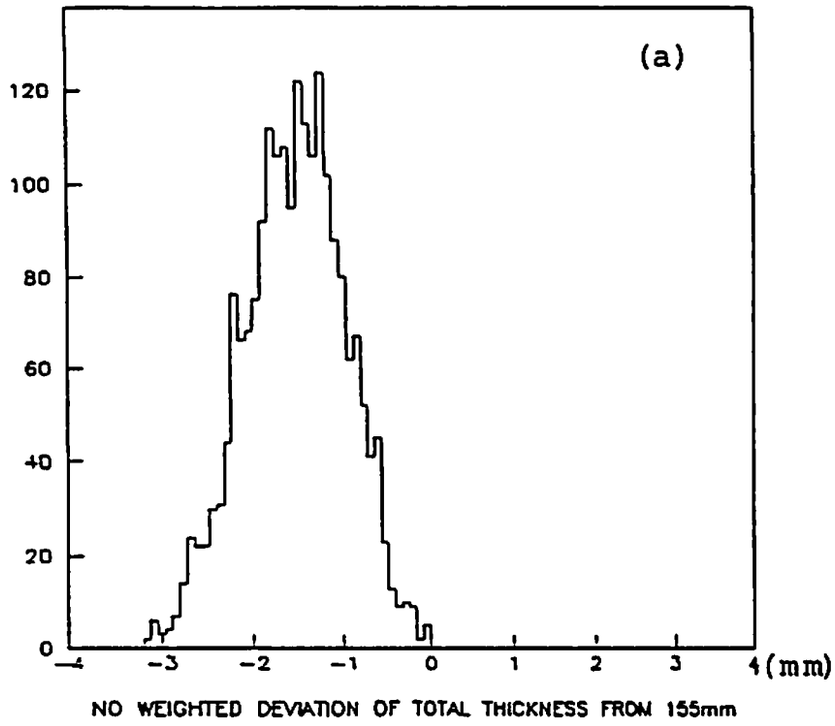

NO WEIGHTED DEVIATION OF TOTAL THICKNESS FROM 155mm

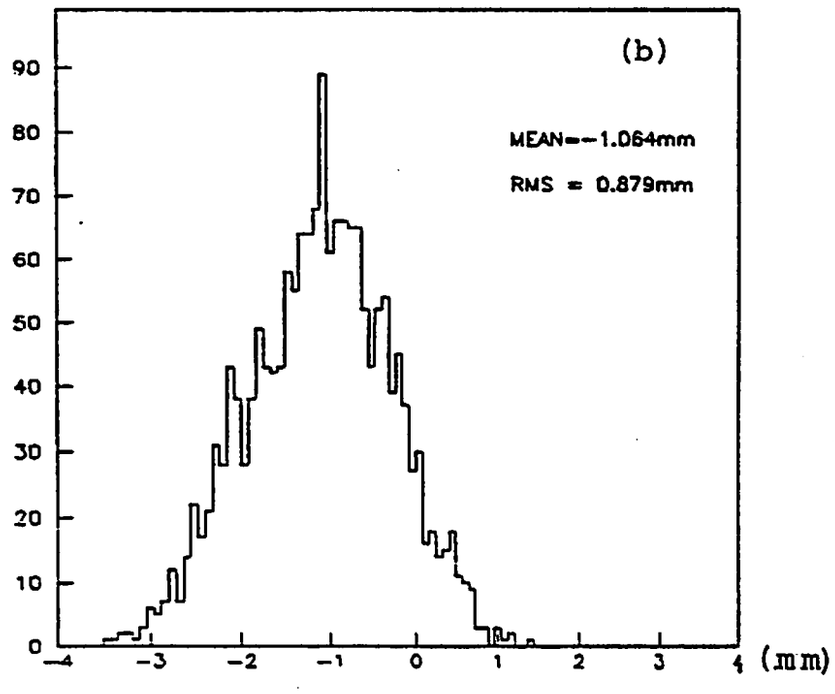

NOWEIGHTED DEVIATION OF TOTAL THICKNESS FROM 155mm

Fig. 3.12

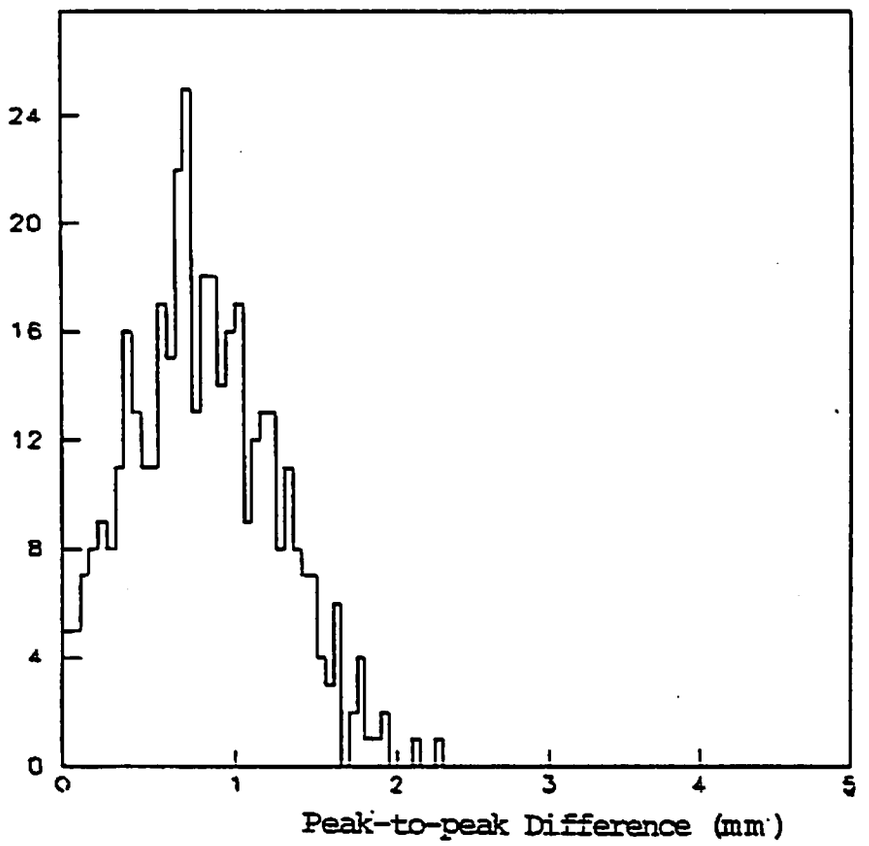

Fig. 3.13

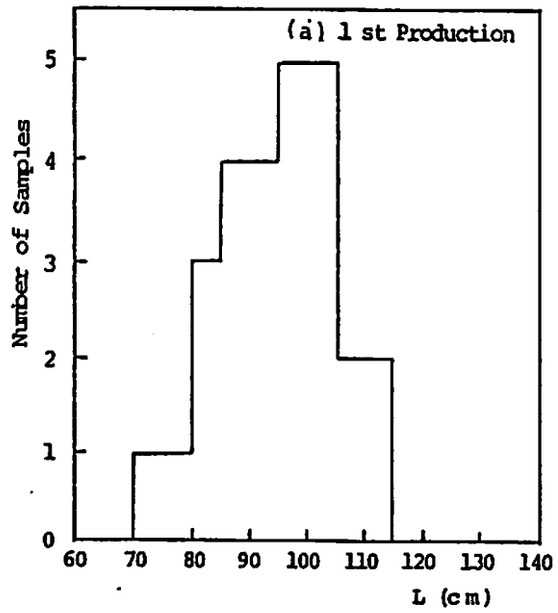
(a) 1 st Production
Number of Samples
0
1
2
3
4
5
60
70
80
90
100
110
120
130
140
L (cm)

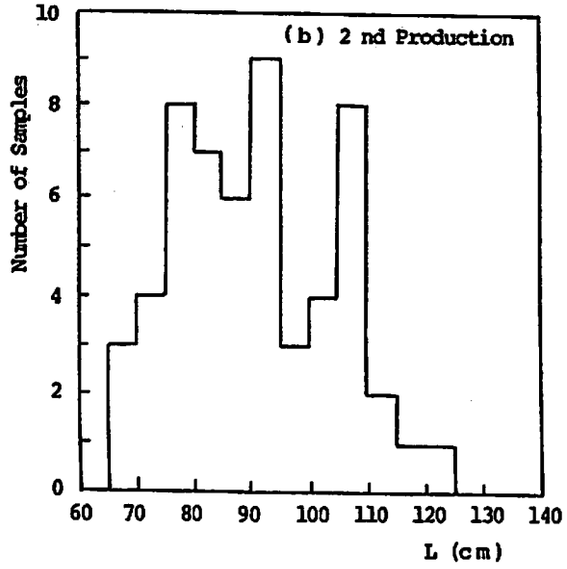
(b) 2 nd Production
Number of Samples
0
2
4
6
8
10
60
70
80
90
100
110
120
130
140
L (cm)

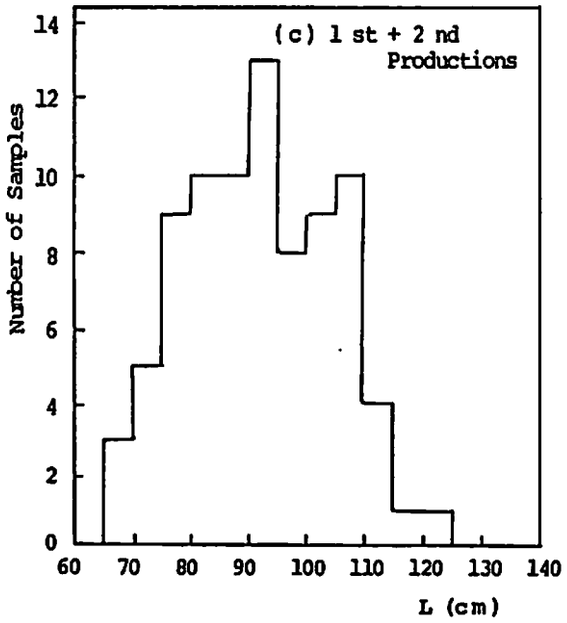
(c) 1 st + 2 nd
Productions
Number of Samples
0
2
4
6
8
10
12
14
60
70
80
90
100
110
120
130
140
L (cm)

Fig. 3.14

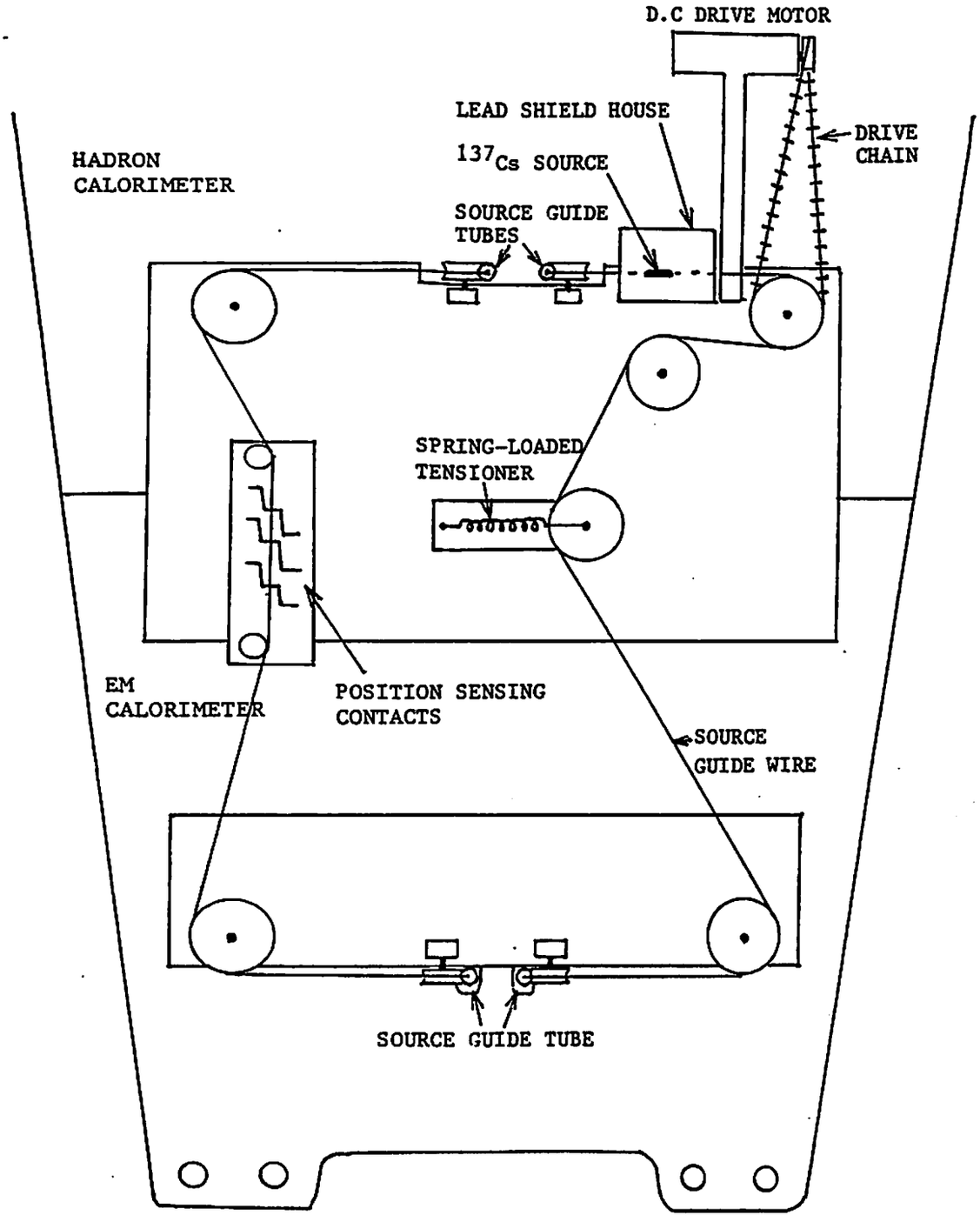

"45° END" of Calorimeter

Fig. 4.1

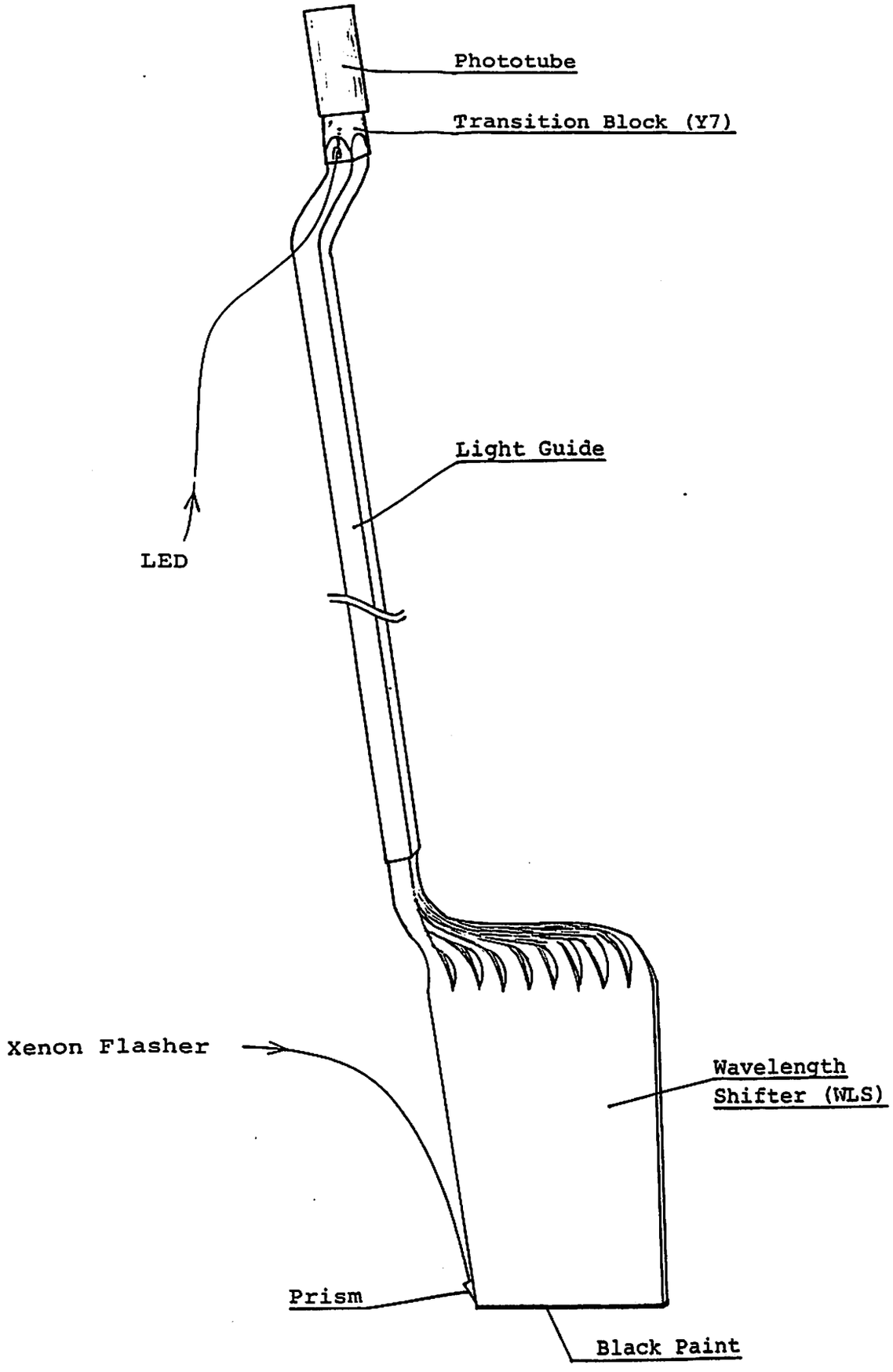
Phototube
Transition Block (Y7)
Light Guide
LED
Xenon Flasher
Wavelength
Shifter (WLS)
Prism
Black Paint

Fig. 4.2

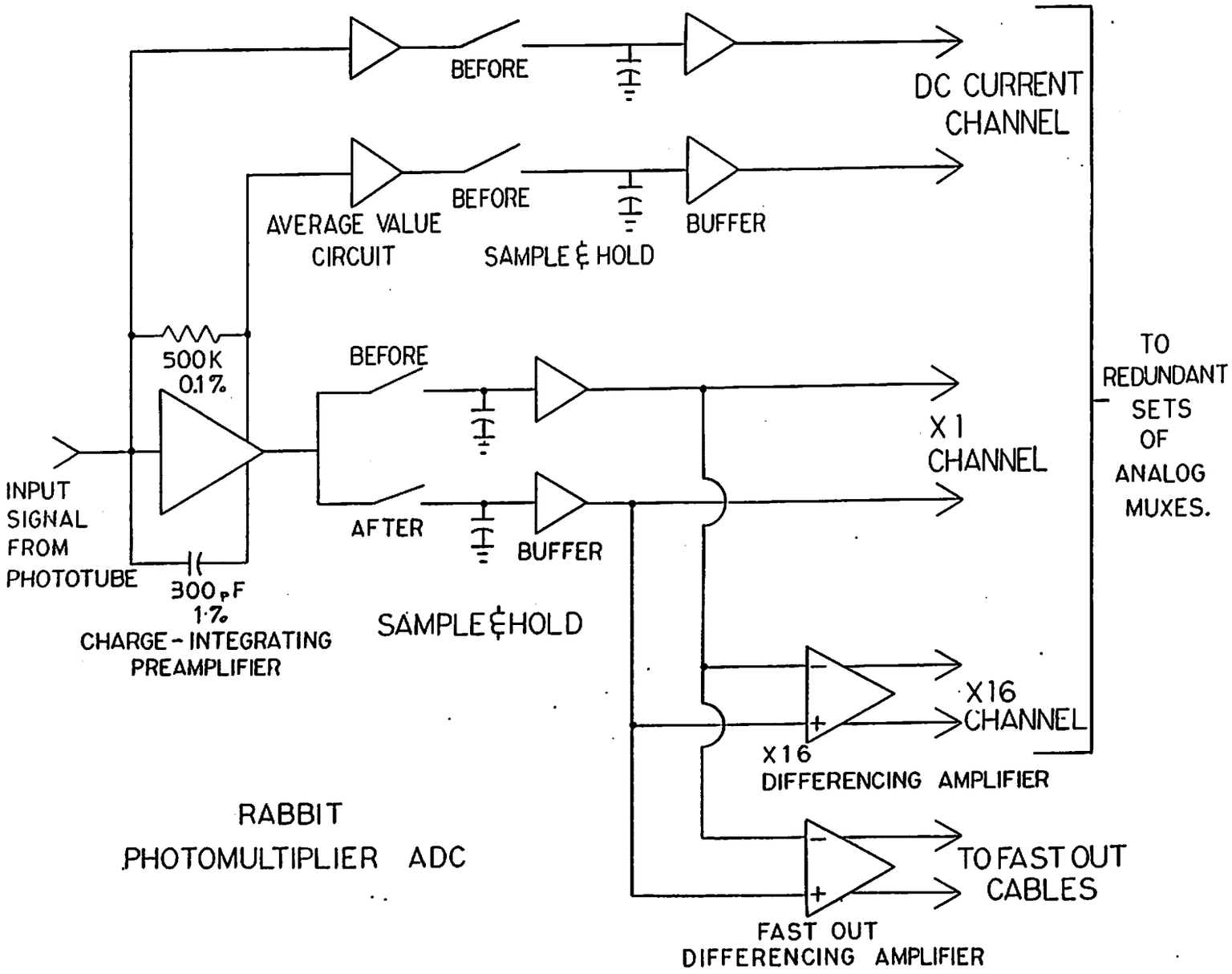
BEFORE
DC CURRENT CHANNEL
AVERAGE VALUE CIRCUIT
BEFORE
SAMPLE & HOLD
BUFFER
500K 0.1%
BEFORE
TO REDUNDANT SETS OF ANALOG MUXES.
X1 CHANNEL
INPUT SIGNAL FROM PHOTOTUBE
AFTER
BUFFER
300 pF 1%
CHARGE-INTEGRATING PREAMPLIFIER
SAMPLE & HOLD
X16 CHANNEL
X16 DIFFERENCING AMPLIFIER
RABBIT PHOTOMULTIPLIER ADC
TO FAST OUT CABLES
FAST OUT DIFFERENCING AMPLIFIER

Fig. 5.1

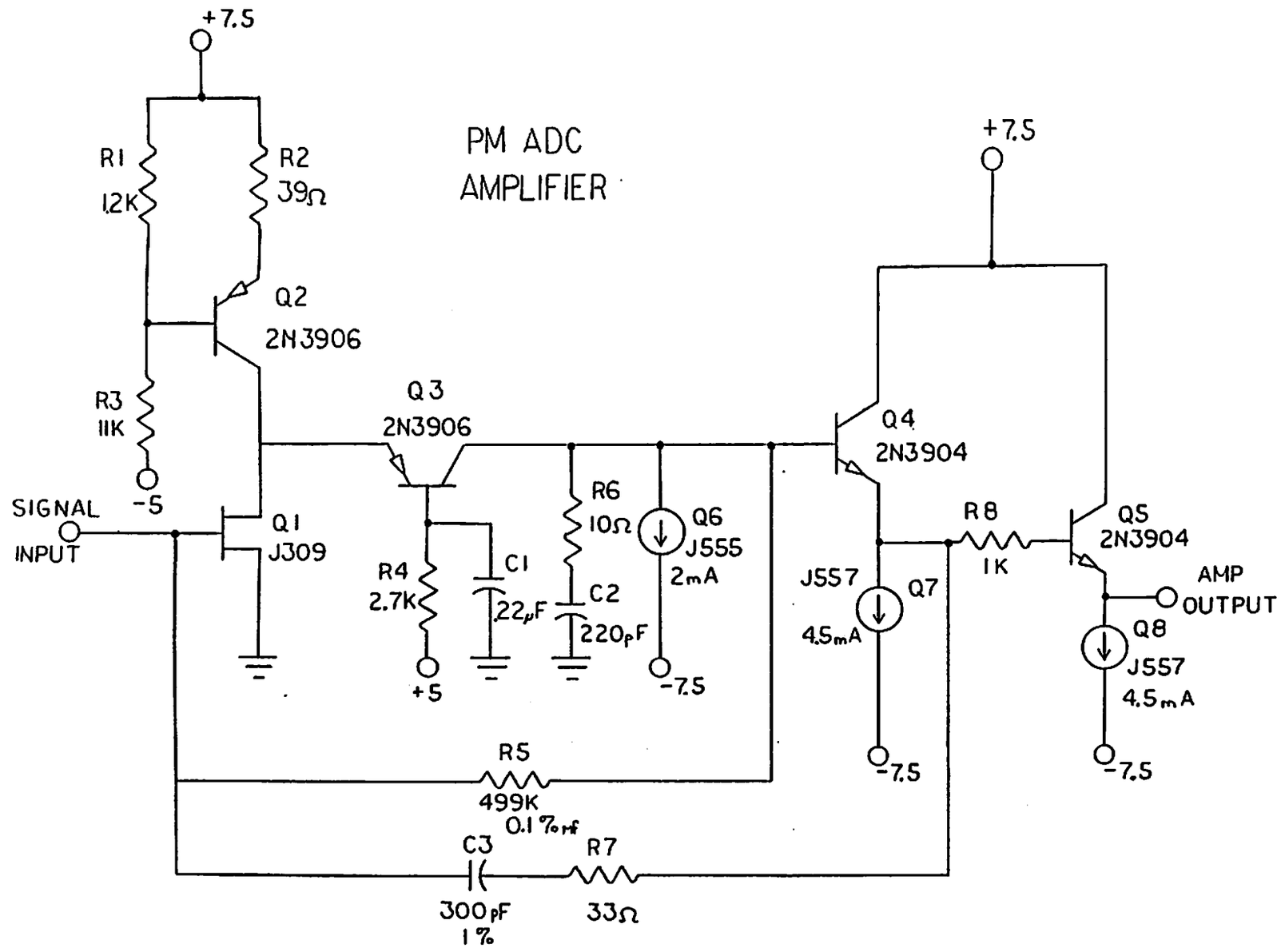
PM ADC
AMPLIFIER
+7.5
R1
1.2K
R2
39Ω
Q2
2N3906
R3
11K
-5
SIGNAL
INPUT
Q1
J309
Q3
2N3906
R4
2.7K
+5
C1
.22μF
R6
10Ω
C2
220pF
Q6
J555
2mA
-7.5
+7.5
Q4
2N3904
R8
1K
Q5
2N3904
AMP
OUTPUT
J557
Q7
4.5mA
-7.5
Q8
J557
4.5mA
-7.5
R5
499K
0.1% mf
C3
300pF
1%
R7
33Ω

Fig. 5.2

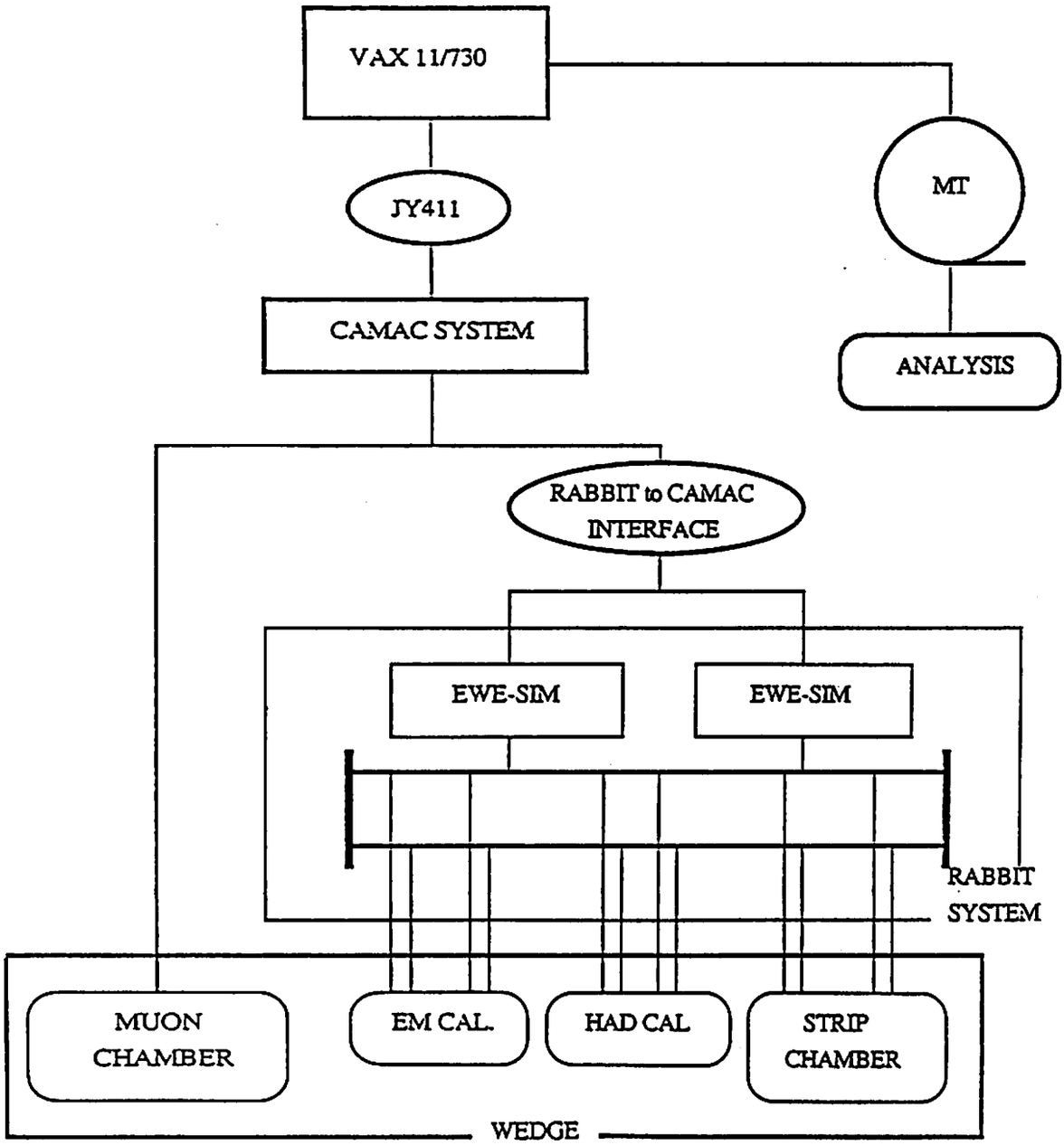
VAX 11/730
MT
JY411
CAMAC SYSTEM
ANALYSIS
RABBIT to CAMAC
INTERFACE
EWE-SIM
EWE-SIM
RABBIT
SYSTEM
MUON
CHAMBER
EM CAL.
HAD CAL
STRIP
CHAMBER
WEDGE

Fig. 6.1

NW Test Beam

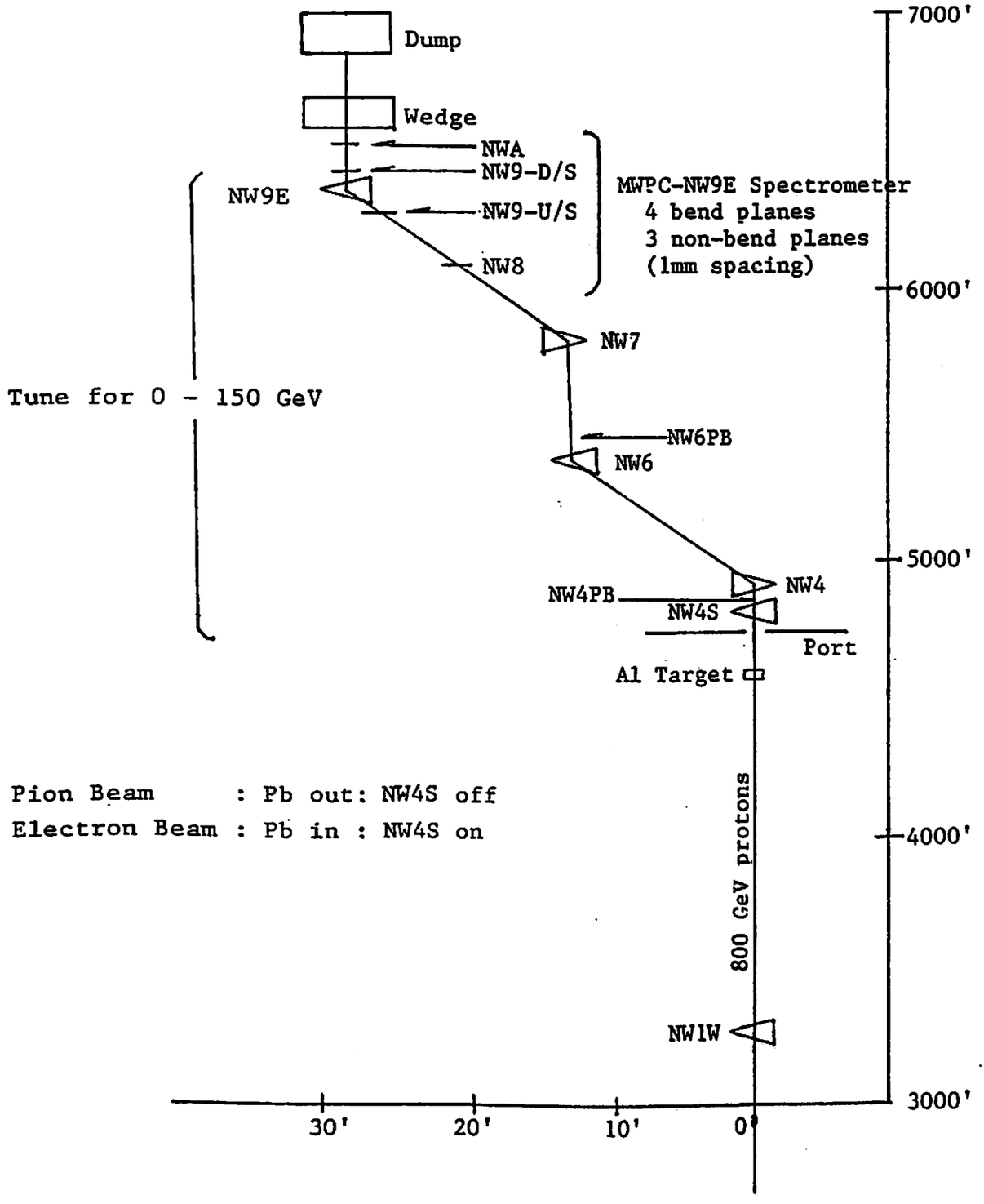

Fig. 6.2

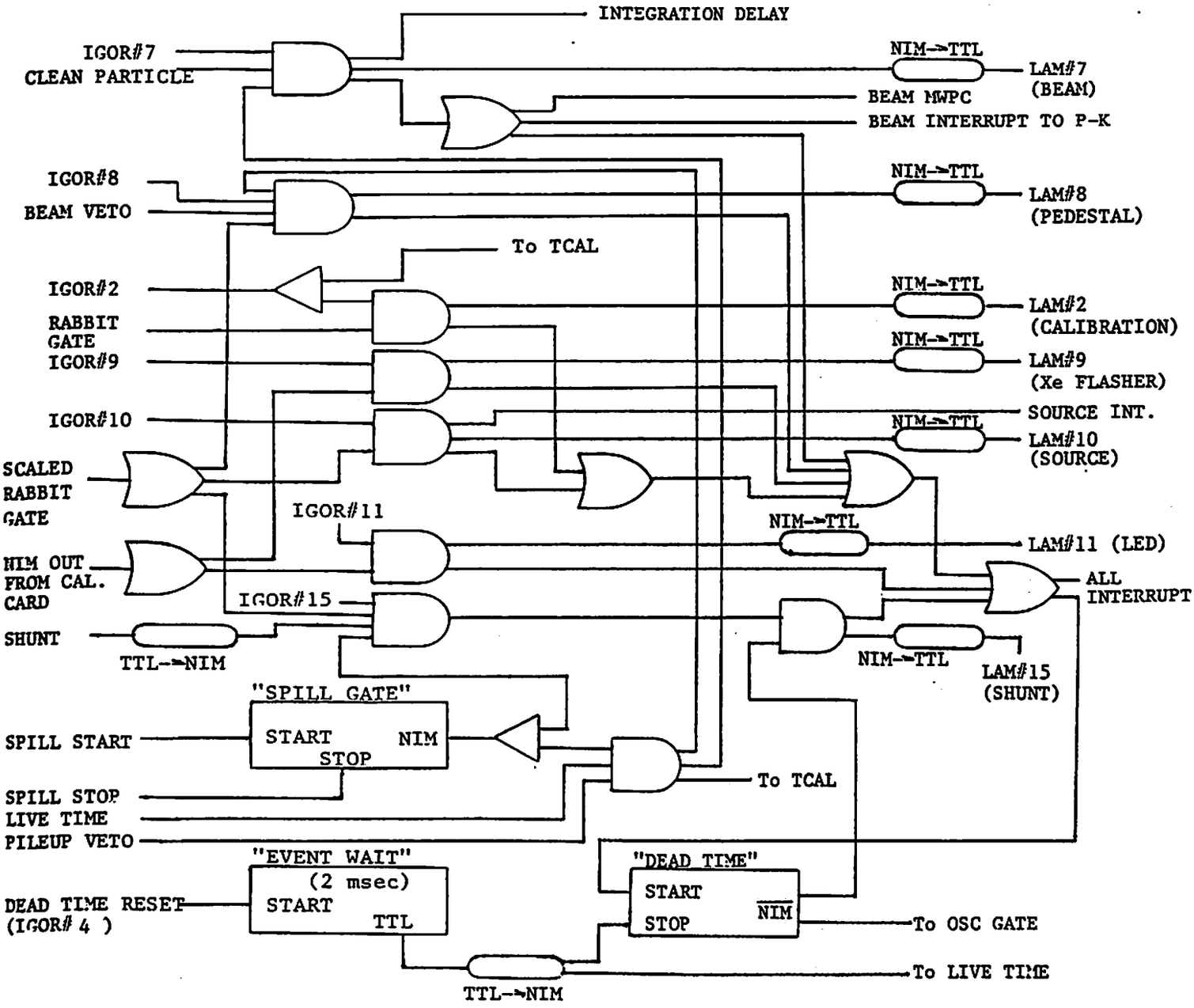
INTEGRATION DELAY
IGOR#7
CLEAN PARTICLE
NIM→TTL
LAM#7
(BEAM)
BEAM MWPC
BEAM INTERRUPT TO P-K
IGOR#8
BEAM VETO
NIM→TTL
LAM#8
(PEDESTAL)
To TCAL
IGOR#2
RABBIT
GATE
IGOR#9
IGOR#10
NIM→TTL
LAM#2
(CALIBRATION)
NIM→TTL
LAM#9
(Xe FLASHER)
SOURCE INT.
NIM→TTL
LAM#10
(SOURCE)
SCALED
RABBIT
GATE
IGOR#11
NIM→TTL
LAM#11 (LED)
NIM OUT
FROM CAL.
CARD
ALL
INTERRUPT
IGOR#15
SHUNT
TTL→NIM
NIM→TTL
LAM#15
(SHUNT)
"SPILL GATE"
SPILL START
START
NIM
STOP
SPILL STOP
LIVE TIME
PILEUP VETO
To TCAL
"EVENT WAIT"
(2 msec)
DEAD TIME RESET
(IGOR# 4)
START
TTL
"DEAD TIME"
START
STOP
NIM
To OSC GATE
TTL→NIM
To LIVE TIME

Fig. 6.3

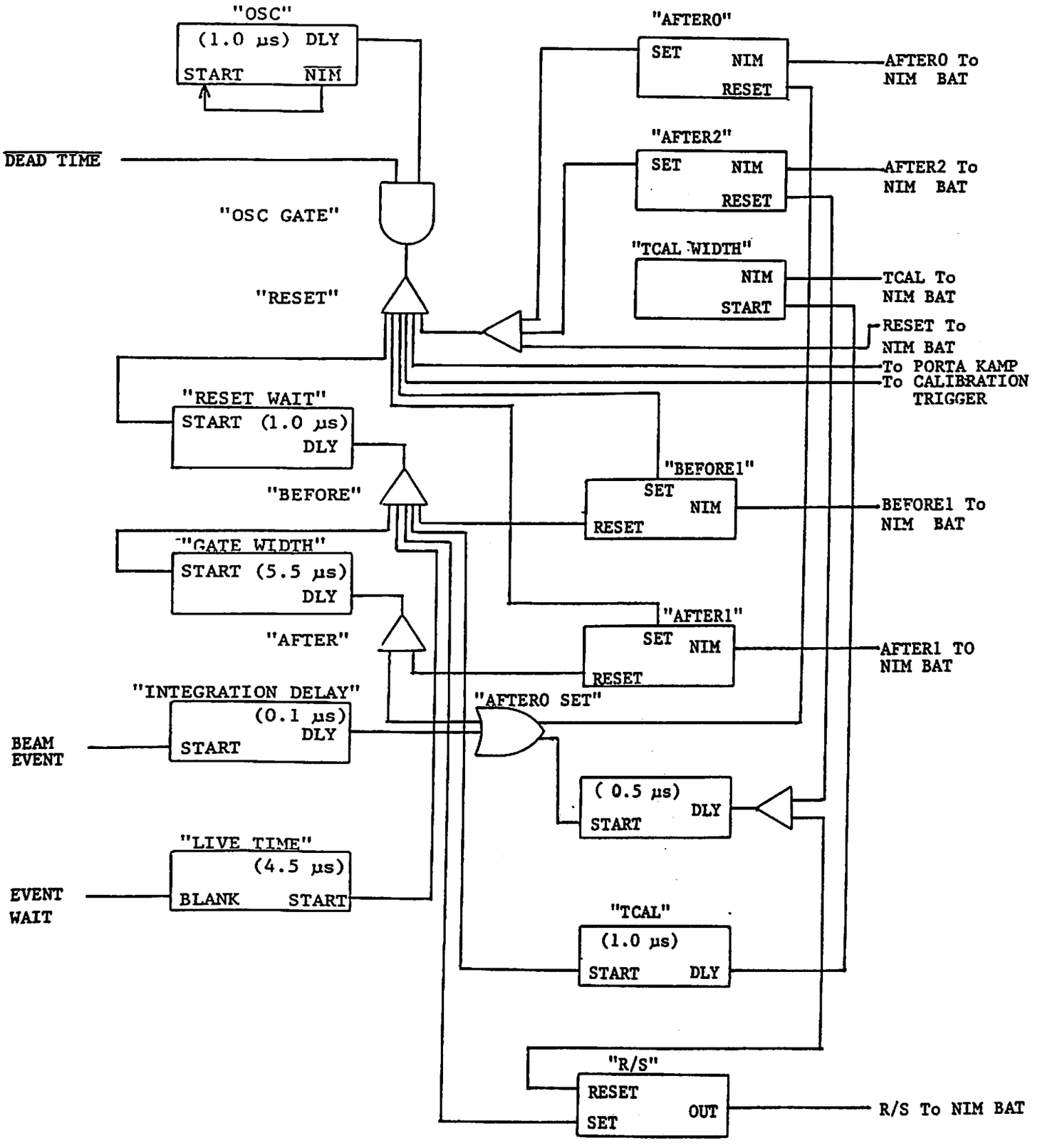
"OSC"
(1.0 μs) DLY
START
NIM
DEAD TIME
"OSC GATE"
"RESET"
"AFTER0"
SET
NIM
RESET
AFTER0 To
NIM BAT
"AFTER2"
SET
NIM
RESET
AFTER2 To
NIM BAT
"TCAL WIDTH"
NIM
START
TCAL To
NIM BAT
RESET To
NIM BAT
To PORTA KAMP
To CALIBRATION
TRIGGER
"RESET WAIT"
START (1.0 μs)
DLY
"BEFORE"
"BEFORE1"
SET
NIM
RESET
BEFORE1 To
NIM BAT
"GATE WIDTH"
START (5.5 μs)
DLY
"AFTER"
"AFTER1"
SET
NIM
RESET
AFTER1 TO
NIM BAT
"INTEGRATION DELAY"
(0.1 μs)
DLY
START
BEAM
EVENT
"AFTER0 SET"
(0.5 μs)
DLY
START
"LIVE TIME"
(4.5 μs)
BLANK
START
EVENT
WAIT
"TCAL"
(1.0 μs)
START
DLY
"R/S"
RESET
SET
OUT
R/S To NIM BAT

Fig. 6.4

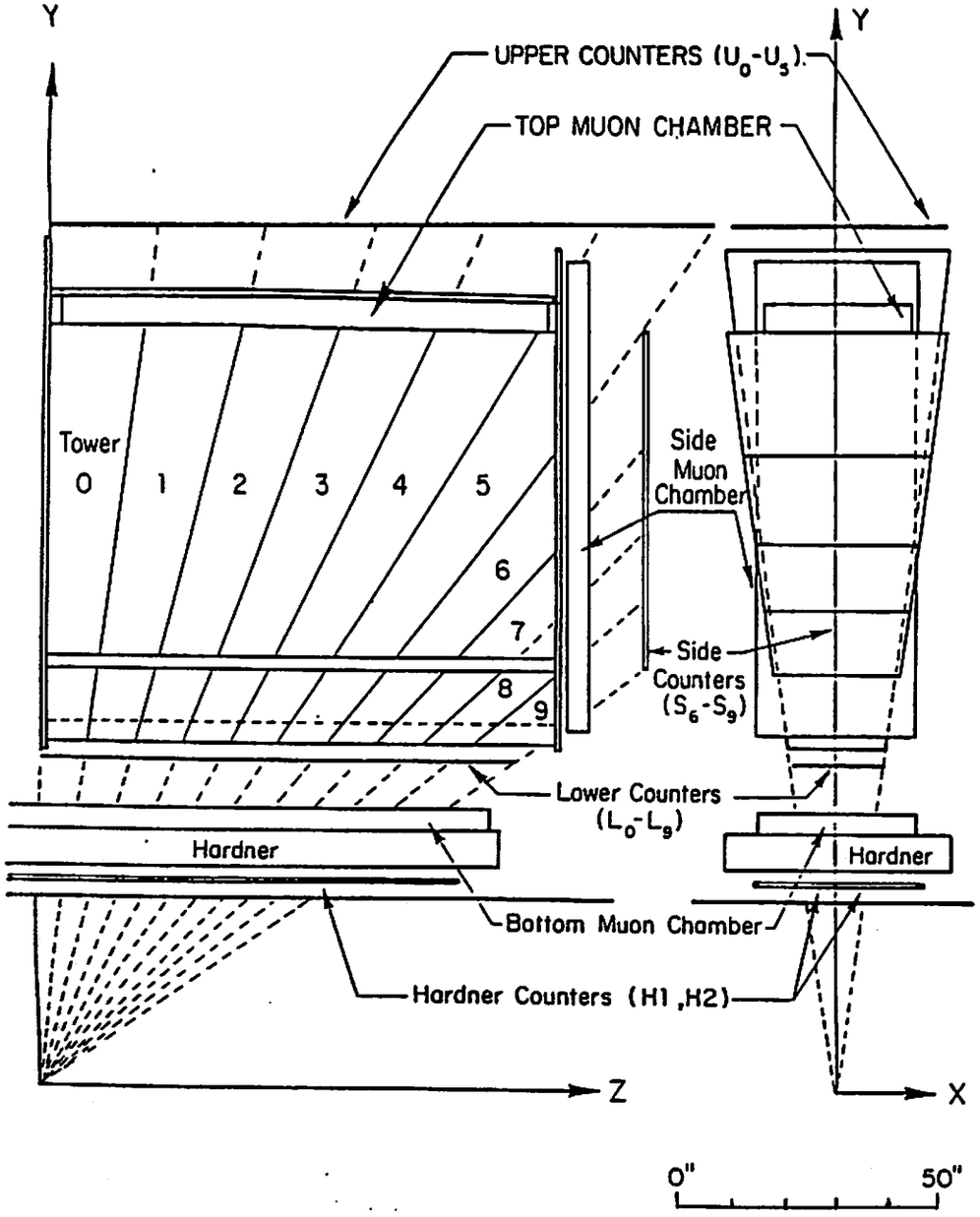
Y
Y
UPPER COUNTERS (U_0-U_5)
TOP MUON CHAMBER
Tower
0
1
2
3
4
5
6
7
8
9
Side
Muon
Chamber
Side
Counters
(S_6-S_9)
Lower Counters
(L_0-L_9)
Hardner
Hardner
Bottom Muon Chamber
Hardner Counters (H1 ,H2)
Z
X
0"
50"

Fig. 6.5

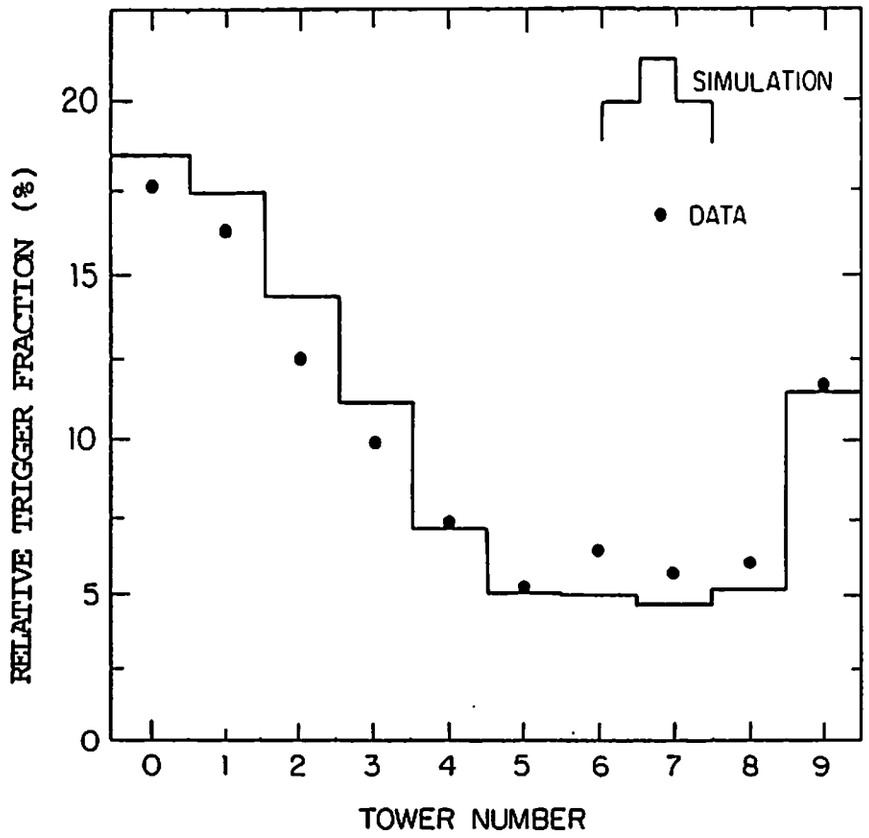
SIMULATION
DATA
RELATIVE TRIGGER FRACTION (%)
TOWER NUMBER
0
5
10
15
20
0
1
2
3
4
5
6
7
8
9

Fig. 6.6

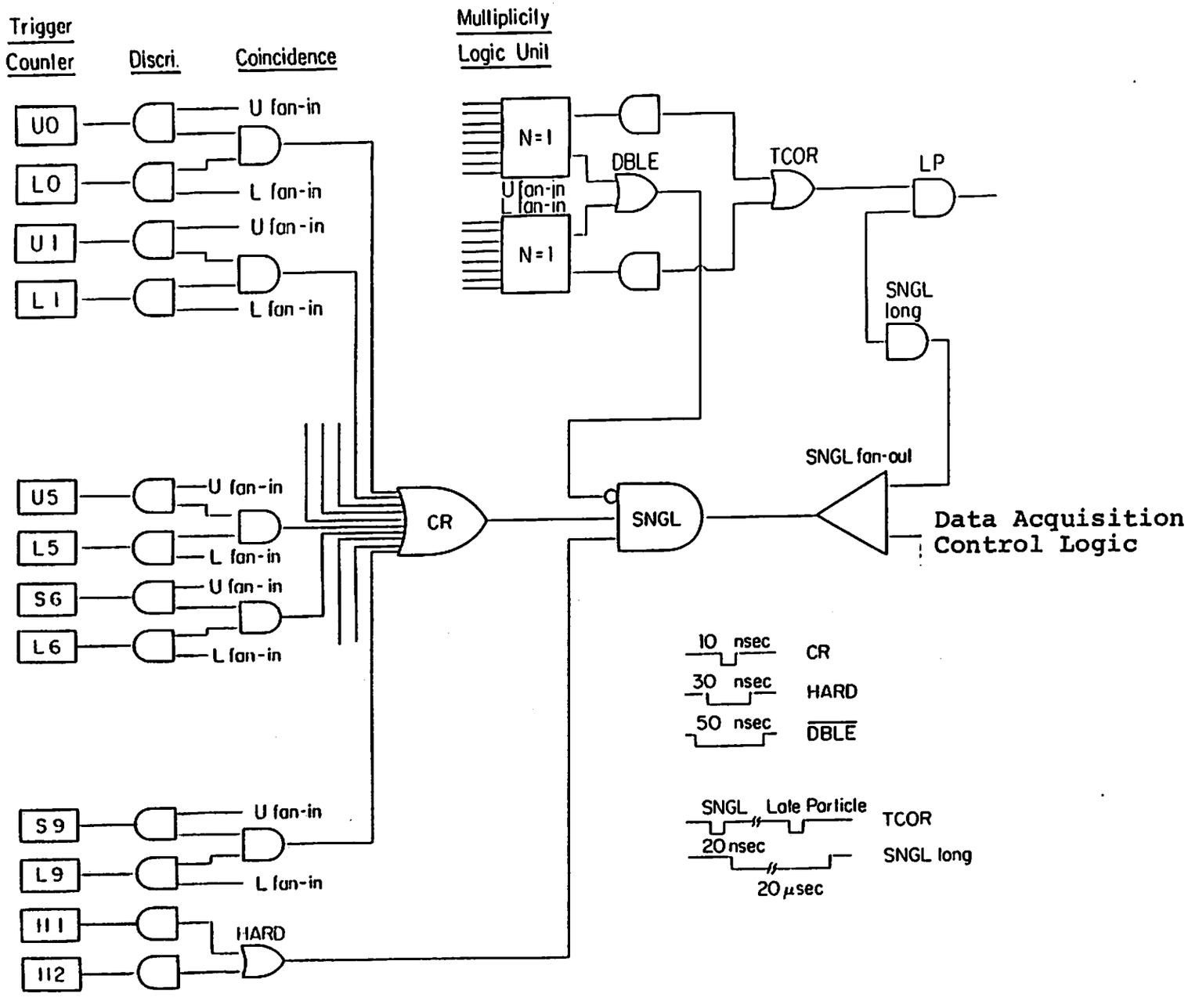
Trigger
Counter
Discri.
Coincidence
Multiplicity
Logic Unit
U0
L0
U1
L1
U fan-in
L fan-in
U fan-in
L fan-in
N=1
N=1
U fan-in
L fan-in
DBLE
TCOR
LP
SNGL
long
SNGL fan-out
U5
L5
S6
L6
U fan-in
L fan-in
U fan-in
L fan-in
CR
SNGL
Data Acquisition
Control Logic
S9
L9
H1
H2
U fan-in
L fan-in
HARD
10 nsec
CR
30 nsec
HARD
50 nsec
DBLE
SNGL
Late Particle
TCOR
20 nsec
SNGL long
20 μsec

Fig. 6.7

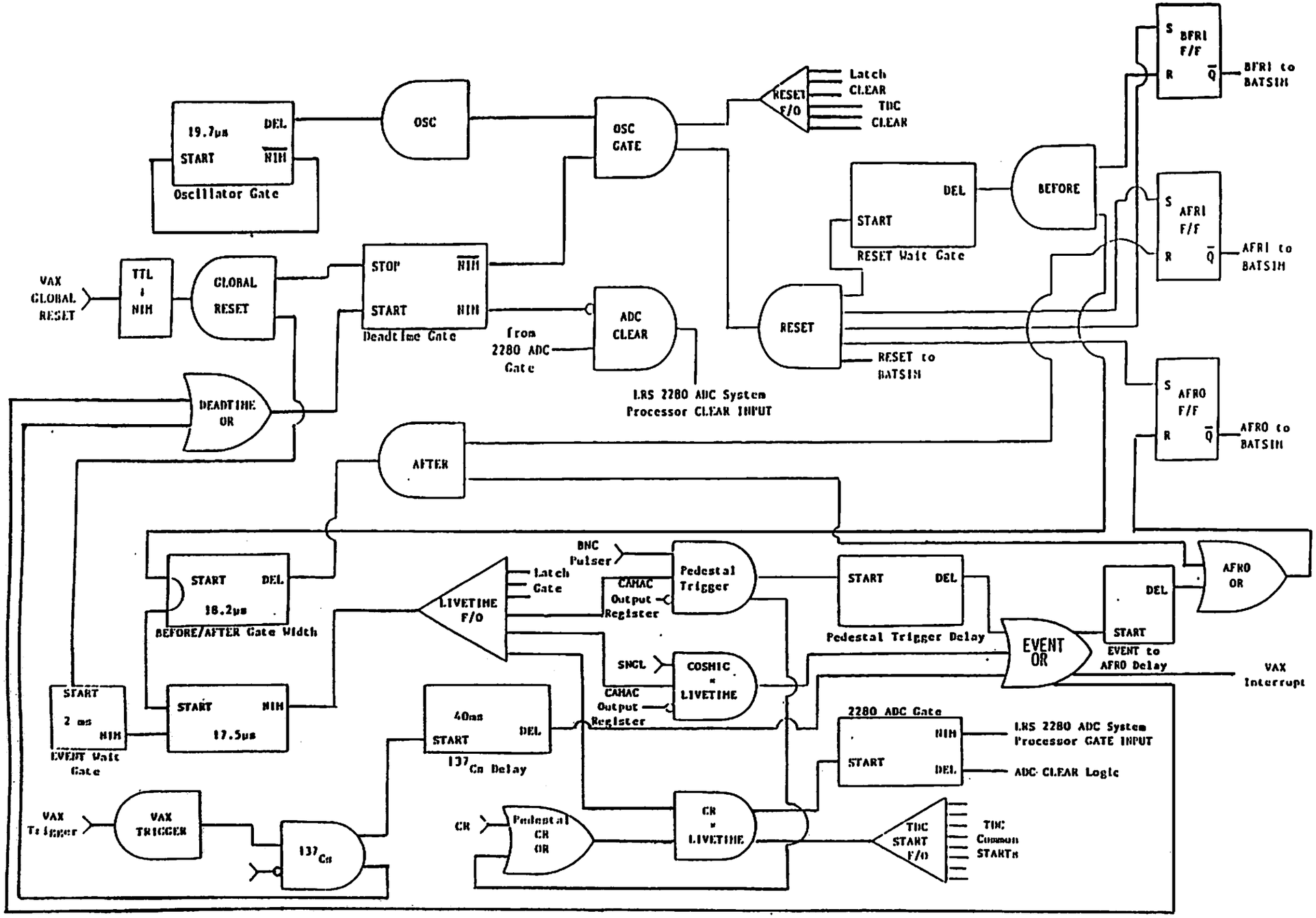
19.7μs
DEL
START
NIM
Oscillator Gate
OSC
OSC GATE
RESET F/O
Latch CLEAR
TDC CLEAR
S
BFRI F/F
R
Q
BFRI to BATSIM
DEL
START
RESET Wait Gate
BEFORE
S
AFRI F/F
R
Q
AFRI to BATSIM
VAX GLOBAL RESET
TTL → NIM
GLOBAL RESET
STOP
NIM
START
NIM
Deadtime Gate
from 2280 ADC Gate
ADC CLEAR
LRS 2280 ADC System Processor CLEAR INPUT
RESET
RESET to BATSIM
S
AFRO F/F
R
Q
AFRO to BATSIM
DEADTIME OR
AFTER
START
DEL
18.2μs
BEFORE/AFTER Gate Width
BNC Pulser
Latch Gate
CAMAC Output Register
LIVETIME F/O
Pedestal Trigger
START
DEL
Pedestal Trigger Delay
DEL
START
EVENT to AFRO Delay
AFRO OR
EVENT OR
VAX Interrupt
START
2 ms
NIM
EVENT Wait Gate
START
NIM
17.5μs
40ms
START
DEL
137Cs Delay
SNGL
CAMAC Output Register
COSMIC * LIVETIME
2280 ADC Gate
NIM
START
DEL
LRS 2280 ADC System Processor GATE INPUT
ADC CLEAR Logic
VAX Trigger
VAX TRIGGER
137Cs
CR
Pedestal CR OR
CR * LIVETIME
TDC START F/O
TDC Common STARTs

Fig. 6.8

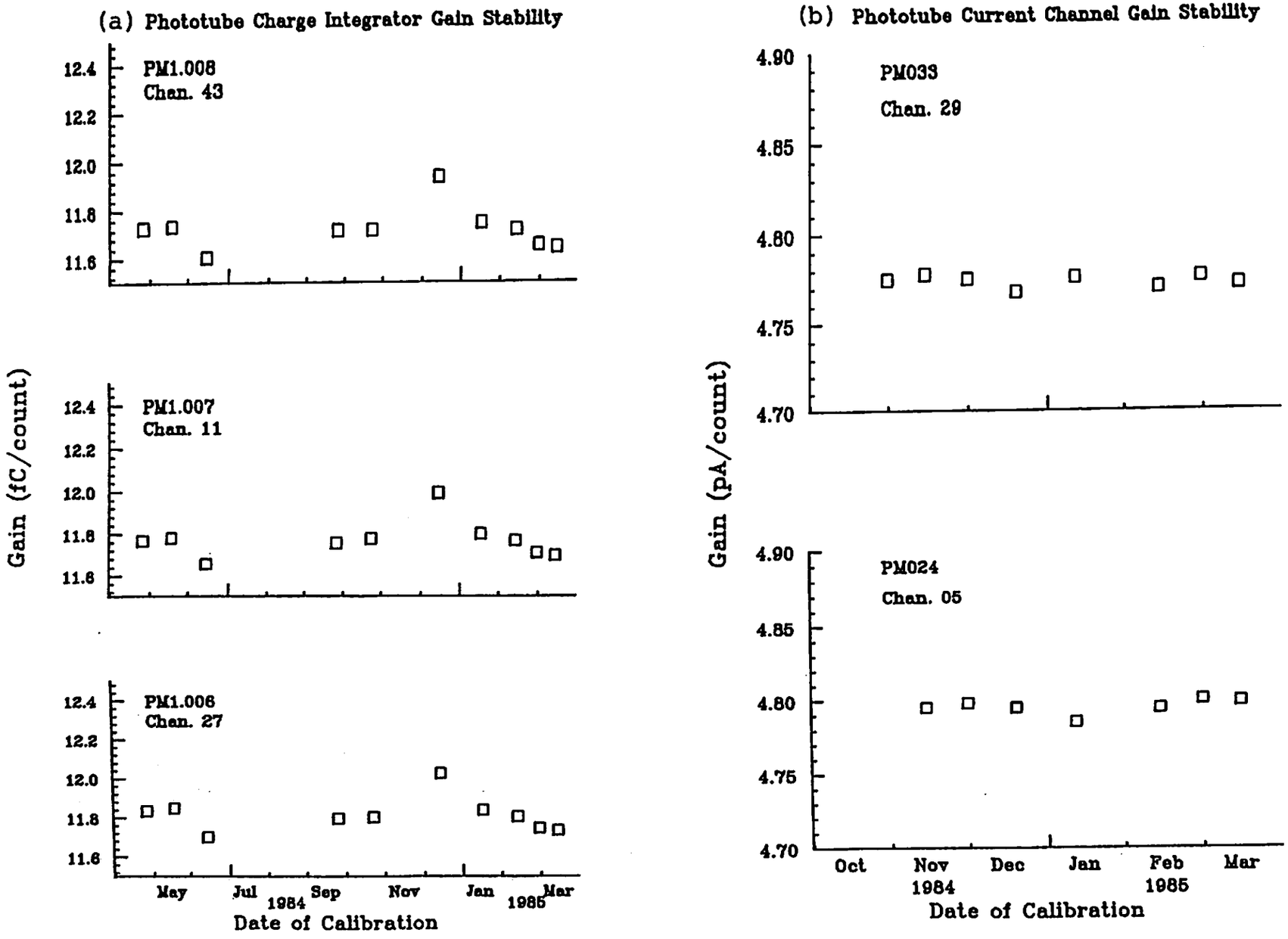
(a) Phototube Charge Integrator Gain Stability
PM1.008
Chan. 43
PM1.007
Chan. 11
PM1.006
Chan. 27
12.4
12.2
12.0
11.8
11.6
Gain (fC/count)
May
Jul
Sep
Nov
Jan
Mar
1984
1985
Date of Calibration
(b) Phototube Current Channel Gain Stability
PM033
Chan. 29
PM024
Chan. 05
4.90
4.85
4.80
4.75
4.70
Gain (pA/count)
Oct
Nov
Dec
Jan
Feb
Mar
1984
1985
Date of Calibration

Fig. 6.9

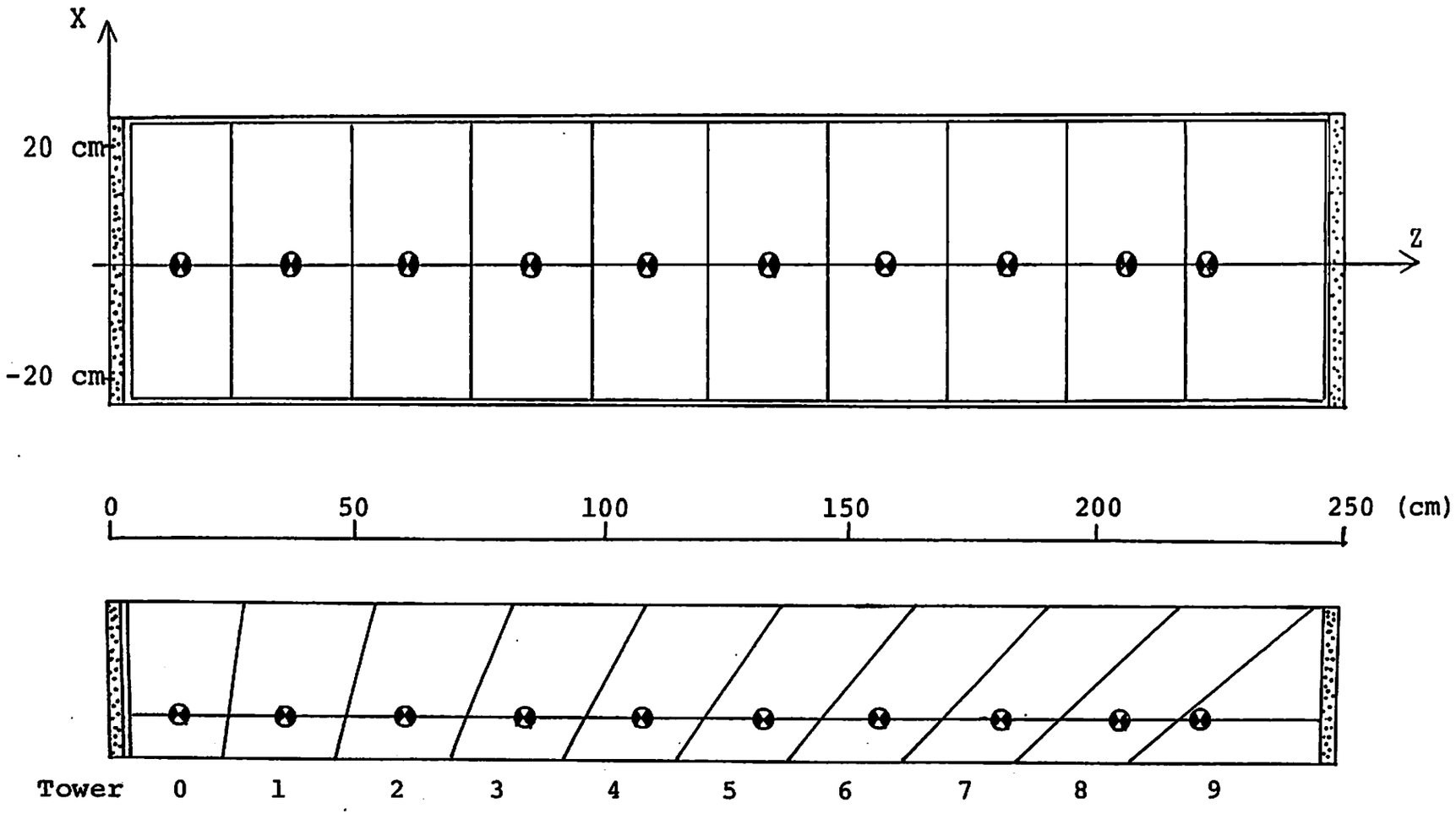

Reference Points on Strip Chamber

Fig. 6.10

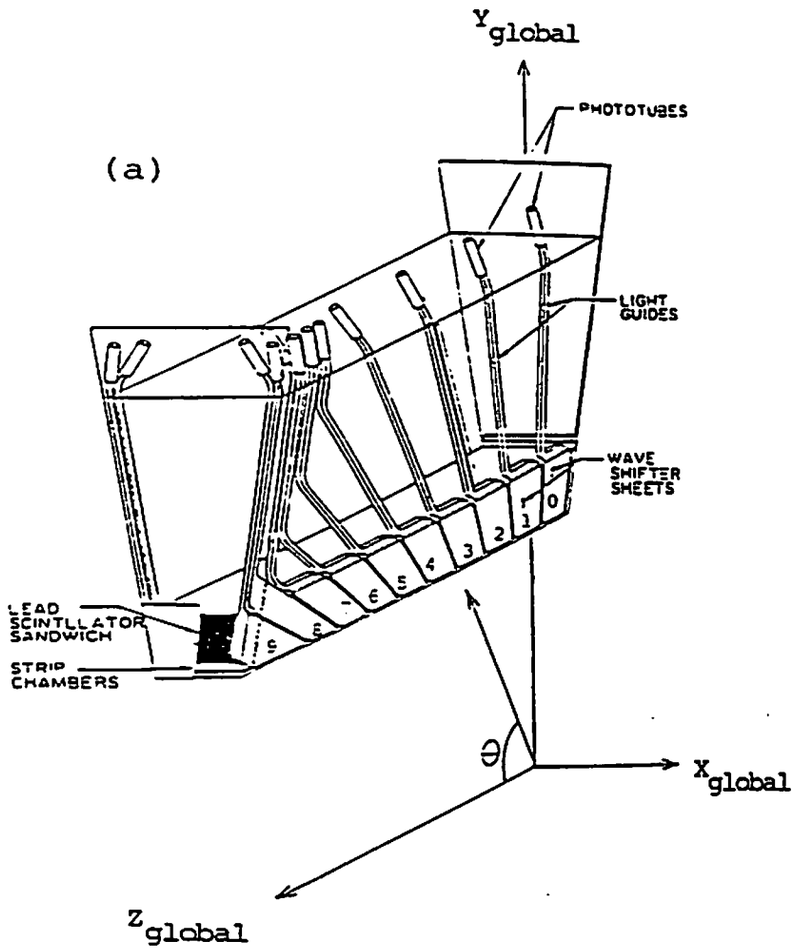
(a)
Y global
PHOTOTUBES
LIGHT GUIDES
WAVE SHIFTER SHEETS
LEAD SCINTILLATOR SANDWICH
STRIP CHAMBERS
θ
X global
Z global

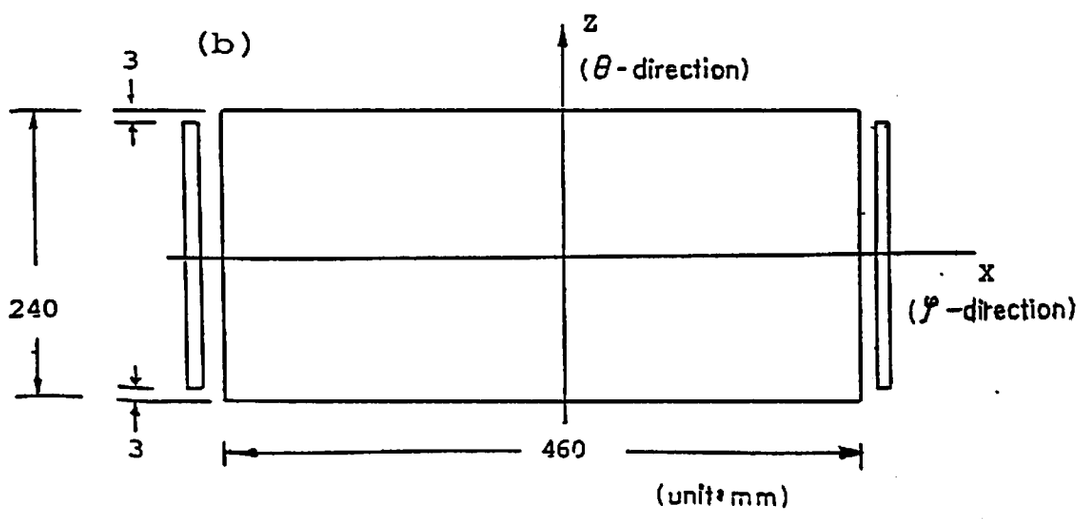
(b)
Z
(θ - direction)
3
240
3
460
X
(φ -direction)
(unit: mm)

Fig. 6.11

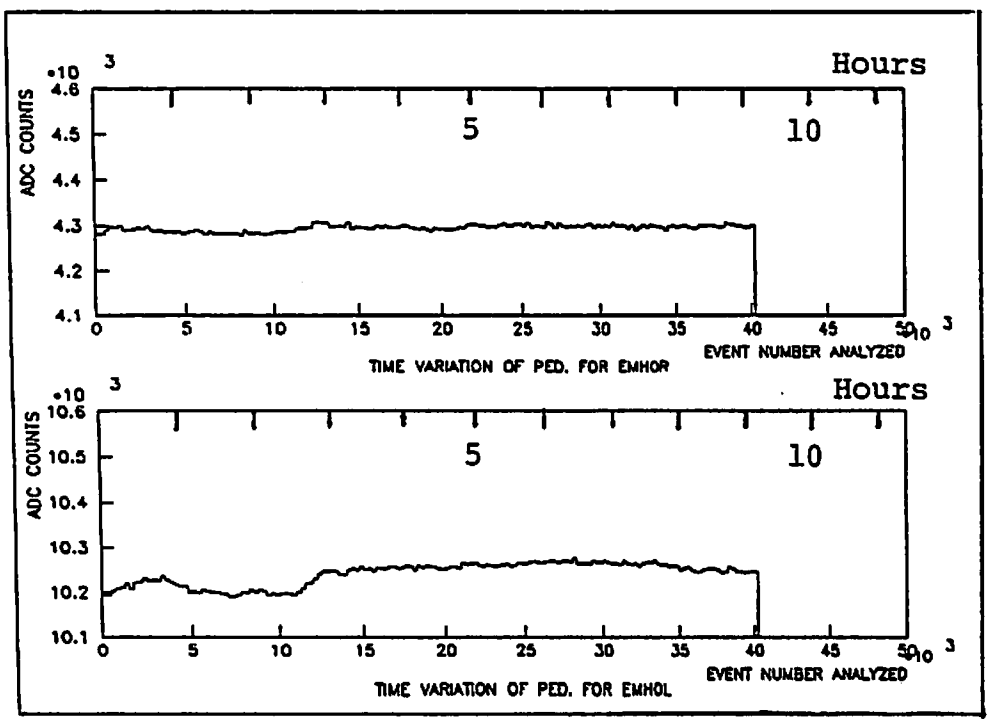
Hours
ADC COUNTS
•10 3
4.6
4.5
4.4
4.3
4.2
4.1
5
10
0 5 10 15 20 25 30 35 40 45 50
•10 3
EVENT NUMBER ANALYZED
TIME VARIATION OF PED. FOR EMHOR
Hours
ADC COUNTS
•10 3
10.6
10.5
10.4
10.3
10.2
10.1
5
10
0 5 10 15 20 25 30 35 40 45 50
•10 3
EVENT NUMBER ANALYZED
TIME VARIATION OF PED. FOR EMHOL

Fig. 6.12

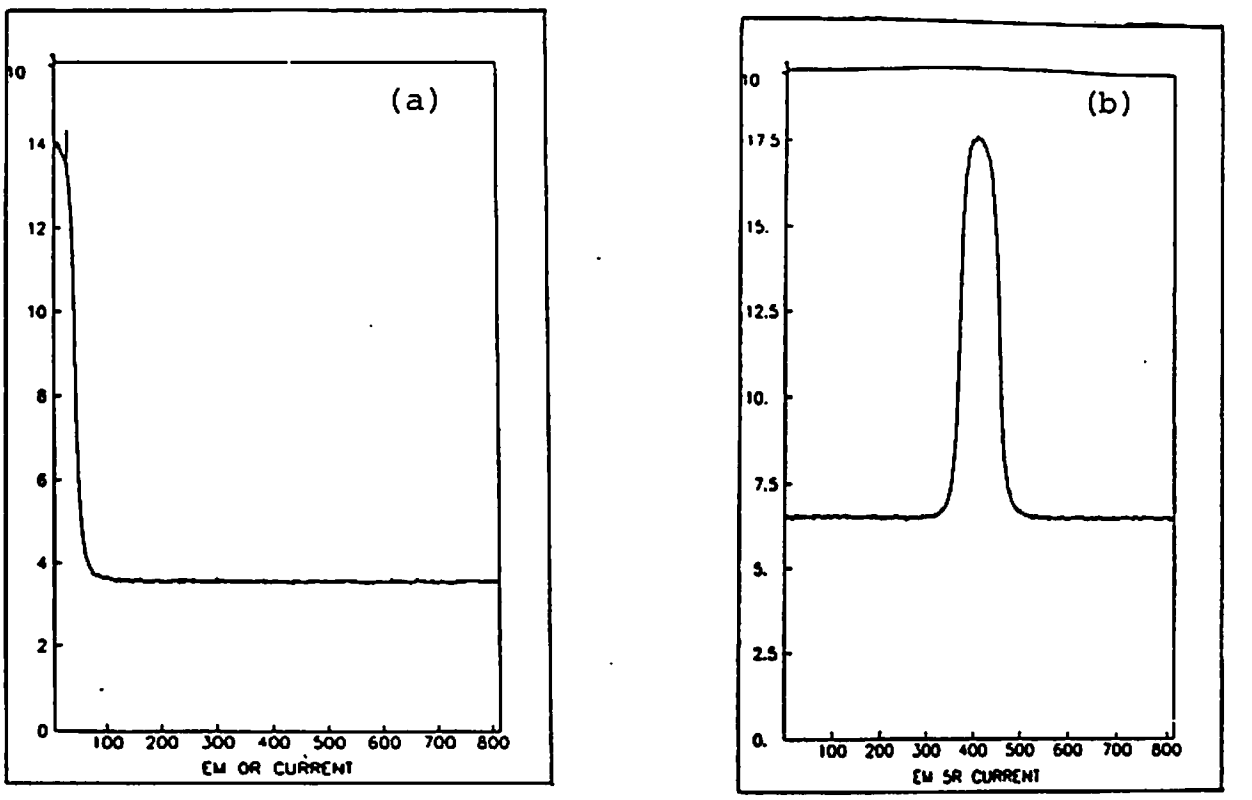

Fig. 6.13

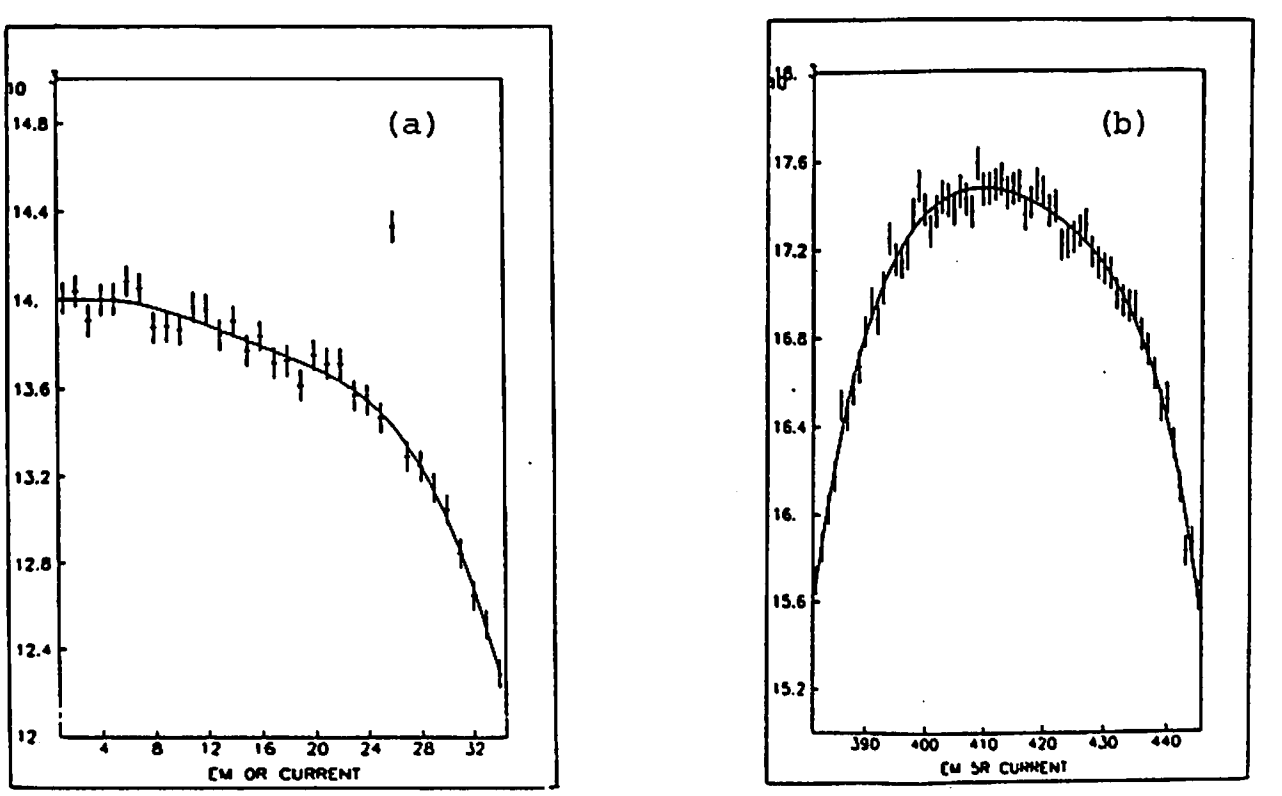

Fig. 6.14

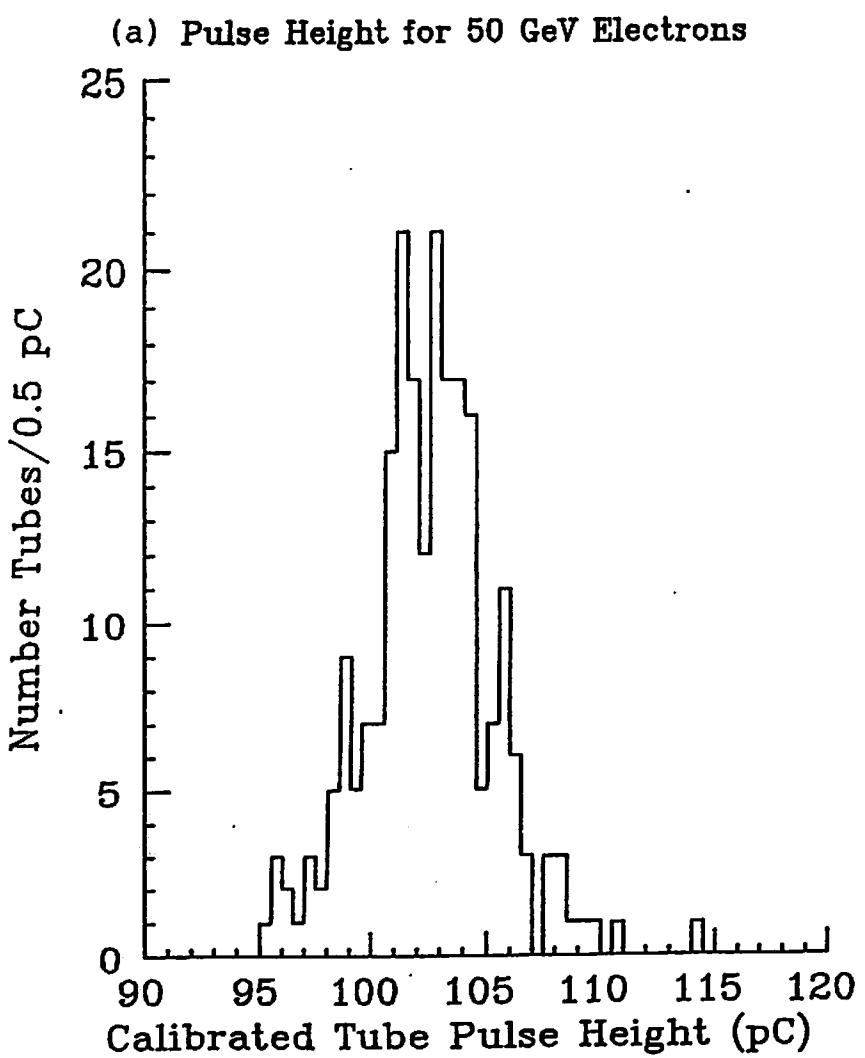
(a) Pulse Height for 50 GeV Electrons
Number Tubes/0.5 pC
0
5
10
15
20
25
90
95
100
105
110
115
120
Calibrated Tube Pulse Height (pC)

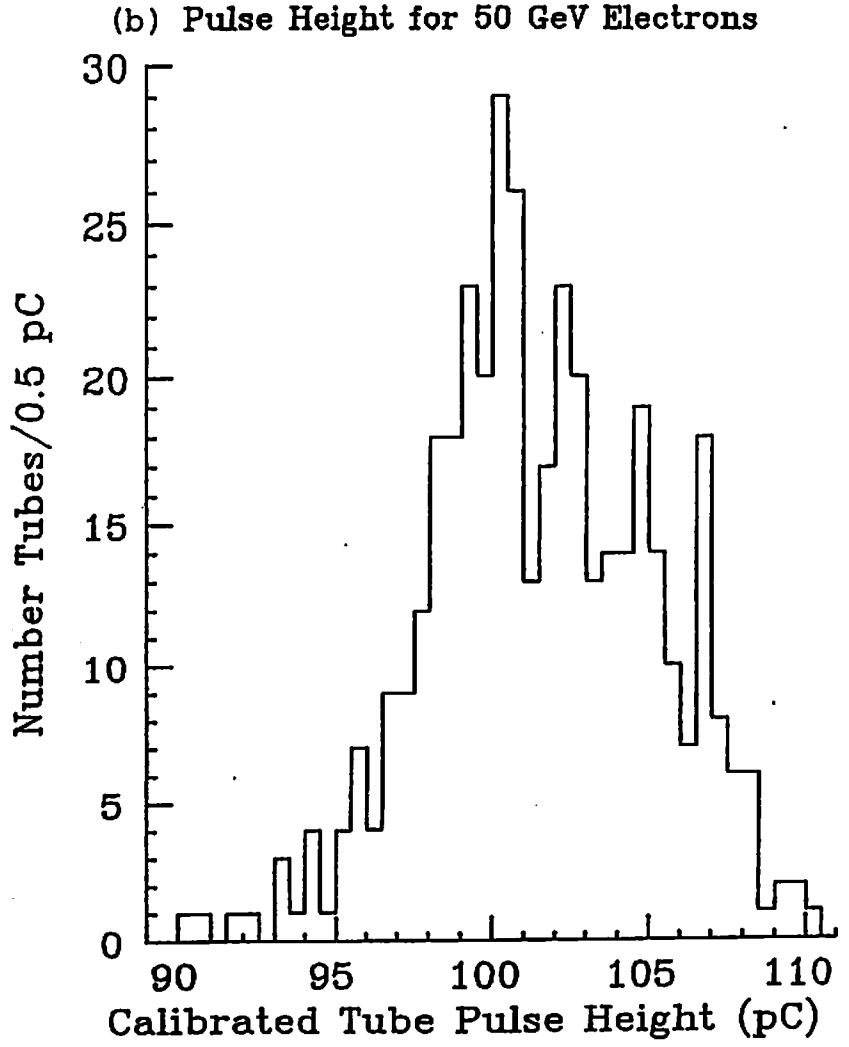
(b) Pulse Height for 50 GeV Electrons
Number Tubes/0.5 pC
0
5
10
15
20
25
30
90
95
100
105
110
Calibrated Tube Pulse Height (pC)

Fig. 7.1

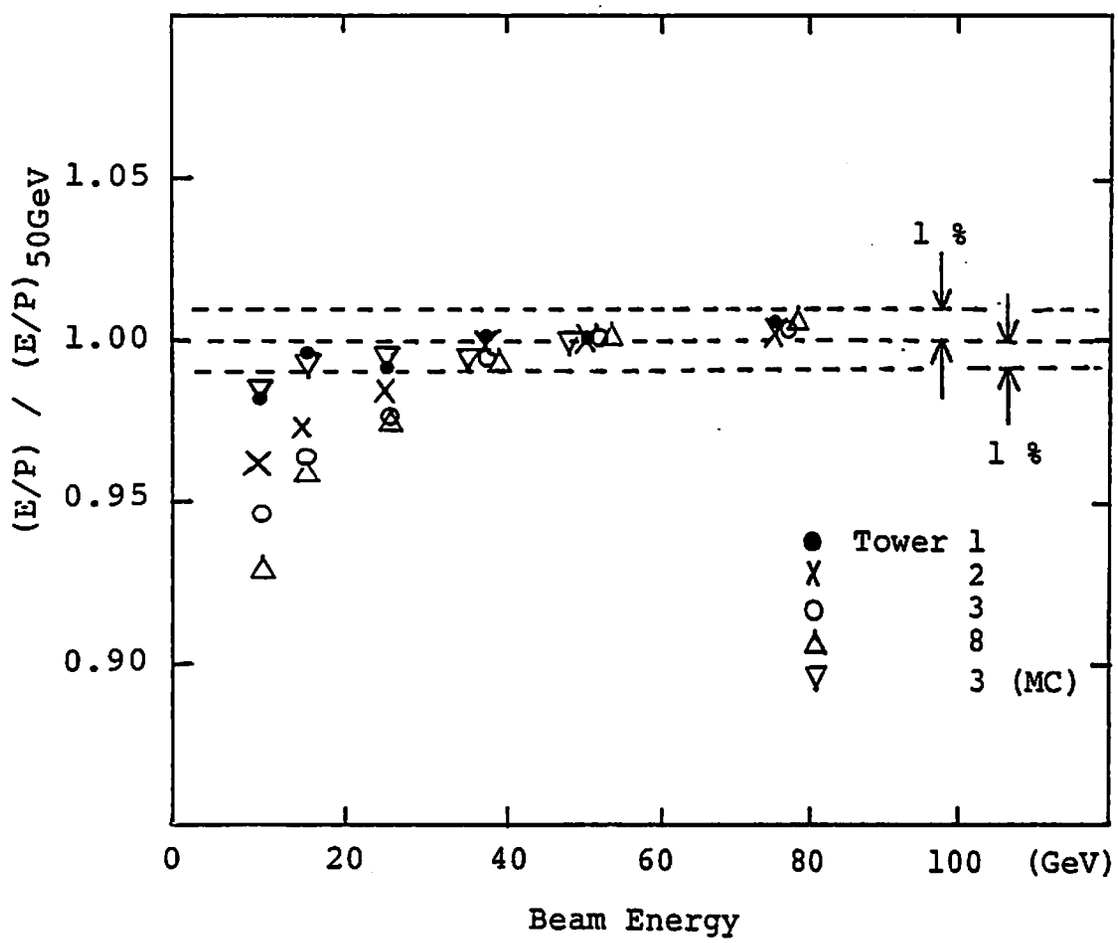
(E/P) / (E/P)50GeV
1.05
1.00
0.95
0.90
1 %
1 %
Tower 1
2
3
8
3 (MC)
0
20
40
60
80
100
(GeV)
Beam Energy

Fig. 7.2

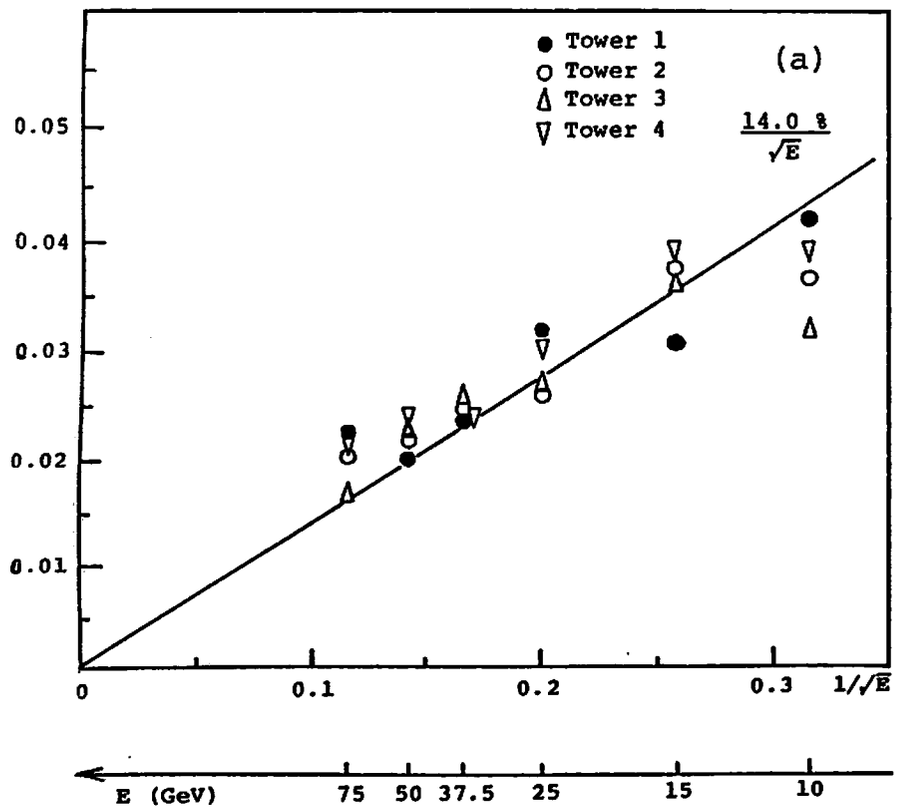
Tower 1
Tower 2
Tower 3
Tower 4
(a)
14.0 %/√E
0.05
0.04
0.03
0.02
0.01
0
0.1
0.2
0.3
1/√E
E (GeV)
75
50
37.5
25
15
10

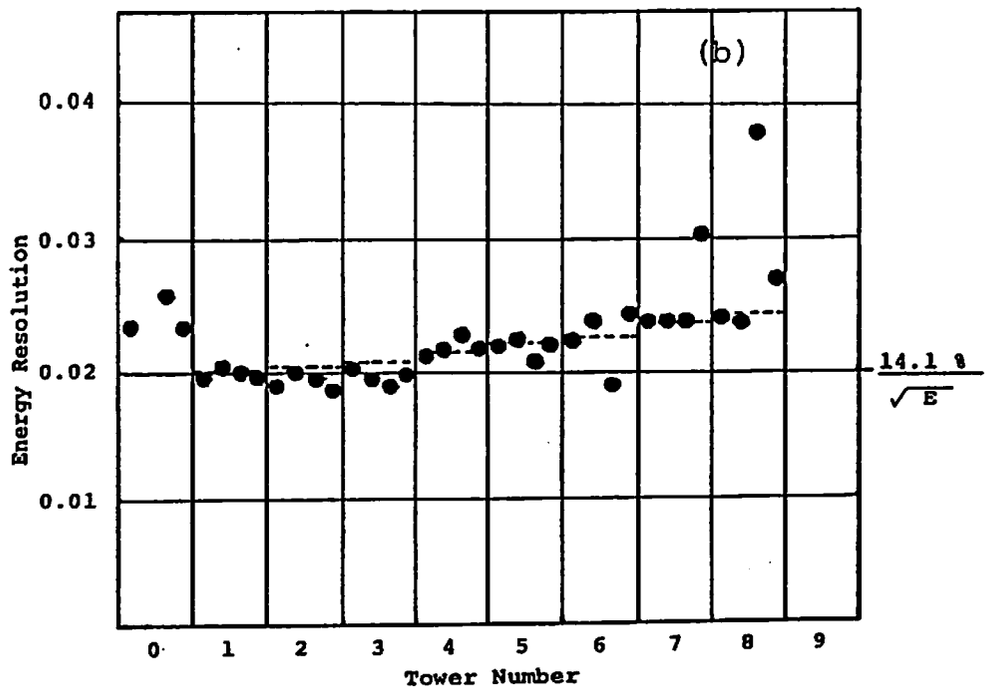
(b)
Energy Resolution
0.04
0.03
0.02
0.01
14.1 %/√E
0
1
2
3
4
5
6
7
8
9
Tower Number

Fig. 7.3

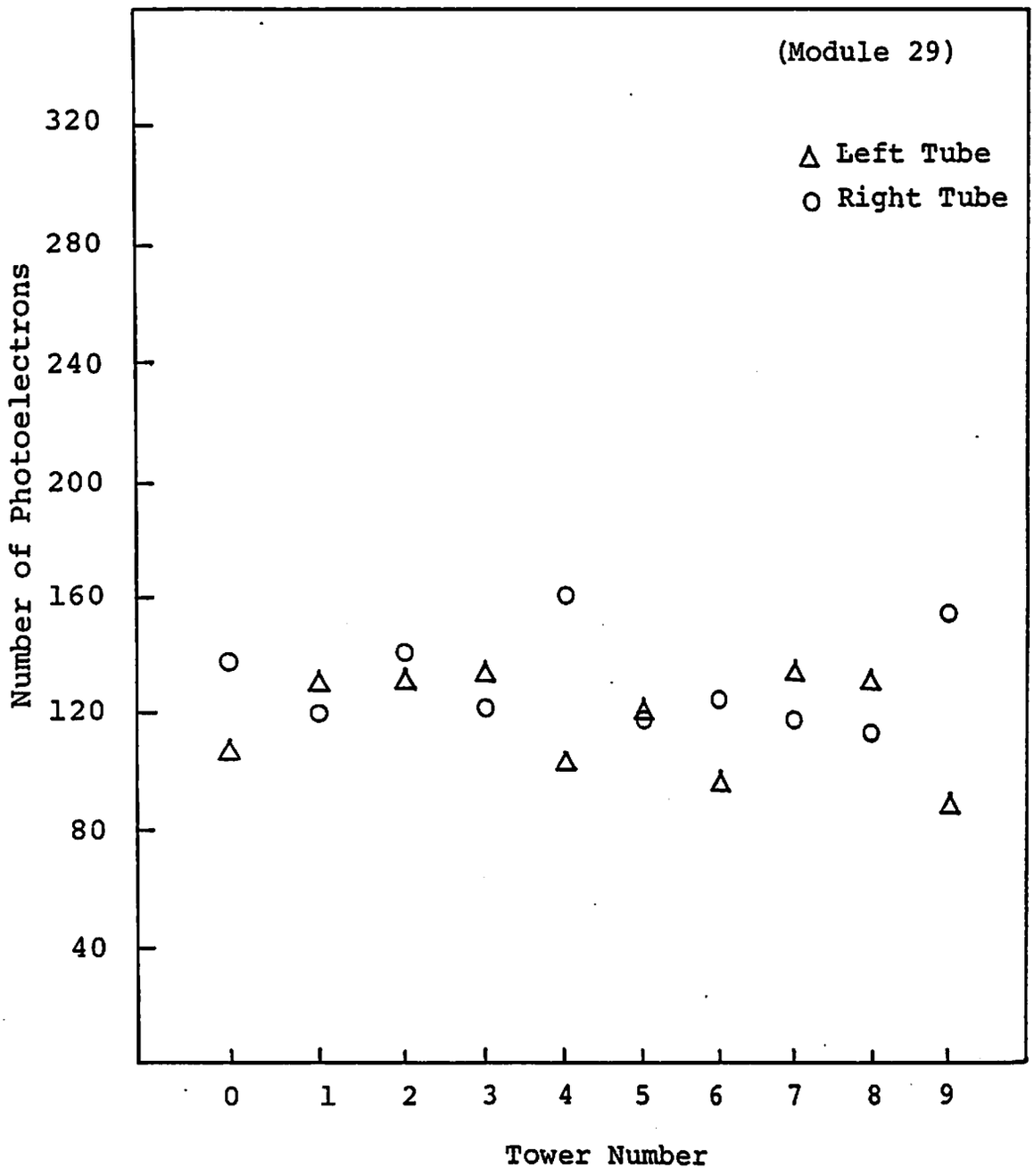
(Module 29)
Δ Left Tube
o Right Tube
Number of Photoelectrons
320
280
240
200
160
120
80
40
0
1
2
3
4
5
6
7
8
9
Tower Number

Fig. 7.4

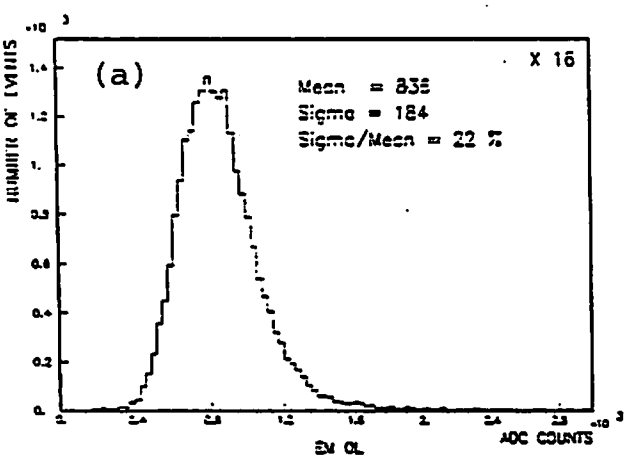
(a)
X 16
Mean = 838
Sigma = 184
Sigma/Mean = 22 %
NUMBER OF EVENTS
ADC COUNTS
EM OL

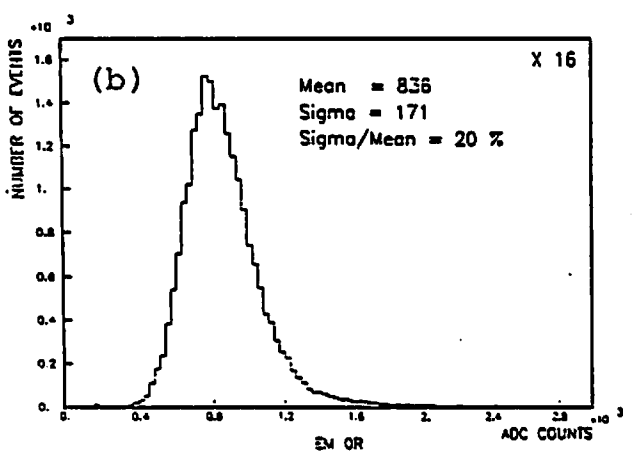
(b)
X 16
Mean = 836
Sigma = 171
Sigma/Mean = 20 %
NUMBER OF EVENTS
ADC COUNTS
EM OR

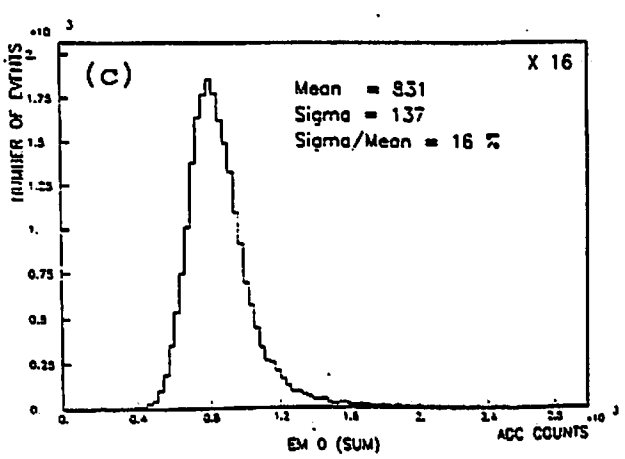
(c)
X 16
Mean = 831
Sigma = 137
Sigma/Mean = 16 %
NUMBER OF EVENTS
ADC COUNTS
EM O (SUM)

Fig. 7.5

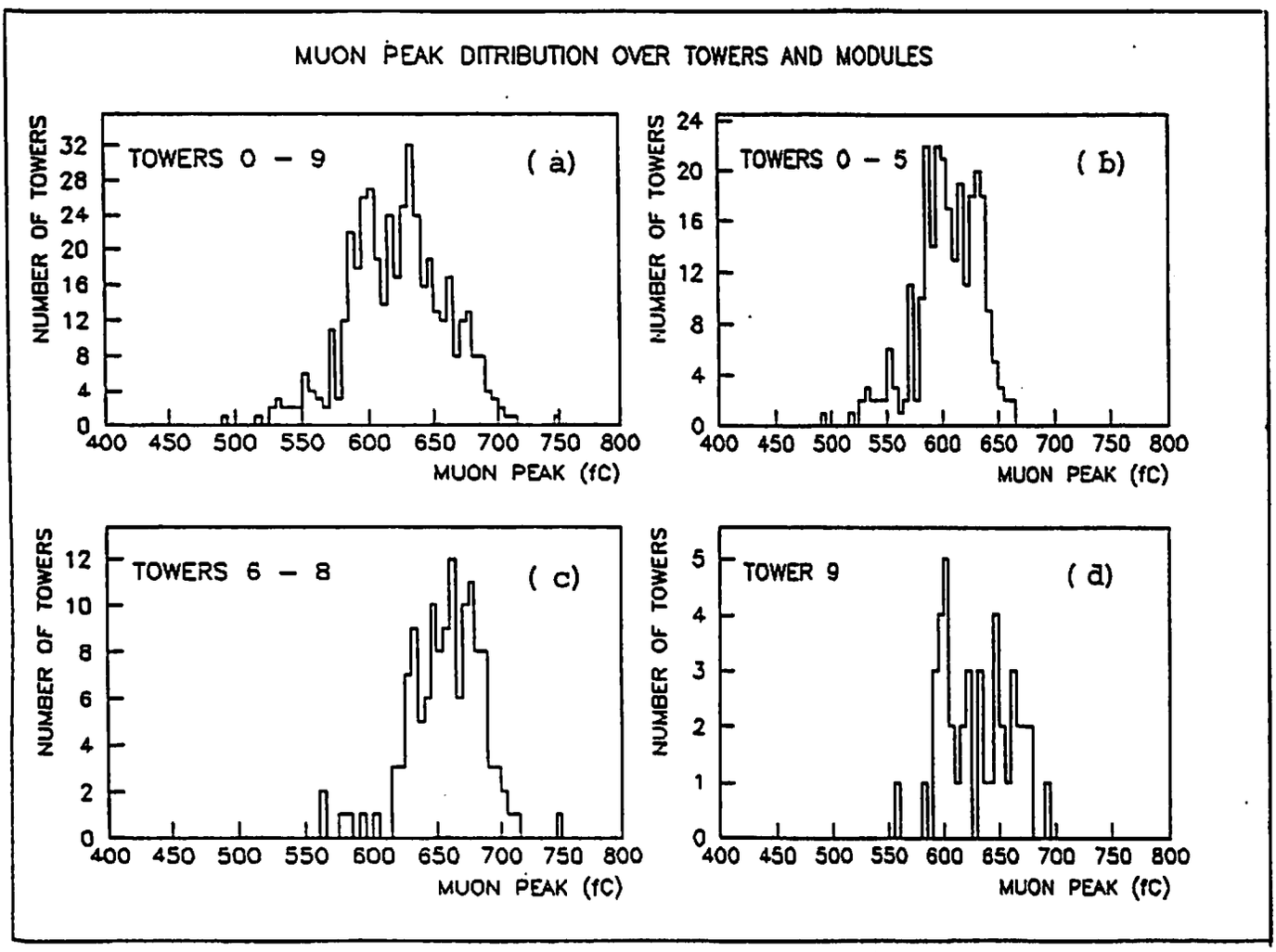
MUON PEAK DITRIBUTION OVER TOWERS AND MODULES
TOWERS 0 – 9
(a)
TOWERS 0 – 5
(b)
TOWERS 6 – 8
(c)
TOWER 9
(d)
NUMBER OF TOWERS
MUON PEAK (fC)
400 450 500 550 600 650 700 750 800

Fig. 7.6

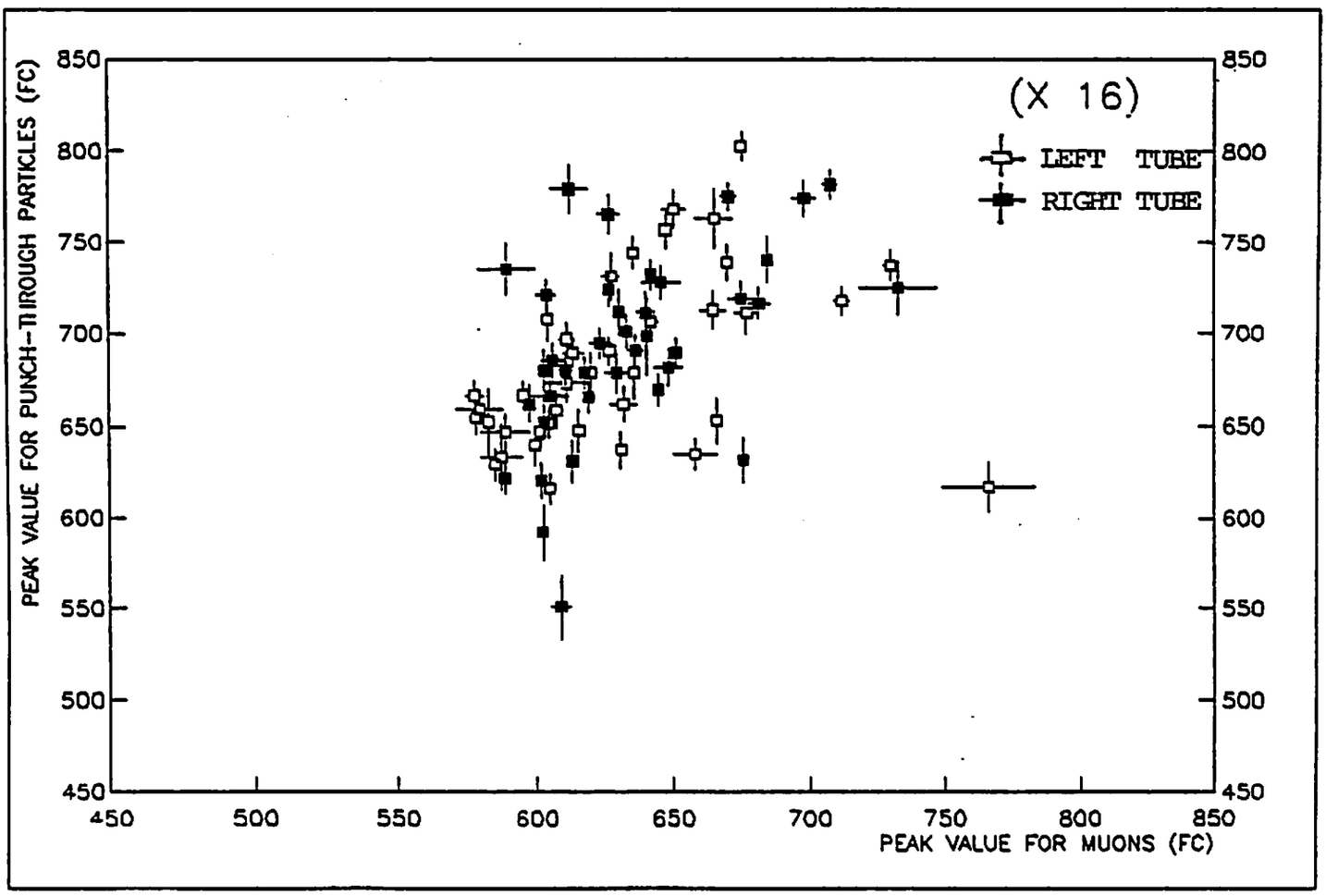
(X 16)
LEFT TUBE
RIGHT TUBE
PEAK VALUE FOR PUNCH-THROUGH PARTICLES (FC)
PEAK VALUE FOR MUONS (FC)
850
800
750
700
650
600
550
500
450
450
500
550
600
650
700
750
800
850

Fig. 7.7

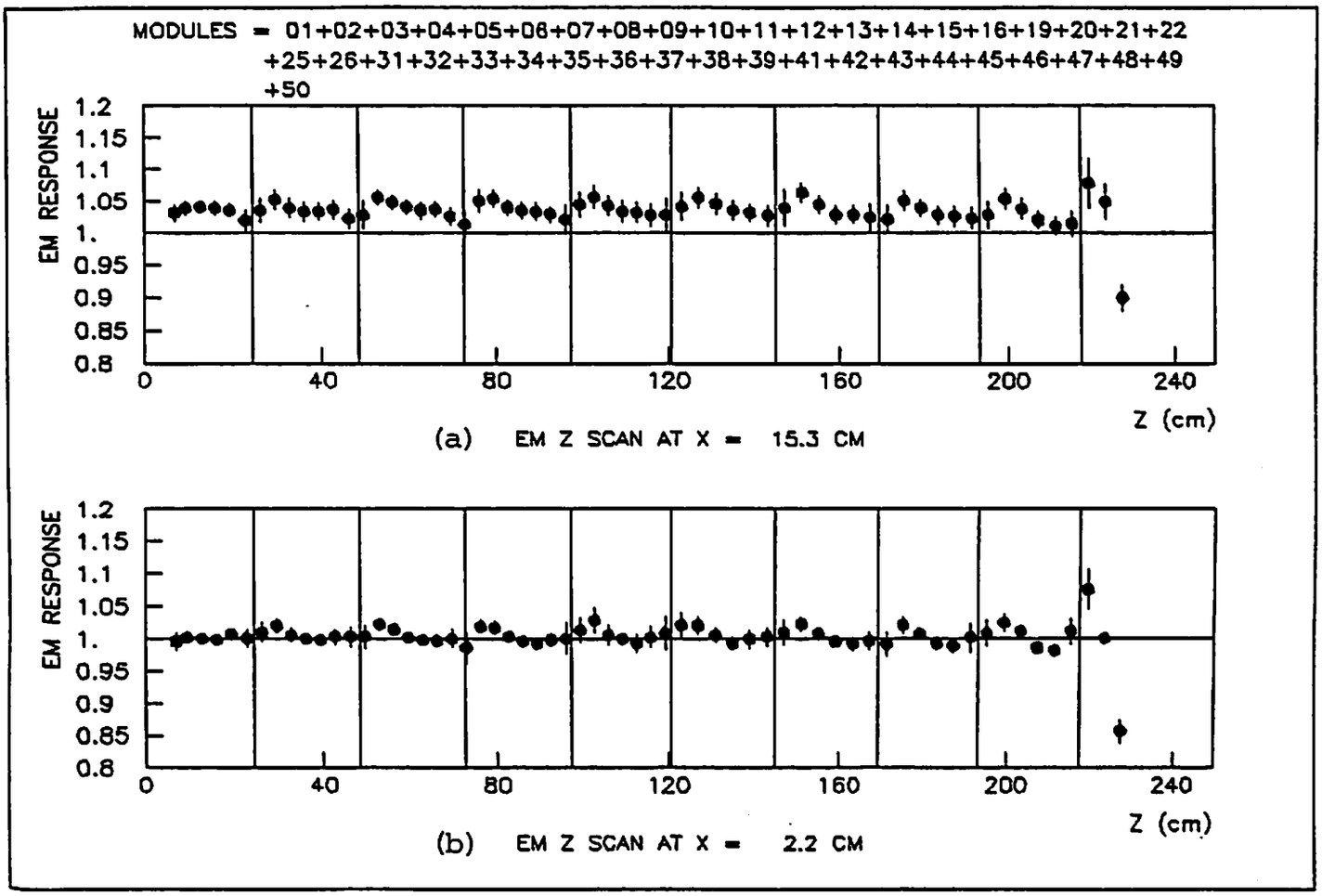
MODULES = 01+02+03+04+05+06+07+08+09+10+11+12+13+14+15+16+19+20+21+22
+25+26+31+32+33+34+35+36+37+38+39+41+42+43+44+45+46+47+48+49
+50
EM RESPONSE
1.2
1.15
1.1
1.05
1.
0.95
0.9
0.85
0.8
0
40
80
120
160
200
240
Z (cm)
(a) EM Z SCAN AT X = 15.3 CM
EM RESPONSE
1.2
1.15
1.1
1.05
1.
0.95
0.9
0.85
0.8
0
40
80
120
160
200
240
Z (cm)
(b) EM Z SCAN AT X = 2.2 CM

Fig. 7.8

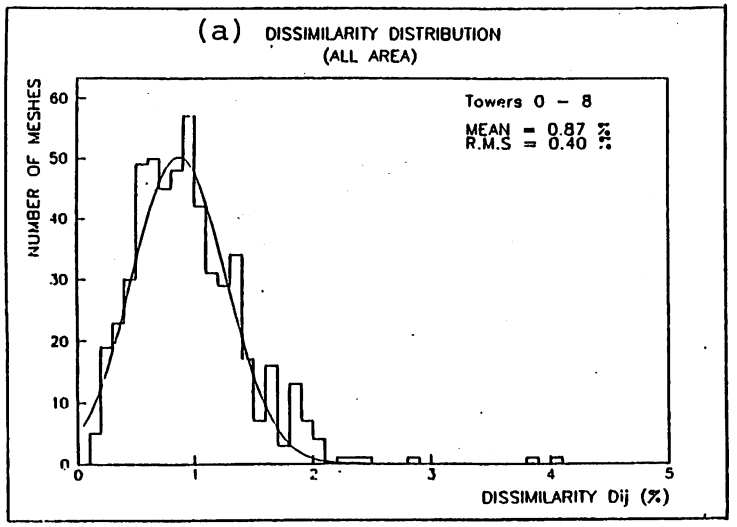
(a) DISSIMILARITY DISTRIBUTION
(ALL AREA)
Towers 0 - 8
MEAN = 0.87 %
R.M.S = 0.40 %
NUMBER OF MESHES
DISSIMILARITY Dij (%)

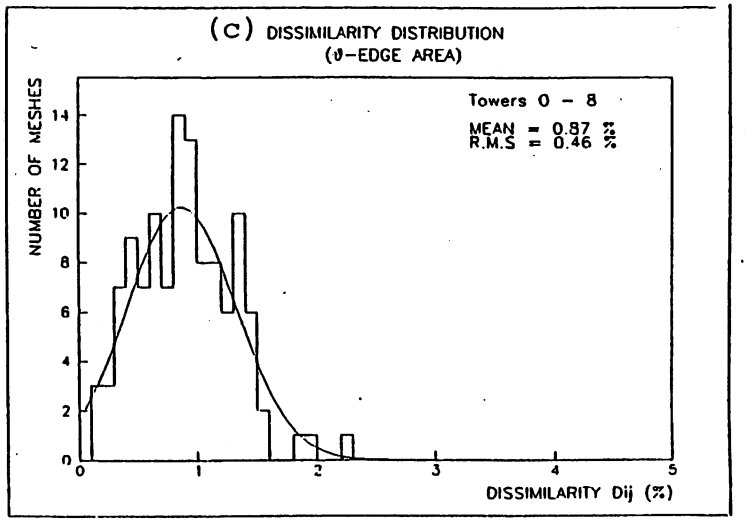
(c) DISSIMILARITY DISTRIBUTION
(ϑ-EDGE AREA)
Towers 0 - 8
MEAN = 0.87 %
R.M.S = 0.46 %
NUMBER OF MESHES
DISSIMILARITY Dij (%)

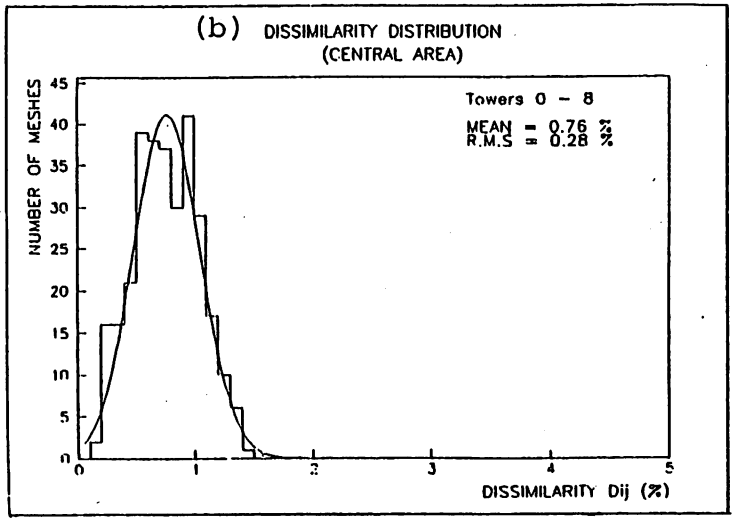
(b) DISSIMILARITY DISTRIBUTION
(CENTRAL AREA)
Towers 0 - 8
MEAN = 0.76 %
R.M.S = 0.28 %
NUMBER OF MESHES
DISSIMILARITY Dij (%)

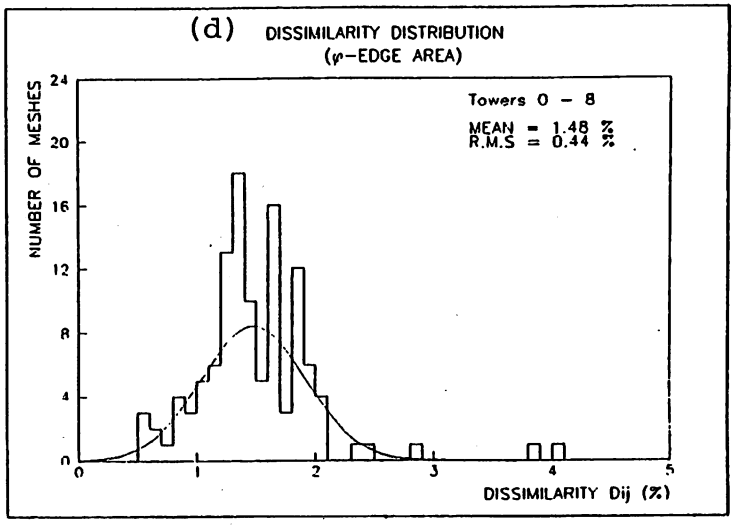
(d) DISSIMILARITY DISTRIBUTION
(φ-EDGE AREA)
Towers 0 - 8
MEAN = 1.48 %
R.M.S = 0.44 %
NUMBER OF MESHES
DISSIMILARITY Dij (%)

Fig. 7.9

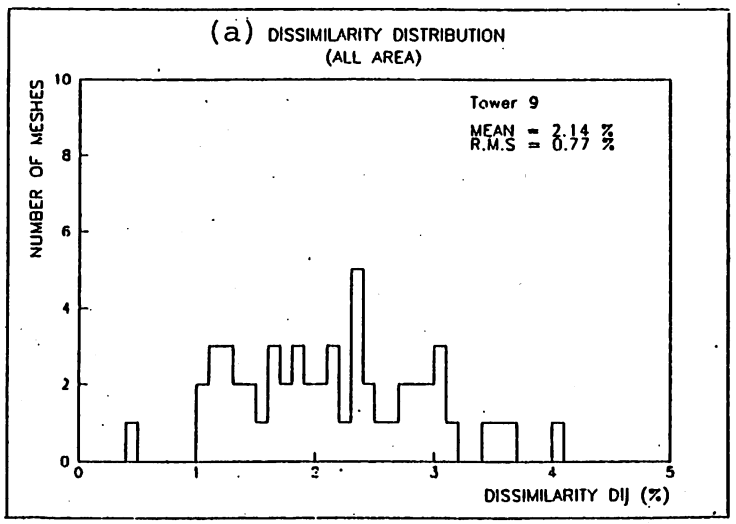
(a) DISSIMILARITY DISTRIBUTION
(ALL AREA)
Tower 9
MEAN = 2.14 %
R.M.S = 0.77 %
NUMBER OF MESHES
DISSIMILARITY DIJ (%)

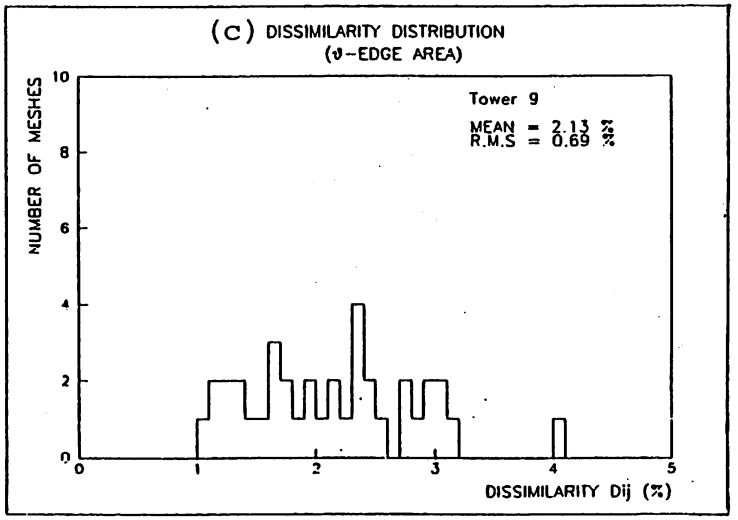
(c) DISSIMILARITY DISTRIBUTION
(ϑ-EDGE AREA)
Tower 9
MEAN = 2.13 %
R.M.S = 0.69 %
NUMBER OF MESHES
DISSIMILARITY Dij (%)

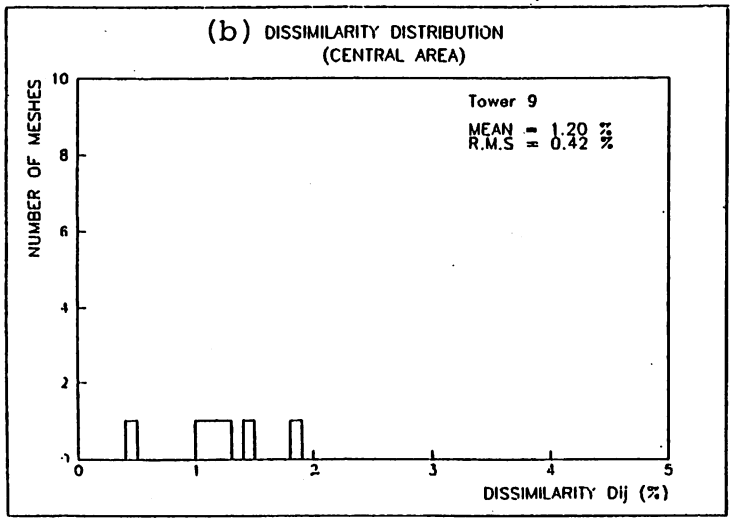
(b) DISSIMILARITY DISTRIBUTION
(CENTRAL AREA)
Tower 9
MEAN = 1.20 %
R.M.S = 0.42 %
NUMBER OF MESHES
DISSIMILARITY Dij (%)

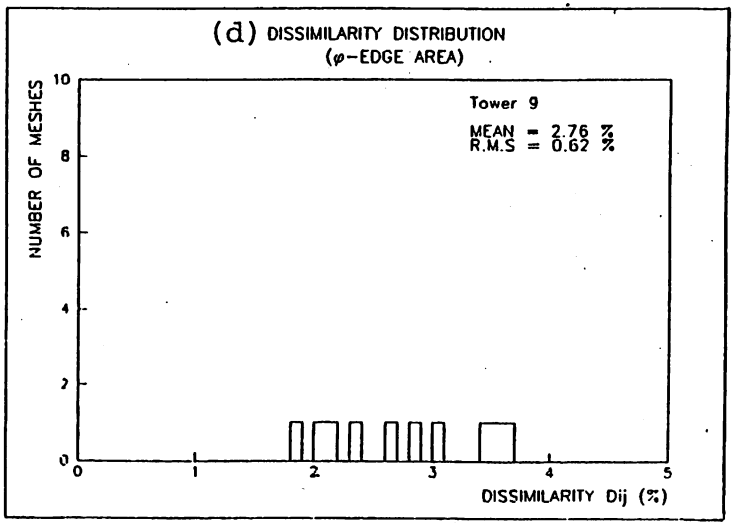
(d) DISSIMILARITY DISTRIBUTION
(φ-EDGE AREA)
Tower 9
MEAN = 2.76 %
R.M.S = 0.62 %
NUMBER OF MESHES
DISSIMILARITY Dij (%)

Fig. 7.10

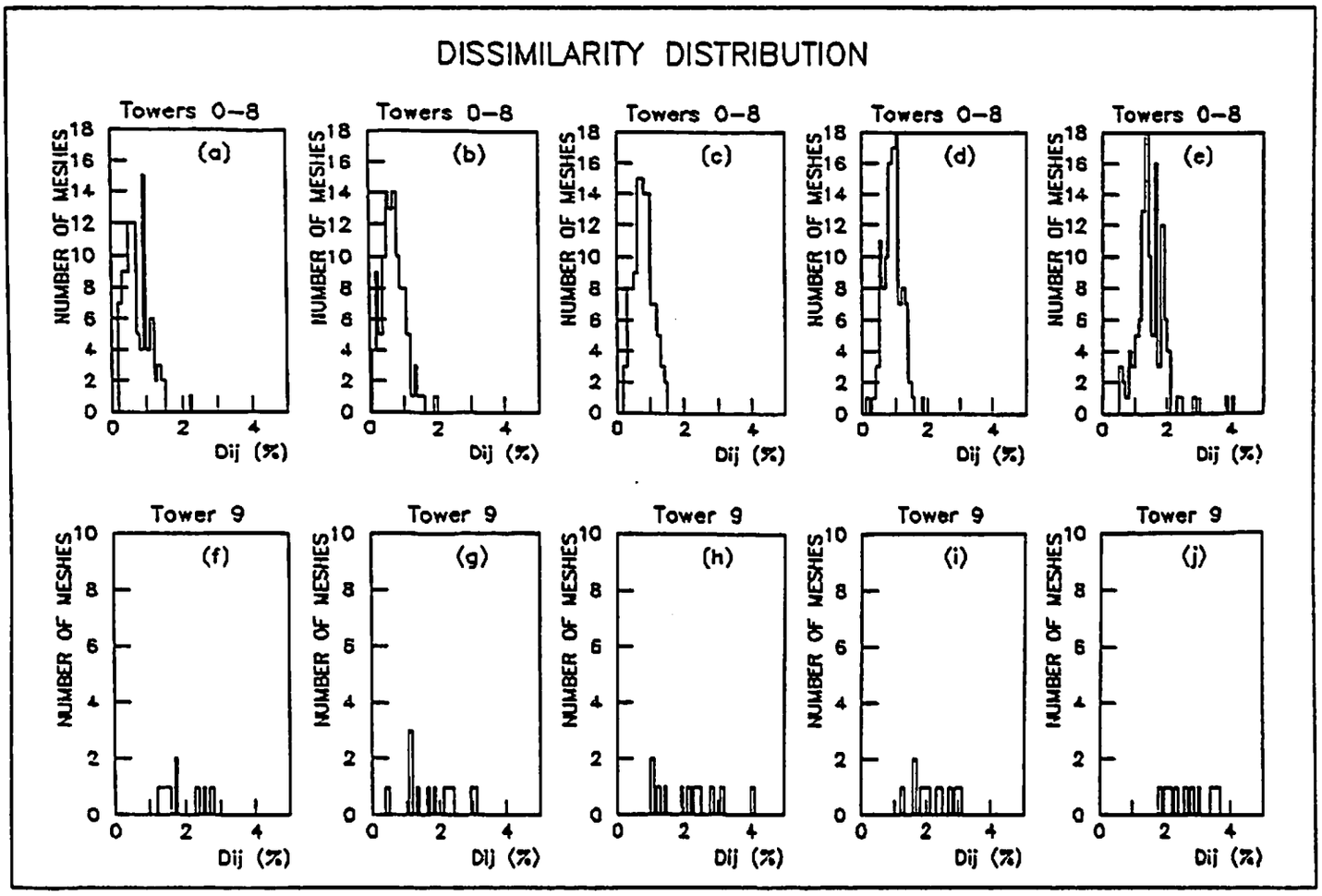
DISSIMILARITY DISTRIBUTION
Towers 0-8
(a)
(b)
(c)
(d)
(e)
Tower 9
(f)
(g)
(h)
(i)
(j)
NUMBER OF MESHES
Dij (%)

Fig. 7.11

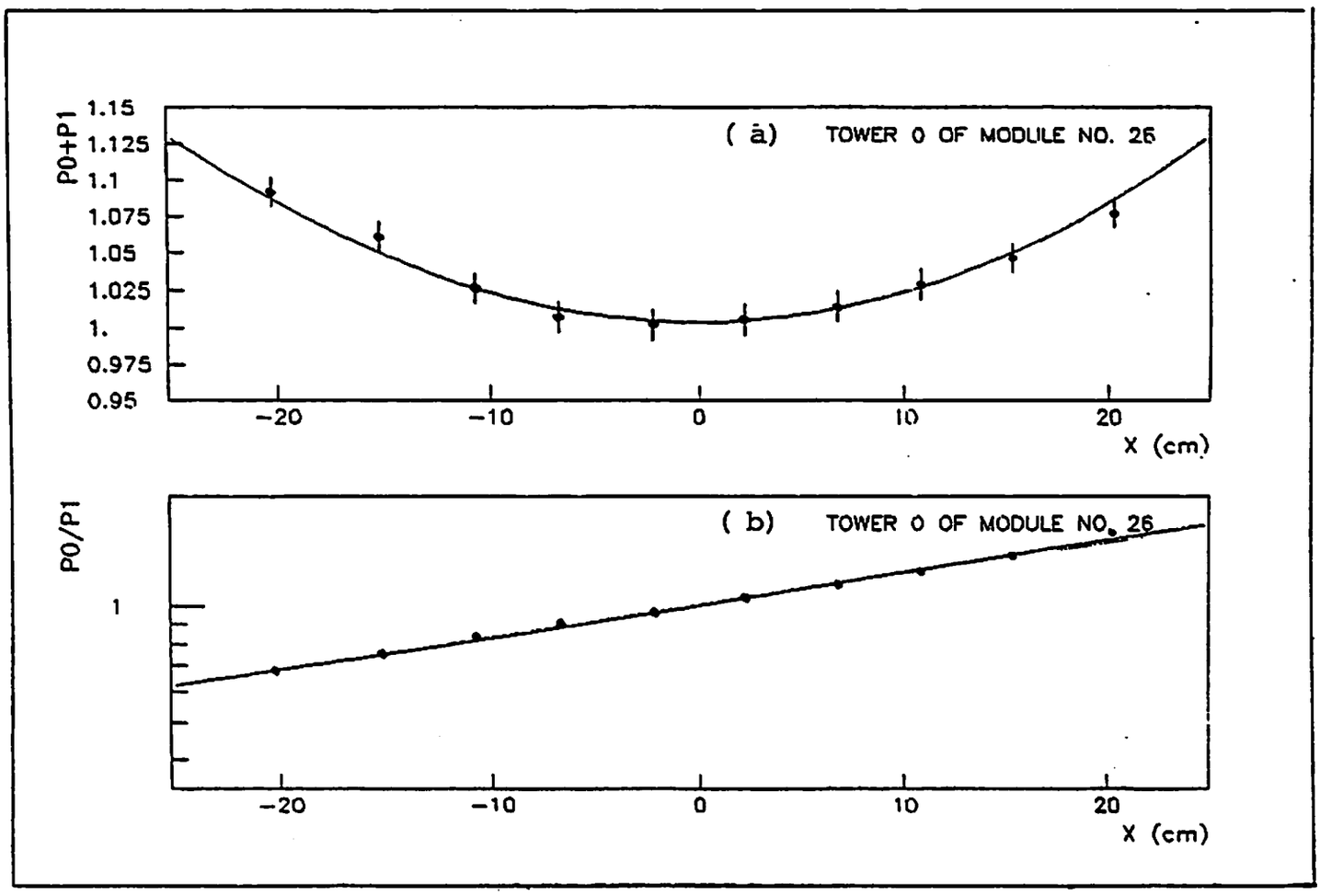
(a) TOWER 0 OF MODULE NO. 26
P0+P1
1.15
1.125
1.1
1.075
1.05
1.025
1.
0.975
0.95
-20
-10
0
10
20
X (cm)
(b) TOWER 0 OF MODULE NO. 26
P0/P1
1
-20
-10
0
10
20
X (cm)

Fig. 7.12

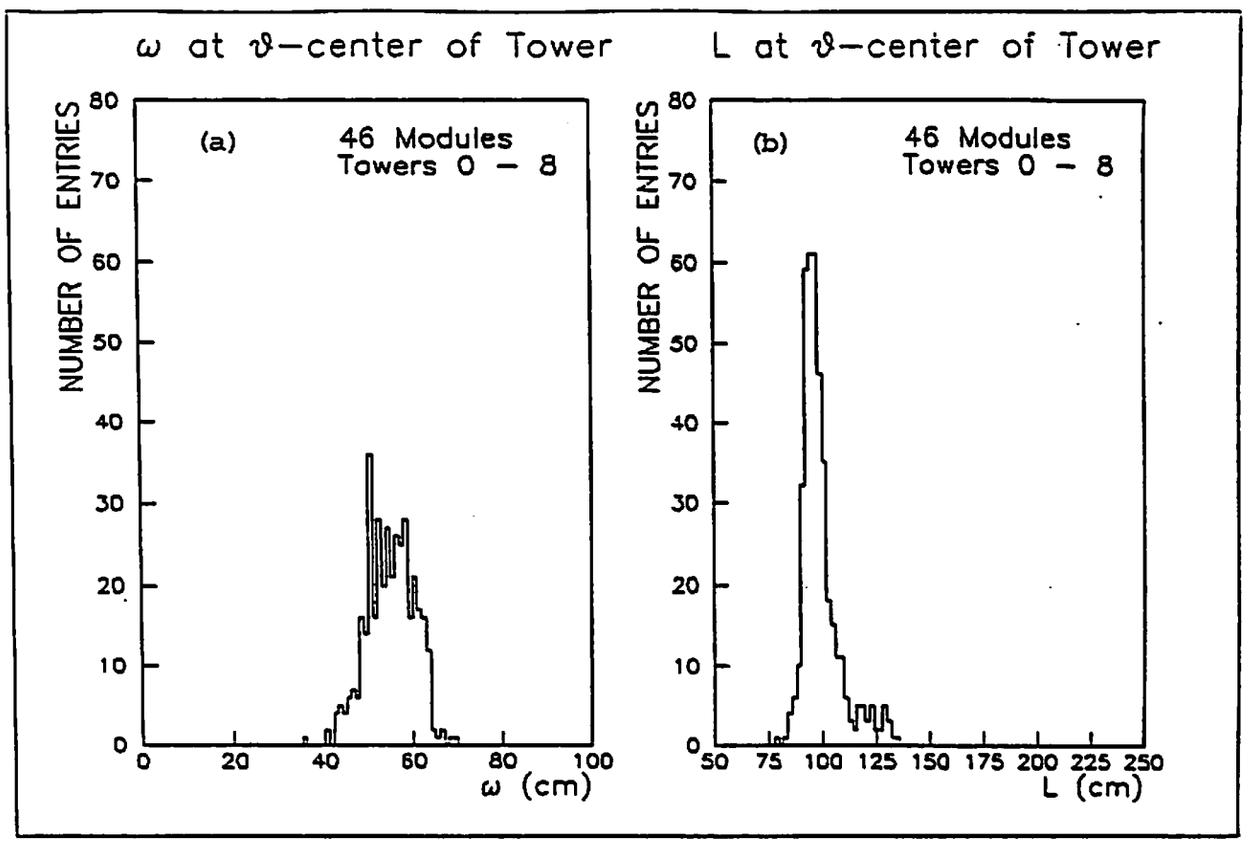

Fig. 7.13

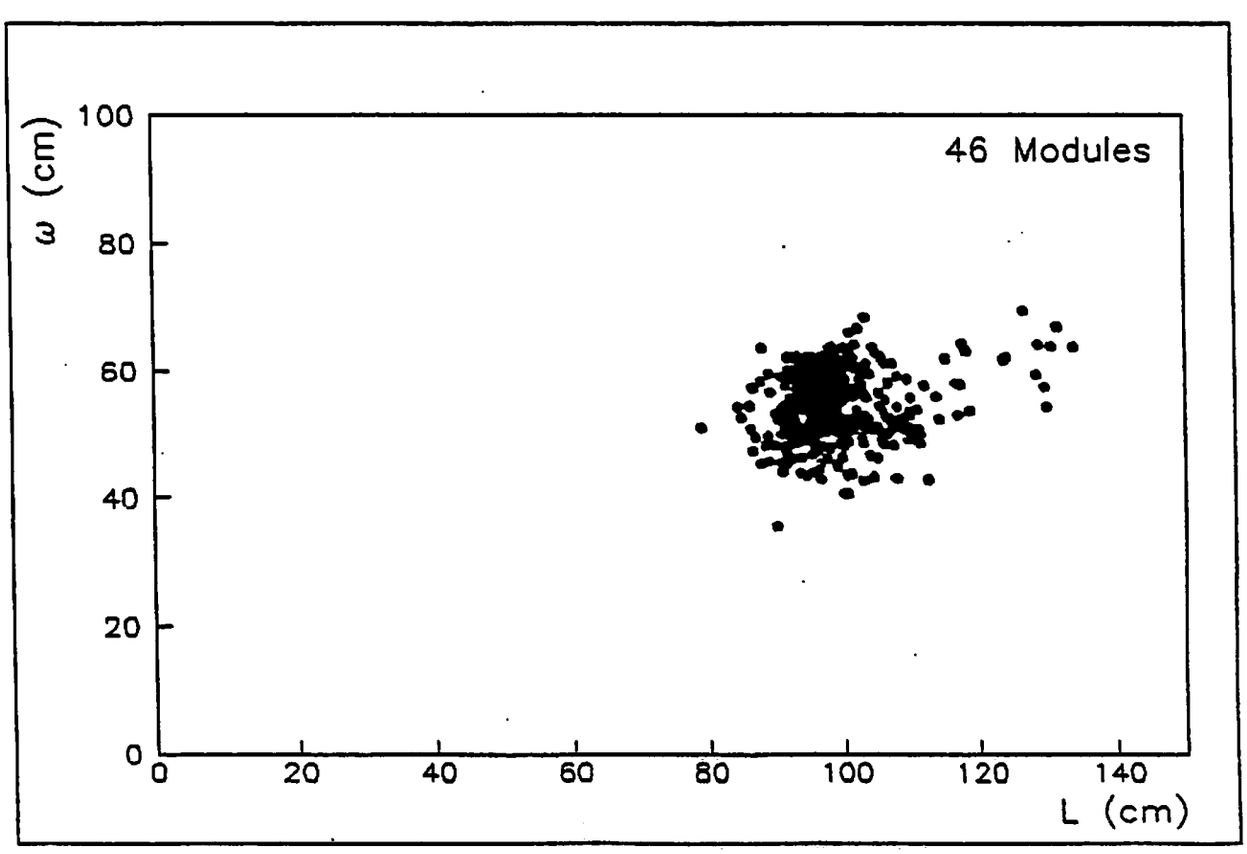

Fig. 7.14

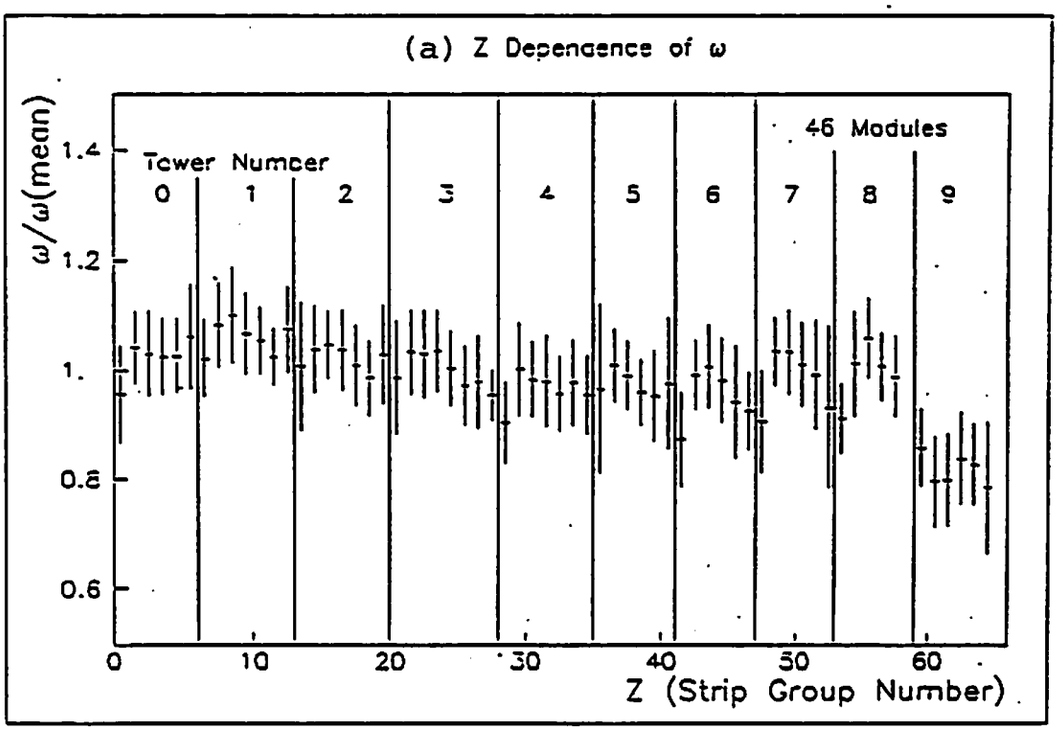
(a) Z Dependence of ω
ω/ω(mean)
46 Modules
Tower Number
0
1
2
3
4
5
6
7
8
9
1.4
1.2
1.
0.8
0.6
0
10
20
30
40
50
60
Z (Strip Group Number)

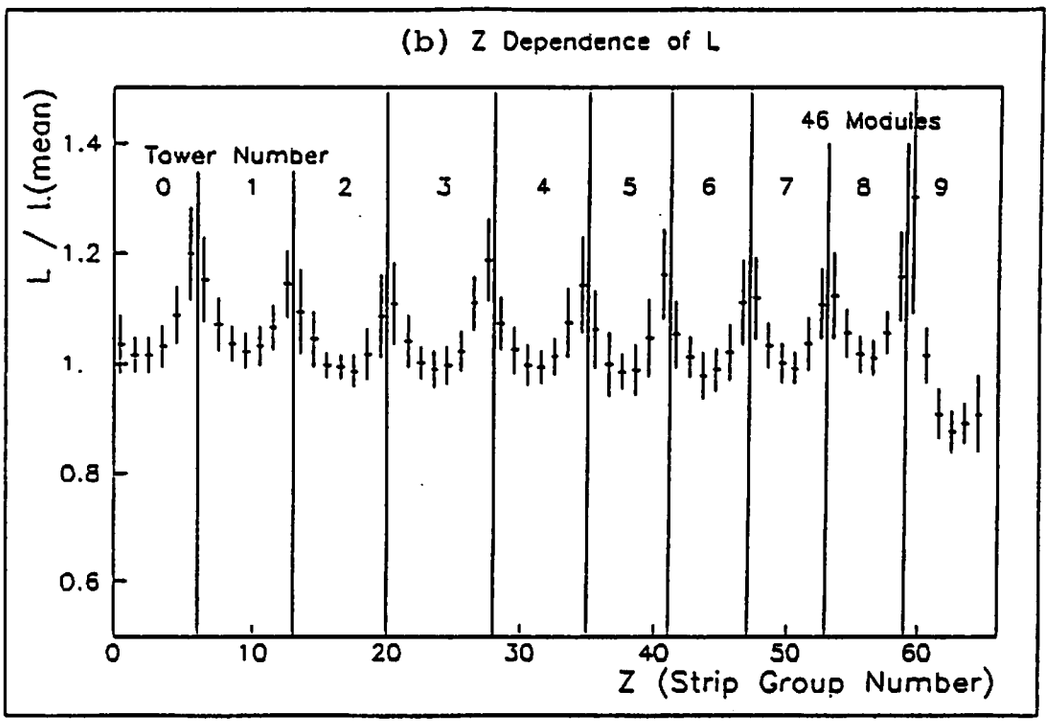
(b) Z Dependence of L
L / L(mean)
46 Modules
Tower Number
0
1
2
3
4
5
6
7
8
9
1.4
1.2
1.
0.8
0.6
0
10
20
30
40
50
60
Z (Strip Group Number)

Fig. 7.15

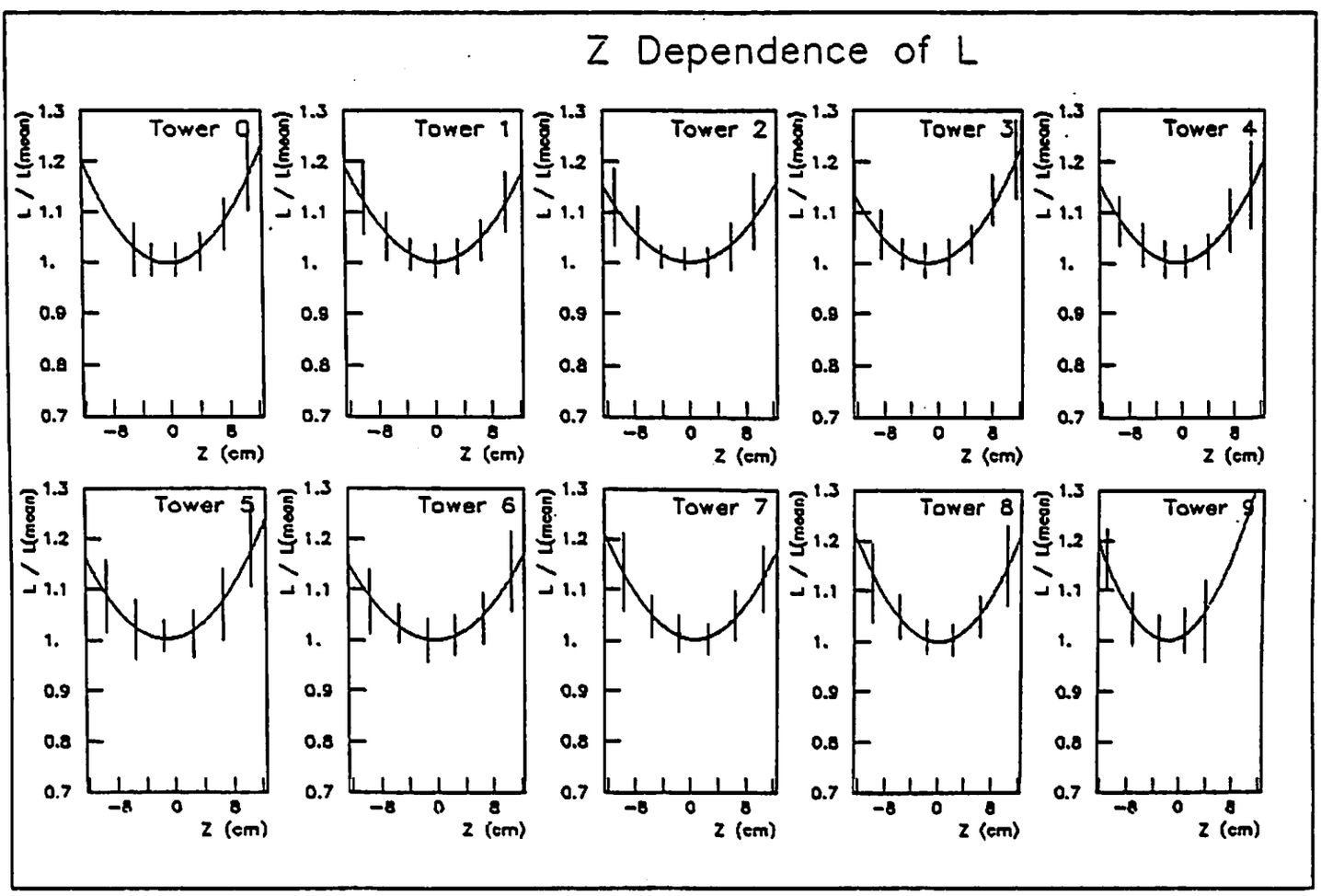
Z Dependence of L
Tower 0
Tower 1
Tower 2
Tower 3
Tower 4
Tower 5
Tower 6
Tower 7
Tower 8
Tower 9
L / L(mean)
Z (cm)

Fig. 7.16

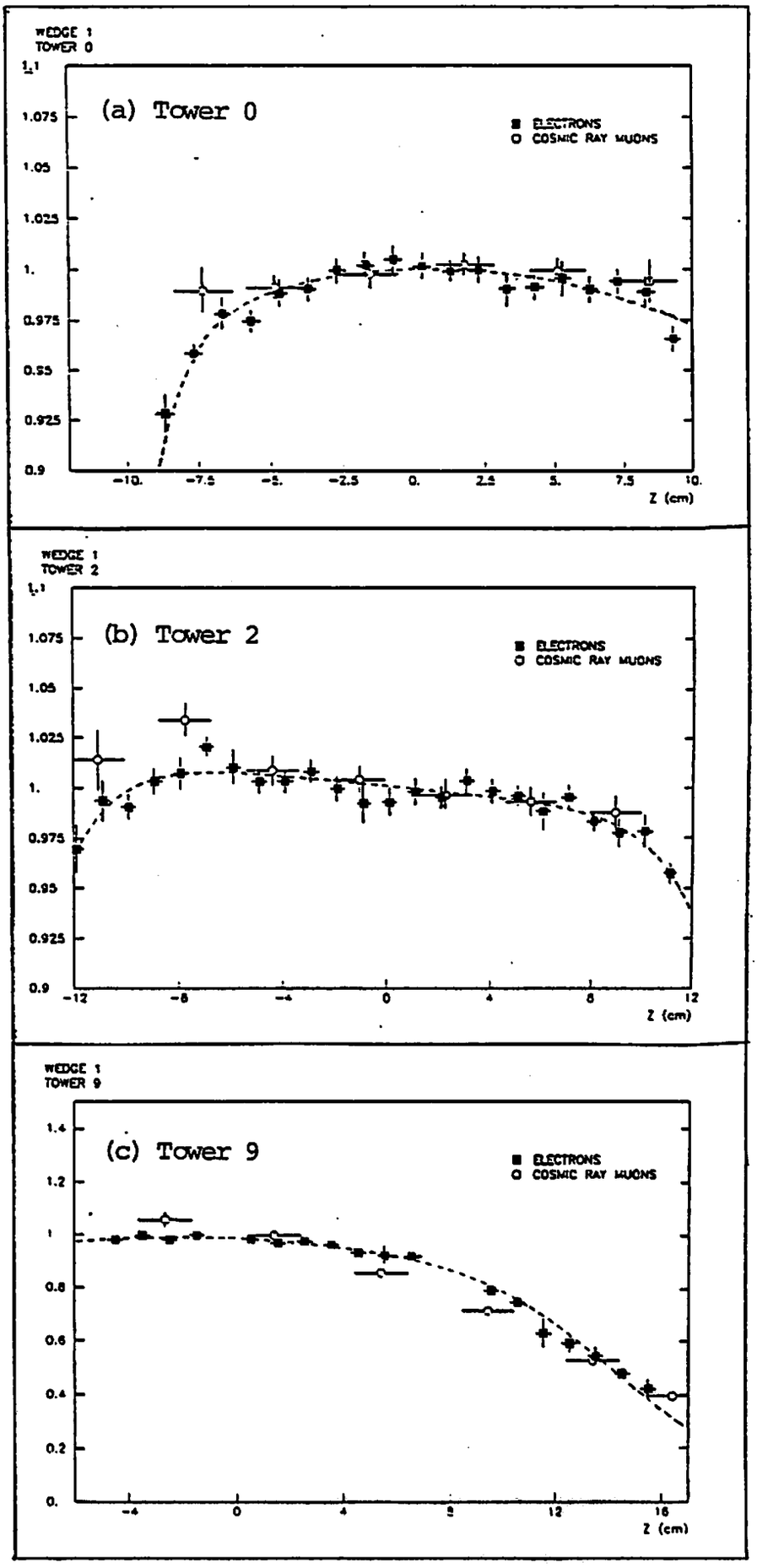
WEDGE 1
TOWER 0
(a) Tower 0
ELECTRONS
COSMIC RAY MUONS
Z (cm)
WEDGE 1
TOWER 2
(b) Tower 2
ELECTRONS
COSMIC RAY MUONS
Z (cm)
WEDGE 1
TOWER 9
(c) Tower 9
ELECTRONS
COSMIC RAY MUONS
Z (cm)

Fig. 7.17

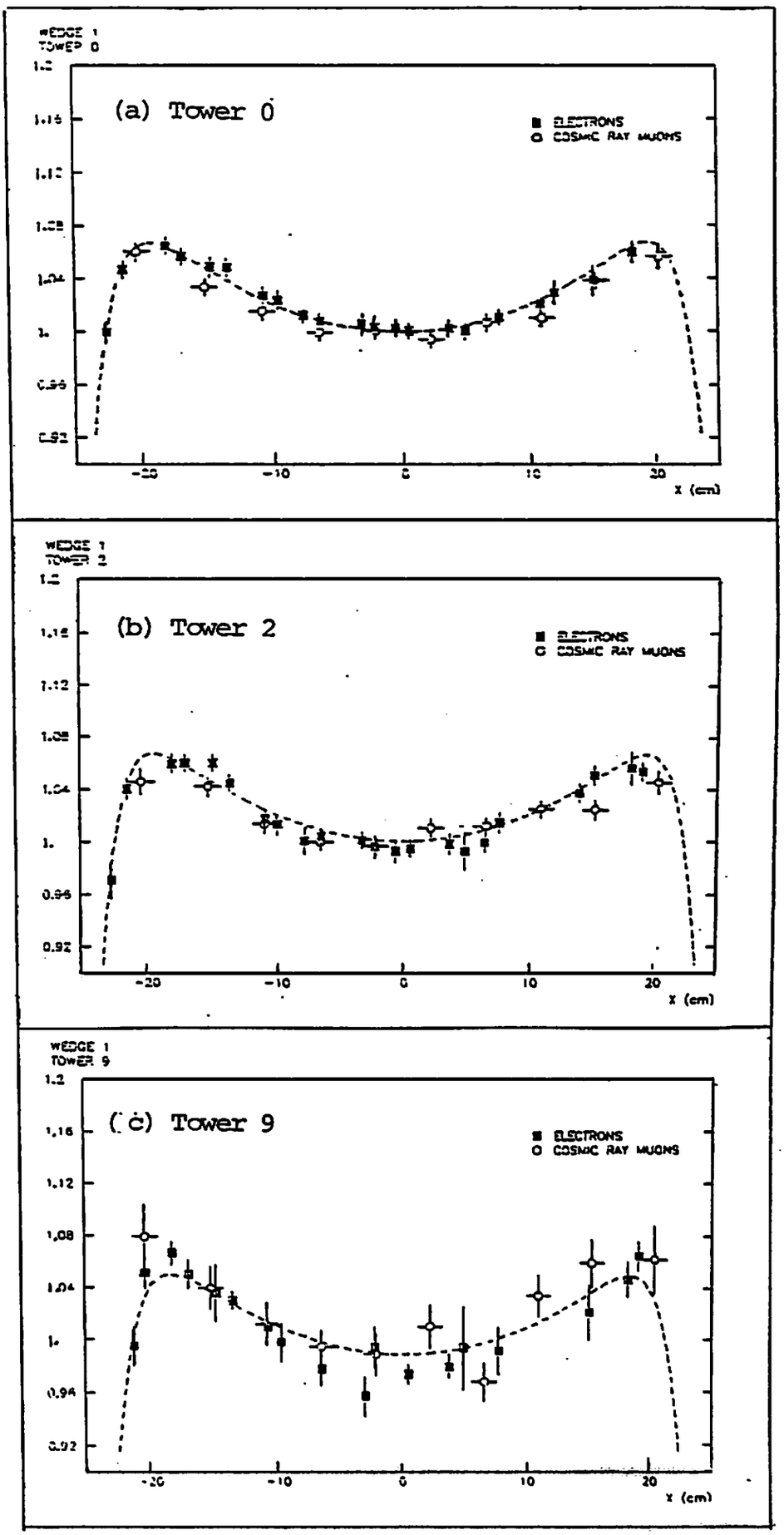
WEDGE 1
TOWER 0
(a) Tower 0
ELECTRONS
COSMIC RAY MUONS
X (cm)
WEDGE 1
TOWER 2
(b) Tower 2
ELECTRONS
COSMIC RAY MUONS
X (cm)
WEDGE 1
TOWER 9
(c) Tower 9
ELECTRONS
COSMIC RAY MUONS
X (cm)

Fig. 7.18

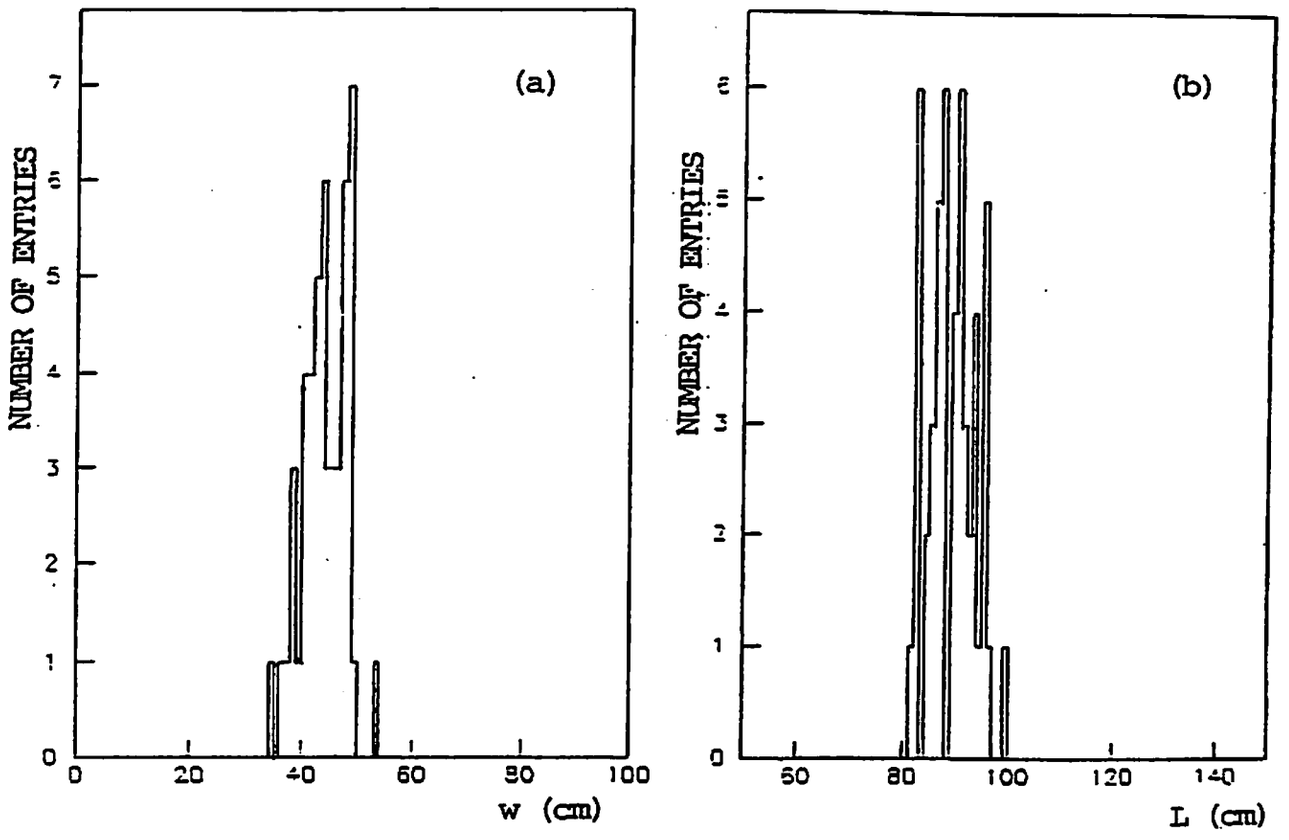

Fig. 7.19

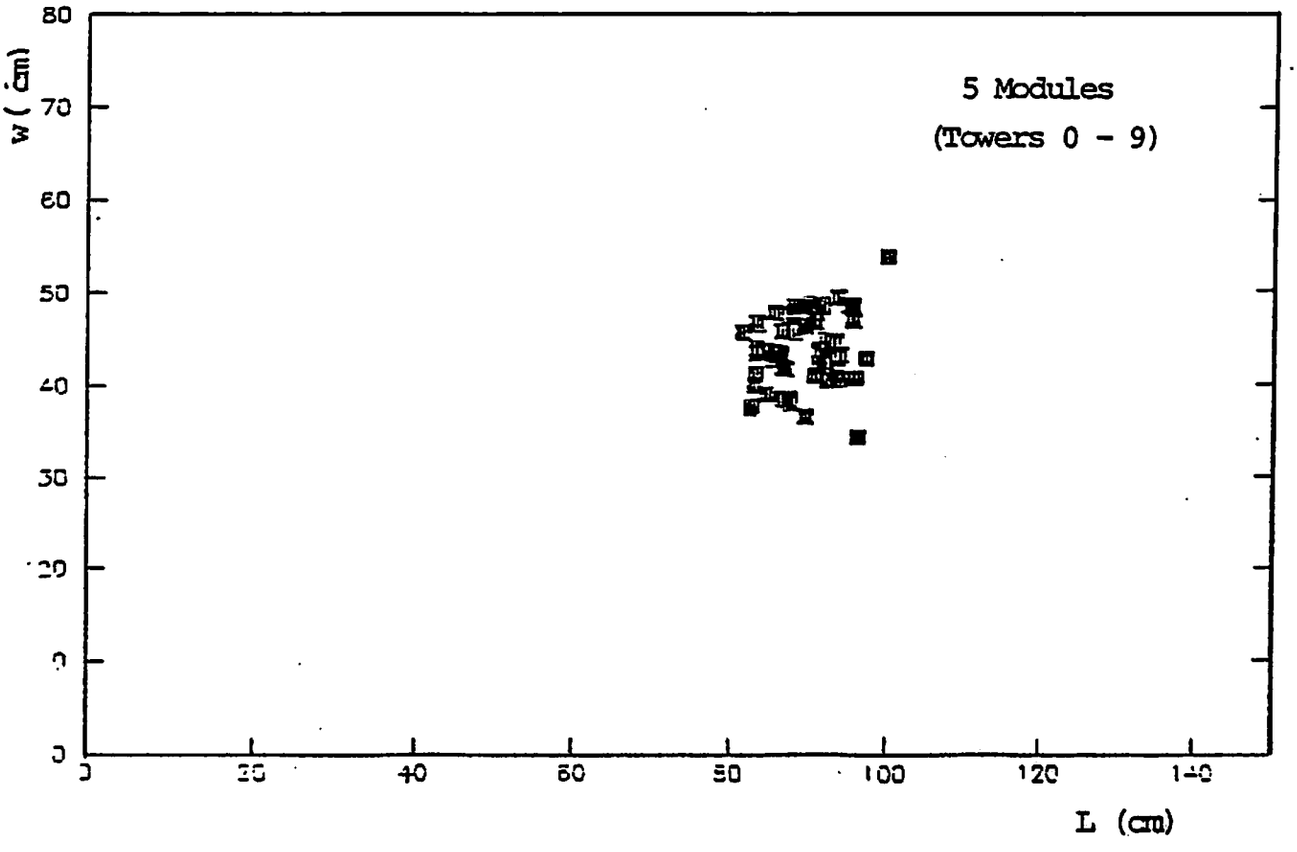

Fig. 7.20

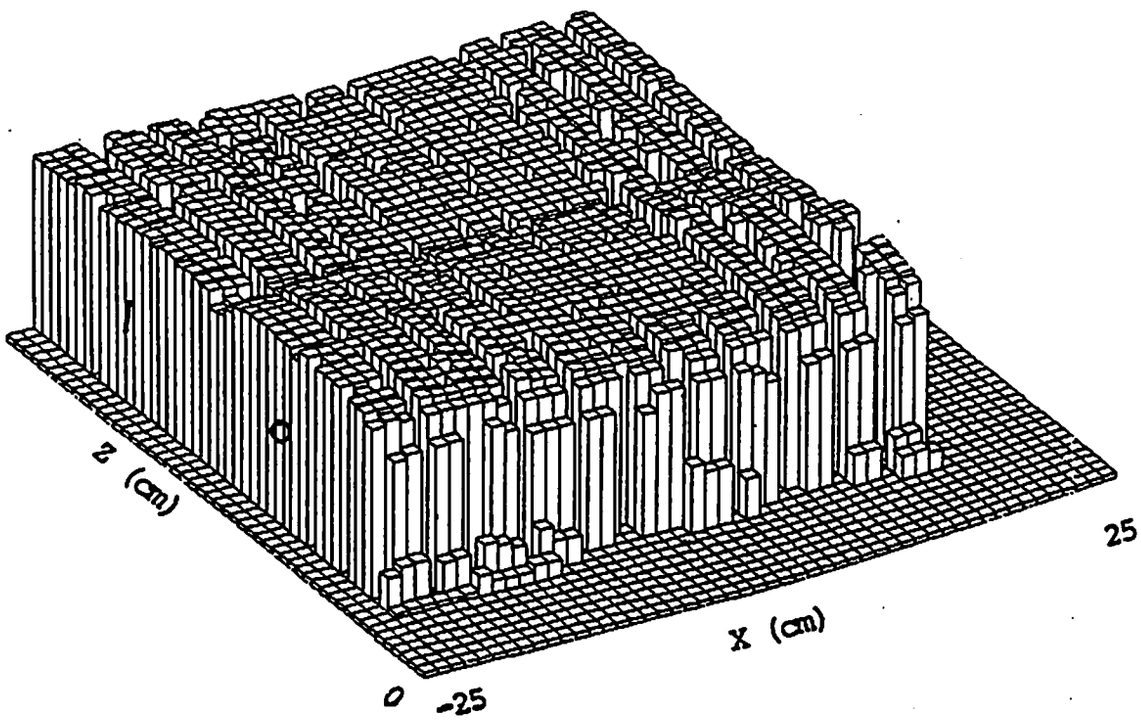

Fig. 7.21

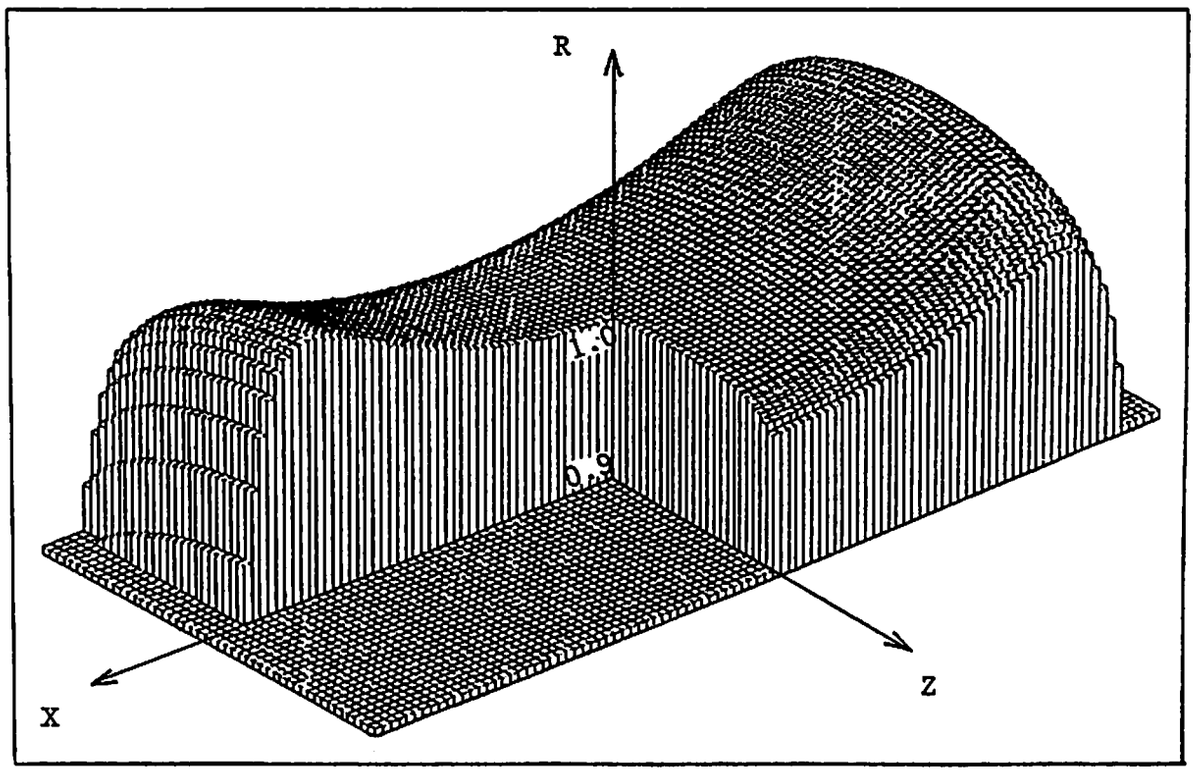

Fig. 7.22

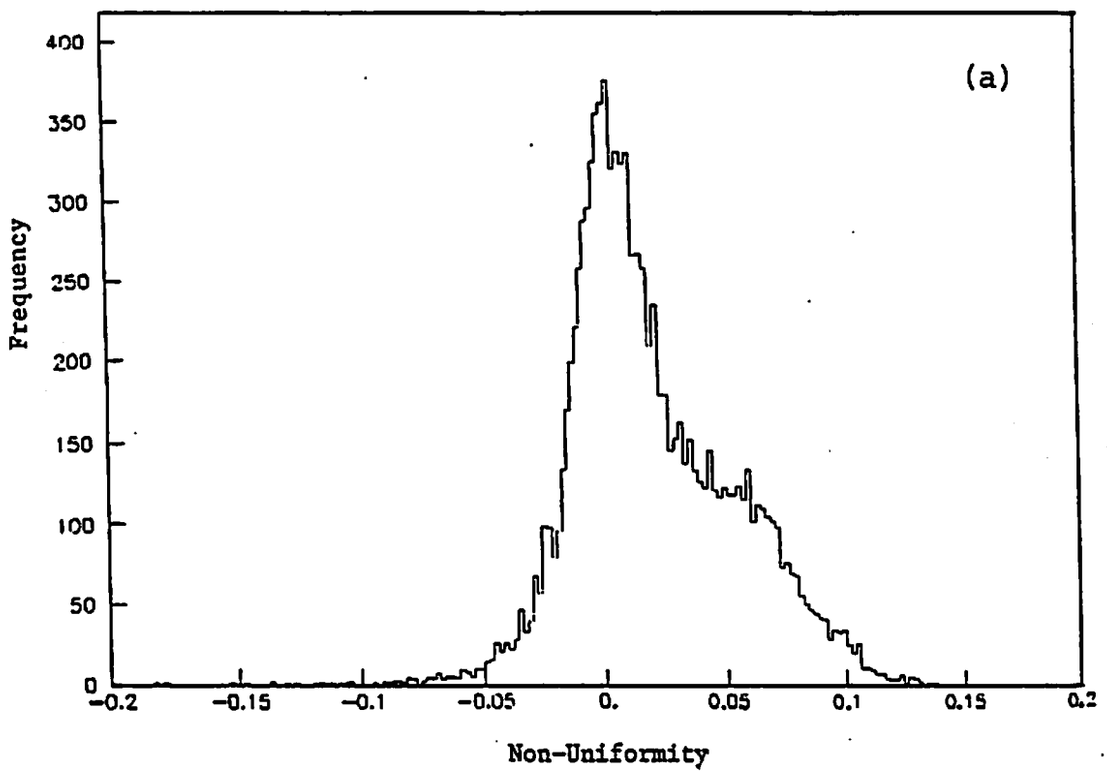
(a)
Frequency
400
350
300
250
200
150
100
50
0
-0.2
-0.15
-0.1
-0.05
0.
0.05
0.1
0.15
0.2
Non-Uniformity

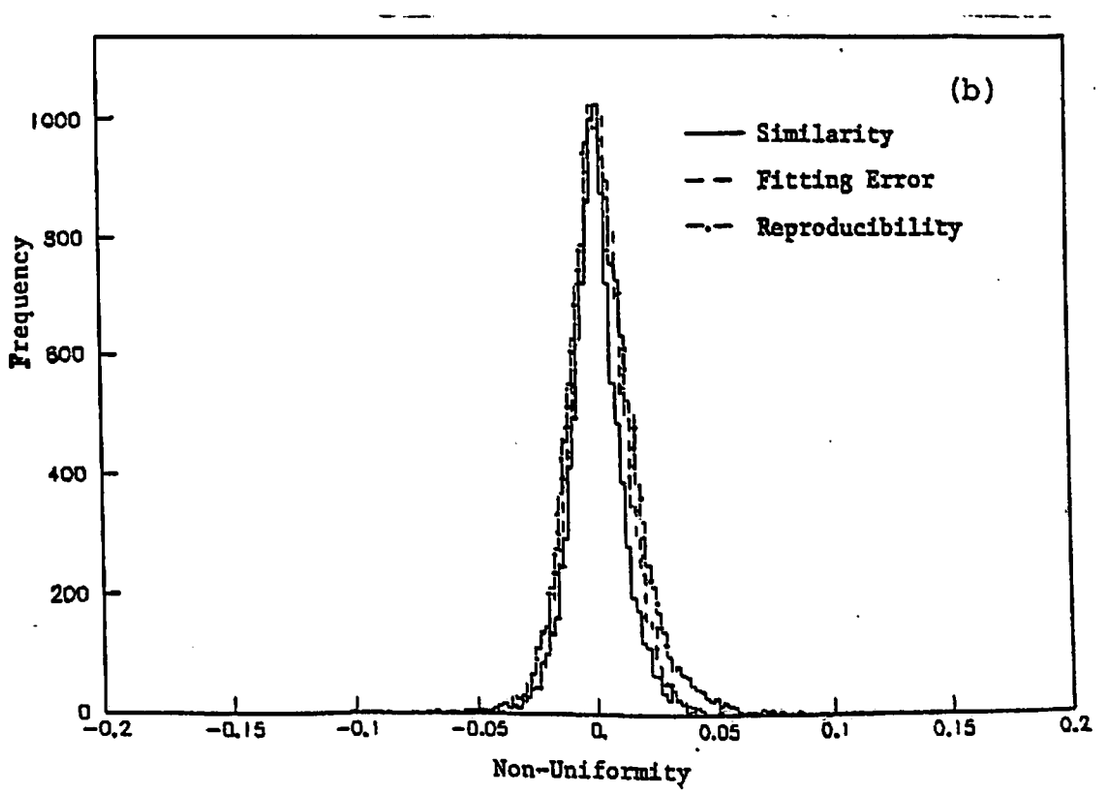
(b)
Similarity
Fitting Error
Reproducibility
Frequency
1000
800
600
400
200
0
-0.2
-0.15
-0.1
-0.05
0.
0.05
0.1
0.15
0.2
Non-Uniformity

Fig. 7.23

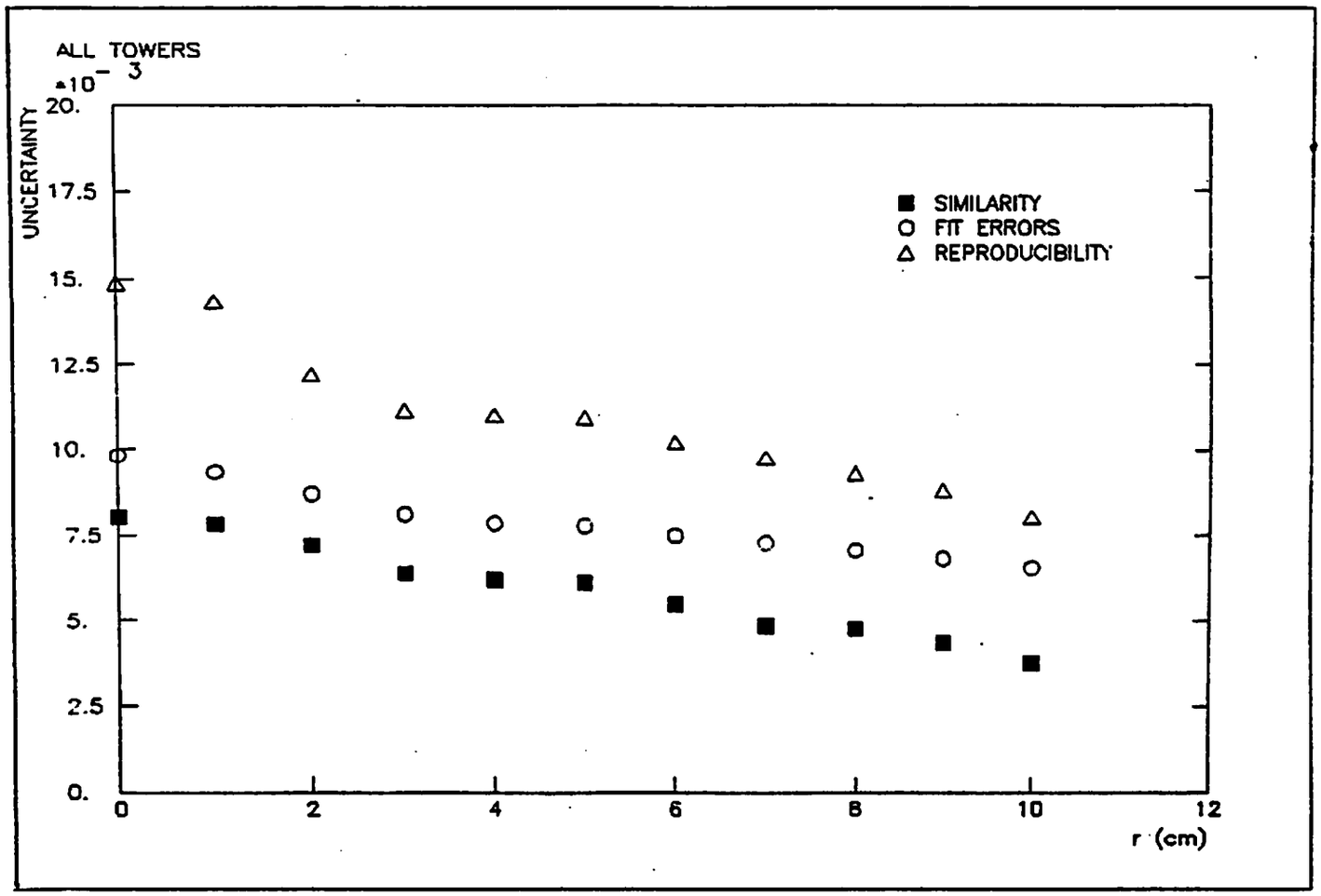
ALL TOWERS
*10^-3
UNCERTAINTY
20.
17.5
15.
12.5
10.
7.5
5.
2.5
0.
0
2
4
6
8
10
12
r (cm)
SIMILARITY
FIT ERRORS
REPRODUCIBILITY

Fig. 7.24

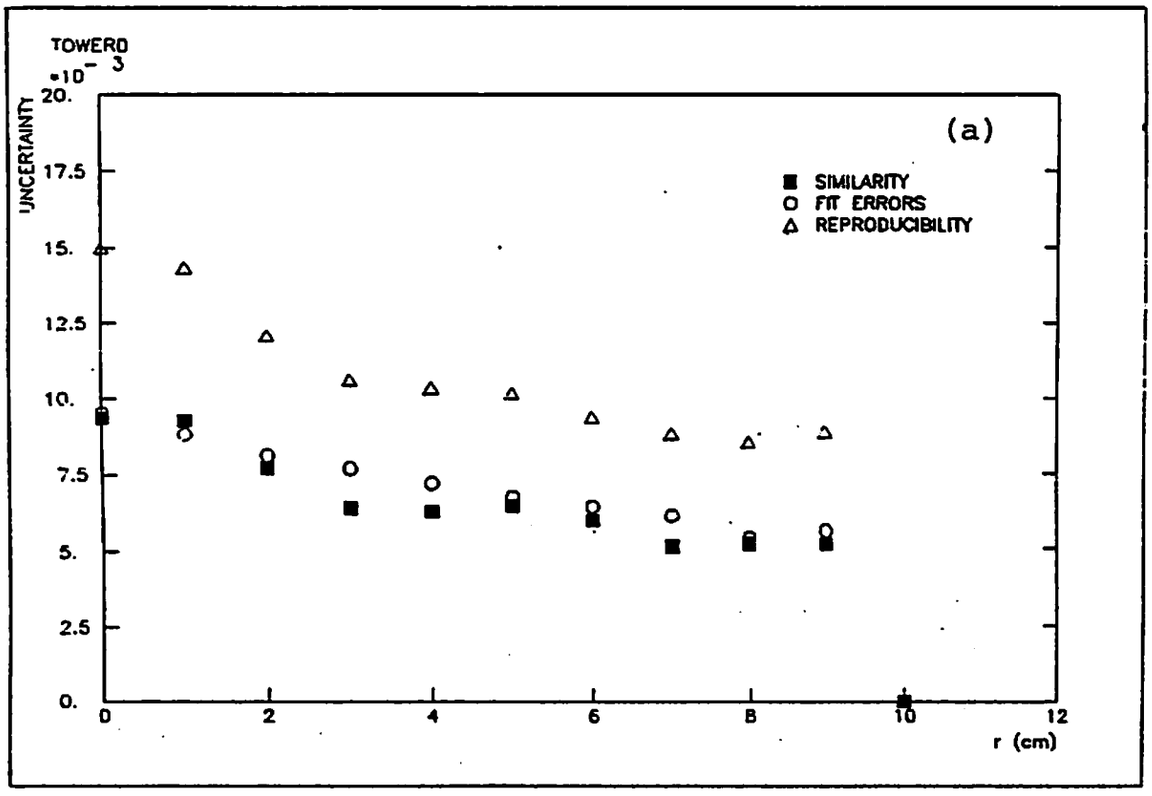
TOWER0
*10^-3
UNCERTAINTY
20.
17.5
15.
12.5
10.
7.5
5.
2.5
0.
0
2
4
6
8
10
12
r (cm)
(a)
SIMILARITY
FIT ERRORS
REPRODUCIBILITY

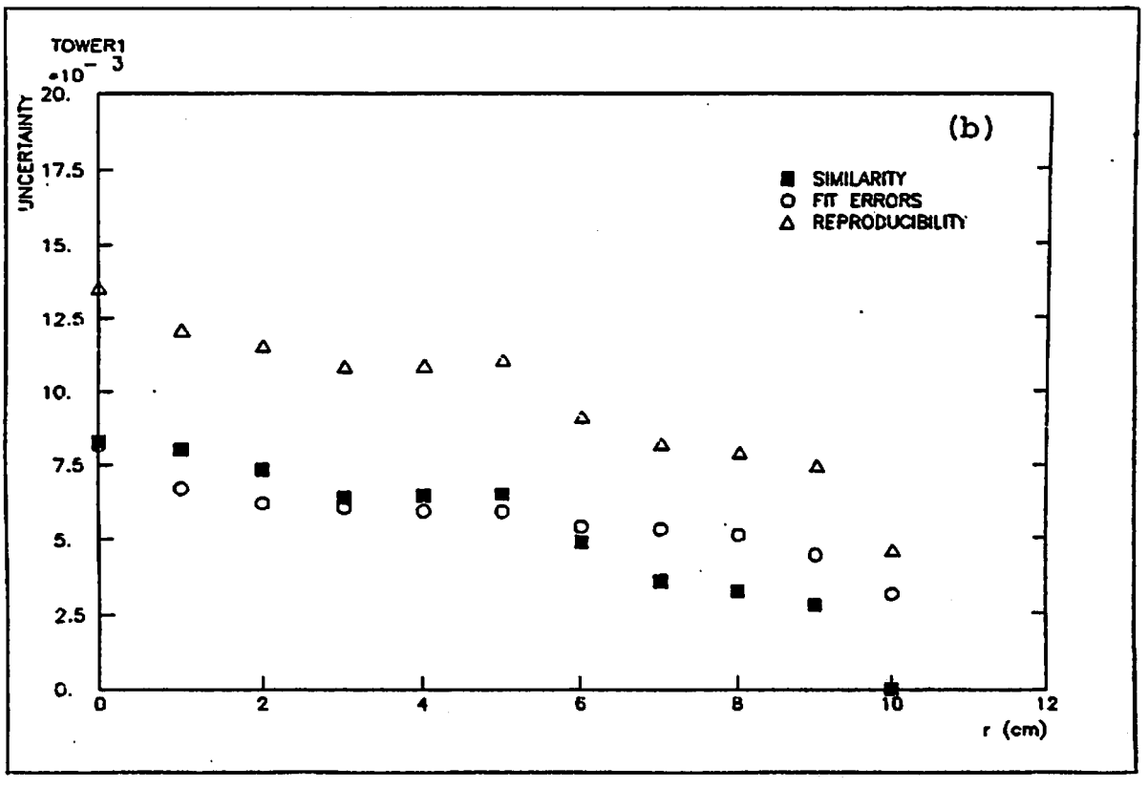
TOWER1
*10^-3
UNCERTAINTY
20.
17.5
15.
12.5
10.
7.5
5.
2.5
0.
0
2
4
6
8
10
12
r (cm)
(b)
SIMILARITY
FIT ERRORS
REPRODUCIBILITY

Fig. 7.25

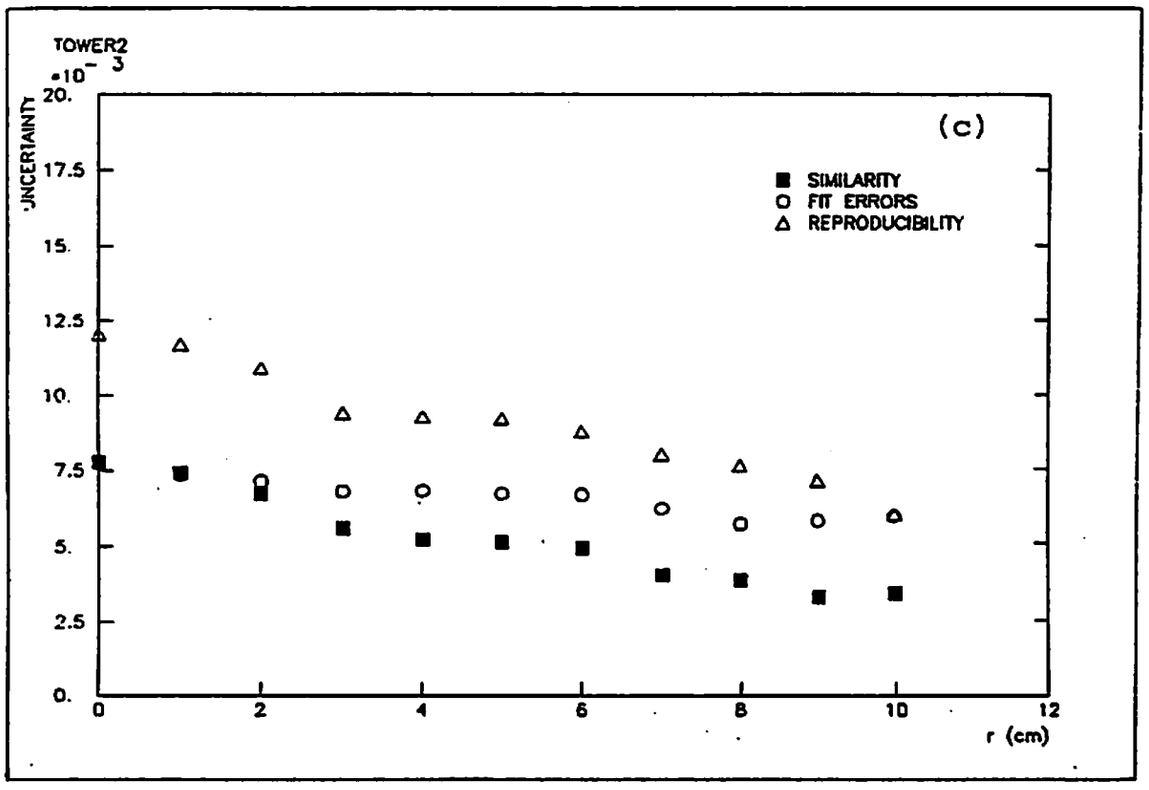
TOWER2
*10^-3
UNCERTAINTY
20.
17.5
15.
12.5
10.
7.5
5.
2.5
0.
0
2
4
6
8
10
12
r (cm)
(c)
SIMILARITY
FIT ERRORS
REPRODUCIBILITY

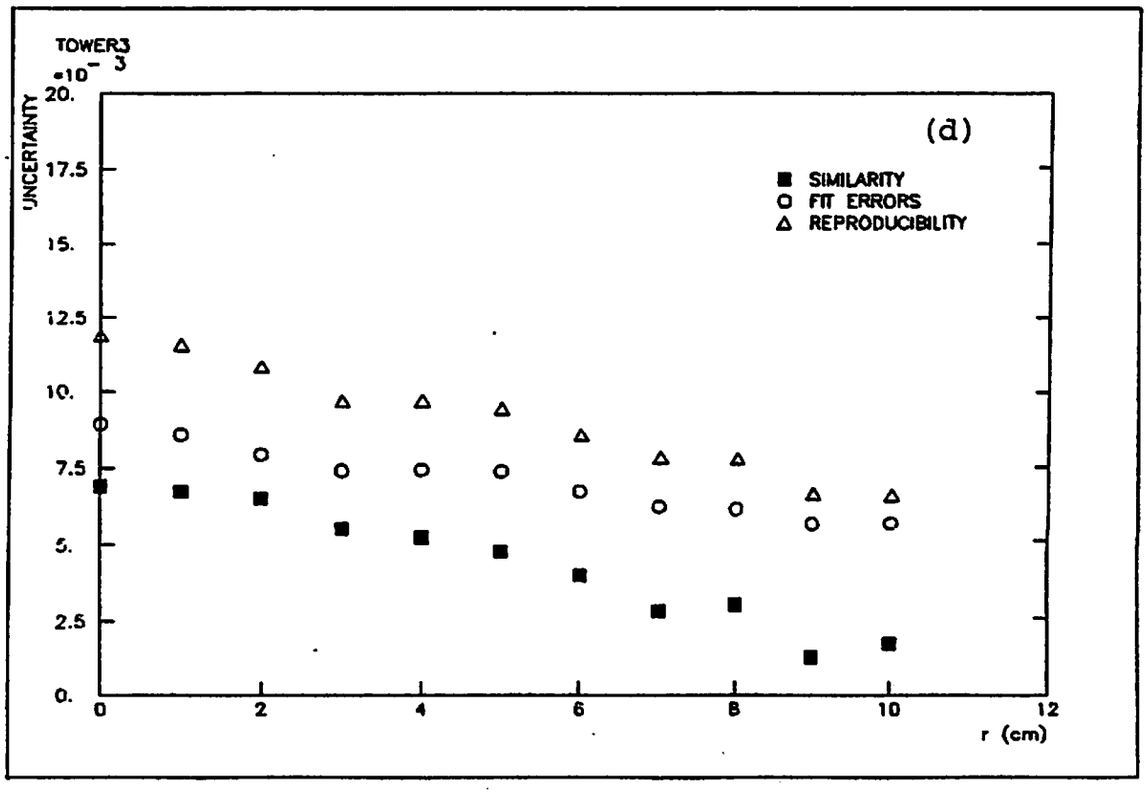
TOWER3
*10^-3
UNCERTAINTY
20.
17.5
15.
12.5
10.
7.5
5.
2.5
0.
0
2
4
6
8
10
12
r (cm)
(d)
SIMILARITY
FIT ERRORS
REPRODUCIBILITY

Fig. 7.25

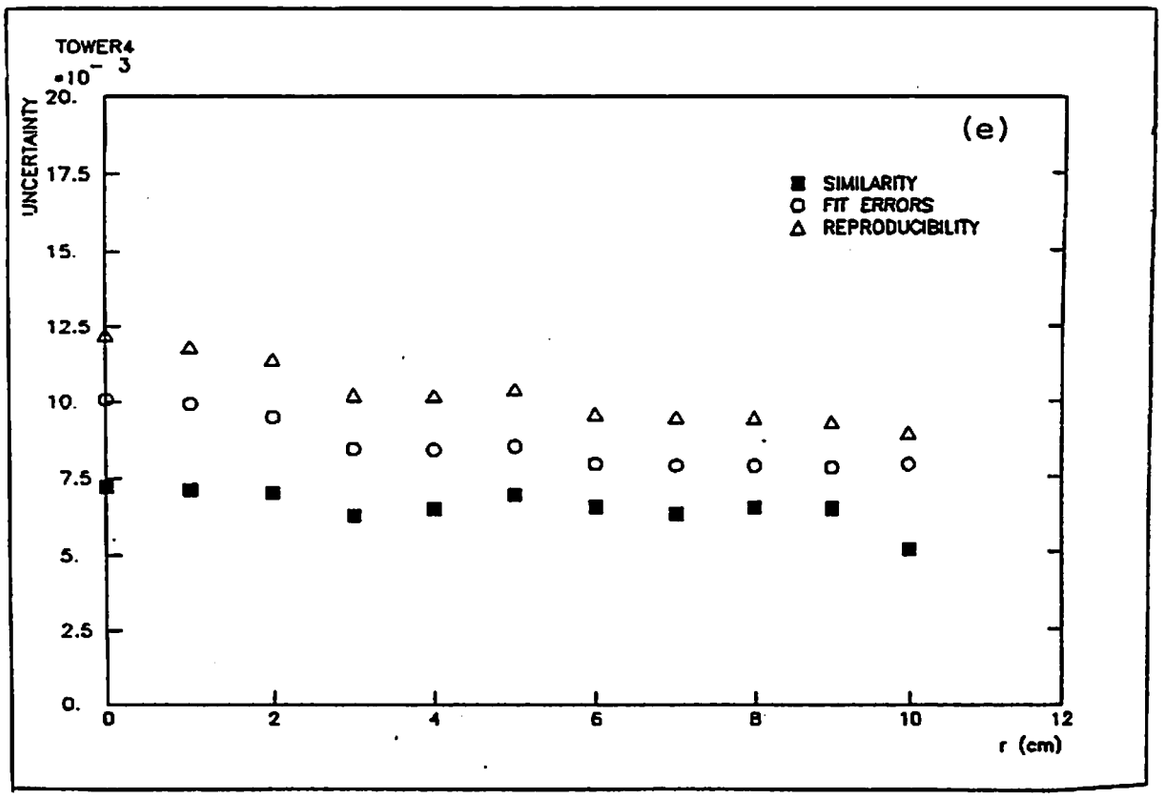
TOWER4
•10⁻ 3
UNCERTAINTY
20.
17.5
15.
12.5
10.
7.5
5.
2.5
0.
0
2
4
6
8
10
12
r (cm)
(e)
SIMILARITY
FIT ERRORS
REPRODUCIBILITY

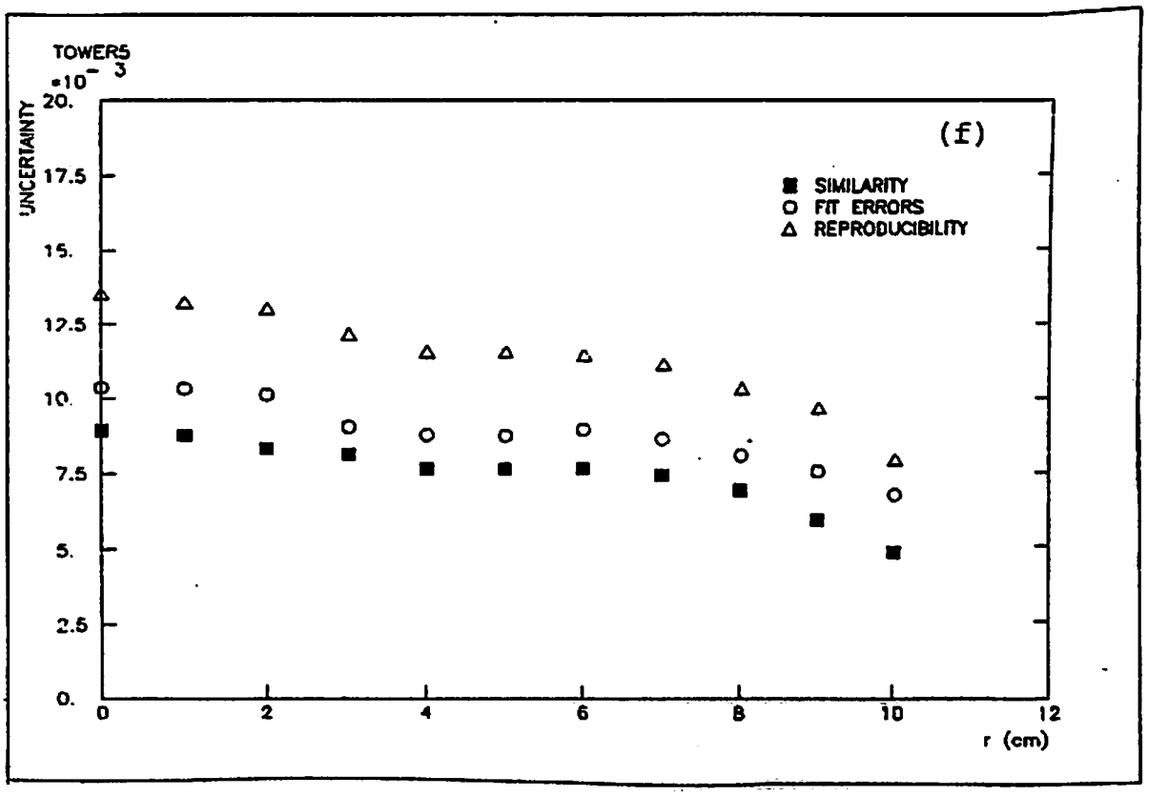
TOWER5
•10⁻ 3
UNCERTAINTY
20.
17.5
15.
12.5
10.
7.5
5.
2.5
0.
0
2
4
6
8
10
12
r (cm)
(f)
SIMILARITY
FIT ERRORS
REPRODUCIBILITY

Fig. 7.25

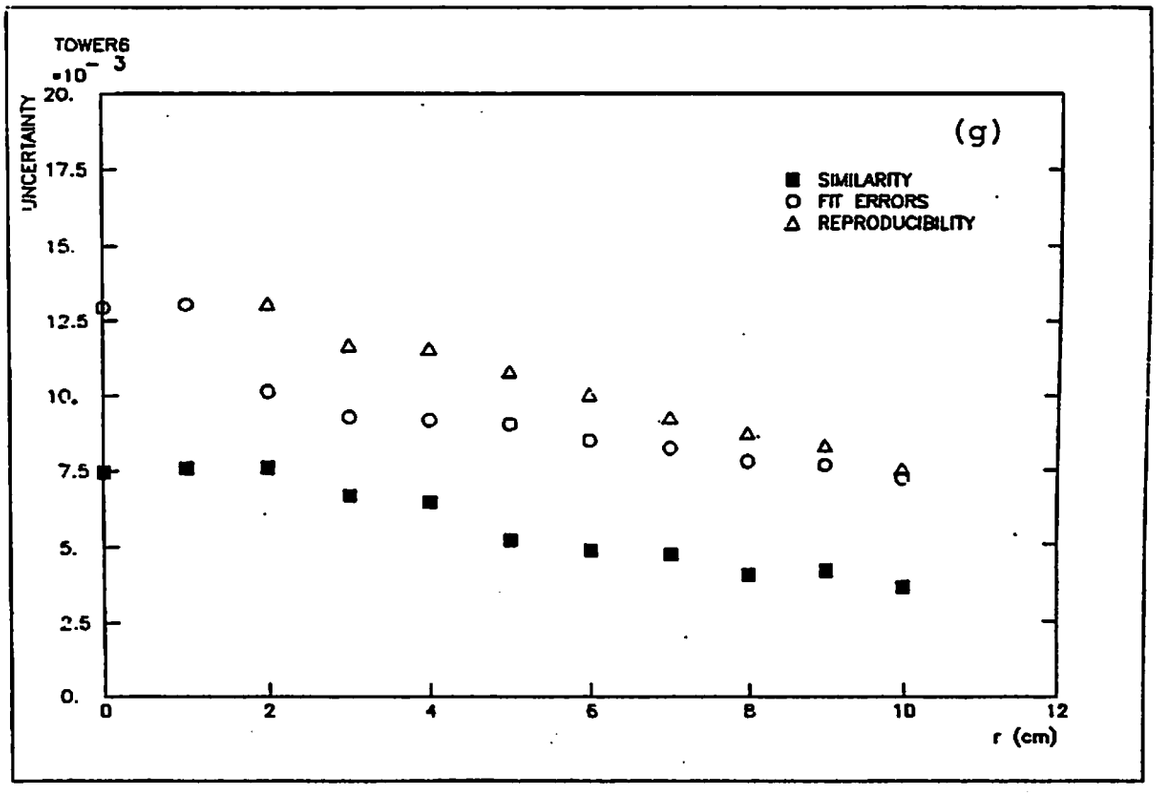
TOWER6
*10^-3
UNCERTAINTY
20.
17.5
15.
12.5
10.
7.5
5.
2.5
0.
0
2
4
6
8
10
12
r (cm)
(g)
SIMILARITY
FIT ERRORS
REPRODUCIBILITY

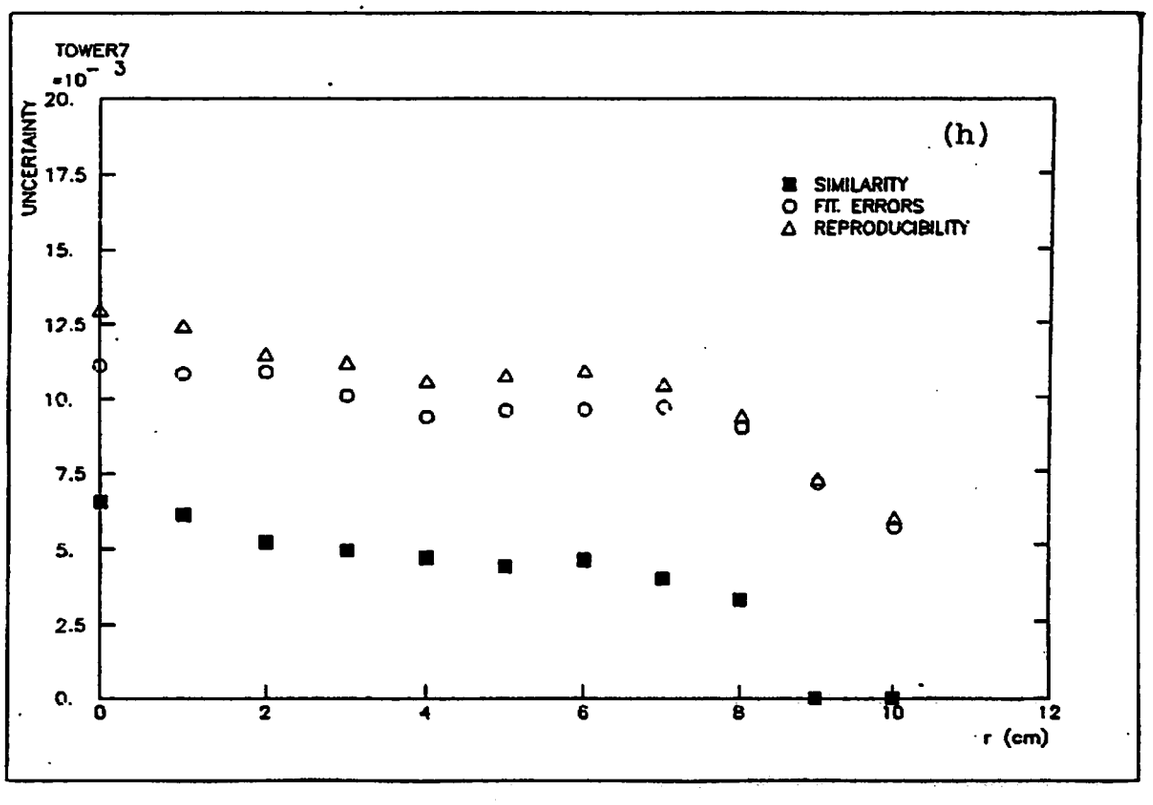
TOWER7
*10^-3
UNCERTAINTY
20.
17.5
15.
12.5
10.
7.5
5.
2.5
0.
0
2
4
6
8
10
12
r (cm)
(h)
SIMILARITY
FIT. ERRORS
REPRODUCIBILITY

Fig. 7.25

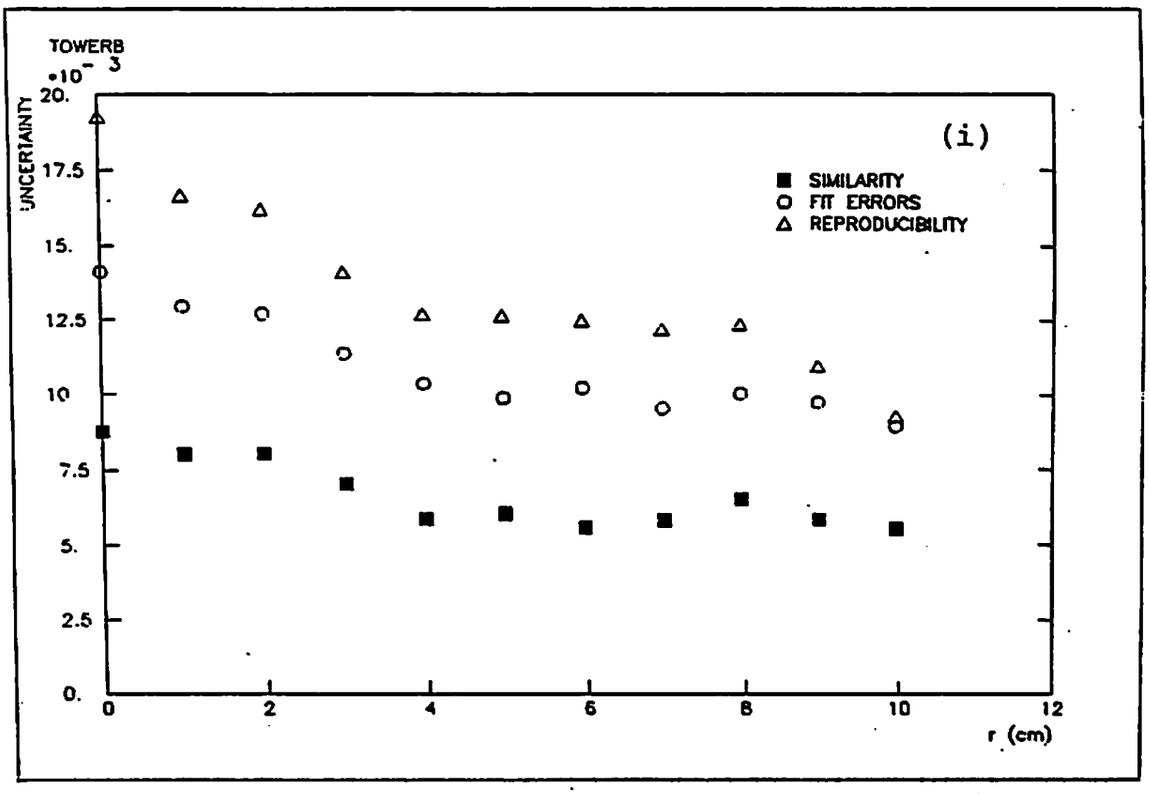
TOWERB
•10⁻ 3
UNCERTAINTY
20.
17.5
15.
12.5
10
7.5
5.
2.5
0.
0
2
4
6
8
10
12
r (cm)
(i)
SIMILARITY
FIT ERRORS
REPRODUCIBILITY

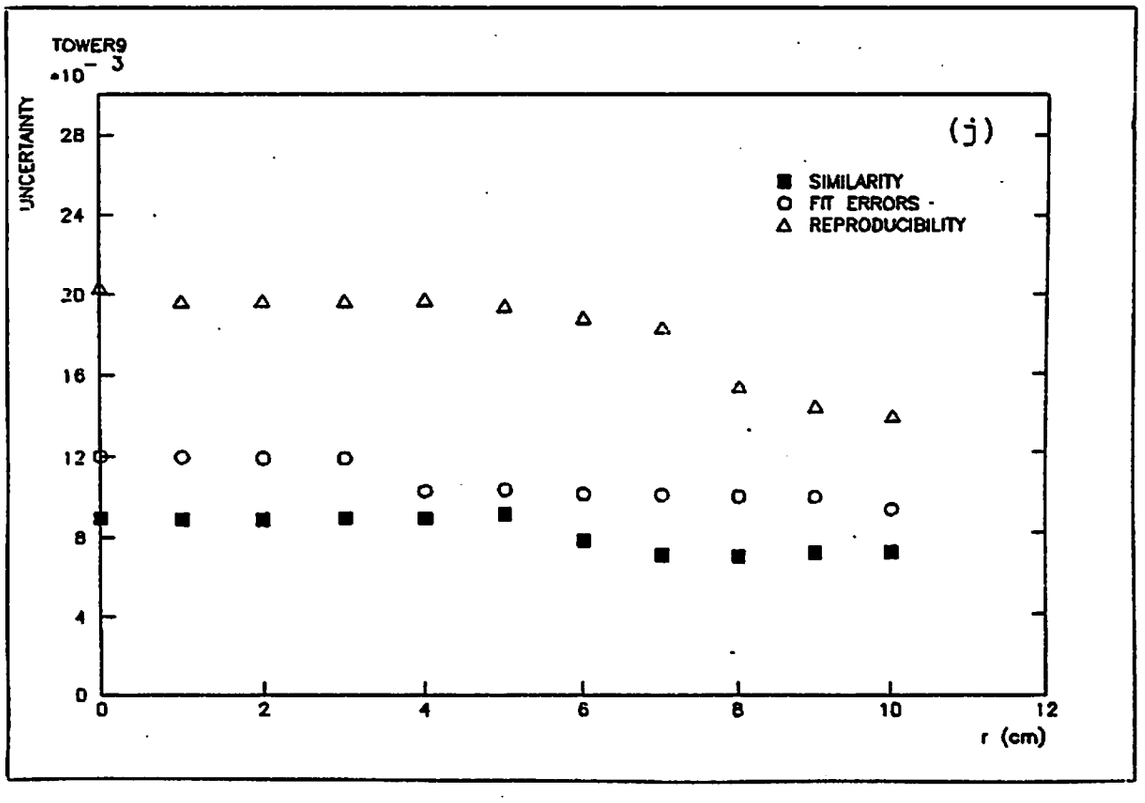
TOWER9
•10⁻ 3
UNCERTAINTY
28
24
20
16
12
8
4
0
0
2
4
6
8
10
12
r (cm)
(j)
SIMILARITY
FIT ERRORS
REPRODUCIBILITY

Fig. 7.25

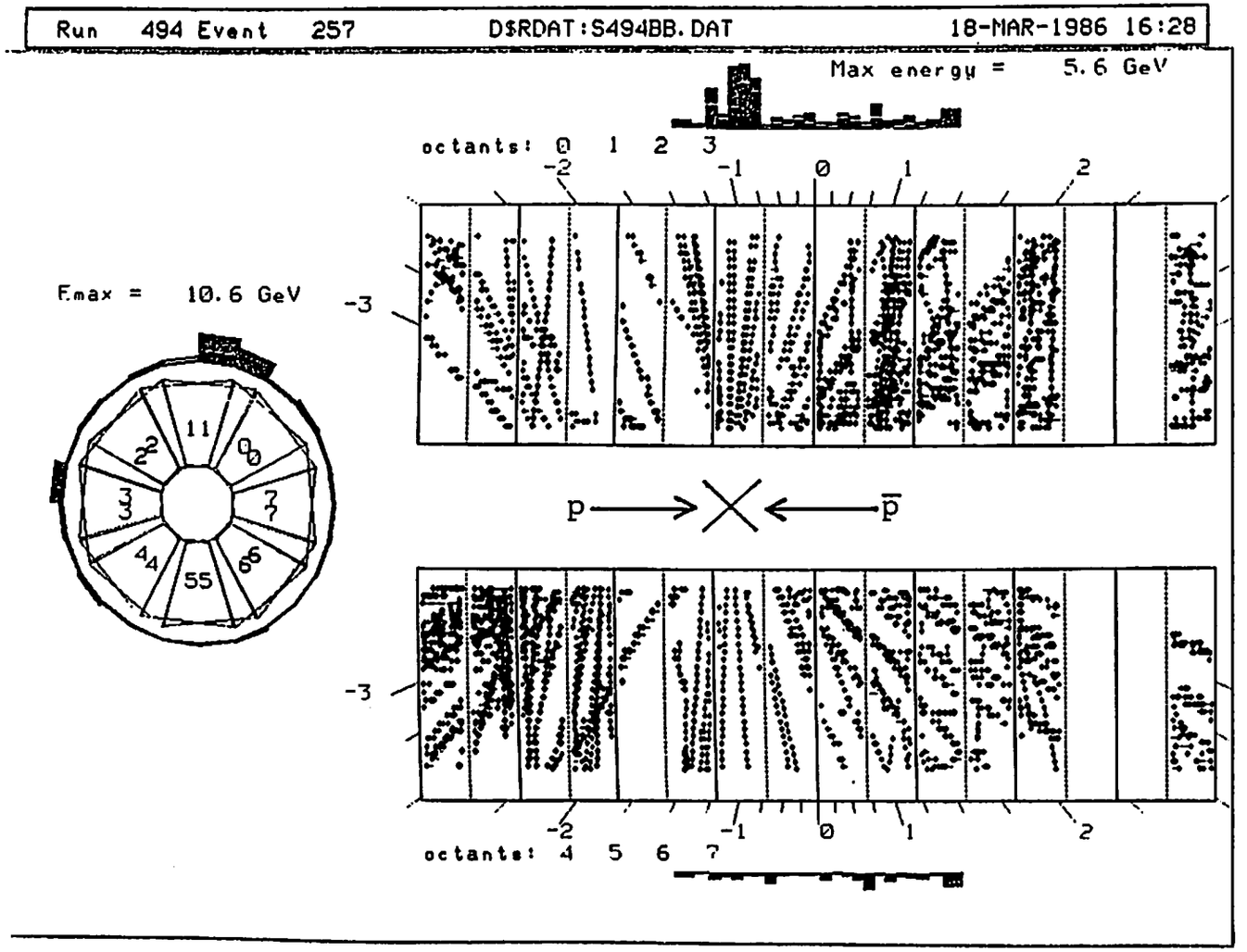
Run 494 Event 257
D$RDAT:S494BB.DAT
18-MAR-1986 16:28
Max energy = 5.6 GeV
octants: 0 1 2 3
-2
-1
0
1
2
Emax = 10.6 GeV
-3
11
00
22
33
77
44
66
55
p
p̄
-3
-2
-1
0
1
2
octants: 4 5 6 7

Fig. 8.1

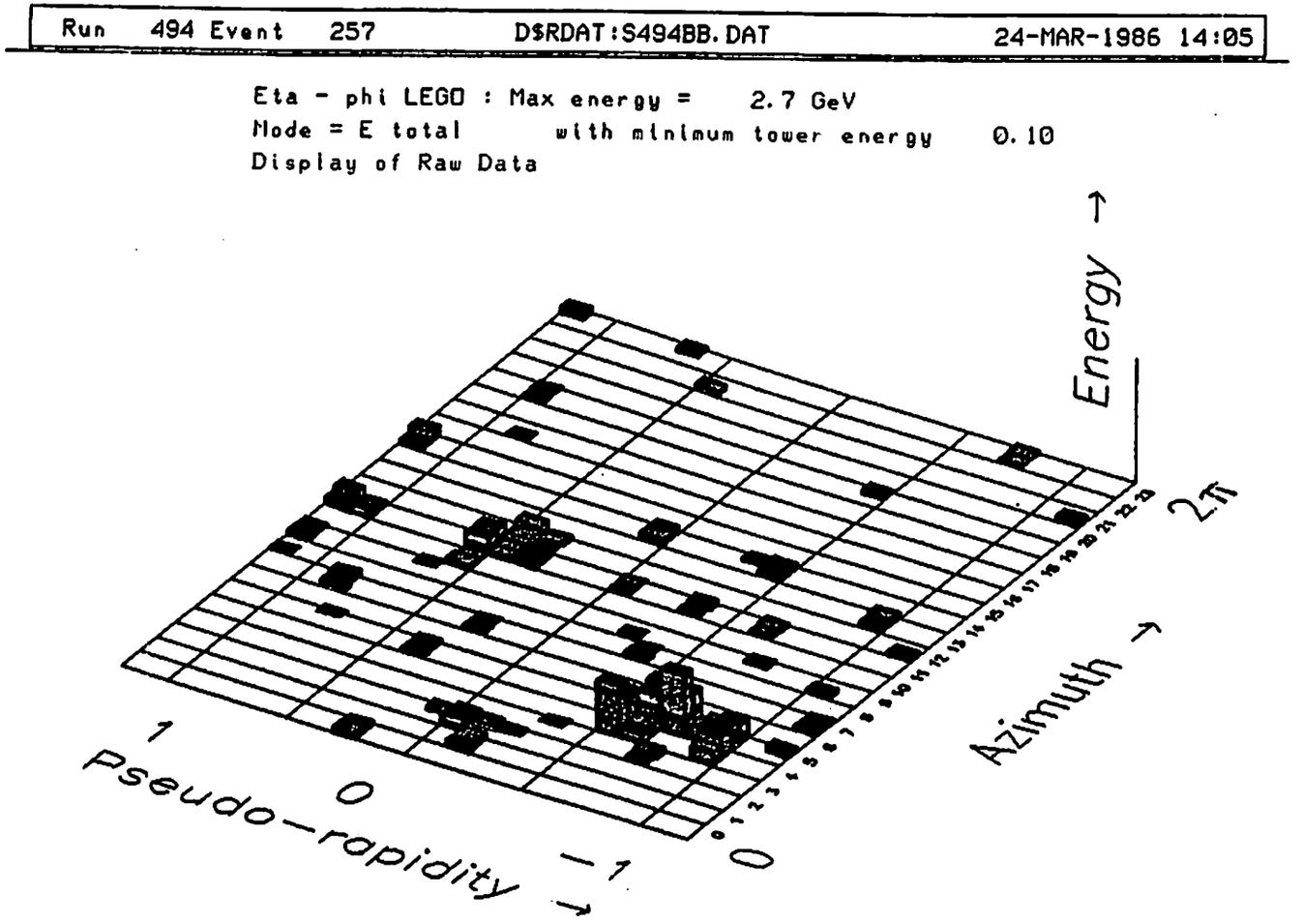
Run 494 Event 257 D$RDAT:S494BB.DAT 24-MAR-1986 14:05
Eta - phi LEGO : Max energy = 2.7 GeV
Mode = E total with minimum tower energy 0.10
Display of Raw Data
Energy →
2π
Azimuth →
0
1
0
−1
Pseudo-rapidity →

Fig. 8.2

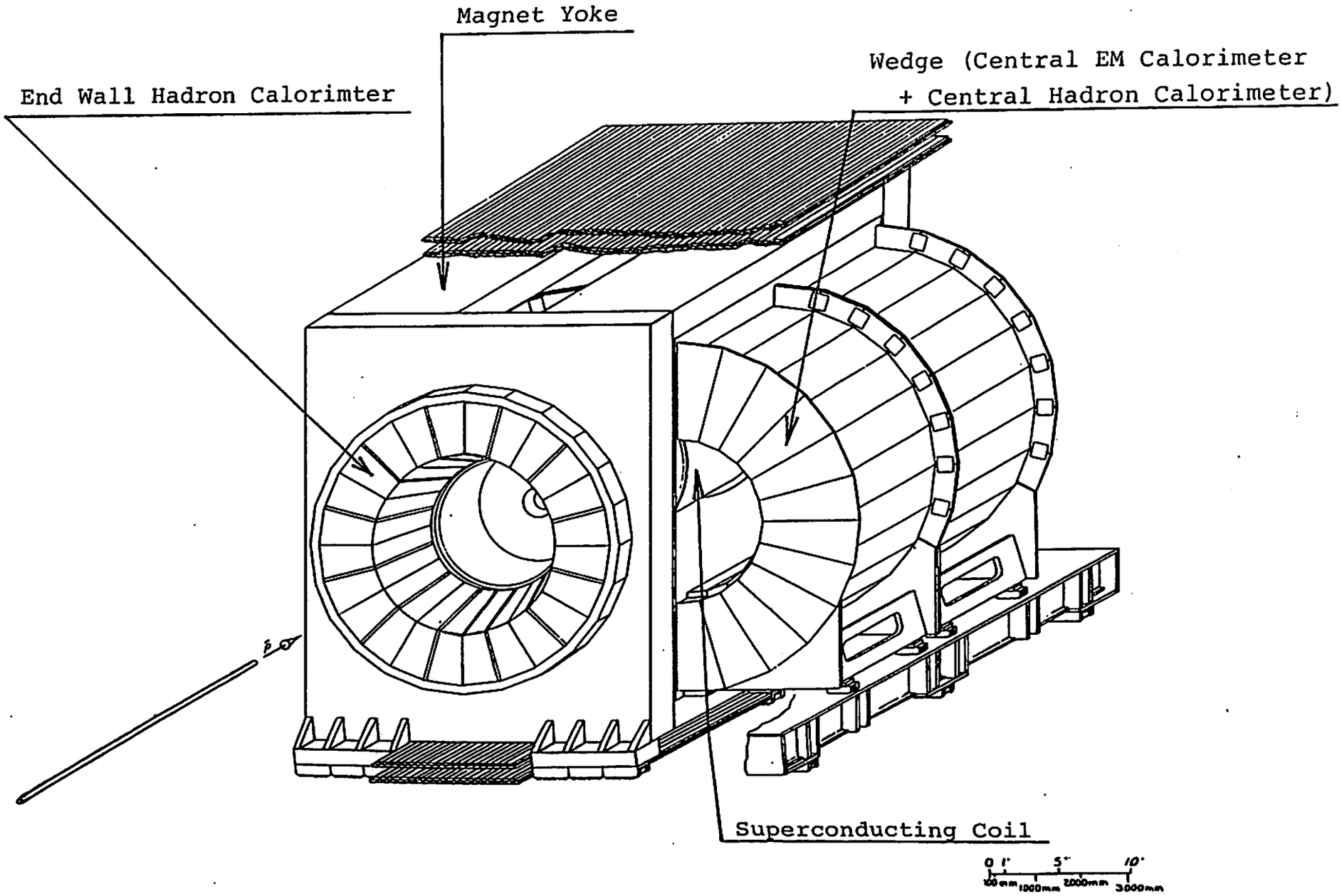
Magnet Yoke
End Wall Hadron Calorimter
Wedge (Central EM Calorimeter
+ Central Hadron Calorimeter)
Superconducting Coil

Fig. 8.3

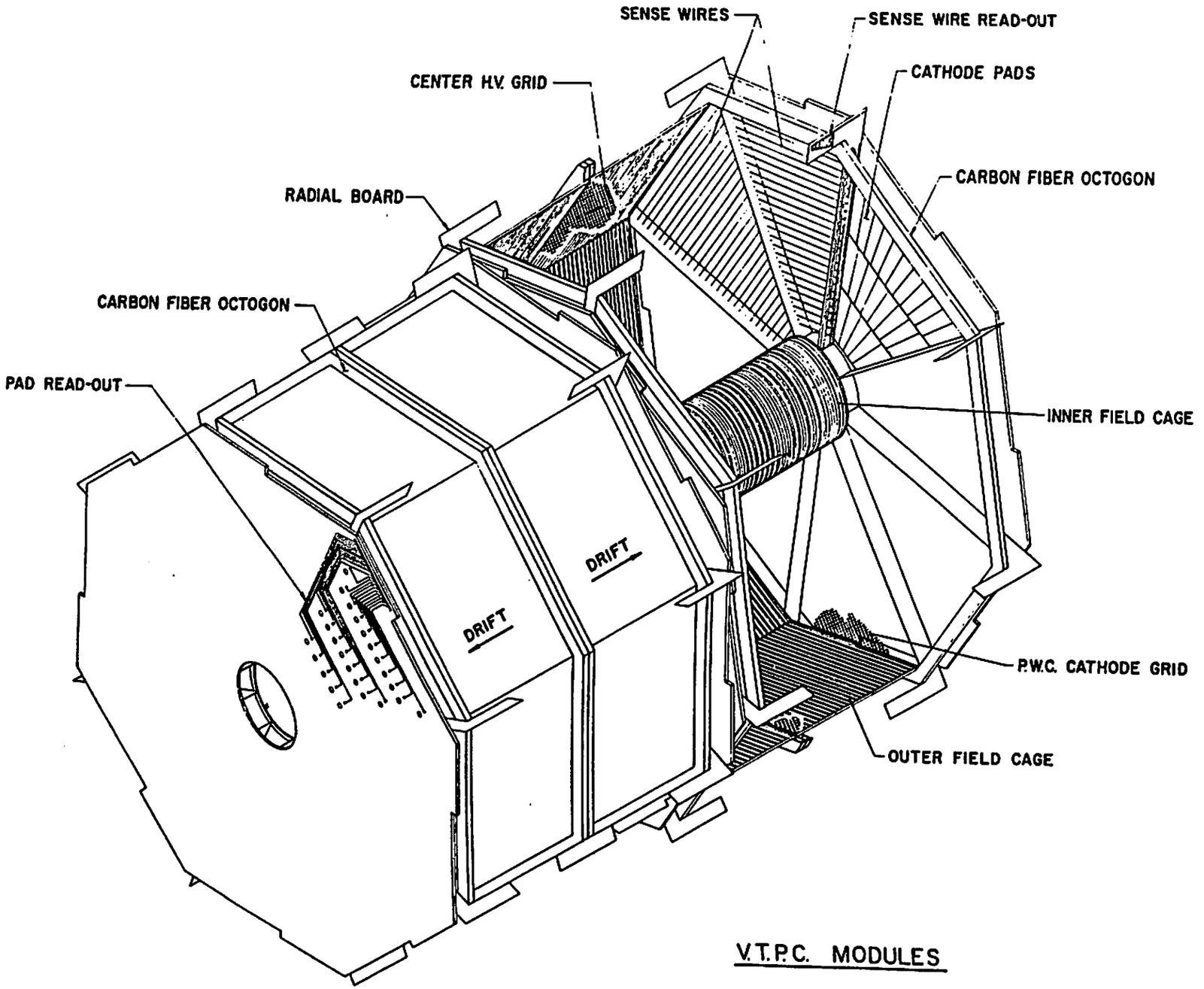

V.T.P.C. MODULES

Fig. 8.4

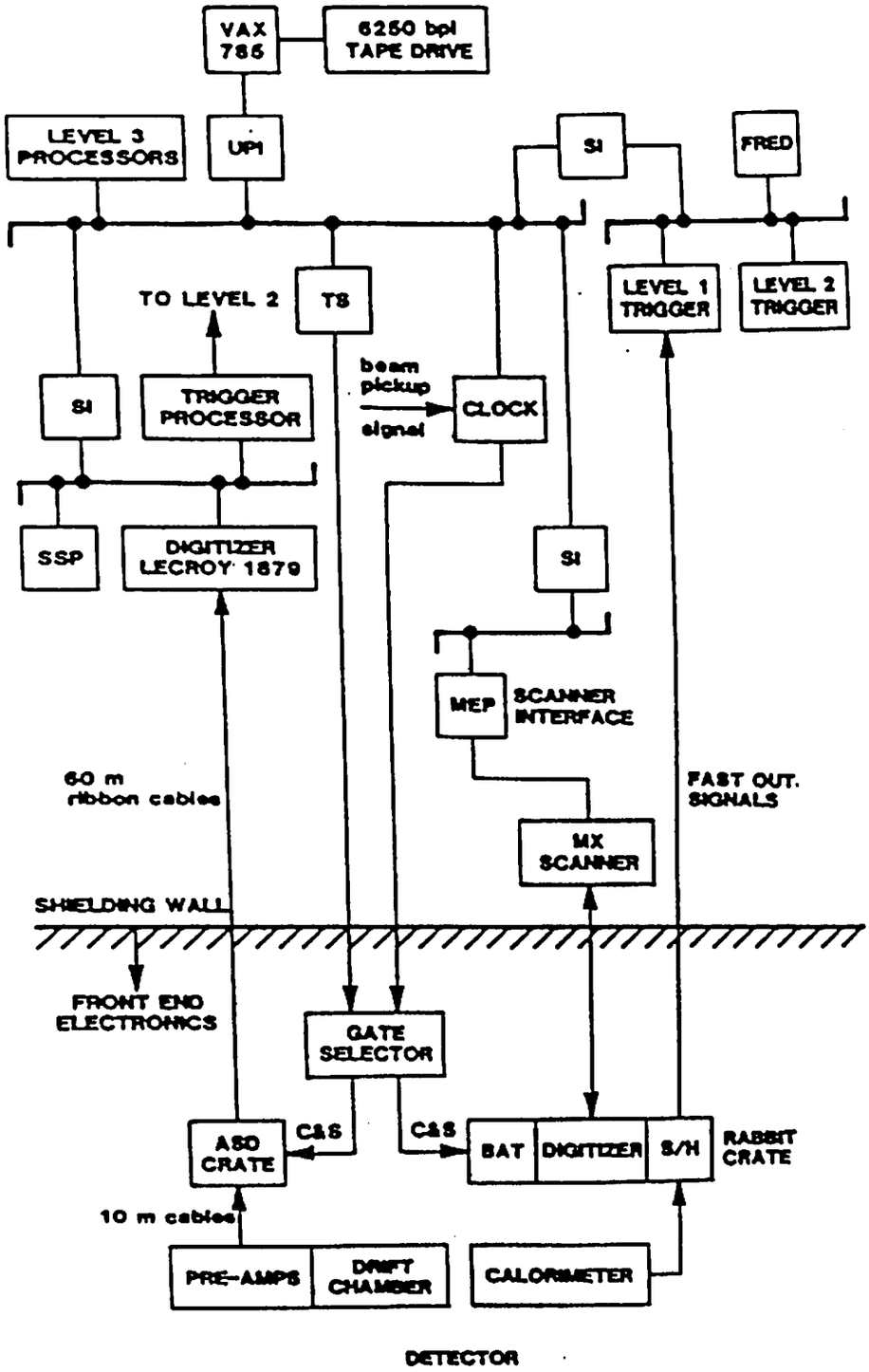

UPI : UNIBUS PROCESSOR INTERFACE
FRED : FINAL ROUTING AND DECISION LOGIC
TS : TRIGGER SUPERVISOR
SI : SEGMENT INTERCONNECT
SSP : SLAC SCANNER PROCESSOR
C&S : CLEAR AND STROBE SIGNAL
ASD : AMPLIFIER / SHAPER / DISCRIMINATOR
S/H : SAMPLE AND HOLD
BAT : BEFORE-AFTER TIMING

Fig. 8.5

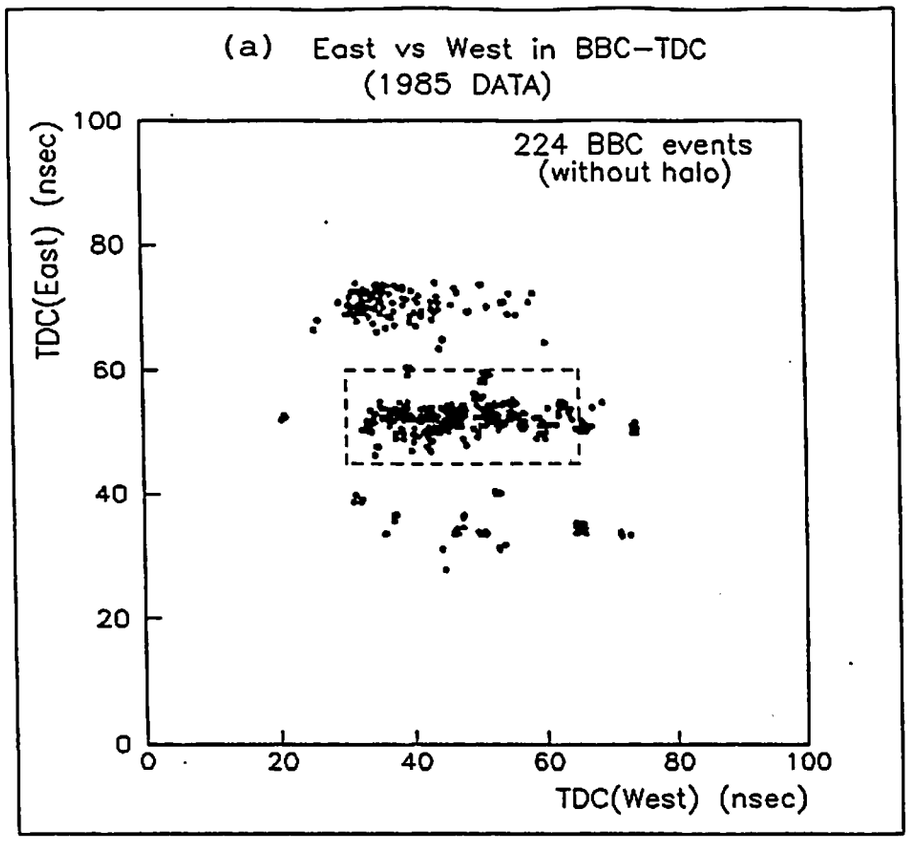
(a) East vs West in BBC–TDC
(1985 DATA)
224 BBC events
(without halo)
TDC(East) (nsec)
TDC(West) (nsec)
0
20
40
60
80
100

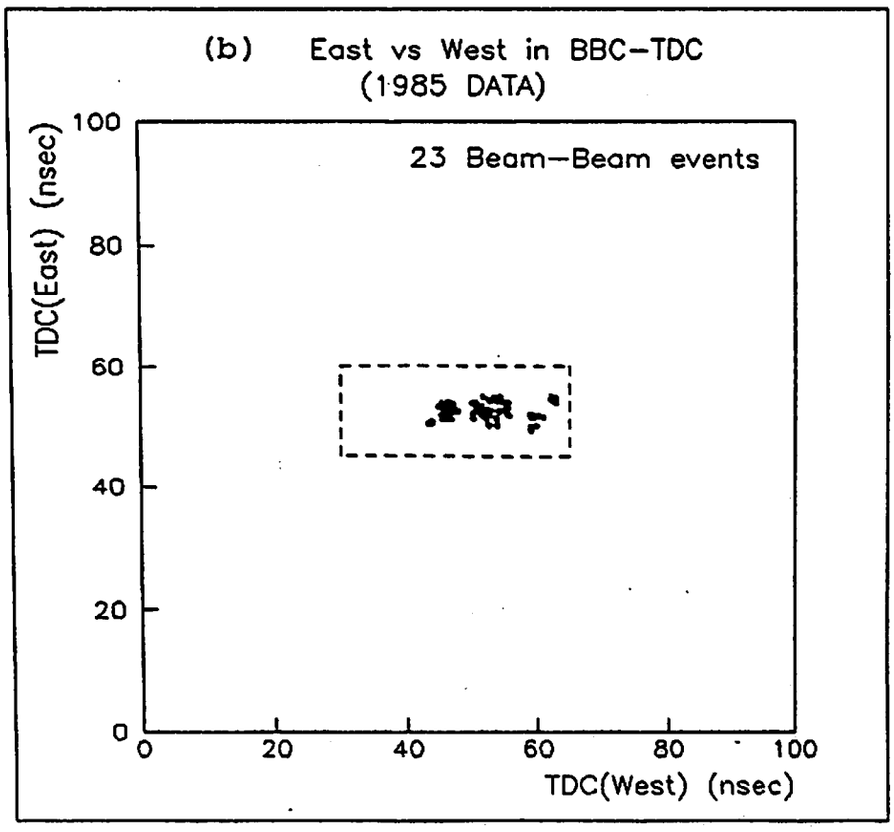
(b) East vs West in BBC–TDC
(1985 DATA)
23 Beam–Beam events
TDC(East) (nsec)
TDC(West) (nsec)
0
20
40
60
80
100

Fig. 8.6

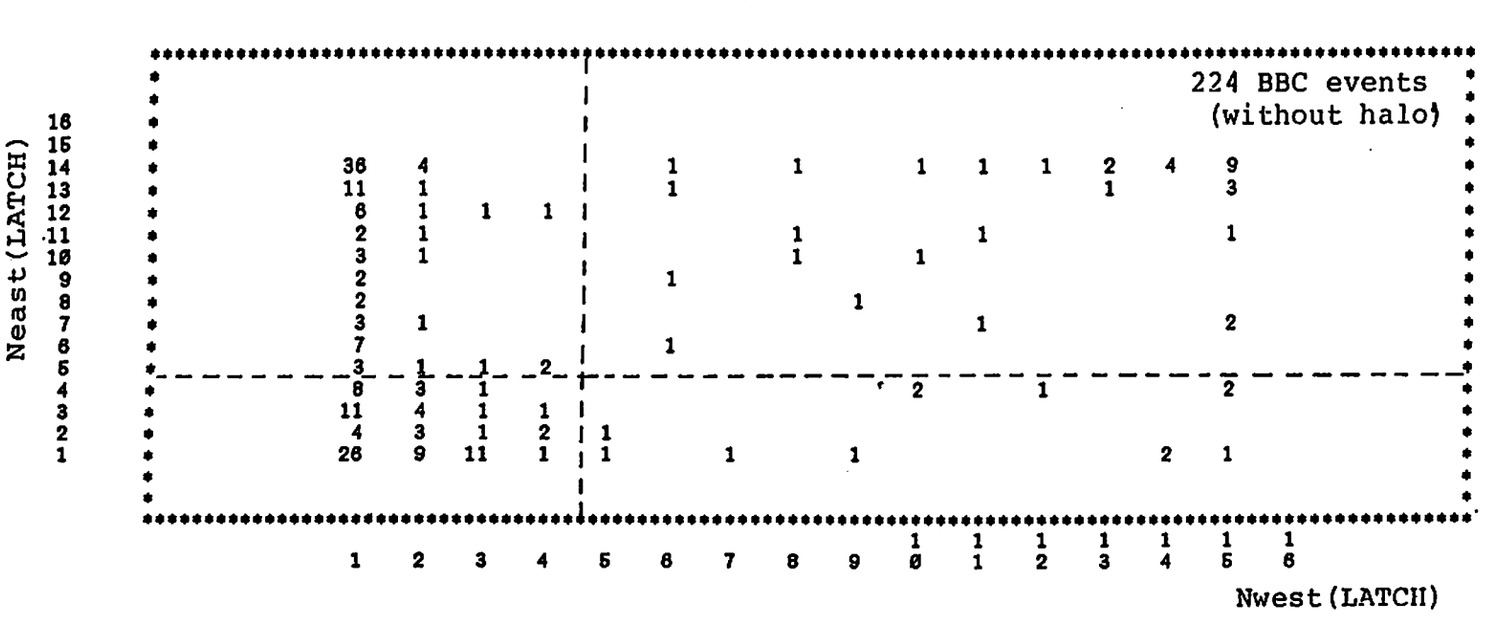
(a) Neast(LATCH) vs Nwest(LATCH)
(1985 Data)
224 BBC events
(without halo)
Neast(LATCH)
Nwest(LATCH)

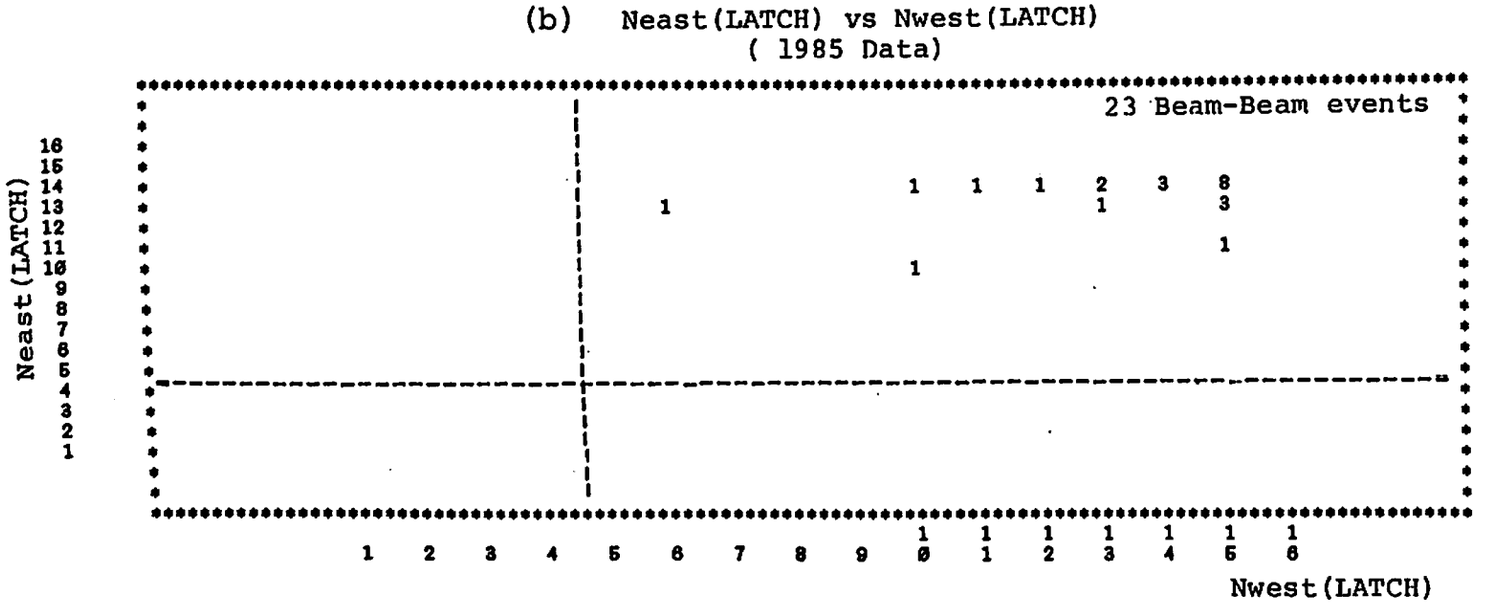
(b) Neast(LATCH) vs Nwest(LATCH)
(1985 Data)
23 Beam-Beam events
Neast(LATCH)
Nwest(LATCH)

Fig. 8.7

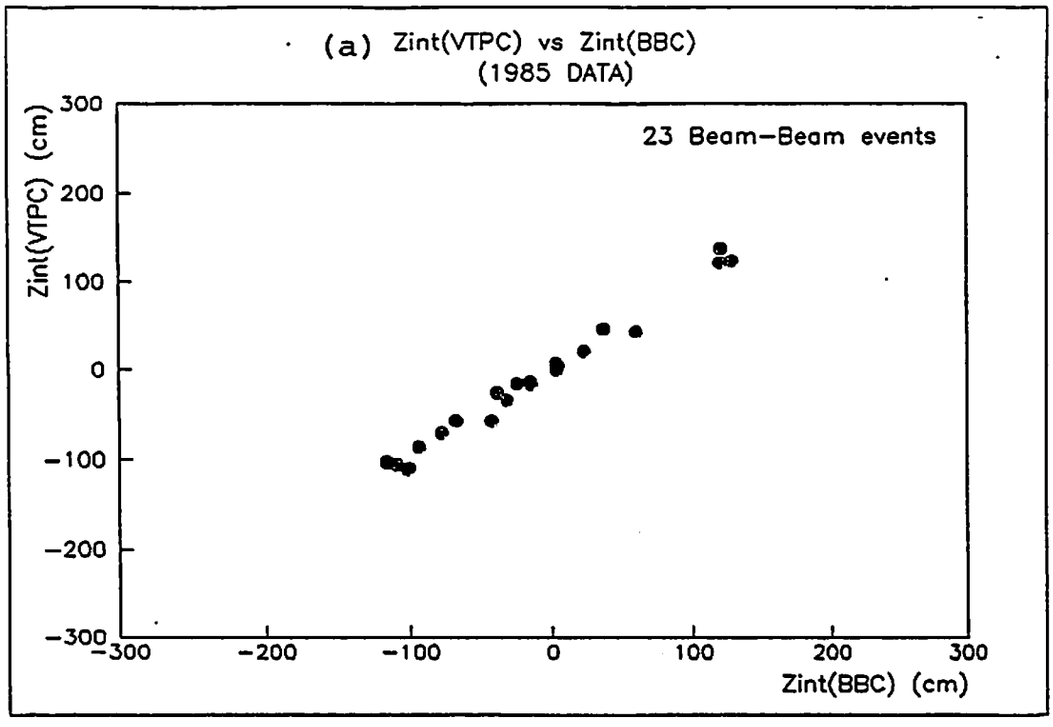
(a) Zint(VTPC) vs Zint(BBC)
(1985 DATA)
23 Beam–Beam events
Zint(VTPC) (cm)
300
200
100
0
−100
−200
−300
−300
−200
−100
0
100
200
300
Zint(BBC) (cm)

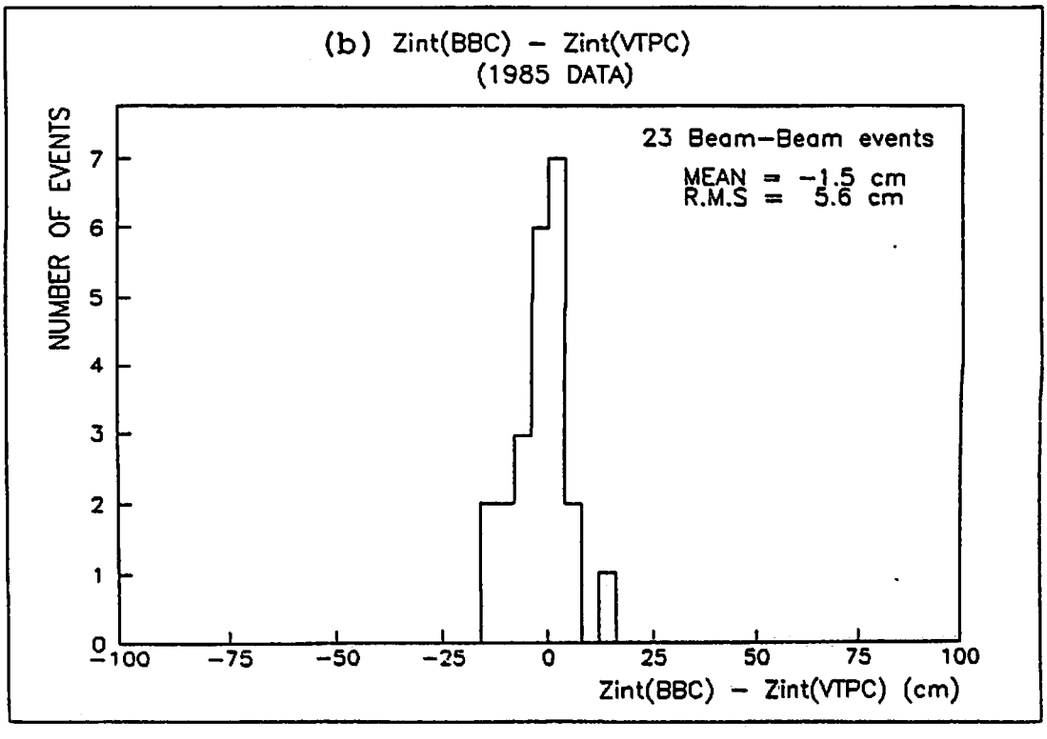
(b) Zint(BBC) − Zint(VTPC)
(1985 DATA)
23 Beam–Beam events
MEAN = −1.5 cm
R.M.S = 5.6 cm
NUMBER OF EVENTS
7
6
5
4
3
2
1
0
−100
−75
−50
−25
0
25
50
75
100
Zint(BBC) − Zint(VTPC) (cm)

Fig. 8.8

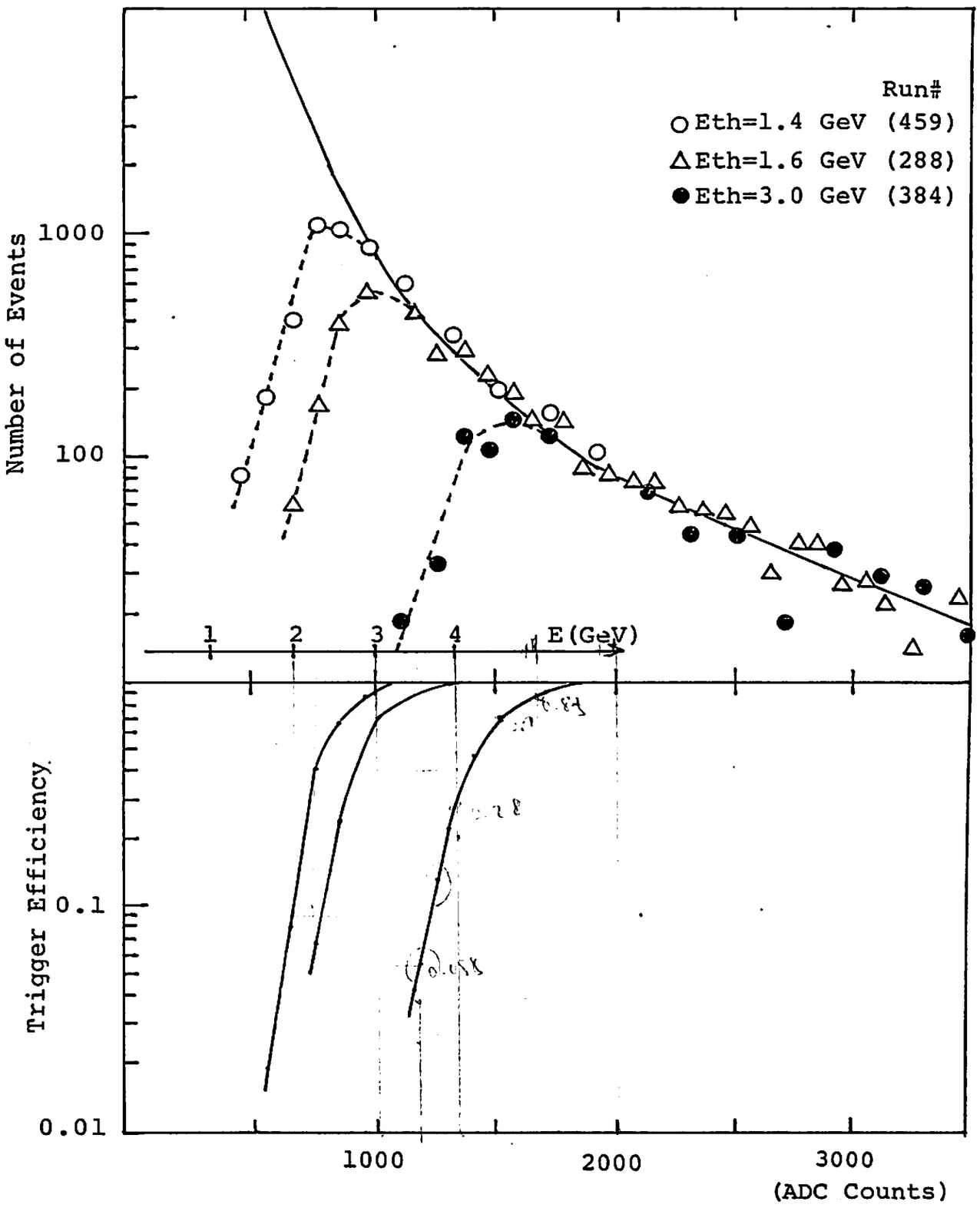
Run#
○ Eth=1.4 GeV (459)
△ Eth=1.6 GeV (288)
● Eth=3.0 GeV (384)
Number of Events
1000
100
1
2
3
4
E(GeV)
Trigger Efficiency
0.1
0.01
1000
2000
3000
(ADC Counts)
Maximum Trigger Tower Pulse Height

Fig. 8.9

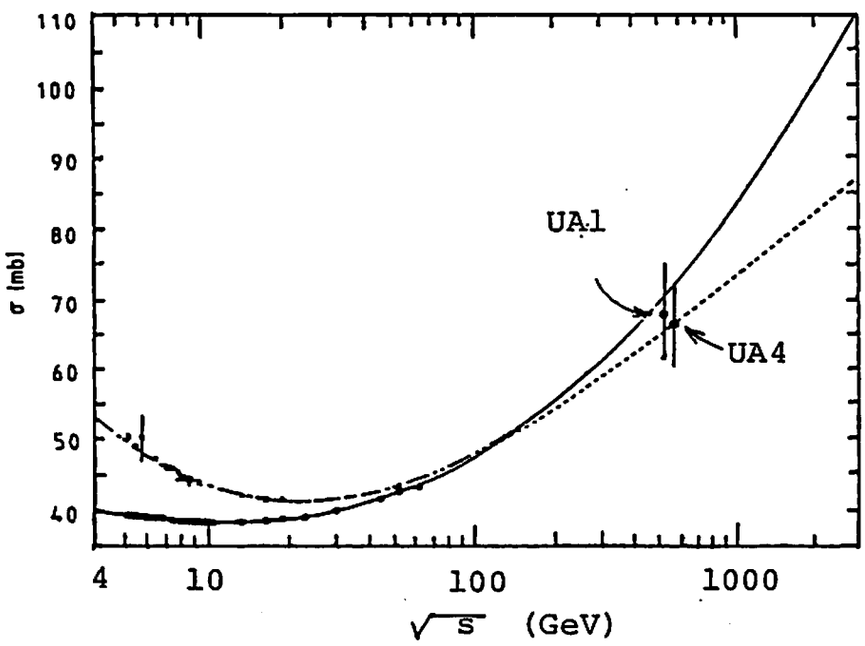

Fig. 8.10

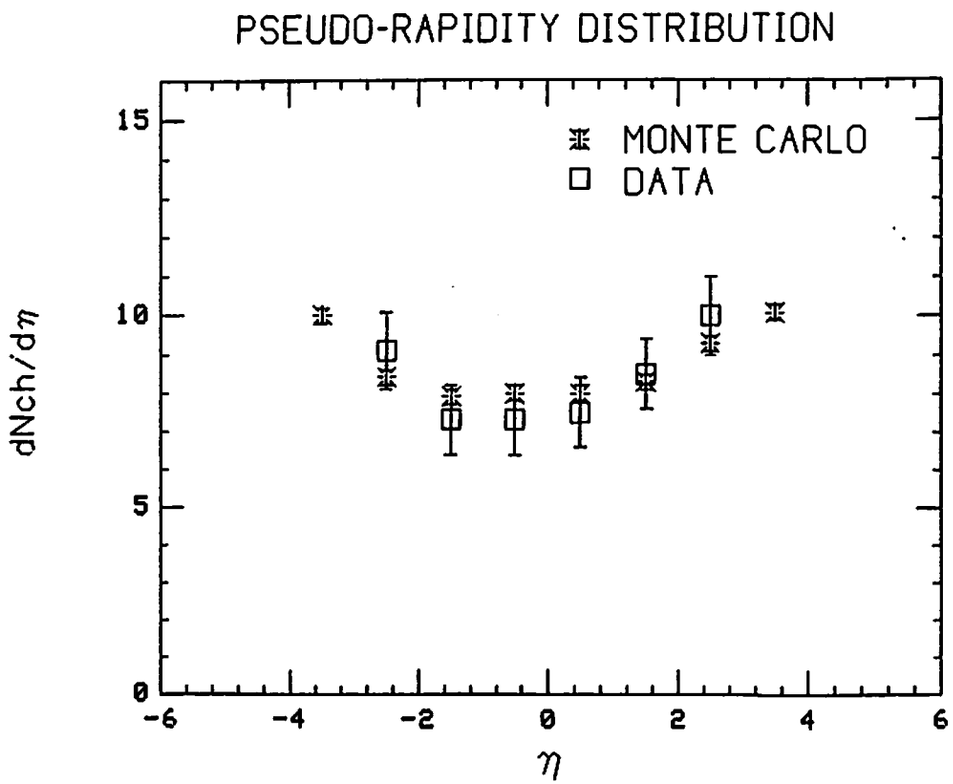
PSEUDO-RAPIDITY DISTRIBUTION
MONTE CARLO
DATA
dNch/dη
15
10
5
0
-6
-4
-2
0
2
4
6
η

Fig. 8.11

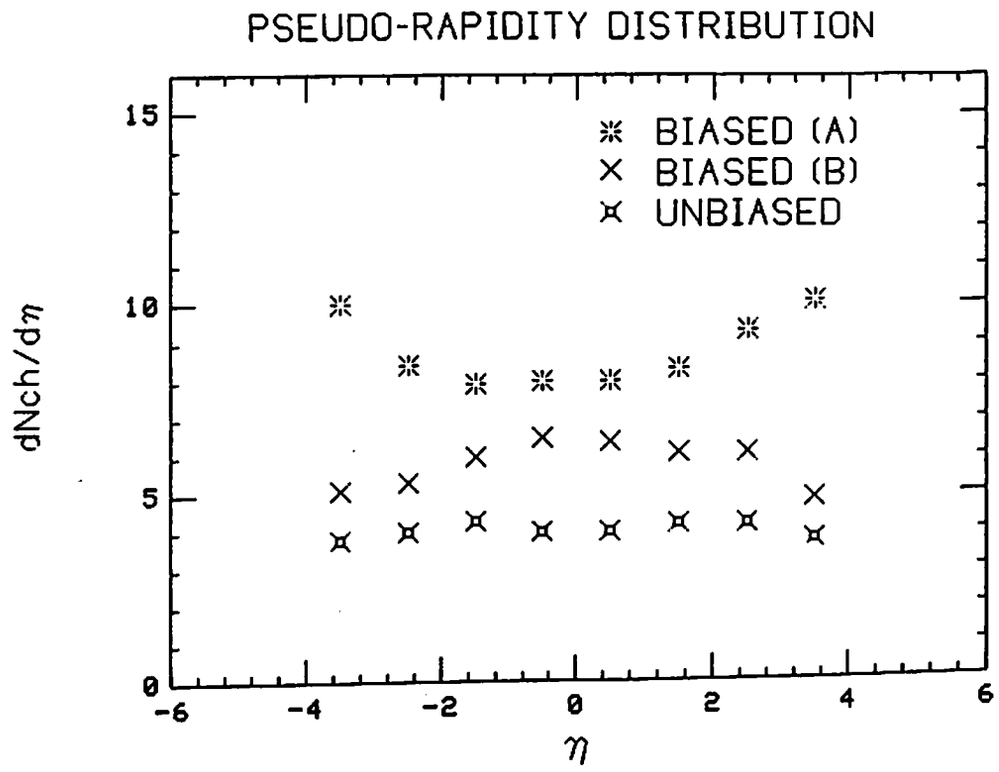
PSEUDO-RAPIDITY DISTRIBUTION
BIASED (A)
BIASED (B)
UNBIASED
dNch/dη
15
10
5
0
-6
-4
-2
0
2
4
6
η

Fig. 8.12

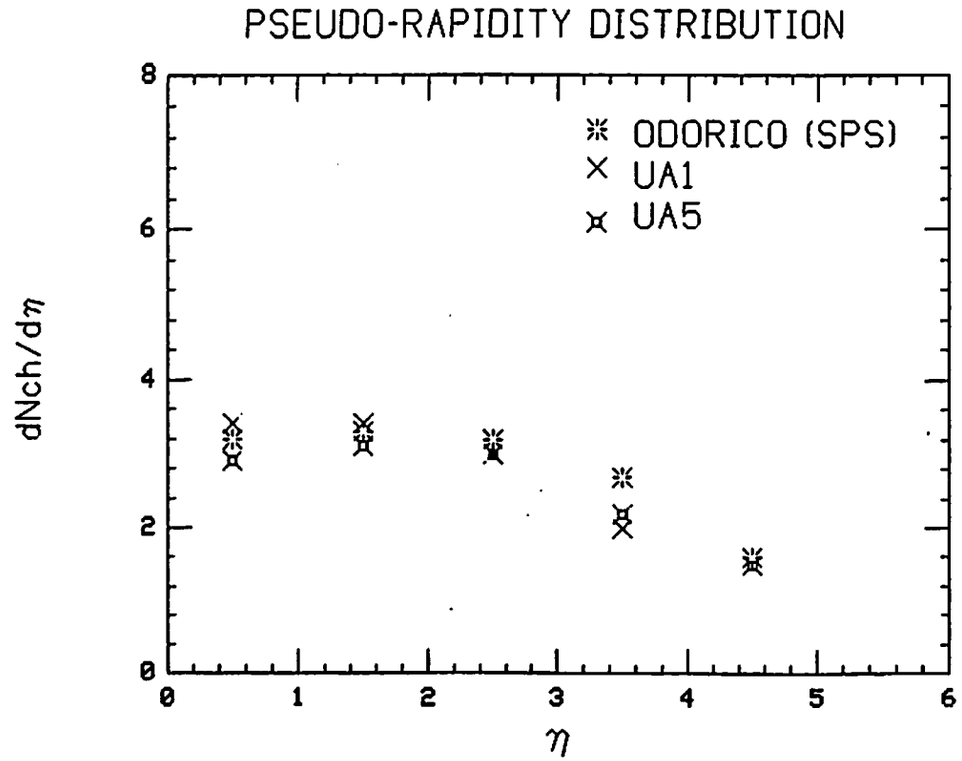
PSEUDO-RAPIDITY DISTRIBUTION
ODORICO (SPS)
UA1
UA5
dNch/dη
η
0
1
2
3
4
5
6
0
2
4
6
8

Fig. 8.13

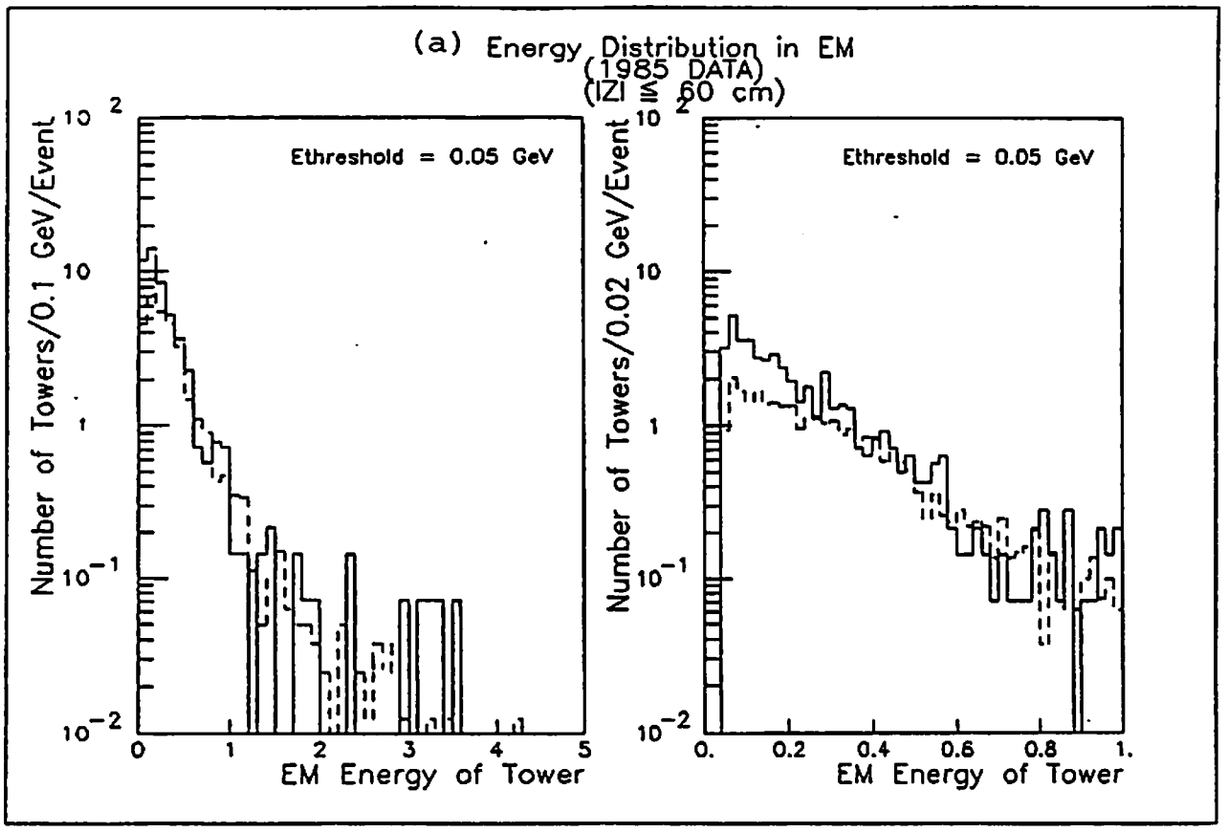
(a) Energy Distribution in EM
(1985 DATA)
(|Z| ≦ 60 cm)
Ethreshold = 0.05 GeV
Number of Towers/0.1 GeV/Event
EM Energy of Tower
Ethreshold = 0.05 GeV
Number of Towers/0.02 GeV/Event
EM Energy of Tower

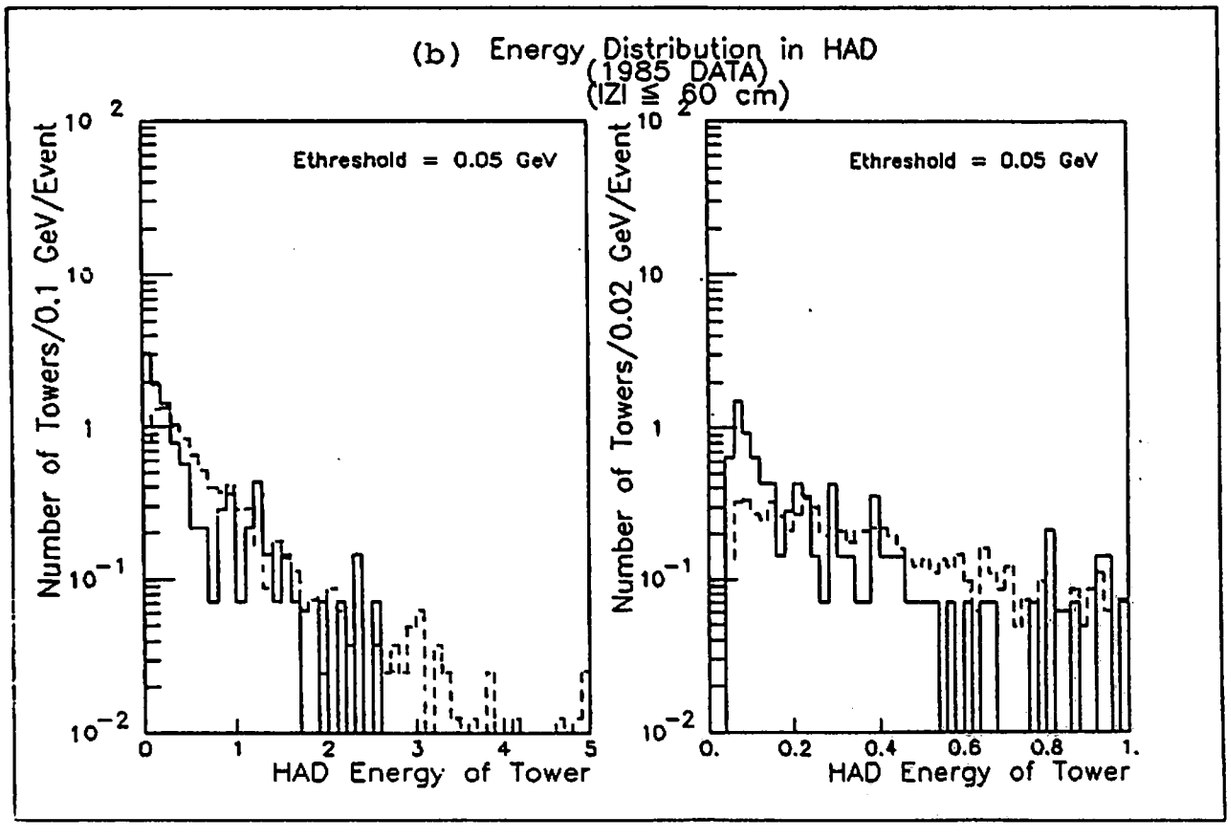
(b) Energy Distribution in HAD
(1985 DATA)
(|Z| ≦ 60 cm)
Ethreshold = 0.05 GeV
Number of Towers/0.1 GeV/Event
HAD Energy of Tower
Ethreshold = 0.05 GeV
Number of Towers/0.02 GeV/Event
HAD Energy of Tower

Fig. 8.14

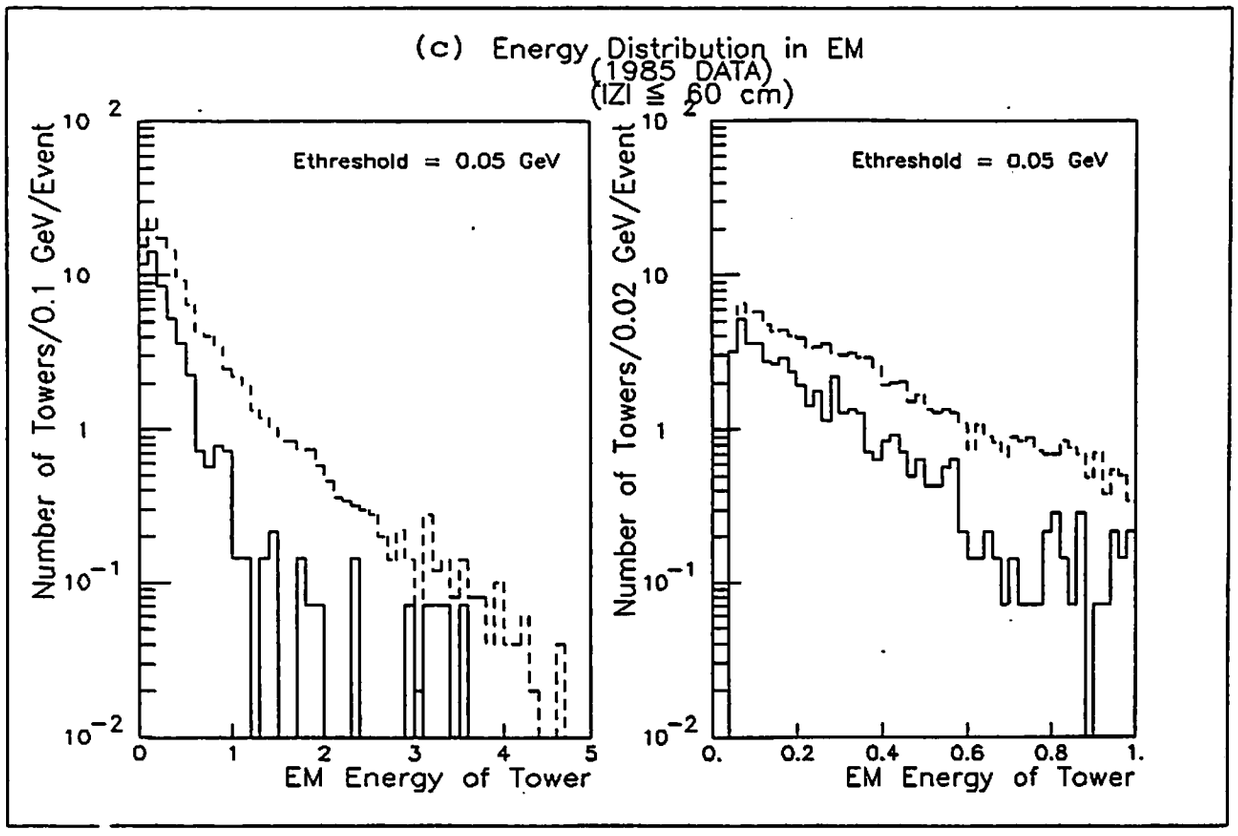
(c) Energy Distribution in EM
(1985 DATA)
(|Z| ≤ 60 cm)
Ethreshold = 0.05 GeV
Number of Towers/0.1 GeV/Event
EM Energy of Tower
Ethreshold = 0.05 GeV
Number of Towers/0.02 GeV/Event
EM Energy of Tower

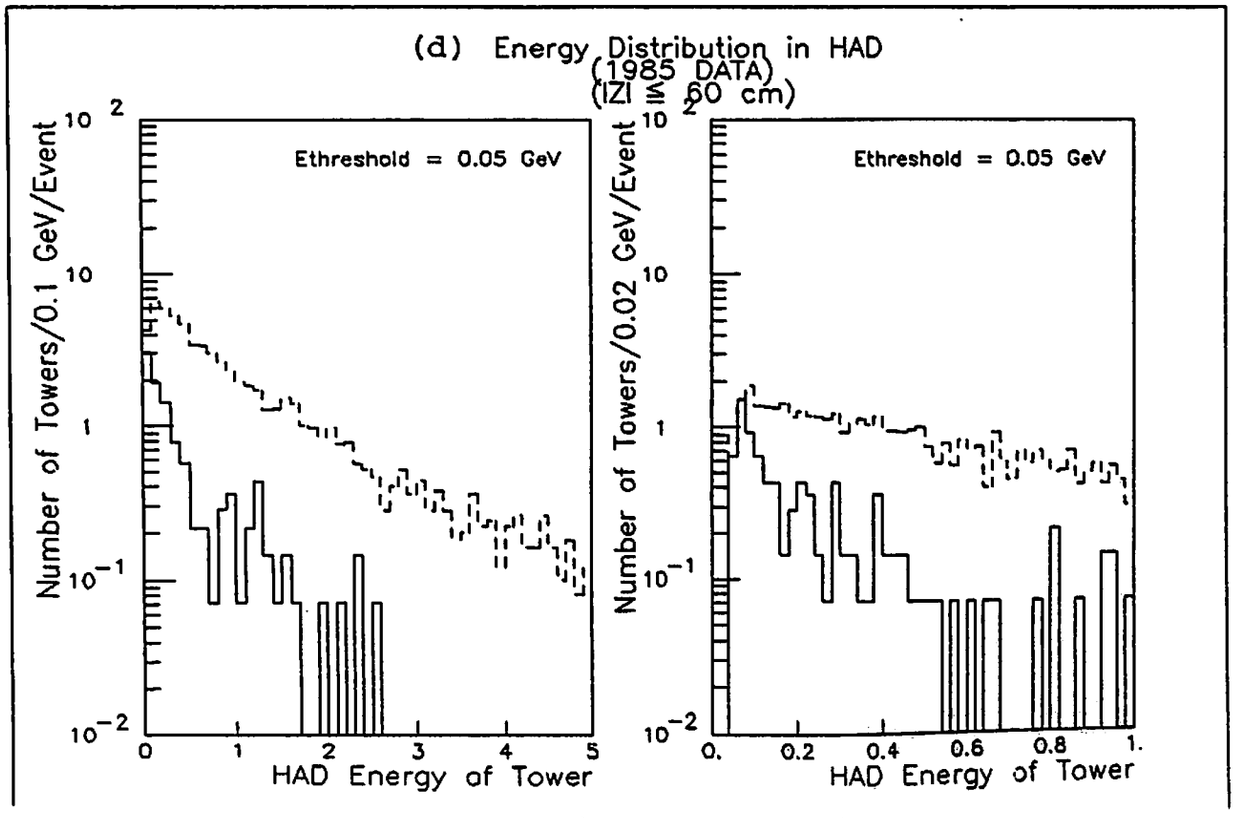
(d) Energy Distribution in HAD
(1985 DATA)
(|Z| ≤ 60 cm)
Ethreshold = 0.05 GeV
Number of Towers/0.1 GeV/Event
HAD Energy of Tower
Ethreshold = 0.05 GeV
Number of Towers/0.02 GeV/Event
HAD Energy of Tower

Fig. 8.14

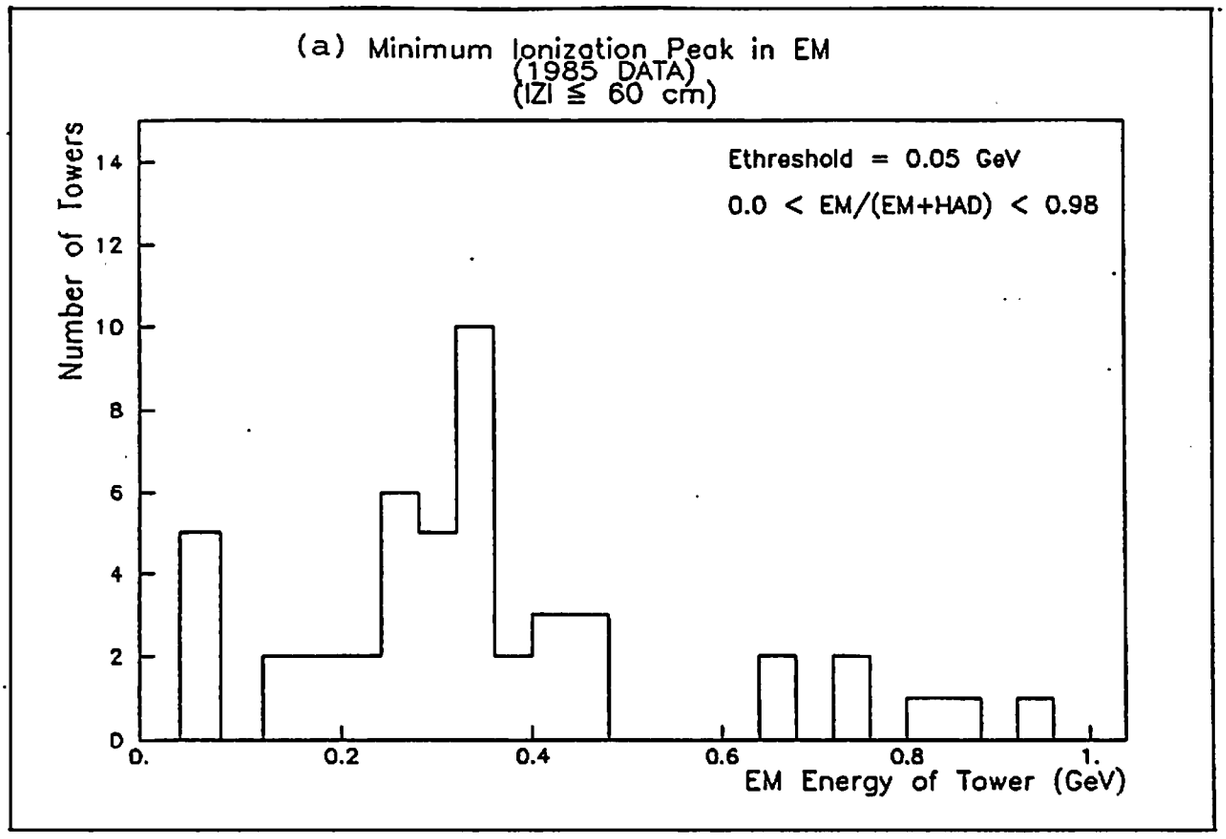
(a) Minimum Ionization Peak in EM
(1985 DATA)
(IZI ≦ 60 cm)
Ethreshold = 0.05 GeV
0.0 < EM/(EM+HAD) < 0.98
Number of Towers
EM Energy of Tower (GeV)

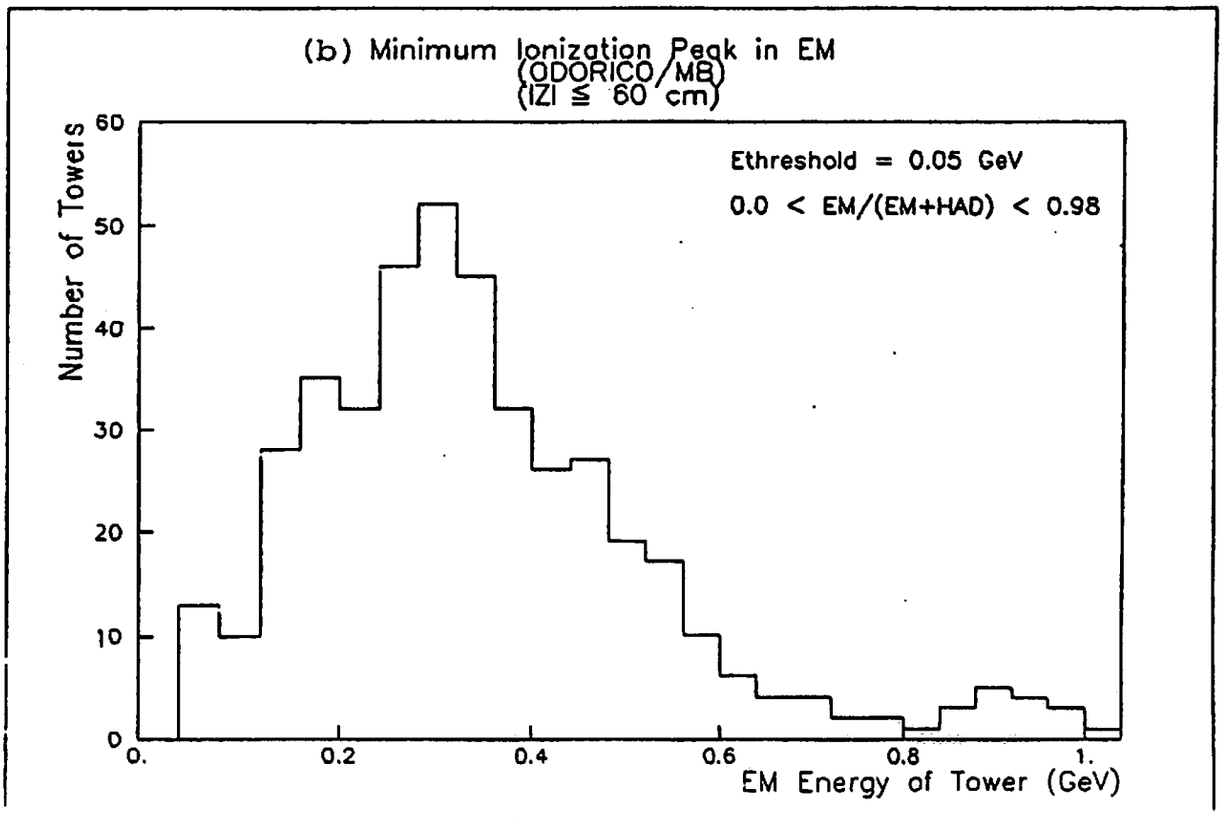
(b) Minimum Ionization Peak in EM
(ODORICO/MB)
(IZI ≦ 60 cm)
Ethreshold = 0.05 GeV
0.0 < EM/(EM+HAD) < 0.98
Number of Towers
EM Energy of Tower (GeV)

Fig. 8.15

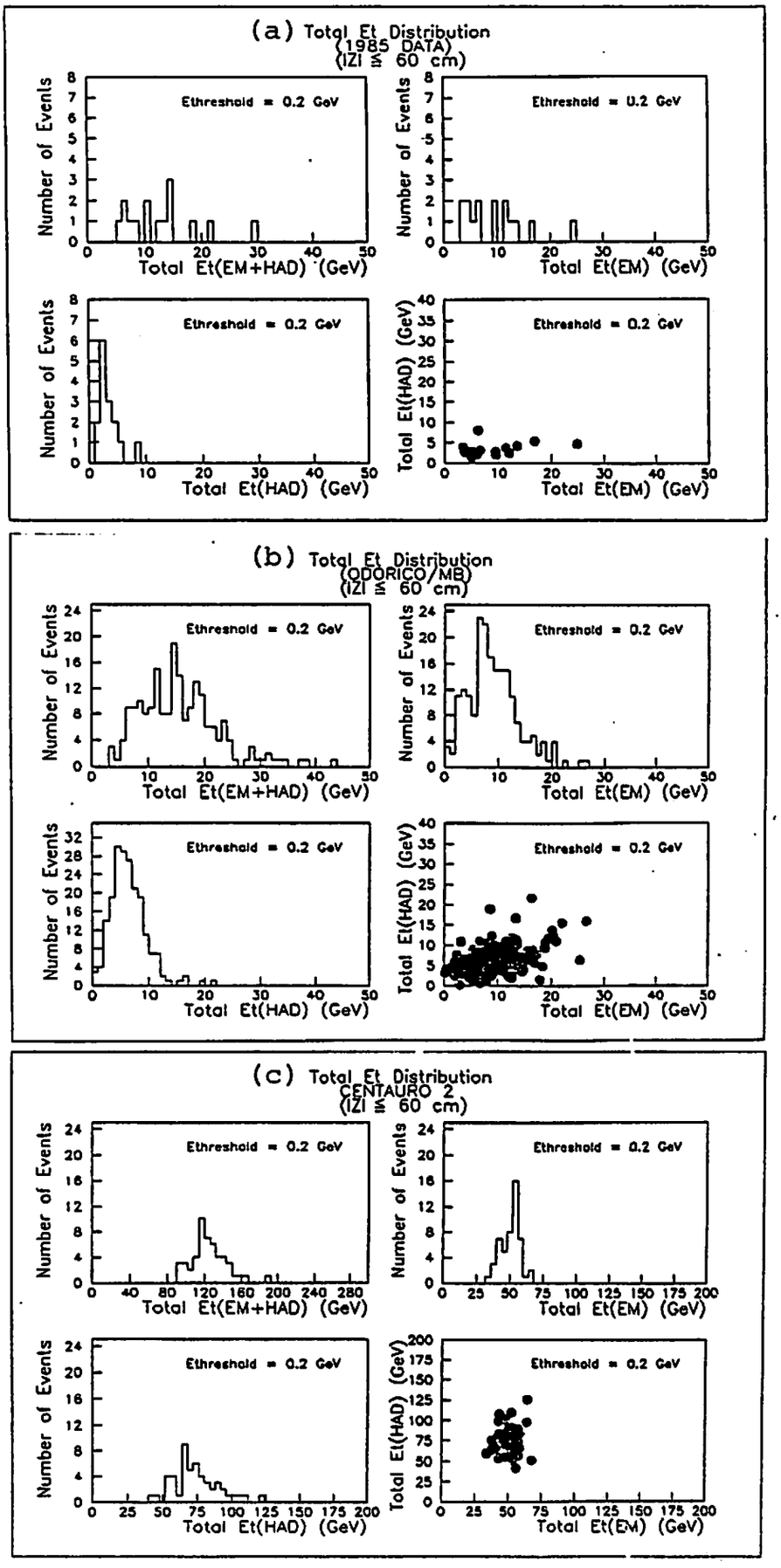
(a) Total Et Distribution
(1985 DATA)
(IZI ≤ 60 cm)
Ethreshold = 0.2 GeV
Number of Events
Total Et(EM+HAD) (GeV)
Total Et(EM) (GeV)
Total Et(HAD) (GeV)
Total Et(HAD) (GeV)
(b) Total Et Distribution
(ODORICO/MB)
(IZI ≤ 60 cm)
(c) Total Et Distribution
CENTAURO 2
(IZI ≤ 60 cm)

Fig. 8.16

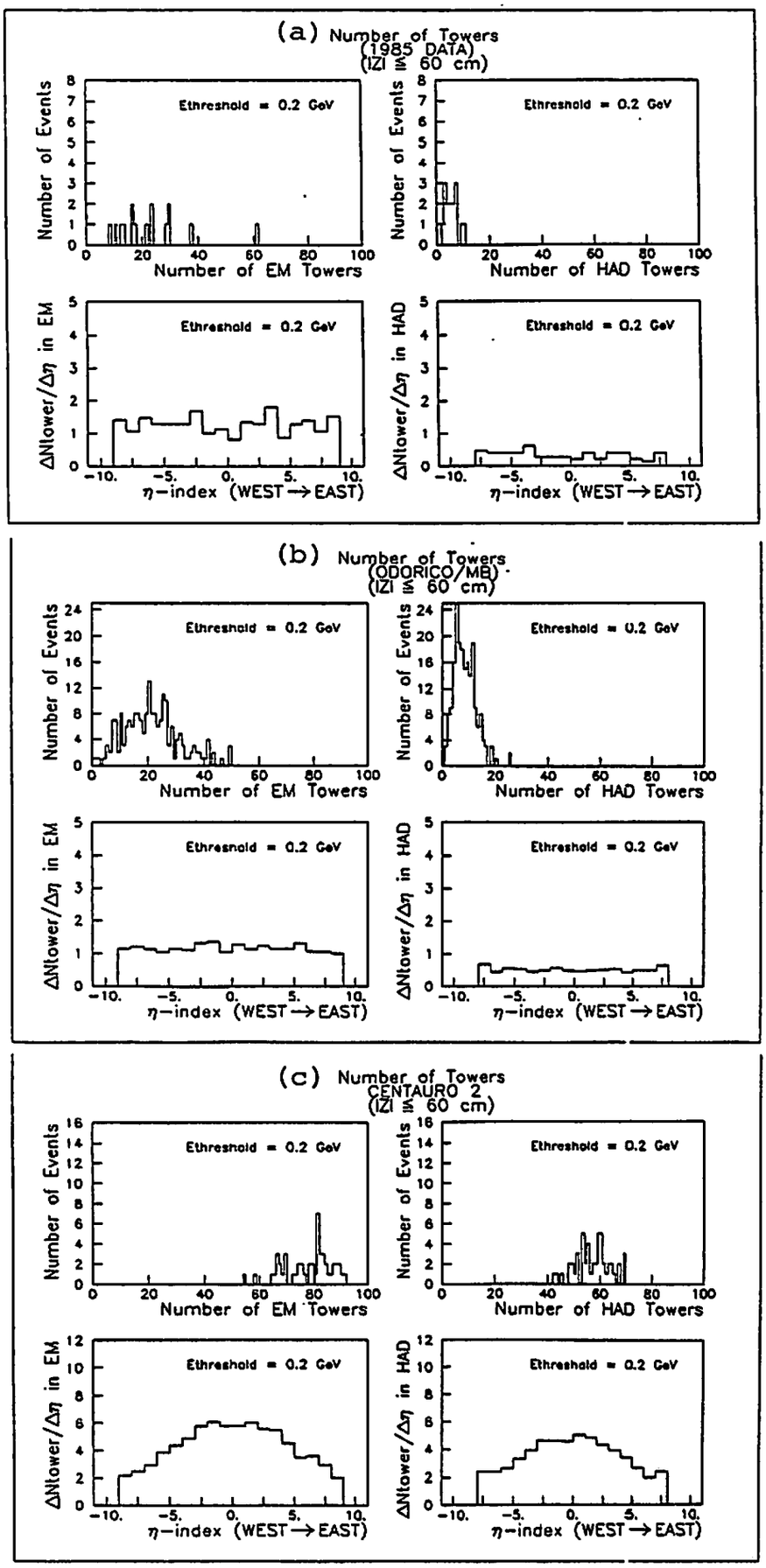
(a) Number of Towers
(1985 DATA)
(|Z| ≤ 60 cm)
Ethreshold = 0.2 GeV
Number of Events
Number of EM Towers
Number of HAD Towers
ΔNtower/Δη in EM
ΔNtower/Δη in HAD
η−index (WEST → EAST)
(b) Number of Towers
(ODORICO/MB)
(|Z| ≤ 60 cm)
(c) Number of Towers
CENTAURO 2
(|Z| ≤ 60 cm)

Fig. 8.17

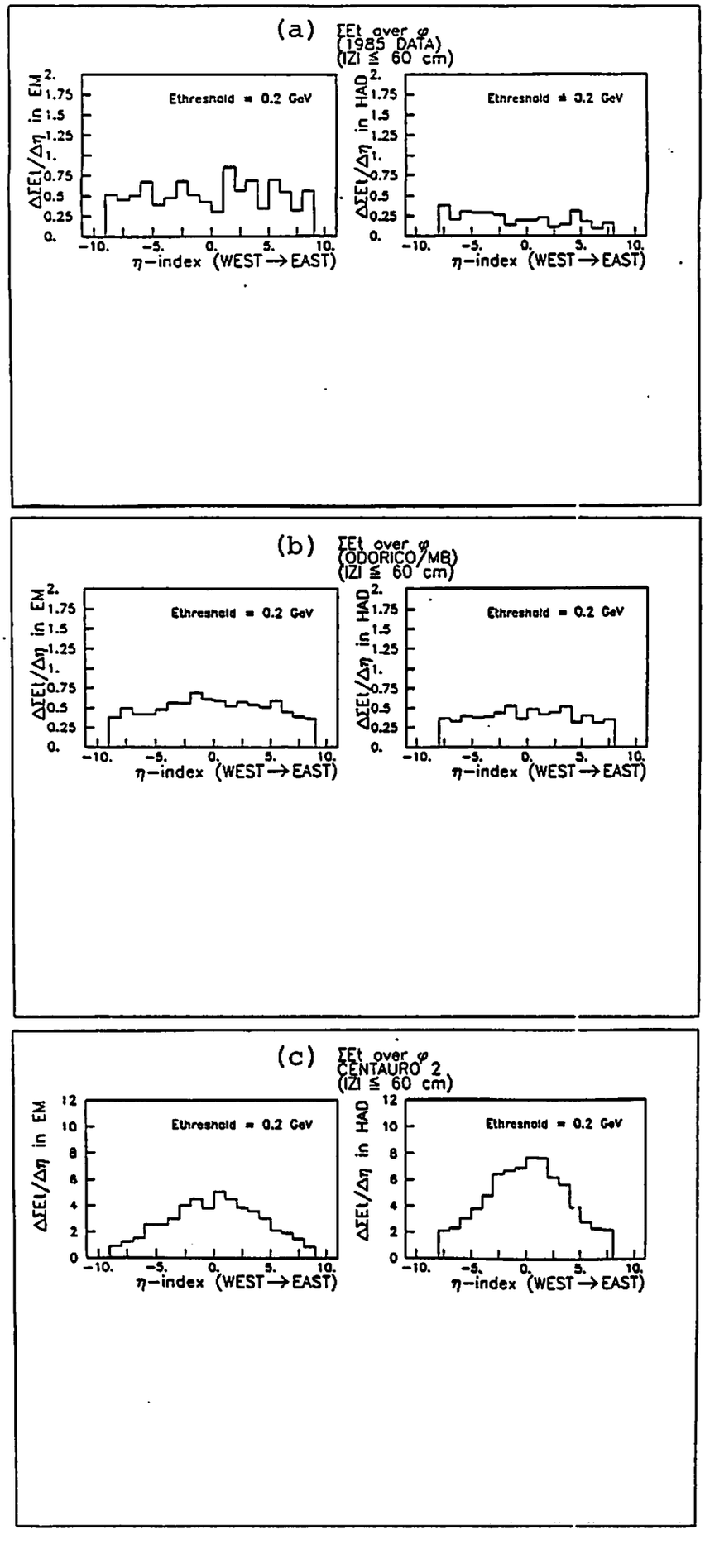
(a)
ΣEt over φ
(1985 DATA)
(IZI ≤ 60 cm)
ΔΣEt/Δη in EM
ΔΣEt/Δη in HAD
Ethresnold = 0.2 GeV
η−index (WEST → EAST)
(b)
ΣEt over φ
(ODORICO/MB)
(IZI ≤ 60 cm)
(c)
ΣEt over φ
CENTAURO 2
(IZI ≤ 60 cm)

Fig. 8.18

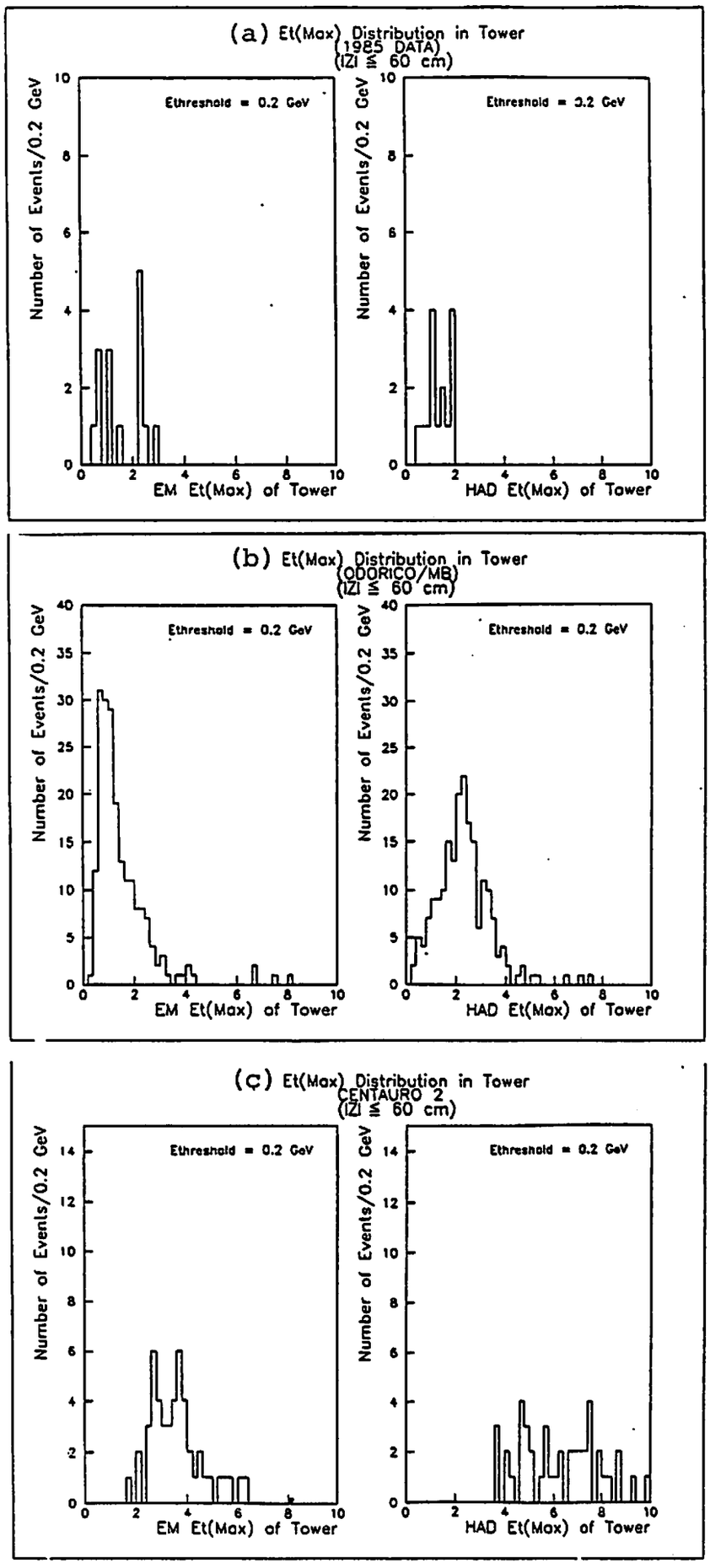
(a) Et(Max) Distribution in Tower
(1985 DATA)
(|Z| ≤ 60 cm)
Ethreshold = 0.2 GeV
Number of Events/0.2 GeV
EM Et(Max) of Tower
HAD Et(Max) of Tower
(b) Et(Max) Distribution in Tower
(ODORICO/MB)
(|Z| ≤ 60 cm)
(c) Et(Max) Distribution in Tower
CENTAURO 2
(|Z| ≤ 60 cm)

Fig. 8.19

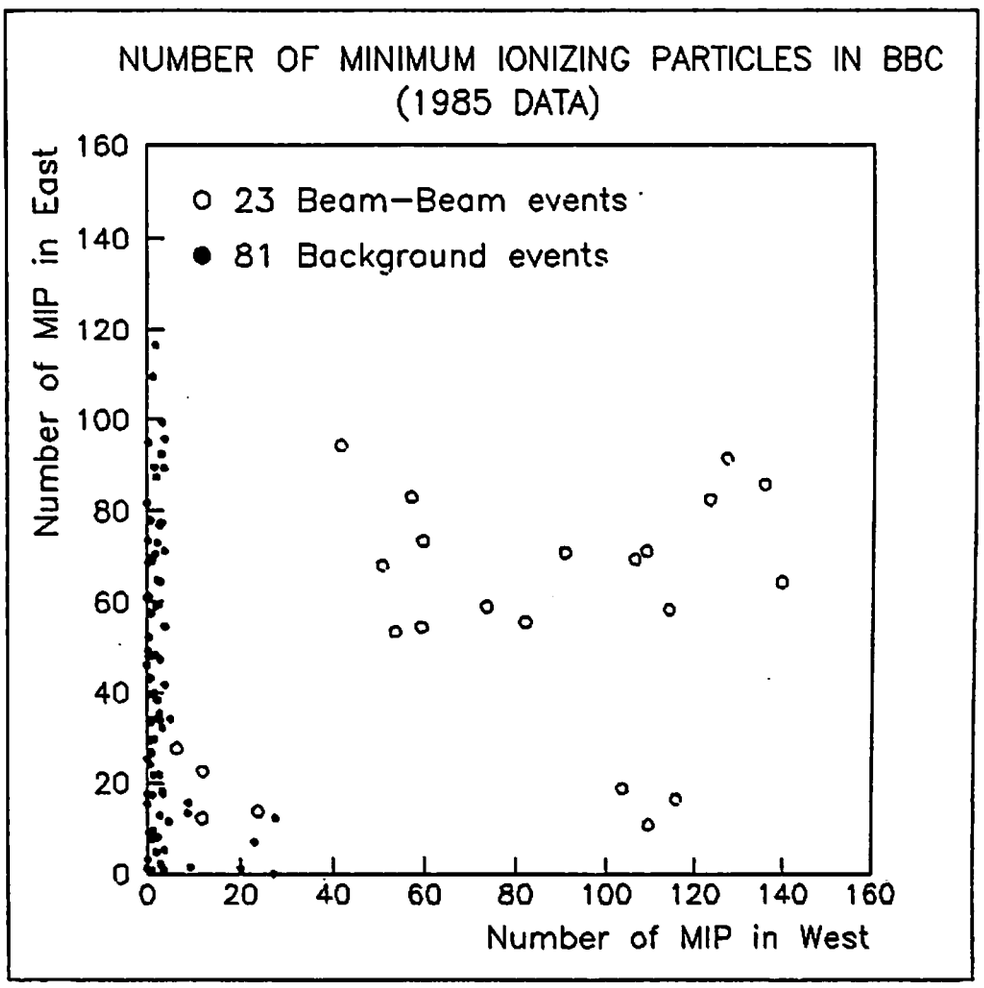
NUMBER OF MINIMUM IONIZING PARTICLES IN BBC
(1985 DATA)
o 23 Beam–Beam events
● 81 Background events
Number of MIP in East
Number of MIP in West
0
20
40
60
80
100
120
140
160

Fig. 8.20

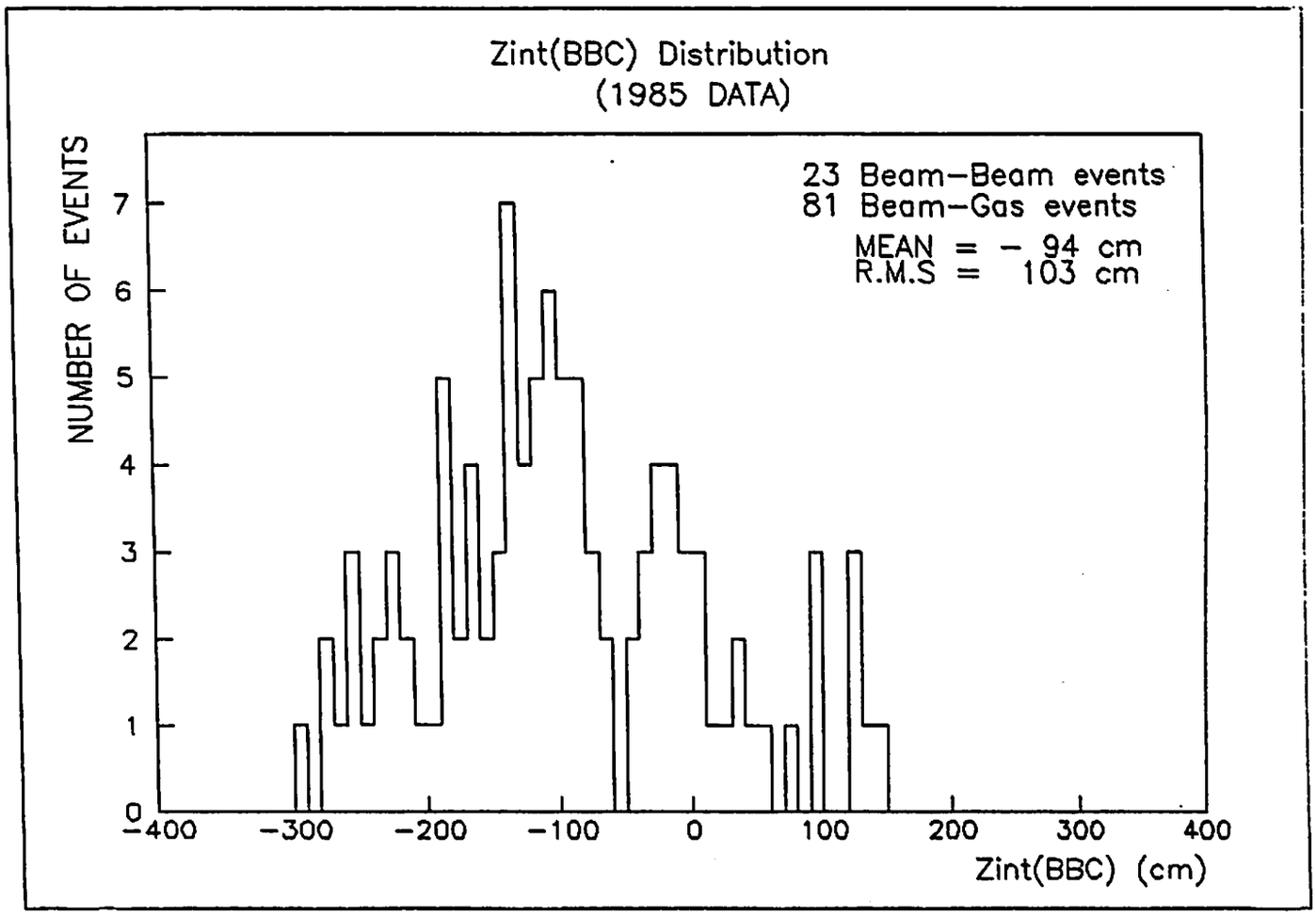
Zint(BBC) Distribution
(1985 DATA)
23 Beam–Beam events
81 Beam–Gas events
MEAN = – 94 cm
R.M.S = 103 cm
NUMBER OF EVENTS
0
1
2
3
4
5
6
7
–400
–300
–200
–100
0
100
200
300
400
Zint(BBC) (cm)

Fig. 8.21

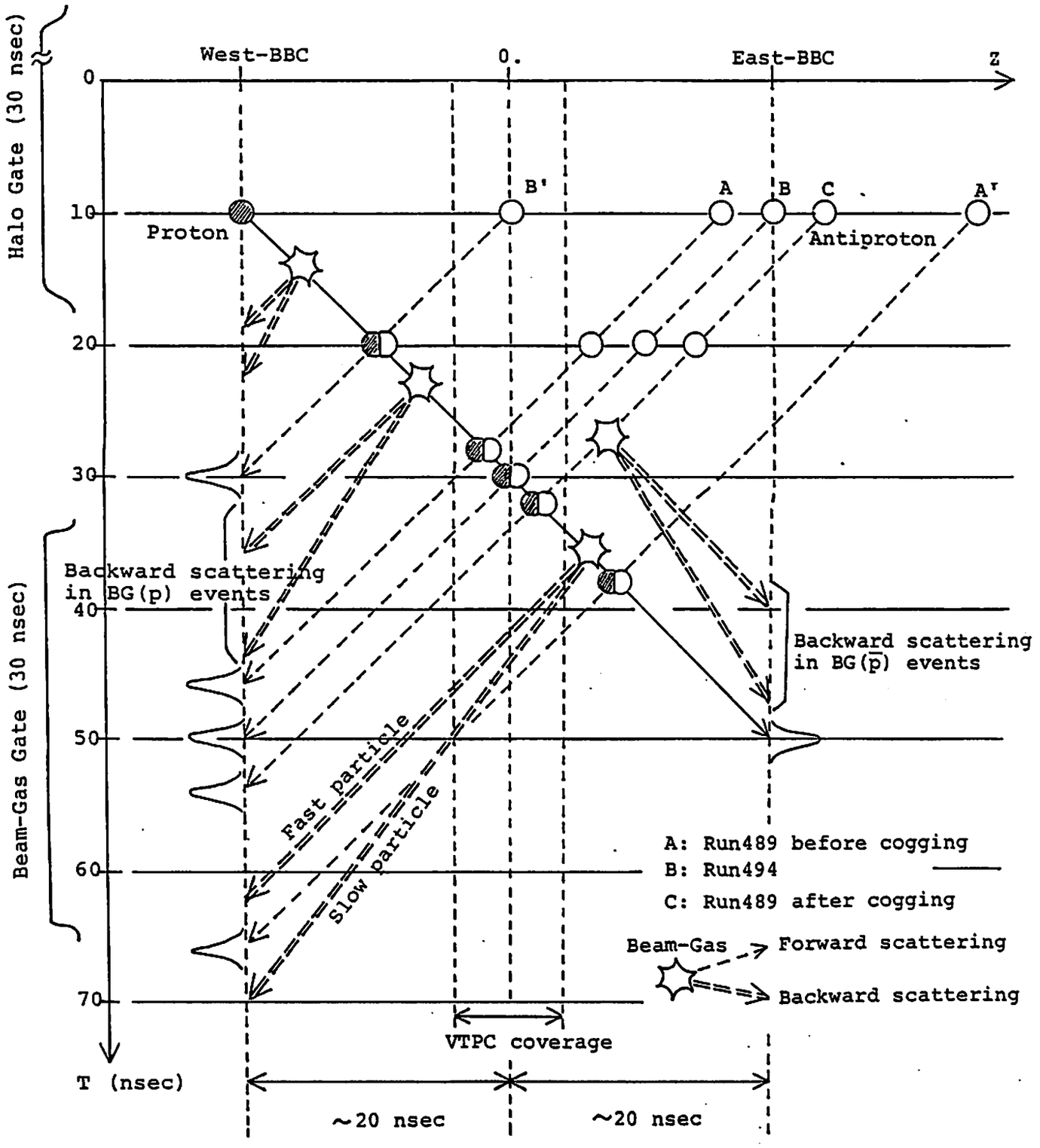
Halo Gate (30 nsec)
West-BBC
0.
East-BBC
Z
0
10
20
30
40
50
60
70
B'
A
B
C
A'
Proton
Antiproton
Backward scattering
in BG(p) events
Backward scattering
in BG($\bar{p}$) events
Beam-Gas Gate (30 nsec)
Fast particle
Slow particle
A: Run489 before cogging
B: Run494
C: Run489 after cogging
Beam-Gas
Forward scattering
Backward scattering
VTPC coverage
T (nsec)
~20 nsec
~20 nsec

Fig. 8.22

(Ref.) Phys. Lett. 107B (1981) 310

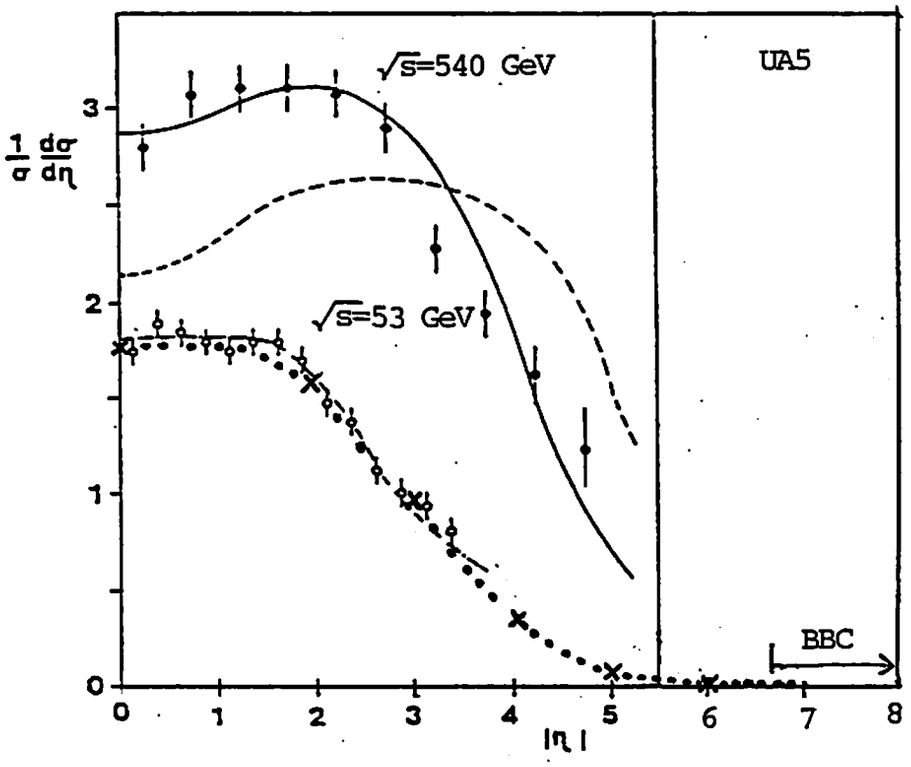

Fig. 8.23

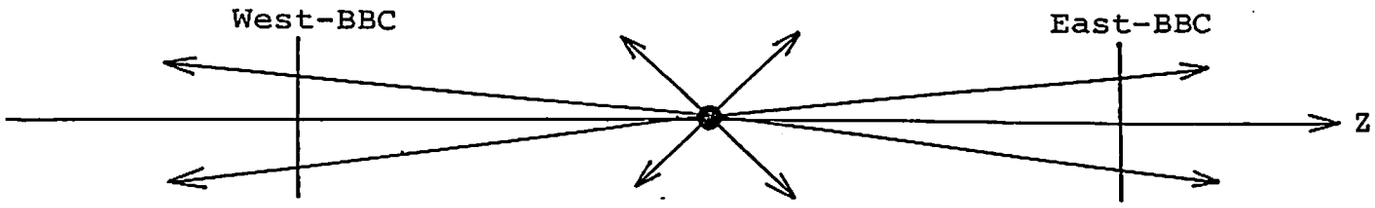

(a) Beam-beam event

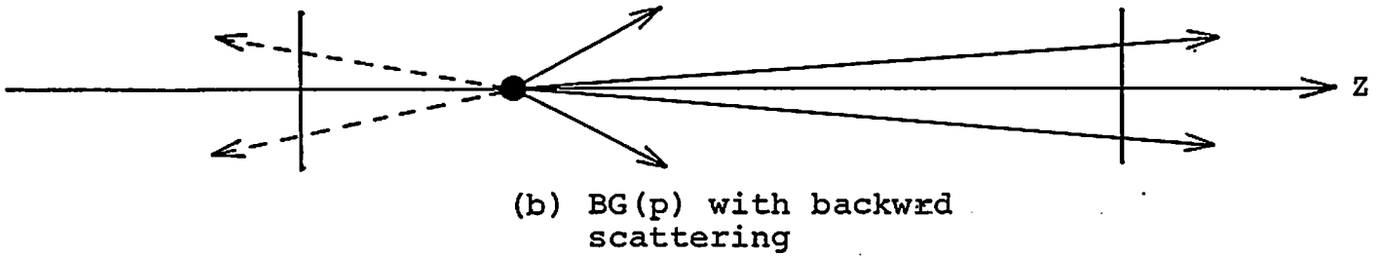

(b) BG(p) with backward scattering

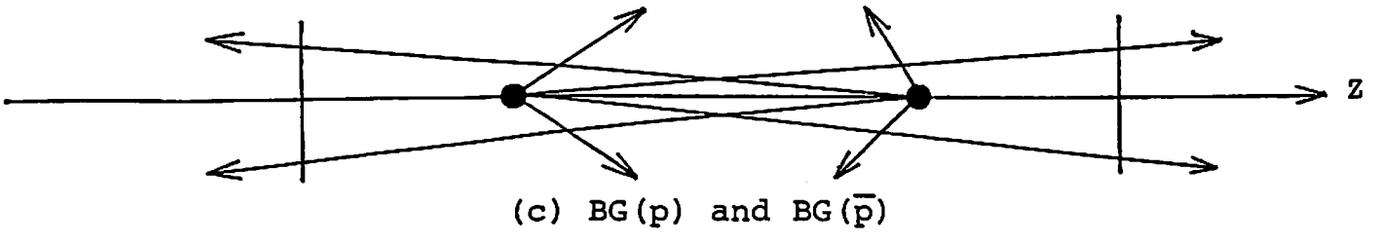

(c) BG(p) and BG($\bar{p}$)

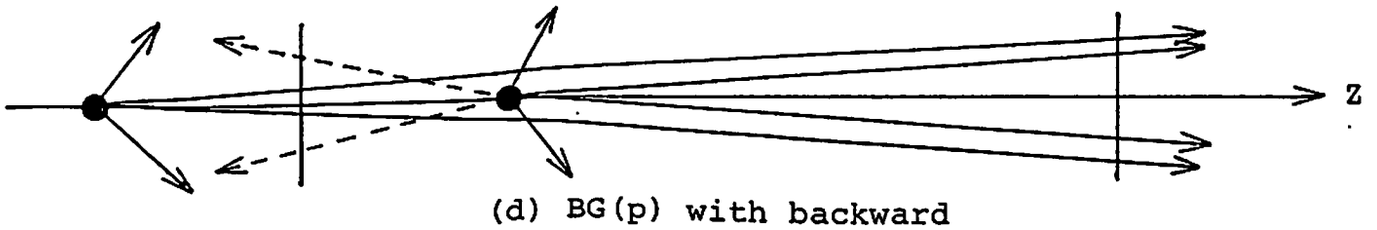

(d) BG(p) with backward scattering and BG(p) outside BBC

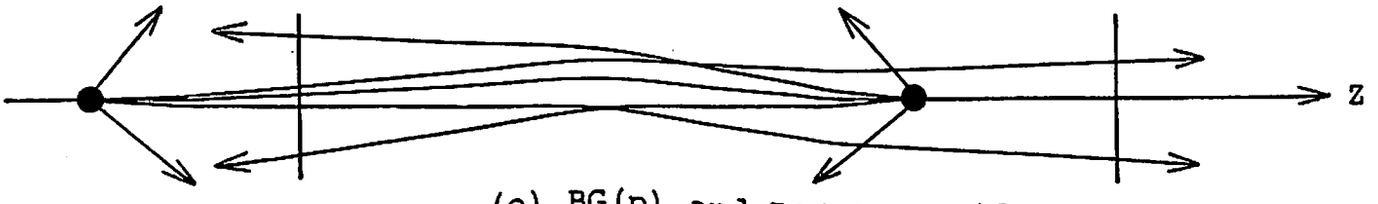

(e) BG(p) and BG(p) outside BBC

Fig. 8.24

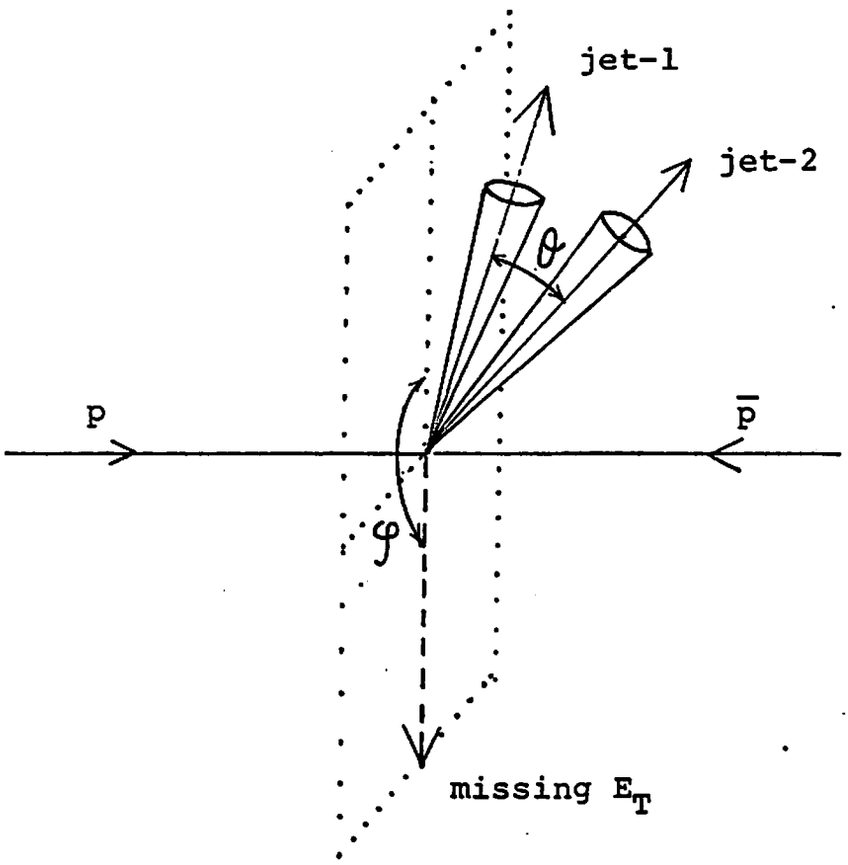

Fig. 9.1

(a) HEAVY LEPTON (M=60 GeV)

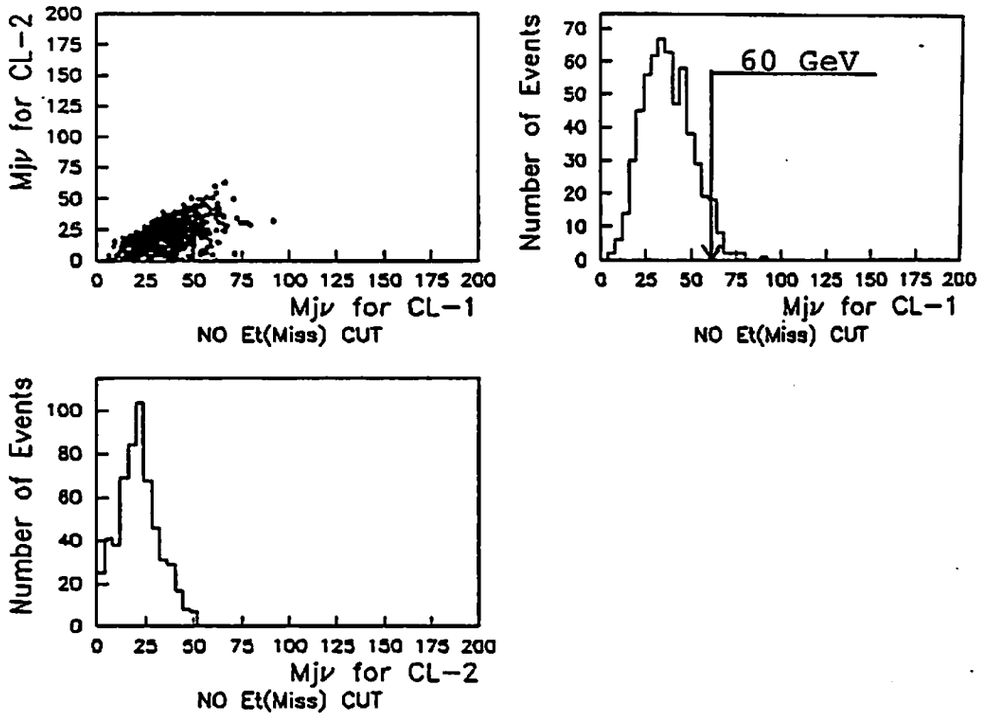

(b) $W \rightarrow \tau \nu$

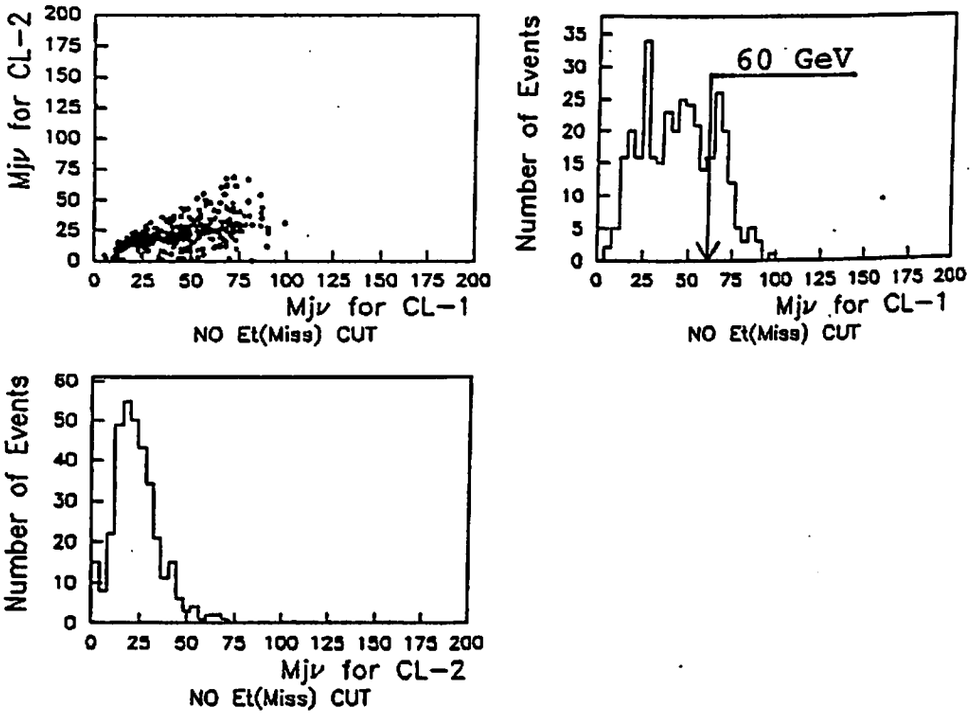

Fig. 9.2

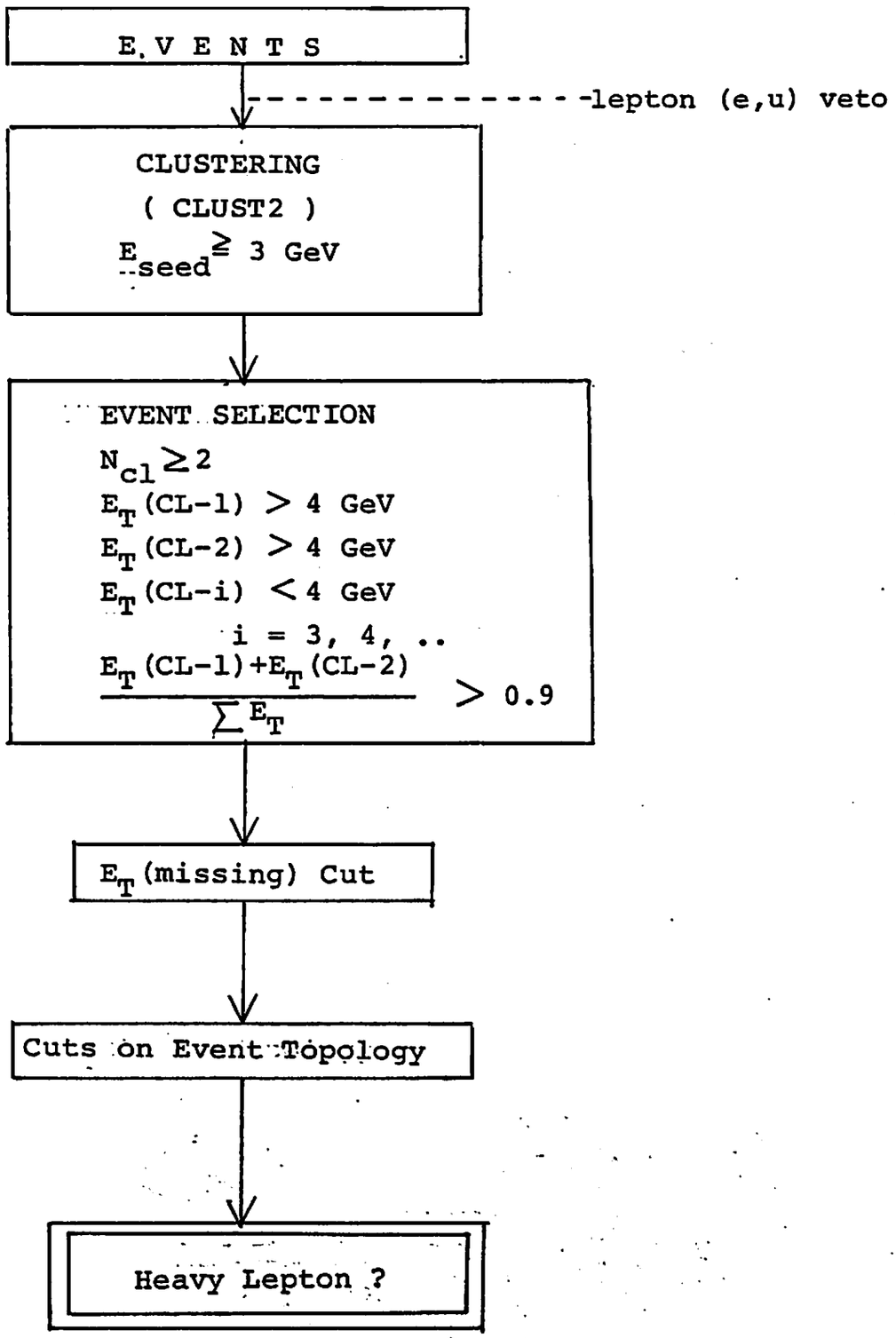
E V E N T S
lepton (e,u) veto
CLUSTERING
(CLUST2)
$E_{seed} \geq 3$ GeV
EVENT SELECTION
$N_{cl} \geq 2$
$E_T(CL-1) > 4$ GeV
$E_T(CL-2) > 4$ GeV
$E_T(CL-i) < 4$ GeV
$i = 3, 4, ..$
$\frac{E_T(CL-1)+E_T(CL-2)}{\sum E_T} > 0.9$
E_T(missing) Cut
Cuts on Event Topology
Heavy Lepton ?

Fig. 9.3

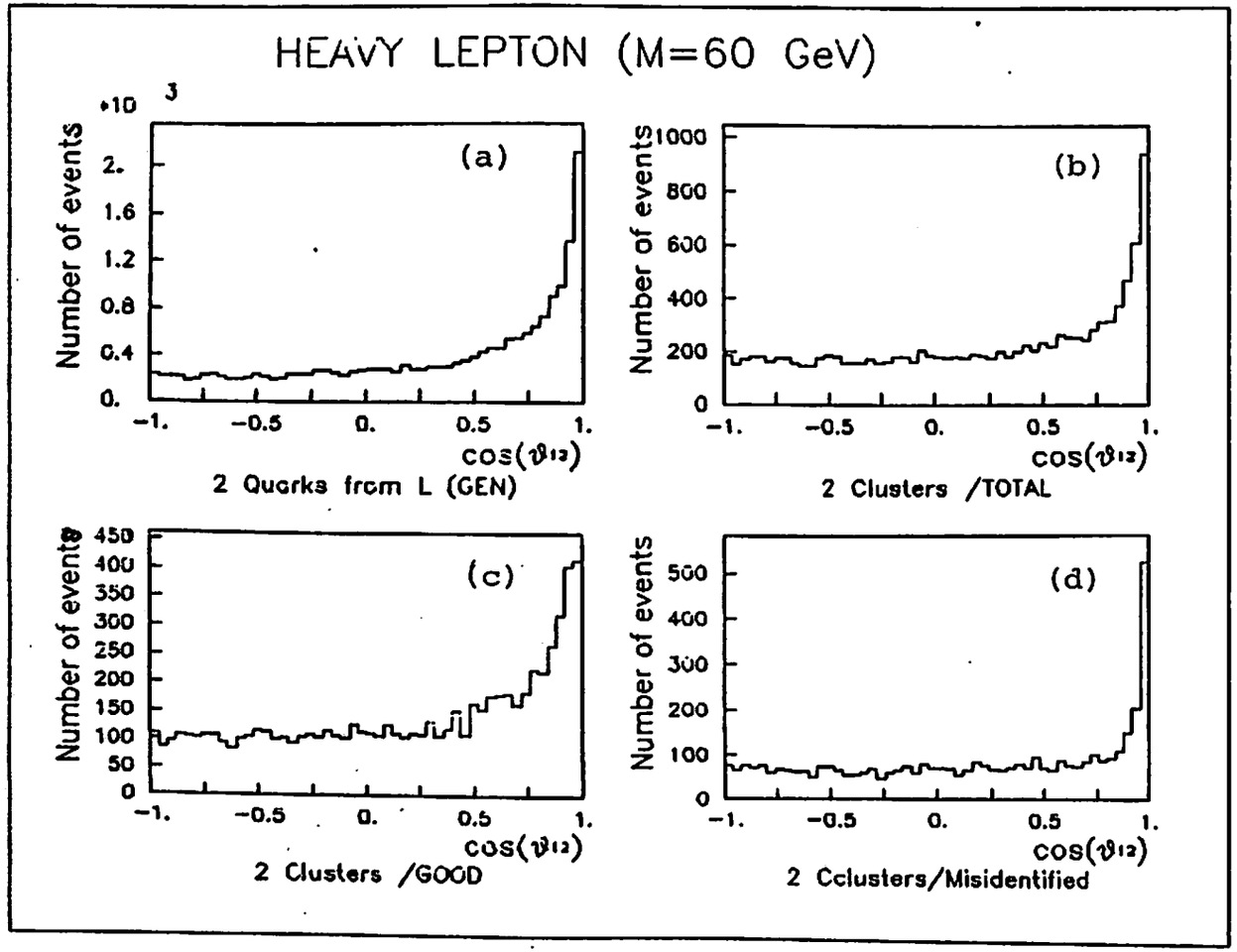
HEAVY LEPTON (M=60 GeV)
(a)
Number of events
×10 3
2 Quarks from L (GEN)
(b)
Number of events
2 Clusters /TOTAL
(c)
Number of events
2 Clusters /GOOD
(d)
Number of events
2 Cclusters/Misidentified
cos(ϑ12)

Fig. 9.4

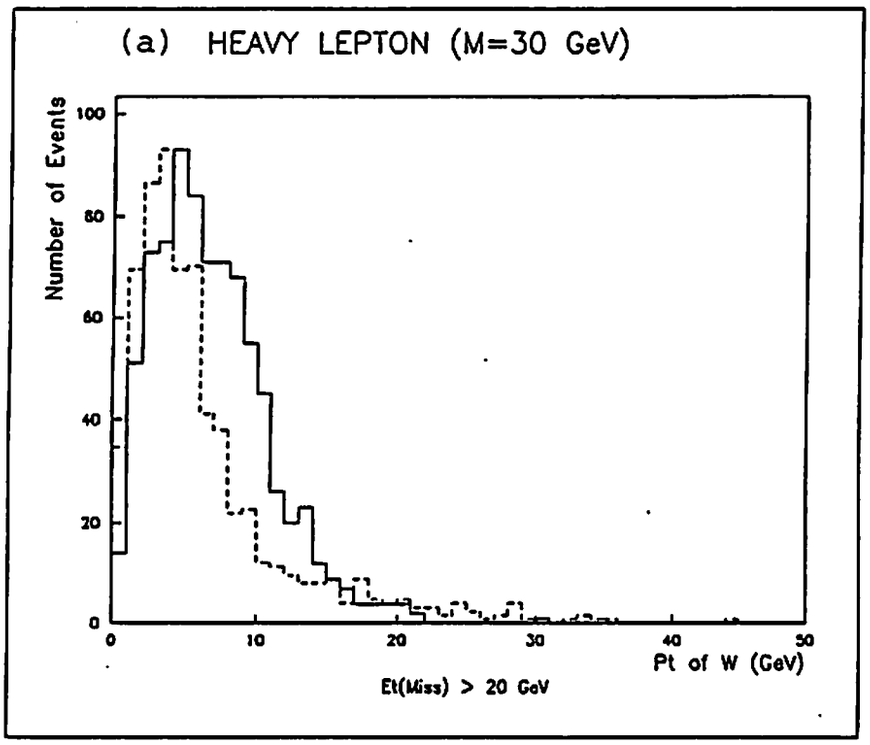
(a) HEAVY LEPTON (M=30 GeV)
Number of Events
100
80
60
40
20
0
0
10
20
30
40
50
Pt of W (GeV)
Et(Miss) > 20 GeV

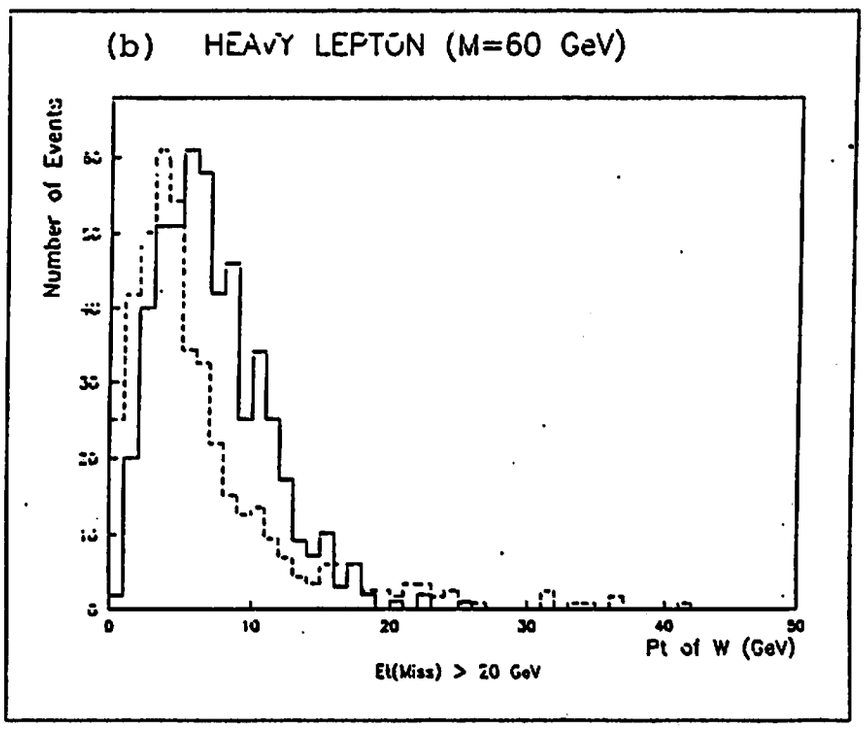
(b) HEAVY LEPTON (M=60 GeV)
Number of Events
0
10
20
30
40
50
Pt of W (GeV)
Et(Miss) > 20 GeV

Fig. 9.5

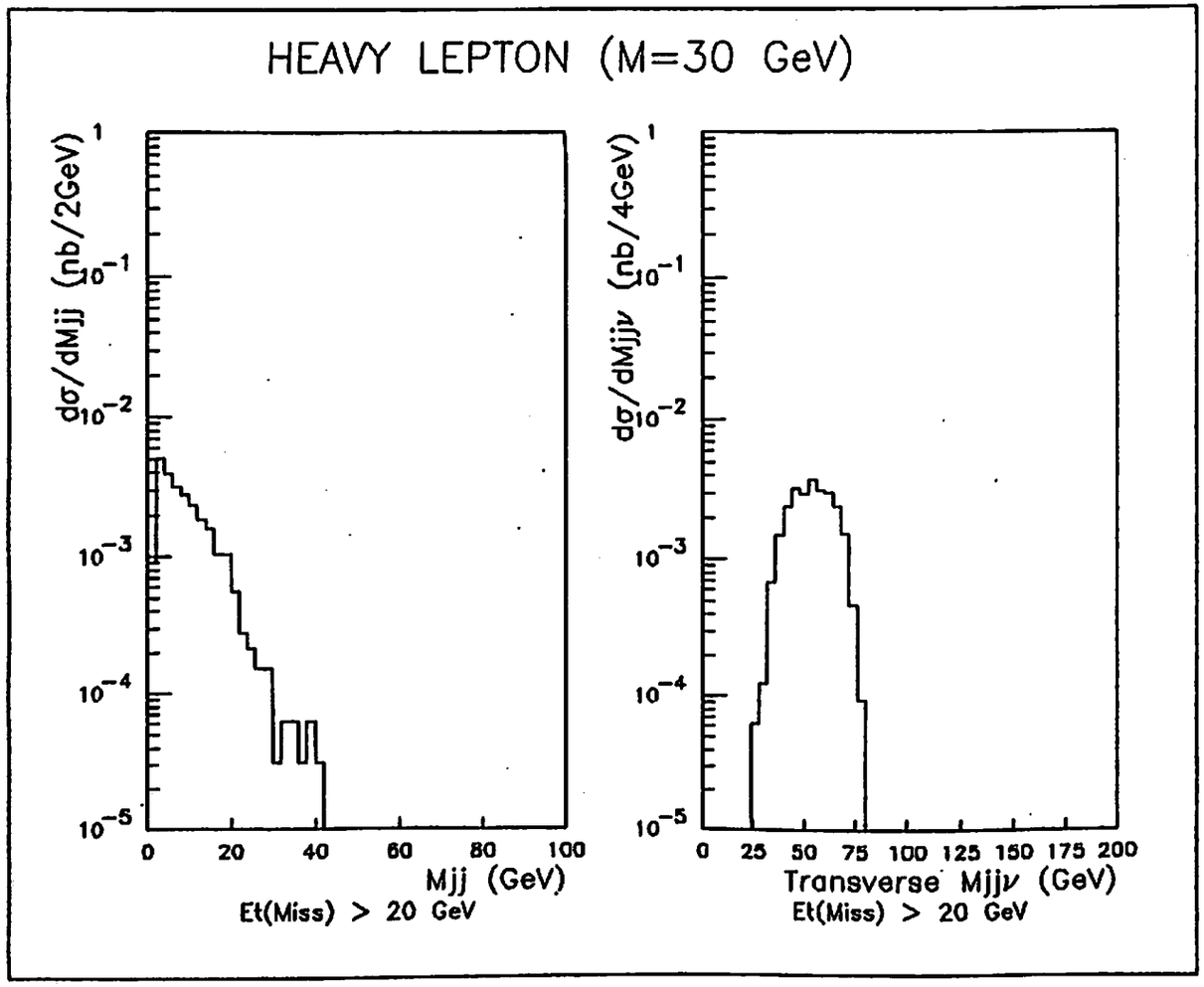
HEAVY LEPTON (M=30 GeV)
dσ/dMjj (nb/2GeV)
1
10^-1
10^-2
10^-3
10^-4
10^-5
0
20
40
60
80
100
Mjj (GeV)
Et(Miss) > 20 GeV
dσ/dMjjν (nb/4GeV)
1
10^-1
10^-2
10^-3
10^-4
10^-5
0
25
50
75
100
125
150
175
200
Transverse Mjjν (GeV)
Et(Miss) > 20 GeV

Fig. 9.6

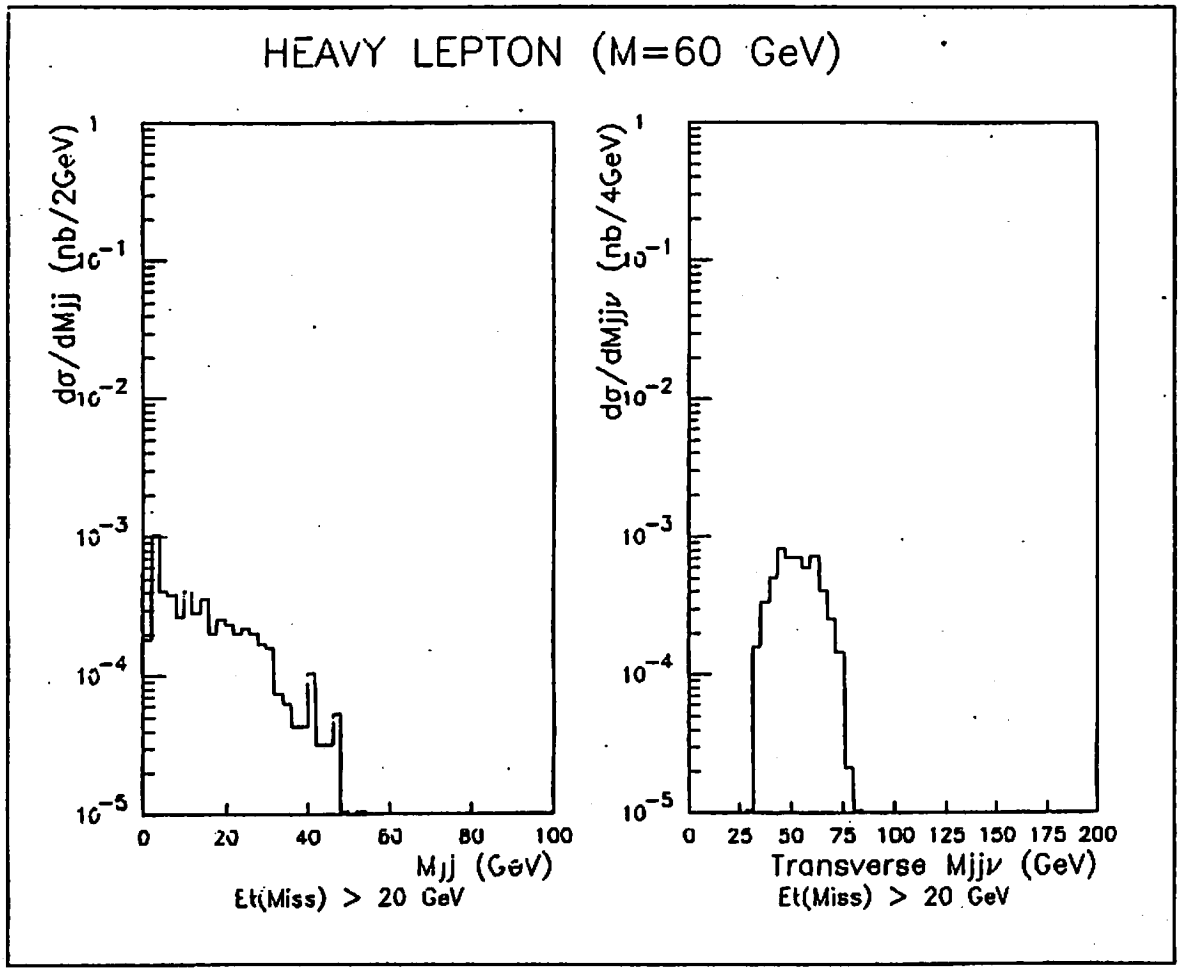
HEAVY LEPTON (M=60 GeV)
dσ/dMjj (nb/2GeV)
1
10^-1
10^-2
10^-3
10^-4
10^-5
0
20
40
60
80
100
Mjj (GeV)
Et(Miss) > 20 GeV
dσ/dMjjν (nb/4GeV)
1
10^-1
10^-2
10^-3
10^-4
10^-5
0
25
50
75
100
125
150
175
200
Transverse Mjjν (GeV)
Et(Miss) > 20 GeV

Fig. 9.7

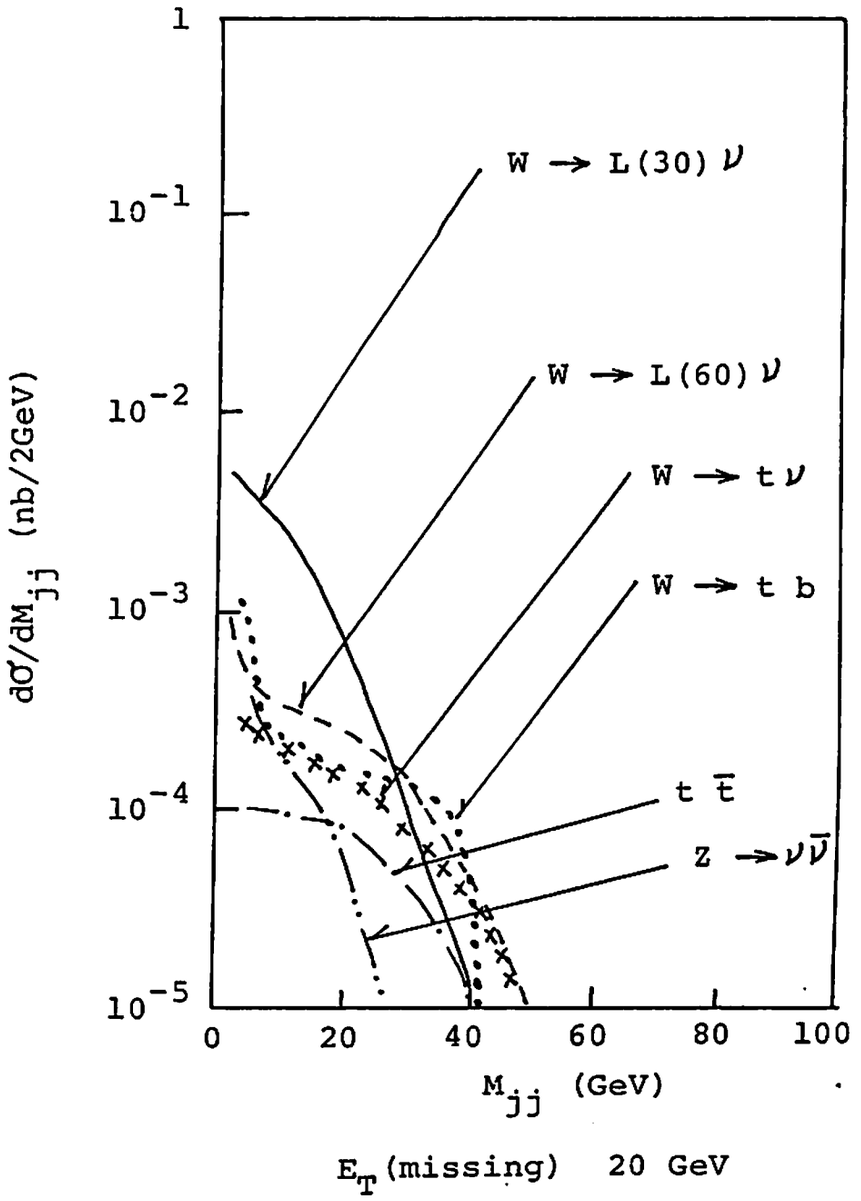
1
10^{-1}
10^{-2}
10^{-3}
10^{-4}
10^{-5}
$d\sigma/dM_{jj}$ (nb/2GeV)
W → L(30) ν
W → L(60) ν
W → t ν
W → t b
t t̄
Z → ν ν̄
0
20
40
60
80
100
M_{jj} (GeV)
E_T(missing) 20 GeV

Fig. 9.8

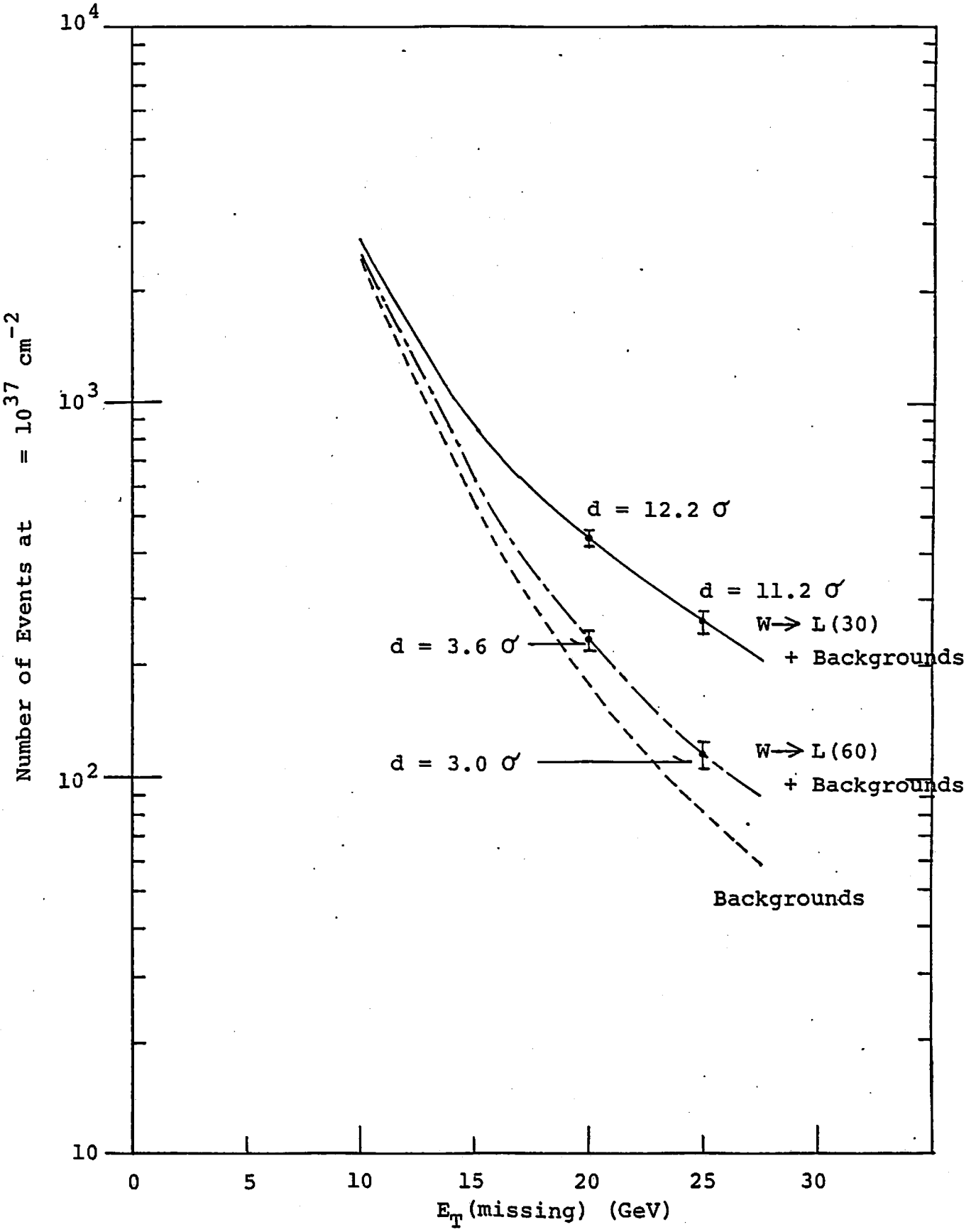
10^4
10^3
10^2
10
Number of Events at = 10^{37} cm^{-2}
d = 12.2 σ
d = 11.2 σ
W→ L(30)
+ Backgrounds
d = 3.6 σ
d = 3.0 σ
W→ L(60)
+ Backgrounds
Backgrounds
0
5
10
15
20
25
30
E_T(missing) (GeV)

Fig. 9.9